POLITECNICO DI MILANO
MECHANICAL ENGINEERING DEPRTMENT
DOCTORAL PROGRAMME IN MECHANICAL ENGINEERING

COLD SPRAY COATING AIMED AT NANOCRYSTALLIZATION: PROCESS CHARACTERIZATION AND FATIGUE STRENGTH ASSESSMENT

Doctoral Dissertation of:
Ramin Ghelichi

Supervisor:
Prof. Mario Guagliano

Tutor:
Prof. Marco Boniardi

Coordinator:
Prof. Gianpiero Mastinu

Year 2011-Cycle XXIV

Dedication

To my lovely parents
Pashootan and **Fatemeh Ghelichi**

Acknowledgement

It is a myth that a dissertation is the soul-wrenching creation solely of its author's time, toil and tenacity. The current thesis is the product of contribution of the people who have been helping me sparingly through these years. Although I am not able to appreciate completely and even mention the value of their support.

I am deeply thankful to my supervisor, **Prof. Mario Guagliano** for his guidance and infinite support in every single step of this research. His intelligence, knowledge, and wise comments have always lit up new ways and ideas. No one should be subjected to the torture of reading my early attempts at technical writing, and thanks to **Mario**, no one will. He helped in different aspects of my life during the years far from home and kindly treated me like a member of his family.

It is difficult to overstate my gratitude to **Prof. Hamid Jahed** from University of Waterloo, who I attribute the level of my Master's degree to his encouragement and efforts; without him, too, this thesis would not have been completed.

I owe my sincere gratitude to **Prof. Bertrand Jodoin** from University of Ottawa. It was an honor to work with his group **Mathieu Bolduc Jean-Louis Pelletier**, **Jean-Michel Roy**, **Jamil Assad**, **Rubén Fernández Urrutia**, and especially **Daniel MacDonald**; without their support and friendly helps I would not able to get this thesis done.

I thank **Prof. Ines Inés Fernández Pariente** from University of Oviedo, for her kind-great efforts and friendly support which gave untiring help during difficult moments.

My great appreciation to **Prof. Marco Verani** from Mathematics Department, for helping me through mathematical approaches; his intelligence along with inspiration has opened new doors for me and has had a remarkable influence on my entire research.

My sincere thanks to **Prof. Laura Vergani**, **Prof. Gianpiero Mastinu**, **Prof. Bianca Maria Colosimo** and especially **Prof. Andrea Bernasconi** for their detailed review, constructive criticism and excellent advices during the preparation of this thesis.

A special mention should be made of the staffs of **C4**, **CLASD** and **Origoni B** Labs, who have been very helpful with experimental set-ups and practical advices: **Luigi Lanzani**, **Mauro De Mori**, **Luciano Lucherini**, **Filippo Spinelli**, **Andrea Del Viscio**, **Sergio Bruno**, **Moreno Riccardi**, **Giuseppe Ghilardi**, **Marco Ghilardi**, **Dario Giusti**, **Pasquale Aquilino**, **Francesco Cacciatore** and **Maurizio Pardi**; in particular **Alessandro Tosi** and **Maurizio Groppi** who readily took time out of their busy schedules to help me frequently with all the experimental tests and machines. **Pietro Pellin** and **Maurizio Pardi** deserve special thanks for their help through the XRD measurements, microscopy sample preparations, etc. I wish to thank **Luca Signorelli** for his contributions of time, ideas and experiences.

I would like to express my gratitude to **Dr. Simone Vezzù** from Nanofab Lab. in Civen for his generous support and execution of coating on our specimens.

I have to appreciate the work of my dear friends **Antonio Mairano** and **Daniele Vago** who as their Master thesis have contributed to this research.

The support and care of my friends helped me overcome setbacks and stay focused on my graduate study. I greatly value their friendship and I deeply appreciate their belief in me: **Francesco Benzoni**, **Dr. Khaydar Valiullin**, **Dr. Chiara Colombo**, **Flavia Libonati**, **Dr. Mauro Madia**, **Luca Patriarca**, **Ermes Tarallo**, **Gabriella Tarantino**, **Augusto Sciuccati**, **Dr. Yonatan Afework Tesfahunegn**, and **Elisa Marchesin**. In particular I owe my deepest gratitude to **Massimo Fossati**, **Davide Crivelli**, **Giorgo Vallone**, and especially **Dr. Edoardo Conrado** who have been always ready to lend a hand and assist with every type of problems.

I am grateful to **Francesca Massaro**, **Liliana Musazzi**, **Alessandra Miceli** and especially **Caterina Barbieri** for teaching me Italian language. Their kind effort through these years is unforgettable.

It is necessary to mention and thank the kind hospitality and support of **Dr. Amin Eshraghi**, **Dr. Morvarid Karimi Ghovanlou**, **Dr. Mohammadreza Noban**, and **Hassan Mahmoudi** during my stay in Canada which made everything simpler to me.

I am grateful to the Department Secretary, **Licia Simonelli** for her various forms of support during my graduate study.

The financial support of **Politecnico di Milano** and **Scuola Interpolitecnica** which gave me the opportunity and encouragement to expand my researches, is gratefully acknowledged.

I owe my loving thanks to **Dr. Sara Bagherifard**. Her dedication, constant encouragement, sparing assistance, and support have always been truly valuable.

Last but not least, I wish I was able to thank my lovely family. I am grateful to my parents **Pashootan and Fatemeh Ghelichi**, who loved me with infinite generosity and provided me with the opportunity to be where I am. Without them, none of this would even be possible.

Abstract

THE ever increasing research of lightness, improved performance, safety and reliability is pushing to look for materials with superior mechanical properties and to meet severe design requirements imposed in many fields of application, in order to obtain competitive products. Nanocrystal (NC) materials are experiencing a rapid development in recent years due to their existing and potential applications in a wide variety of technological areas; thanks to their superior mechanical properties that by some means are different from their conventional coarse grained polycrystalline counterparts. The commercial applications of nanomaterials, beyond the boundaries of laboratories, lie on the successful production and consolidation of these materials into components preserving the nanostructures. Cold Spray (CS) coating is an innovative deposition technique which uses elements of both physical deposition and severe plastic deformation for generating NC. CS is an emerging coating process in which, in contrast to other well-known thermal spray processes such as flame, arc, and plasma spraying, powders do not melt before impacting the substrate. This character makes CS process commendable for many different coating applications dealing with various materials not only metals but also polymers, composites, etc. Bonding of particles to the substrate occurs due to the high kinetic energy upon impact; therefore, the velocity of the particle plays the most important role in material deposition. During the process, powders are accelerated by injection into a high velocity stream of gas. The high velocity stream is generated through a converging-diverging nozzle. It is well recognized that particle velocity prior to impact is a key parameter in CS process. It determines what phenomenon occurs upon the impact of spray particles, whether it would be the deposition of the particle or the erosion of the substrate. Critical velocity (CV) for a given powder is defined as the velocity that an individual particle must attain in order to deposit after impacting the substrate. Experimental measurement of the CV is practically almost impossible due to the fact that the whole deposition process for a single particle lasts less than few nano seconds. A finite element (FE) model using commercial Abaqus/Explicit has been developed in order to simulate the phenomenon and broaden the horizon of the physical background of the process. The general agreement supports the idea that adiabatic shear instability plays an important role in the bonding of the particles. Having used a material model which considers softening phenomenon and strain rate effect, CV, is numerically estimated by characterizing the shear instability that appears in the discrete outputs of the software as a singularity in their functions. The singularity has been found by transferring the results in frequency domain using Wavelet transform and analyzing the smoothness of the function by calculating its second derivative in Sobolev space. The results for tested material show a good correspondence with the experimental measurements. Another FE model has been developed in order to examine the peening effect of the particles on the substrate. particle's peening effect, induces residual stress and high plastic deformation. The compressive residual stress generally increases the fatigue endurance of structures; moreover, recrystallization can occur as a result of high plastic deformation of the specimen's surface. In CS, particle diameters have a Rosin-Rammler distribution; their velocity and temperature are functions of particle diameter based on the initial condition of the process. Although, the numerical model considers the randomness of the particles in size and impact position with the appropriate distribution and for each particle, based on its size, uses related velocity and temperature, unfortunately, the results of the numerical simulation, in case of residual stress assessment, are not in a good agreement with the experimental measurement performed by X-ray diffraction (XRD). It might be due to the fact that the FE simulation cannot model the bonding phenomenon which seems very important in the process. The FE simulation predicts the possibility of nanograin generation on the substrate due to the fact

that the equivalent plastic strain caused by particles' impact is measured to be more than the threshold value suggested by scholars as a criterion for grain size refinement. The grain size of the coated samples, not only on the deposited material but also on the substrate by removing the deposited material using an electro-polishing device, has been measured through XRD measurements. The in-situ XRD test machine has been employed to extract the diffraction peaks which are usually used for stress measurements. Voigt formulation is applied on the output of the XRD device in order to separate the grain size and micro strain data and consequently measure the grain size of the treated samples. The results approve the existence of nanograins on the substrate, as was assessed also by the numerical simulation. The effect of CS coating on fatigue strength of specimens coated by different powders has been studied using the specimen design suggested by standard (ASTM593). A load control test machine which satisfies the perquisite requirements of the standard has been developed in the Labs. of Mechanical Engineering Department, Politecnico di Milano; The machine has been calibrated using strain gauges and checking the effective distance and frequency on the specimens under different loads. In this regard, six aluminum alloy series have been prepared with different treatments using diverse aluminum alloy powders. The results of the pure bending fatigue tests indicate that CS coating, regardless of the deposited material type, increases the fatigue strength of the treated specimens. Depositing powders with higher hardness compared to the substrate, will improve the fatigue strength more than the softer powders. It is also observed that the softer deposition, in some cases, do not participate to the load bearing process due to partial delamination of the deposited material from the substrate. The last tentative, has been to produce nanostructures through severe shot peening after application of CS coating. This combined process was expected to result in benefiting from advantages of both coating and shot peening on the samples. In this case, the fatigue strength does not increase with respect to the previous not shot peened series. Although the grain size on the samples after shot peening are measured to be less than 100 nm, due to the existence of micro cracks and severely deformed surface of the samples that act as surface defects, it is not possible to benefit the advantages of the generated NC to improve fatigue strength.

Contents

List of Figures

List of Tables

Nomenclature

$\bar{\epsilon}^f$	The equivalent strain to fracture, see equation (4.4), page 62
β	Integral breadth, see equation (6.3), page 110
$\dot{m}$	mass rate, see equation (5.2), page 89
$\dot{\epsilon_p}, \dot{\epsilon_{p0}}$	Equivalent plastic strain rate, see equation (4.3), page 60
ϵ_P	Plastic strain, see equation (4.3), page 60
ϵ_p	Equivalent plastic strain, see equation (4.2), page 58
γ	ratio of specific heat, see equation (5.2), page 89
λ	Wavelength, see equation (6.5), page 110
μ	Viscosity, see equation (5.8), page 90
ν	Poisson's ratio, see equation (1.1), page 7
ω	Damage parameter, see equation (4.3), page 62
ϕ	$= 2\omega/\beta$, see equation (6.4), page 110
ρ	Density, see equation (5.2), page 89
ρ_g	Density of the gas, see equation (2.1), page 27
ρ_p	Density of the particle, see equation (2.1), page 27
ρ_p	Particle density kg/m^3, see equation (4.1), page 57
σ_y	Yield strength, see equation (1.2), page 9
σ_{eq}	Equivalent stress, see equation (4.3), page 60
σ_e	Equivalent stress, see equation (4.2), page 58
$\sigma_{friction}$	Friction stress, see equation (1.2), page 9
σ_m	The average of the three normal stresses, see equation (4.4), page 62
σ_u	Ultimate strength MPa, see equation (4.1), page 57
θ	Bragg angle, see equation (6.5), page 110
A	Nozzle sectino, see equation (5.2), page 89
A, B, C, n, m	Johnson-Cook constant, see equation (4.3), page 60
a_n, b_n	Coefficients, see equation (6.4), page 110

C	Suffix:Cauchy function, see equation (6.2), page 110
C_D	Drag coefficient, see equation (2.1), page 27
C_D	Drag coefficient, see equation (5.8), page 90
d_{cr}	The grain size, see equation (1.2), page 9
D_p	Particle diameter, see equation (2.1), page 27
e	Strain, see equation (6.6), page 110
E_0	Young's modulus of the material without any porosity, see equation (1.1), page 7
f	Suffix: pure diffraction profile; including contributions due to crystallite size and strain, see equation (6.2), page 110
f_b	Shifted frequency in Doppler test, see equation (4.0), page 54
G	Suffix:Gaussian function, see equation (6.2), page 110
g	Suffix: instrumental profile, including wavelength distribution and contribution from instrumental aberrations, see equation (6.2), page 110
h	Suffix:experimental profile, see equation (6.2), page 110
$I(x)$	Voigt function, see equation (6.1), page 110
$I_C(x)$	Cauchy function, see equation (6.1), page 110
$I_G(x)$	Gaussian function, see equation (6.1), page 110
k	Thermal conductivity, see equation (5.12), page 93
k_{HP}	the Hall-Petch slope, see equation (1.2), page 9
M	Mach number, see equation (5.3), page 89
P	Pressure, see equation (5.2), page 89
P_r	Prandtl number, see equation (5.12), page 93
Q,D_{rr}	Rosin-Rammler parameters, see equation (5.1), page 86
R	Specific gas constant, see equation (5.2), page 89
R	The pore size, see equation (1.1), page 7
R_e	Reynold's number, see equation (5.9), page 90
S	Molecular speed ratio, see equation (5.9), page 90
S	The flaw size emanating from the surface of the pore, see equation (1.1), page 7
SL	Shear Localization factor, see equation (4.2), page 58
T	Temperature, see equation (5.2), page 89
T_{init}	Initial temperature K, see equation (4.1), page 57
T_{melt}	Melting temperature K, see equation (4.1), page 57
V_{cr}	Critical velocity m/s, see equation (4.1), page 57
V_g	Velocity of the gas m/s, see equation (2.1), page 27

V_{pore} The pore volume fraction, see equation (1.1), page 7

V_p Velocity of the particle m/s, see equation (2.1), page 27

X_* Throat properties, see equation (5.2), page 89

X_0 Initial condition, see equation (5.2), page 89

X_∞ Properties in infinity, see equation (5.9), page 90

X_e Nozzle exit properties, see equation (5.5), page 90

X_p Particle properties, see equation (5.8), page 90

Part I

Introduction

Chapter 1

Introduction to Nano-crystalline Material

1.1 Introduction

The ever increasing research of lightness, improved performance, safety and reliability is pushing to look for materials with superior mechanical properties and to meet severe design requirements imposed in many fields of application in order to obtain competitive products. Admittedly, it is well known that the majority of failures in engineering structural materials, such as fatigue fracture, fretting fatigue, wear, aging, and corrosion, are very sensitive to the structure and properties of the surface, and that, quite often, failures originate from the outer layer of the component and then propagate inward; this makes surface improvement as an effective approach to enhance material properties. Nanocrystalline (NC) materials have become an interesting field of research with emerging applications in recent years; one of the common properties of their various material forms is the nanoscale structure, i.e., at least one dimension less than 100 nm, more typically less than 50 nm [1, p. xvii]. NC materials, are experiencing a rapid development in recent years due to their existing and/or potential applications in a wide variety of technological areas such as electronics, biotechnology, catalysis, ceramics, magnetic data storage, structural components etc; thanks to the fact that they possess superior mechanical properties by some means different from their conventional coarse grained polycrystalline counterparts [2–4]. It is naturally expected that the global performance can be enhanced when forming a NC layer with superior properties on material surface; this process actually combines the superior properties of nanomaterials and the conventional engineering materials in order to increase the service lifetime of the work piece [1]. The interesting mechanical behavior of NC materials originates from their unique mechanical properties, as observed by Gleiter *et al.* [5] in specimens prepared by the gas condensation method:

- lower elastic modulus compared to coarse grained size materials by as much as 30%-50%;
- very high hardness and strength values for NC pure metals $(10$ nm grain size$)$ that are 2 to 10 or more times higher than those of coarse grained (≥ 1 μ m) metals;
- increased ductility perhaps even superplastic behavior at low homologous temperatures in even normally brittle ceramics or inter metallic at nanoscale.

Apart from the the latter superior properties of these materials, the enhancement of fatigue strength due to the presence of NC layer, has also been studied and the results confirmed that a NC thin film on the structure surface can notably improve the fatigue behavior of the component. Structural nanomaterials are finding applications in bulk materials, films, coatings, and composites in different forms such as wear-resistance coatings and load-bearing structures. They are also being used in electronics, refractory, biological, catalytic applications and many other industrial fields [6]. The production methods of NC materials can be mainly divided into two different categories: deposition-based processes [7–9] and severe plastic deformation (SPD) [10]. In this chapter, a short review on NC thin film characteristics will

be presented in three different sections:
In Section1.2 the mechanical properties of NC material, presented in the literature, will be studied. The physical parameters which are affected by grain size have been investigated through a review on the works of other scholars.
The quality and functionality of the final product, considering the superior properties of NC material, strongly depends on the implemented technique which shall be able to produce high quality NC layer of material on different components with different shapes. In Section1.3 different practical existing methods which are being used for producing the NC structure has been reviewed.
In Section1.4 it is tried to study some nanoscale structural measuring techniques; this section includes the common methods which are nowadays used in the laboratories to investigate different properties of NC material.
In Section1.5 different applications of NC material have been reviewed, considering the broad existing or potential fields of application of NC structure in the industry.

1.2 Mechanical properties of NC material

It is well recognized that some of the physical properties of the material are significantly changed by decreasing the grain size. The research of Gleiter *et al.* [5], for the first time showed the notable dependency of different properties of the components on grain size [6]. The review, presented in this section, is developed mostly based on the reviews of Koch [1, 6], evidencing some updates in the literature.

1.2.1 Elastic properties

One the most important properties affected by NC structure is Elastic modulus (*E*). The early measurements of the elastic constants on NC materials prepared by the inert-gas-condensation method, showed lower Young's modulus for smaller grain size [11]; while many justifications were given for decreasing values of *E*, it was suggested by Krstic *et al.* [12] that the presence of defects was the main responsible for the low values of *E* in NC materials. Young's modulus of some NC metal alloys prepared by mechanical milling/alloying of powders, were measured by a nanoindentation technique [13]. The *E* values for NC Cu, Ni, and Cu-Ni alloys with grain sizes ranging from 17 nm to 26 nm, were found to be essentially identical to those of the corresponding coarse grained size materials. El-Sherik *et al.* [14] discussed the effects of porosity on E and magnetic properties and showed that the measured value of *E* can be significantly affected by the presence of porosity and cracks in the consolidated material [15]. Eq.1.1 [15] shows the variation of *E* with porosity. If the pore size is *R* and the flaw size emanating from the surface of the pore is *S* then:

$$E = \frac{E_0}{1 + 4V_{pore}(1 - \nu^2)\phi\pi} \tag{1.1}$$

Where E_0 is the Young's modulus of the material without any porosity, V_{pore} is the pore volume fraction, ν is the Poisson ratio, and ϕ is the function of S and R. Fig.1.1 shows the behavior of the elastic modulus of the material by decreasing the grain size. In this figure, which has been presented by Shen *et al.* [13], the calculated ratio of Young's (E) and shear (G) modulus of the polycrystalline structure as a function of grain size are presented. In Fig.1.1, dashed and solid curves correspond to grain-boundary thickness of 0.5 nm and 1.0 nm respectively and the open circles show E/E_0 values of NC Fe vs. grain size. The experimental observations and numerical calculations based on the porosity hypothesis, have been proven by numerical studies developed through Atomistic simulations. Schiøtz *et al.* [16] have shown the stress-strain curve for different grain size, by using the atomistic simulation for polycrystalline materials. The results of their study have been presented in Fig.1.2. The results, as expected, indicate that by decreasing the grain size, the elastic modulus decreases slightly. The variations of the crystalline size in Fig.1.2 is quite slight; therefore, not a considerable change shall be expected in elastic modulus; nevertheless, even for these slight changes, significant decrease is observed for *E*.

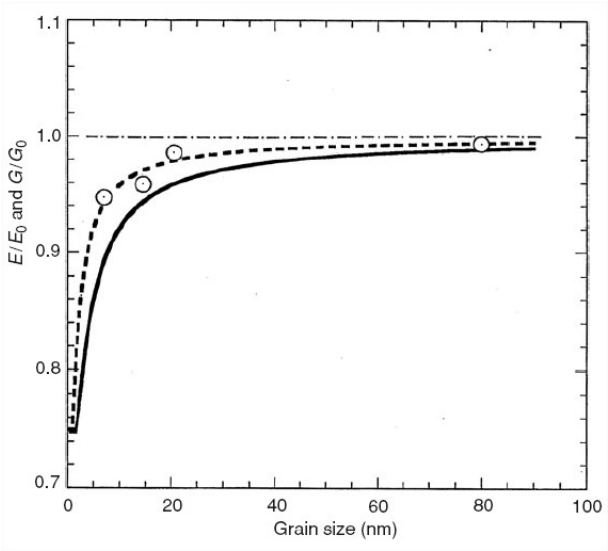

Figure 1.1: *Calculated ratios of Young's (E) and shear (G) modulus of NC material to those of polycrystalline as a function of grain size [13]*

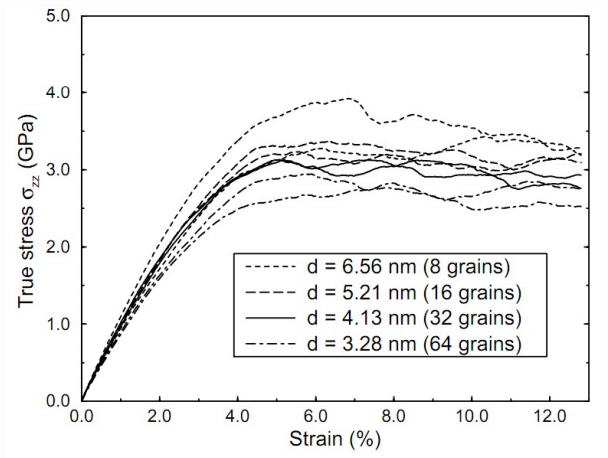

Figure 1.2: *Stress-strain curves for eight simulations with four different grain sizes [16]*

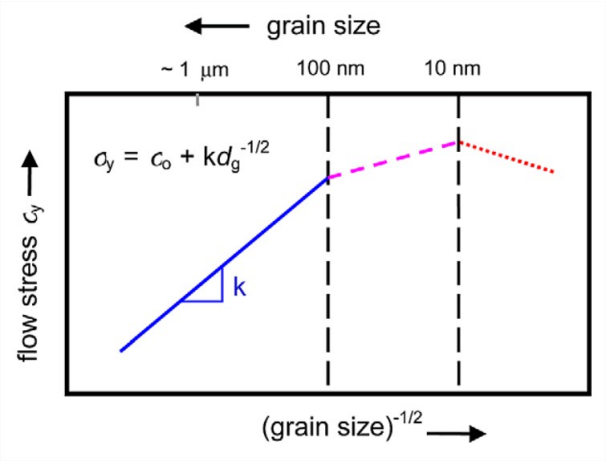

Figure 1.3: *Schematic representation of yield stress variation as a function of grain size in micro, ultra-fine, and NC metals and alloys [18]*

1.2.2 Hardness and strength

The hardness alterations of various materials due to grain size, is quite different, considering that the focus in this section is on the effect of grain size on metals and alloys. Because of the difficulties in preparing artifact-free NC materials of sufficient size for the standard mechanical testing methods, the most measured mechanical property of NC materials as a function of grain size is hardness [6]. It is clear from the data on hardness and strength that the hardness/strength of NC metals can be much higher than their conventional coarse grained counterparts [17, 18]. Reducing grain size to the smallest nanoscale values, about 10 nm, can result in hardness increase with factors of 2 to over 10. Youssef *et al.* [19] show the yield strength of NC Cu to be 22 times the conventional coarse grained material [6]. Fig.1.3 presented by Kumar *et al.* [18] shows a schematic representation of the size dependency of yield stress on grain size for nano, ultra-fine, and micro grain size of the structure. The formula presented in this graph describes the so called Hall-Petch [20, 21] effect (Eq.1.2). It is to be mentioned that there is no general agreement on the mechanism(s) responsible for this hardening improvement. For conventional coarse grained materials (grain sizes ≥ 1 μm), the empirical Hall-Petch [20,21] equation is presented in Eq.1.2

$$\sigma_y = \sigma_{friction} + \frac{k_{HP}}{\sqrt{d_{cr}}} \tag{1.2}$$

where σ_y is the yield strength, $\sigma_{friction}$ is the friction stress below which dislocations will not move in a single crystal, k_{HP} is the Hall-Petch slope, and d_{cr} is the grain size. A similar expression can be given for hardness regarding its dependency on grain size. Hall-Petch behavior is well documented for conventional coarse grained materials as the grain size is reduced [6]. The mechanism for the Hall-Petch behavior in conventional coarse grained materials has been generally explained by a pile-up of dislocations in one grain, producing a stress concentration that activates a dislocation source in the adjacent grain [6, 22]. Alternative mechanisms have involved the elastic and plastic incompatibility stress between neighboring grains [6,23]. The experimental results indicate that for smallest grain size ($\sim$10nm), the hardness of the material starts decreasing again; this phenomenon is called *inverse Hall-Petch*. It is predicted therefore that dislocations are absent in the smallest NC and that the deformation must involve other than conventional dislocation creation and motion [6].
To come to the point, the studies have revealed that the strength and hardness values of NC metals can be much larger than those of conventional coarse grained material; factors of over 20 times have been reported [19].

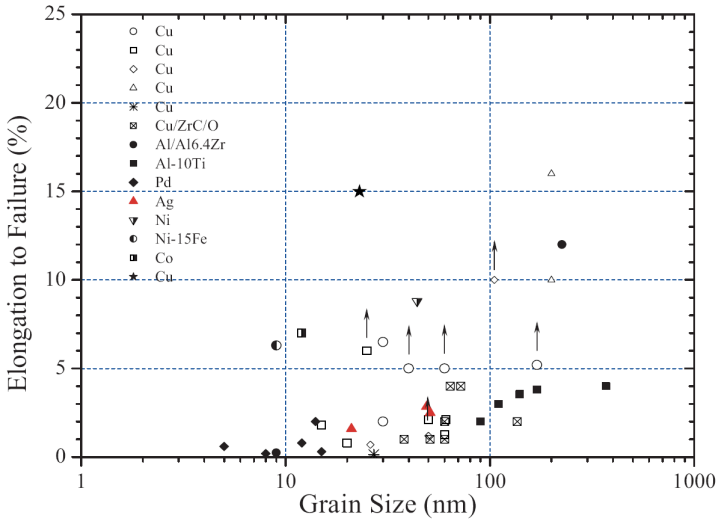

Figure 1.4: *Elongation to failure in tension versus grain size for a variety of metals and alloys [25]*

1.2.3 Ductility

In material science, the behavior of solid materials under tensile stress defines their ductility, that is often characterized by the material's ability to be stretched into a wire [24]. Ductility is a property of NC materials which might be predicted to be enhanced by extrapolation of its grain size dependence in conventional polycrystalline materials [6, p.151]. Bohn *et al.* [3] show in their article that the change of microstructure to the nanoscale will lead to an increase in ductility. By considering the fact that yield and fracture stresses show different dependencies on grain size [6, p.151], ductility may be affected by extreme reduction of grain size to the nanoscale which can be considered the ductility limitation of NC materials. The elongation vs. failure for different materials by different grain sizes, presented by Koch *et al.* [25] has been shown in Fig. 1.4. It shows for most metals with grain sizes below 30 nm, the elongation to failure are very low, typically less than $2-3\%$ [25]. As it is mentioned in [25], there are three major limitations to ductility for NC materials:

1. **Artifacts from processing:** many of the methods for producing bulk NC materials, involve synthesis of nanoscale particulate or powders with NC internal grain structure.

2. **Force instability in tension:** necking generally begins at maximum load during tensile testing. Materials with a high capacity for strain hardening are therefore stable, while those with low capacity for strain hardening are potentially unstable.

3. **Crack nucleation instability**

The production method might introduce one of the above mentioned limitations for ductility. For example, one-step processing methods are more likely to provide NC samples free from artifacts , while in the case of two-step processing methods which require a subsequent consolidation step, perfect artifact free bulk samples are difficult to obtain [25]. In this regard, it might be necessary to minimize mechanical instability which mostly enhances the strain hardening of the material.
Although NC metals show higher hardness and strength than conventional coarse grained material, sometimes they demonstrate very low ductilities. However, by changing the production process parameters, good ductility can also be obtained by removing all the artifacts [25] .

1.2.4 Fatigue and fracture

Developing and understanding the damage tolerance of NC metals and alloys, is essential for evaluating their overall functionality as structural materials in engineering components. Hanlon *et al.* [26] have

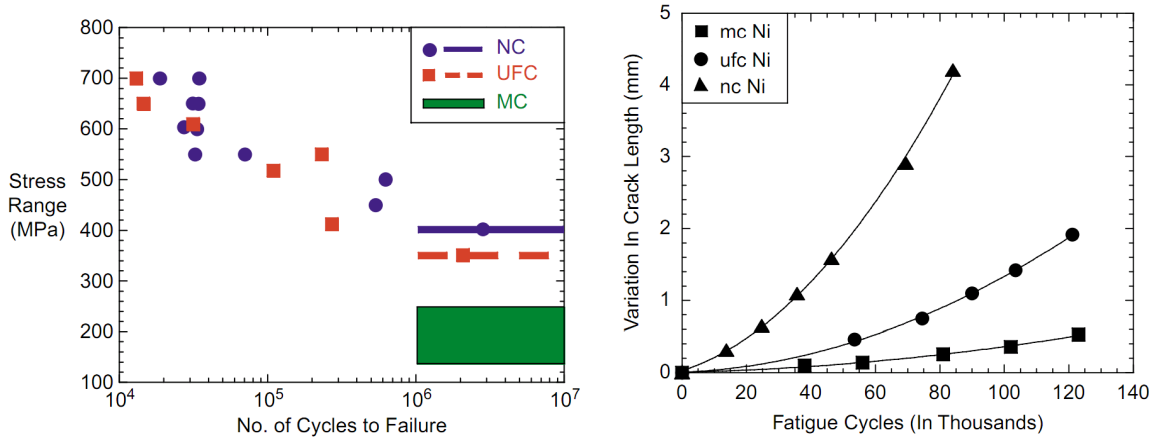

Figure 1.5: *(a) Comparison of the S-N fatigue response showing the stress range versus number of cycles to failure (b). Comparison of the variation of fatigue crack length as a function of number of cycles [26]*

studied the fatigue response of electro-deposited NC pure Ni and a cryomilled ultra-fine crystalline Al-Mg alloy. For the electro-deposited, fully dense *Ni*, two different grain sizes were obtained using similar processing methods. The fatigue crack growth experiments for NC, ultra-fine crystalline (*ufc*) were conducted using edge notched samples. It was found that grain refinement generally leads to an increase in resistance to failure under stress controlled fatigue, whereas a generally deleterious effect was observed on the resistance to fatigue crack growth. The results of their study is presented in Fig. 1.5 which shows that decreasing the grain size even from ultra-fine to nano size, results in notable fatigue endurance improvements. Study of fatigue crack initiation processes in NC metals has relied mainly on post mortem micro-scale observations to draw conclusions about the relevant mechanisms. In NC metals, both internal and surface defects have been noted as nucleation sites for fatigue cracks. Subsurface initiation is much less common in coarse grained materials by contrast [10, 27]. Ronalnd *et al.* [28] studied the effect of NC surface layer on fatigue behavior of a 316L stainless steel. The results show significant enhancements of the yield stress and the fatigue strength through surface mechanical attrition treatment (SMAT). To achieve the surface NC layer on the samples ultrasonic-assisted SMAT has been used. The study revealed the presence of a 40μm nanostructured surface layer with a grain size of about 20 nm. The S-N curve for different treatments in their study has been presented in Fig. 1.6. The fatigue strength of the nanostructured stainless steel is increased considerably compared to the untreated material and it is to be noted that this is not only limited to the high cycle fatigue (HCF) regime. The two latter articles of Hanlon *et al.* and Ronald *et al.* which studied two different categories of NC production methods as well as many other investigations [29–31], show improvement in fatigue strength by adding NC film on the compnent surface. On the contrary, there are reports by Bagherifard *et al.* [32] showing that the presence of NC thin films on the structure surface might not always increase the fatigue life due to side effects of the production procedure, in their case, comparatively high surface roughness. It can be concluded, by considering different results in the literature, that the existence of NC surface layer, can improve the overall fatigue endurance of the structure.

1.3 Production of NC structure

The commercial applications of nanomaterials, beyond the boundaries of laboratories, lie on the successful production and consolidation of these materials into components preserving the nanostructures. The traditional consolidation techniques have the strong limitation of not being able to retain the nanograin

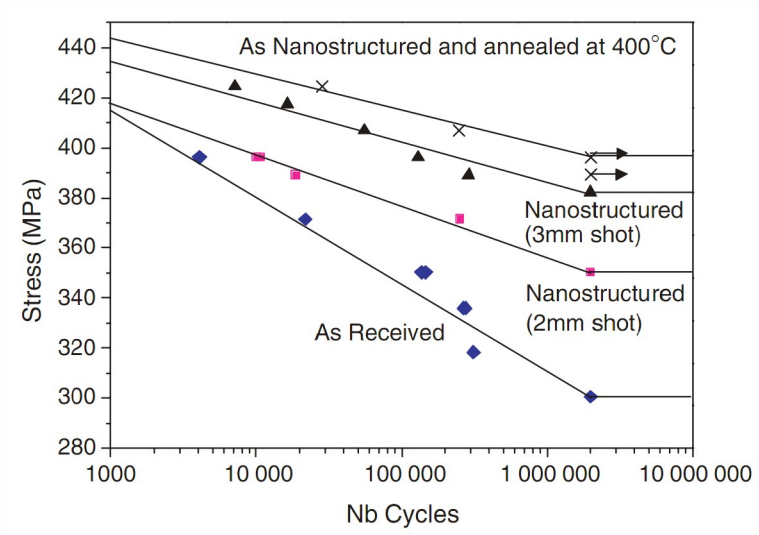

Figure 1.6: *S-N curves of different SMATed samples [28]*

size owing to the problem of grain growth [6, p.25]. Many of these methods involve the synthesis of nanoscale particulate, or powders with a NC internal grain structure, followed by consolidation to bulk samples [6, p.151]. These can be categorized as *two-step* methods. Porosity is a major artifact, especially for metals made by the inert-gas-condensation method. Electrodeposition, on the other hand, is categorized as *one-step*, that is it does not require consolidation of particulate and does not have the associated problems; however most of the NC materials made by electrodeposition have also exhibited very poor ductility. Other approach for categorizing the NC production techniques is dividing them based on the intrinsic of each technique. In this regard, it would be possible to divide them into two different classes: deposition-based processes and deformation-based or severe plastic deformation (SPD) based processes [10]. Deposition-based processes include *electrodeposition* and *physical vapor deposition* such as *magnetron sputtering* and *pulsed laser deposition*, while deformation based techniques include equal *channel angular pressing*, *high pressure torsion*, *rapid forging*, and *surface mechanical attrition treatment* [10]. Another distinctive process named **cold spray coating**, uses elements of both physical deposition and SPD to create bulk NC structures. In this section, a brief review of some of these technique has been presented except for the cold spray coating, for which a more detailed review will be presented in the next chapter.

1.3.1 Electrodeposition

To date, the majority of NC metals used in experiments are produced by electrodeposition [10]. A Watts electrochemical bath is often used in this process, in which the current is passed between two electrodes submersed in an aqueous bath of metal salts Ions that are dissolved from the anode and deposited on the cathode by the addition of free electrons. Fig. 1.7 shows an example of typical electrodeposition of Cr presented by [33]. Due to the fact that electrodeposition of NC operates far from equilibrium conditions, the resulting materials are nonequilibrium structures [1, p.240]. In addition, alloys produced by electrodeposition can show considerable extensions of the solid solubility range similar to what is observed in materials produced by other nonequilibrium processing techniques, such as rapid solidification [1, p.241]. Incidentally, electrodeposition can be used to synthesize a large number of NC metals, alloys, and composite materials. There is considerable opportunity to control their microstructure by process parameters such as bath composition, pH, temperature, current density, and current waveform. The properties of NC electrodeposits have been shown to fall into two categories: properties exhibiting strong grain size dependence, and properties that, over large grain size ranges, are relatively unaffected by grain size [1, p.283]

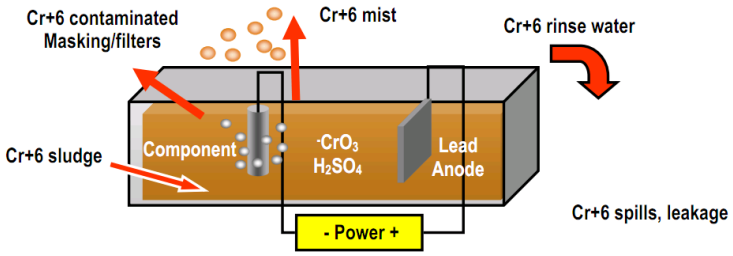

Figure 1.7: *Typical electrodeposition of hard chromium bath [33]*

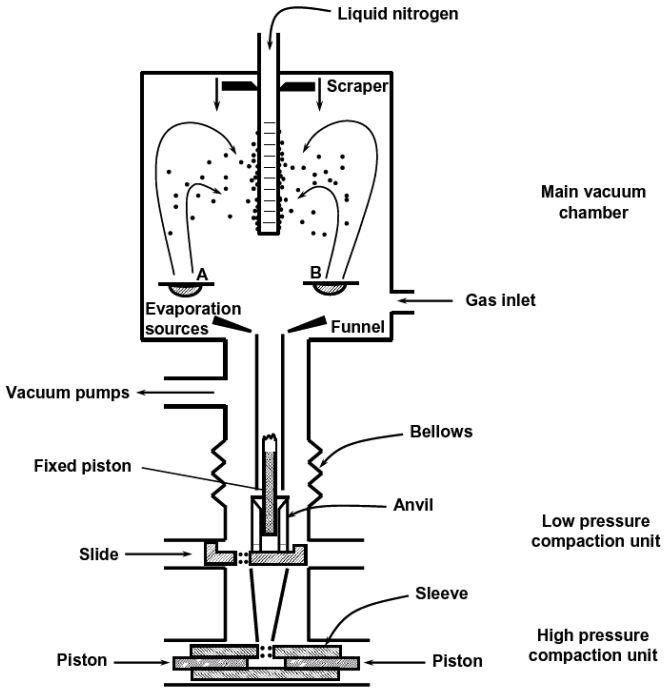

Figure 1.8: *Schematic of an inert-gas condensation chamber for the NC synthesis [34]*

1.3.2 Inert-gas condensation

Inert-gas condensation (IGC) is a bottom-up approach in which individual atoms or molecules are put together to form the required nanoparticles; synthesizing nanostructured materials, involves two basic steps [1, p.47]. The first step is the evaporation of the material and the second step involves a rapid controlled condensation to produce the required particle size. Fig. 1.8 shows a schematic of a typical apparatus that is widely used nowadays [34]. In this unit, the chamber is evacuated by an oil diffusion pump. A crucible containing the metal to be evaporated is slowly heated via radiation from a graphite heater element. After evacuation, an inert gas (He, Xe, or Ar) is leaked into the chamber at a low pressure, the ultra-fine metal particles that nucleate and grow in the gas phase are collected on a water-cooled surface. A carbon-coated electron-microscope grid, attached to the center of the water-cooled surface, allows the powder particles to be collected and directly observed in the transmission electron microscope. With the use of a shutter, it is possible to sample less than a monolayer of particles on the grid. There are different evaporation techniques such as thermal evaporation, laser evaporation, sputtering, electrical arc discharge and plasma heating [1, p. 56-60]. The followings are some of the most noted favorable characteristics of IGC technique [1, p.79]: a very flexible technique; wide range of materials; conventional restrictions of phase equilibria and kinetics; the possibility of reacting, mixing,

and coating various material types, sizes, and morphologies; particle synthesis is usually a continuous process; high levels of purity can be maintained.
Conversely, the following items can be named as the problems and difficulties in IGS technique [1, p.80]:

- Agglomeration of particles is a problem in consolidated nanopowders;
- Maintaining a clean vacuum may not always be easy;
- Neutral clusters produced require ionization, which is usually an inefficient process;
- It may be difficult to adjust conditions to obtain high fluxes for very small clusters of just a few atoms;

In conclusion, it can be stated that IGC is a simple method involving evaporation of material from a source in flowing gas, followed by condensation into nanoparticles in the cooler parts of the system. Despite drawbacks such as cost and small volume production, this technique serves as a useful tool for the synthesis of extremely pure nanostructured materials.

1.3.3 Solid state processing methods

Severe plastic deformation (SPD) technique has received the greatest attention due to its simplicity and applicability for different classes of materials. NC materials are reported to have been obtained by non-homogeneous deformation SPD processes methods with large strain gradients [32]. Mechanical deformation under shear conditions and high strain rates (10^1-$10^4\ s^{-1}$) lead to the formation of nanostructures within powder particles and thin foils or at the surface of metals and alloys exposed to friction-induced wear conditions [1, p.119]. There are many different techniques which can apply such high strain rates to the surface of the structure. The basis of all these methods is to increase the free energy of the polycrystals and generate many defects and interfaces (grain boundaries) in various nonequilibrium processes such as high pressure torsion [35,36], ball milling [37,38], sliding wear [39,40], drilling [41], shot blasting and annealing [42], ultrasonic shot peening [43,44] and air blast shot peening [41,45]. Milling is the techniques that is being used the most; by milling, the main objectives are particle size reduction, solid state alloying, mixing or blending, and particle shape changes [1, p.120]. A variety of ball mill apparatus have been developed for different purposes including lumber mills, attrition mills, saker mills, vibratory mills, planetary mills, etc [46]. High-energy milling forces can be obtained by using high frequencies and small amplitudes of vibration. Since the kinetic energy of the balls is a function of their mass and velocity, dense materials (steel or tungsten carbide) are preferable to ceramic balls [1, p.121]. In the milling process, for all NC materials, surface and interface contamination, constitutes a major problem. By minimizing the milling time and using the purest, most ductile metal powders available, a thin coating of the milling tools by the respective powder material can be obtained, which considerably reduces Fe-contamination.
Not only the high deformation rate, but also plastic deformation would reduce the size of the grain in the structures. As mentioned before, there are many different methods such as equal channel angular pressing (ECAP) or equal channel angular extrusion (ECAE) as well as severe shot peening (SSP) which use the idea of SPD. Although the use of ECAP on coarse grained metals does not seem to be consistently capable of producing grain sizes below 100 nm, the process has been used to consolidate NC powders and produce bulk material with grain sizes below this limit [47]. The solid state processing methods of mechanical attrition and mechanical alloying have been developed as a versatile alternative to other processing routes in preparing nanoscaled materials with a broad range of chemical composition and atomic structure [1, p. 164]. In this kind of process, lattice defects are produced within the initially single-crystalline powder particles. Mechanical attrition offers interesting perspectives in preparing nanostructured powders with a number of different interface types in terms of structure (crystalline/crystalline, crystalline/amorphous) as well as atomic bonding (metal/metal, metal/semiconductor, metal/ceramic, etc.). In this project, shot peening has been used in order to produce nano coating on the structure surface; in Chapter 3, this process will be reviewed in more details.

1.4 Measurement techniques

The advancement of nanotechnology without development of measuring instruments capable of observing and measuring their particular structure has not been possible. Many of these systems are very large and expensive, in the million-dollar price range, often requiring specialists to operate them. The aim of the present section is to explain the principles behind the operation of some of these systems, and to delineate their capabilities.

1.4.1 Crystallography

Most nanostructures are crystalline, meaning that their thousands of atoms have a regular arrangement in space called a crystal lattice. This lattice can be described by assigning the positions of the atoms in a unit cell; thus the overall lattice arises from continual replication of this unit cell throughout space. Some properties of nanostructures depend on their crystal structure, while other properties such as catalytic reactivity and adsorption energies depend on the type of exposed surface [48, p.37]. The wavelength λ of the X-rays expressed in nanometers is related to the X-ray energy E expressed in the units kilo-electron-volts through the expression [49]. To obtain a complete crystal structure, X-ray spectra have to be recorded for rotations around three mutually perpendicular planes of the crystal. This provides comprehensive information on the various crystallographic planes of the lattice. The next step in the analysis is to convert these data on the planes to a knowledge of the positions of the atoms in the unit cell [48, p.50].
For measuring the particle size, it is also possible to use the X-ray diffraction. The particle size depends on the relationship of the grain size and the wavelength of the X-ray. This method will be presented in detail in Chapter 6. The other method for grain size measurement is using a monochromatic(single-wavelength) laser beam scattered at a particular angle for parallel and perpendicular polarizations. The detected intensities can provide the particle size, the particle concentration, and the index of refraction. The Rayleigh-Gans [50] theory is used to interpret the data for particles with sizes d less than 0.1λ, which corresponds to the case for nanoparticles measured by optical wavelengths. To obtain crystallographic information about the surface layers of a material, a technique called low-energy electron diffraction (LEED) can be employed, since at low energies (10-100 eV) the electrons penetrate only very short distances into the surface, so their diffraction pattern reflects the atomic spacings in the surface layer. If the diffraction pattern arises from more than one surface layer, the contribution of lower-lying crystallographic planes will be weaker in intensity.

1.4.2 Microscopy

In a transmission electron microscope (TEM) [48, p.47], the electrons entered from a source such as an electron gun, are scattered as they pass through the sample, are focused by an objective lens, are amplified by a magnifying (projector) lens, and finally produce the desired image. Electrons interact much more strongly with matter than do X-rays or neutrons with comparable energies or wavelengths [48, p.47]. A technique called image processing can he used to increase the information obtainable from a TEM image, and enhance some features that are close to the noise level. If the image is Fourier-transformed by a highly efficient technique called *fast fourier transform* [51], then it provides information similar to that in the direct diffraction pattern.
Another instrumental technique in which the resolution approaches interatomic dimensions is *field ion microscopy* (FIM) which is an analytical technique that can be used to image the arrangement of atoms at the surface of a sharp metal tip. It was the first technique by which individual atoms could be spatially resolved. In a FIM, a wire with a fine tip located in a high-vacuum chamber is given a positive charge. The electric field and electric field gradient in the neighborhood of the tip are both quite high; residual gas molecules that come close to the tip become ionized by them, transferaing electrons to the tip, thereby acquiring a positive charge [48, p.51].
A scanning electron microscope (SEM) is a type of electron microscope that images a sample by scanning it with a high-energy beam of electrons in a raster scan pattern. The electrons interact with the atoms that make up the sample producing signals that contain information about the sample's surface

Table 1.1: *Potential applications and future markets for nanoscience and nanotechnology [6]*

Topic	Current	1-5 years	6-10 years	10-50 years
Structural/heavy use sector	Nanoparticles for pigments, paints Self-cleaning windows for commercial use	Smart/responsive nanocoatings for food packaging	Labon a chip Nanotechnology for screening Synthesis/catalysis for enviromental control	Ultra-light material for cheaper construction and transportation High strength, light-weight, structures
Energy	Nanocatalyst Enhanced fuels for better efficiency	Nanomaterials for fuel cells/batteries Nanotechnology	Efficient solar cells using fuel cells, Alternative energy sources	Nanomaterials for hydrogen storage
Health care/medicine	Sun screens	Bio nanosensors for diagnostics	Artificial muscle lab on a chip Technology for more efficient drug discovery	Nanomachines for in vivo treatments Nanopumps/valves for tissues Engineering/artificial organs
Security		Nano bar coding and tagging Nanotubes for thermal protections	Remote detection	
Electronics			Carbon nanotubes Electronic components	Nanomaterials in light-emitting diodes/PV devices, Single electron/molecule devices
Communications			Flat-panel flexible displays using nanotechnology High density data storage	Fast processing using quantum computing DNA computers

topography, composition, and other properties such as electrical conductivity [48, p.51]. The SEM observation with more detail has been presented in Chapter 6.
There are many other methods, not in the scope of this thesis, such as Raman spectrum, scanning tunneling microscopy, atomic force microscopy, etc which can be used in order to measure the dimension of the grains or producing an image of surface topography.

1.5 Application of NC material

Structural nanomaterials are finding applications in bulk materials, films, coatings, and composites. Applications vary from wear-resistance coatings to load-bearing structures. Nanophase or NC materials are also being used in electronics, refractory, biological, and catalytic applications. Progress in a wide range of structural applications for nanomaterials crucially depends on the development of new fabrication and processing technologies, along with a fundamental understanding of the relationship between the structure and properties of the feedstock powders and consolidated parts. Several companies have demonstrated injection-molded parts or composite parts with increased impact strength. Full-scale prototypes of such parts are now in field evaluation, and use in the vehicle fleet is possible within 3-5 years or even sooner [6, p.342]. Several aerospace companies have programs under way for the use of nanosized particles of aluminum or hafnium for rocket-propulsion applications. The improved burn and speed of ignition of such particles are significant factors for this market for further technological advancement. In this Section the application of NC materials in some different industries has been briefly reviewed. The trend of growing application of nanotechnology due to their superior properties, shows an immense future in industries for nanomaterials. Some present and possible future applications for nanotechnology with a suggested time-frame are presented in Tab. 1.1 [6, p. 360].

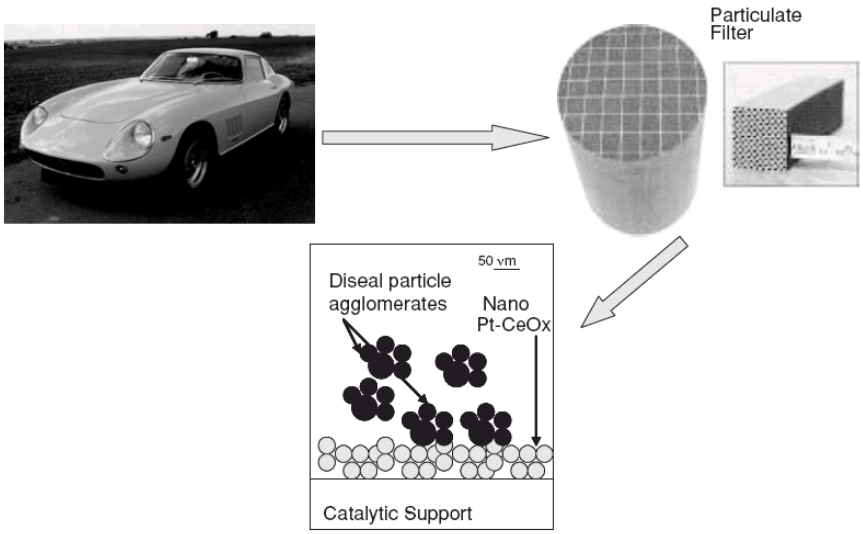

Figure 1.9: *Use of nanoparticles in a future diesel particulate filter [6, p. 344]*

1.5.1 Nanotechnology in automotive applications

Nanocomposites are currently used in big car companies instead of regular material. In addition to being stronger and longer-lasting, it is important for a car to be as light as possible. Lighter cars use less fuel, which means that they are less expensive for people to own. The new bumpers that Toyota has been making for its cars are 60% lighter than the old bumpers and twice as hard to scratch [6, p. 345].
The 2002 Chevrolet Astro and GMC Safari mid size vans are the first vehicles to use an advanced thermoplastic olefin nanocomposite on an exterior application, according to General Motors Corp., but not the last. About the vehicles' optional step-assist a running board designed to help people enter and exit a vehicle. GM and three supplier partners Basell, Southern Clay Products, and Black hawk Automotive Plastics, Inc., worked to bring the TPO-based nanocomposite to production. Basell, the world's largest producer of polypropylene resins for plastics, provides the resin and processing technology for the new nanocomposite [6, p. 345]. Fig.1.9 shows the use of nanoparticles in a future diesel particulate filter [6, p. 344].

1.5.2 Industrial applications of nanocomposite coatings

The industrialization of the "Ti-Al-Si-N"' coatings with Si dissolved in the "Ti-Al-Si-N" metastable solid solution was pioneered by Tanaka *et al.* [52]. Hitachi company, also, recently announced the development of a new coating material based on the "Ti-Si-N" system [53]; development at other places is on the way. According to the available information [53], the material of their coatings consists of nanocomposites with a Ti-rich Ti-Si-N crystallite phase and Si rich Ti-Si-N amorphous phase. Much higher hardness and higher oxidation resistance than in a conventional solid solution hardened coating, such as TiAlN, is reported. Tools with these coatings are suitable for high-speed cutting and highly efficient machining of hardened die steels for molding. Hence the majority of the current development in the companies is proprietary, little information is available about these progresses. Therefore we shall limit our discussion to the examples which are well documented in the publications or accessible via internet.

1.5.3 Biomechanics and prosthesis

One of the most exciting new applications for magnetorheological fluid technology is that of real-time controlled dampers for use in advanced prosthetic devices. In such systems a small magnetorheological fluid damper is used to control, in real-time, the motion of an artificial limb based on inputs from a group

of sensors. A ŞsmartŤ prosthetic knee system based on a controllable magnetorheological fluid damper was commercially introduced to the orthopedics and prosthetics market in 2000. The benefit of such an artificial knee is a more natural gait that automatically adapts to changing gait conditions [54].

1.6 Conclusion

NC materials are novel materials that are not only scientifically interesting but also hold great potential for a number of technological applications. Their properties are different from and often superior to those of conventional coarse grained poly-crystalline materials and also amorphous alloys of the same composition. Widespread use and search for technological applications of NC materials require the availability of large (tonnage) quantities of well-characterized material with reproducible properties. Even though NC powders are now more expensive than the more commercially available coarse grained powders, greater usage and tonnage production will bring down the cost. A solution to the barriers for commercial utilization of NC materials can be to identify well-defined applications for these materials; this aspect can be a driver for accelerated research. In this context, development of novel synthesis methods to produce NC materials in commercially viable quantities is an urgent necessity [15]. It must be recognized that the real benefits of nanotechnology are likely to be many years away as demonstrated in Tab. 1.1.

Bibliography

[1] C. Koch, *Nanostrucutred Materials, Processing, Properties and Applications*. Willian Andrew Publishing, 2007.

[2] R. W. Cahn, "Nanostructured materials," *Nature*, vol. 348, pp. 389–390, 1990.

[3] R. Bohn, T. Haubold, R. Birringer, and H. Gleiter, "Nanocrystalline intermetallic compounds: an approach to ductility," *Scripta metall. mater.*, vol. 25, pp. 811–816, 1991.

[4] D. Morris, *Mechanical behavior of nanostuctured materials*. Trans. Tech. Publications Ltd, 1998.

[5] H. Gleiter, "Nanocrystalline materials," *Materials Science*, vol. 33, pp. 223–315, 1989.

[6] C. C. Koch, I. A. Ovid'ko, S. Seal, and S. Veprek, *Structural Nanocrystalline Materials, Fundamentals and applications*. Cambridge University, 2007.

[7] P. Ayyub, R. Chandra, P. Taneja, A. K. Sharma, and R. Pinto, "Synthesis of nanocrystalline material by sputtering and laser ablation at low temperatures," *Appl. Phys. A*, vol. 73, pp. 67–73, 2001.

[8] Y. M. Wang, A. F. Jankowski, and A. V. Hamza, "Strength and thermal stability of nanocrystalline gold alloys," *Scripta Materialia*, vol. 57, pp. 301–304, 2007.

[9] A. F. Jankowski, C. K. Saw, J. F. Harper, R. F. Vallier, J.L.Ferreira, and J.P.Hayes, "Nanocrystalline growth and grainsize effects in au-cu electrodeposits," *Thin Solid Films*, vol. 494, pp. 268–273, 2006.

[10] H. A. Padilla and B. L. Boyce, "A review of fatigue behavior in nanocrystalline metals," *Experimental Mechanics*, vol. 50, pp. 5–23, 2010.

[11] C. Suryanarayana, "Nanocrystalline materials," *Int. Mater.*, vol. 40, pp. 41–64, 1995.

[12] V. Krstic, U. Erb, and G. Palumbo, "Effect of porosity on young's modulus of nanocrystalline materials," *Scripta Metall. Material*, vol. 29, pp. 1501–1504, 1993.

[13] T. D. Shen, C. C. Koch, T. Y. Tsui, and G. M. Pharr, "On the elastic moduli of nanocrystalline fe, cu, ni and cu−ni alloys prepared by mechanical milling/alloying," *Materials research*, vol. 10, pp. 2892–2896, 1995.

[14] A. M. El-Sherik, J. Shirokoff, and U. Erb, "Stress measurements in nanocrystalline ni electrodeposits," *Journal of Alloys and Compounds*, vol. 389, pp. 140–143, 2005.

[15] C. Suryanarayana and C. C. Koch, "Nanocrystalline materials - current research and future directions," *Hyperfine Interactions*, vol. 130, pp. 5–44, 2000.

[16] J. Schiøtz, T.Vegge, F. Tollay, and K.W.Jacobsen, "Simulation of mechanics and structure of nanomaterials-from nanoscale to coarser scales," in *The 19th RisøInternational Symposium on Materials Science:Modelling of Structure and Mechanics of Materials from Microstructure to Product*, 1998.

[17] D. G. Morris and M. A. Morris, "Microstructure and strength of nanocrystalline copper alloy prepared by mechanical alloying," *Acta Metall. Mater.*, vol. 39, pp. 1763–1770, 1991.

[18] K. S. Kumara, H. V. Swygenhovenb, and S. Suresh, "Mechanical behavior of nanocrystalline metals and alloys," *Acta Materialia*, vol. 51, pp. 5743–5774, 2003.

[19] K. M. Youssef, R. O. Scattergood, and a. C. C. K. K. L. Murty, "Ultratough nanocrystalline copper with a narrow grain size distribution," *Applied Physics Letters*, vol. 85, pp. 929–931, 2004.

[20] E. Q. Hall *Proc Soc London*, pp. 643–747, 1951.

[21] N. J. Petch *J Iron Steel Inst*, vol. 174, 1953.

[22] A. H. Cottrell *Trans. TMS-AIME*, vol. 212, 1958.

[23] M. Meyers and E. Ashworth *Phil. Mag.*, vol. 737, 1982.

[24] J. C. Rich, *The Materials and Methods of Sculpture*. Courier Dover Publications, 1947.

[25] C. C. Koch, K. M. Youssef, R. O. Scattergood, and K. L. Murty, "Breakthroughs in optimization of mechanical properties of nanostructured metals and alloys," *Advanced Engineering Materials*, vol. 7, pp. 787–794, 2005.

[26] T. Hanlon, Y. N. Kwon, and S. Suresh, "Grain size effects on the fatigue response of nanocrystalline metals," *Scripta Materialia*, vol. 49, pp. 675–680, 2003.

[27] X. P. Jiang, X. Y. Wang, and J. X. L. D. Y. L. C. S. Man, "Shepard m.j., zhai t., enhancement of fatigue and corrosion properties of pure ti by sandblasting," *Material science and Engineering A*, vol. 429, pp. 30–35, 2006.

[28] T. Roland, D. Retraint, K. Lu, and J. Lu, "Fatigue life improvement through surface nanostructuring of stainless steel by means of surface mechanical attrition treatment," *Scripta Materialia*, vol. 54, pp. 1949–1954, 2006.

[29] G. J. Fan, L. F. Fu, G. Y. Wang, H. Choo, P. K. Liaw, and N. D. Browning, "Mechanical behavior of a bulk nanocrystalline ni-fe alloy," *Journal of Alloys and Compounds*, vol. 434, pp. 298–300, 2007.

[30] S. Cheng, A. D. Stoica, X. L. Wang, G. Y. Wang, H. Choo, and P. K. Liaw, "Fracture of ni with grain-size from nanocrystalline to ultrafine scale under cyclic loading," *Scripta Materialia*, vol. 57, pp. 217–220, 2007.

[31] P. Cavaliere, "Low cycle fatigue of electrodeposited pure nanocrystalline metals. mater sci forum," *Materials Science Forum*, vol. 561, pp. 1299–1302, 2007.

[32] S. Bagherifard and M. Guagliano, "Fatigue behaviour of a low-alloy steel with a nanostructured surface obtained by severe shot peening," *Engineering Fracture Mechanics*, 2011.

[33] R. A. Prado, D. Facchini, N. Mahalanobis, F. Gonzalez, and G. Palumbo, "Electrodeposition of nanocrystalline cobalt alloy coating as a hard chrome alternative," in *NAVAIR Public Release 09-776, DoD Corrosion Conference*, 2009.

[34] R. W. Siegel and J. A. Eastman, *Multicomponent Ultrafine Microstructures*. MRS Proceedings, 1989.

[35] R. Z. Valiev, A. V. Korznikov, and R. R. Mulyukov, "Structure and properties of ultrafine-grained materials produced by severe plastic deformation," *Materail Science and Enginnering A*, vol. 168, pp. 141–148, 1993.

[36] A. V. Korznikov, Y. V. Ivanisenko, D. V. Laptionok, I. M. Safarov, V. P. Pilyugin, and R. Z. Valiev, "Influence of severe plastic deformation on structure and phase composition of carbon steel," *Nanostructured Materials*, vol. 4, pp. 159–167, 1994.

[37] J. S. C. Jang and C. C. Koch, "The hall-petch relationship in nanocrystalline iron produced by ball milling," *Scripta Metallurgica et Materialia*, vol. 24, pp. 1599–1604, 1990.

[38] H. J. Fecht, E. Hellstern, Z. Fu, and W. L. Johnson, "Nanocrystalline metals prepared by high-energy ball milling," *Metallurgical and Materials Transactions A*, vol. 21, pp. 2333–2337, 1990.

[39] P. Heilmann, W. A. T. Clark, and D. A. Rigney, "Orientation determination of subsurface cells generated by sliding," *Acta Metall*, vol. 31, pp. 1293–1305, 1983.

[40] D. A. Hughes and D. B. D. J. S. K. L. I. Weingarten, "A microstructurally based method for stress estimates," *Wear*, vol. 181, pp. 458–468, 1995.

[41] Y. Todaka, M. Umemoto, S. Tanaka, and K. Tsuchiya, "Formation of nanocrystalline structure at the surface of drill hole in steel," *Materials Transactions*, vol. 45, pp. 2209–2213, 2004.

[42] X. Y. Wang and D. Y. Li, "Mechanical and electrochemical behavior of nanocrystalline surface of 304 stainless steel," *Electrochim. Acta.*, vol. 47, pp. 3939–3947, 2002.

[43] N. R. Tao, M. L. Sui, J. Lu, and K. Lu, "Surface nanocrystallozation of iron induced by ultrasonic shot peening," *Nanostructured Materials*, vol. 11, pp. 433–440, 1990.

[44] G. Liu, J. Lu, and K. Lu, "Surface nanocrystallization of 316l stainless steel induced by ultrasonic shot peening," *Materials Science and Engineering*, vol. 286, pp. 91–95, 2000.

[45] M. Umemoto, Y. Todaka, and K. Tsuchiya, "Formation of nanocrystalline structure in steels by air blast shot peening," *Materials Transactions*, vol. 44, pp. 1488–1493, 2003.

[46] W. E. Kuhn, I. L. Friedman, W. Summers, and A. Szegvari, *Powder Metallurgy*. ASM, Metals Park, Metals Handbook, 1984.

[47] D. Canadinc, H. J. Maier, M. Haouaoui, and I. Karaman, "On the cyclic stability of nanocrystalline copper obtained by powder consolidation at room temperature," *Scripta Materialia*, vol. 58, pp. 307–310, 2008.

[48] C. J. Poole and F. J. Owens, *Introduction to Nanotechnology*. A John Wiley & Sons, Inc., Publication, 2003.

[49] B. E. Warren, *X-Ray Diffraction*. Dover Publications, 1990.

[50] C. F. Bohren and D. R. Huffman, *Absorption and Scattering of Light by Small Particles*. A John Wiley & Sons, Inc., Publication, 1983.

[51] N. Brenner and C. Rader, "A new principle for fast fourier transformation," *IEEE Acoustics, Speech & Signal Processing*, vol. 24, pp. 264–266, 1976.

[52] Y. Tanaka, N. Ichimiya, Y. Onischi, and Y. Yamada, "Structure and properties of al-ti-si-n coatings prepared by the cathodic arc ion plating method for high speed cutting applications," *Surf. Coat. Technol.*, vol. 146, pp. 215–211, 2001.

[53] N. W. Hitachi Tool Engineering, Ltd., "http://www.hitachi-tool.co.jp," 2005.

[54] J. D. Carlson, W. Matthis, and J. R. Toscano, "Industrial and commercial applications of smart structures technologies (lord corporation)," *Anna-Maria R. McGowan. Proceedings of SPIE*, vol. 4332, p. 308, 2001.

Chapter 2

Introduction to Cold Spray Coating

2.1 Introduction

The demands to manufacture weight efficient structures that are damage tolerant and can operate at elevated temperatures have fueled the development of novel alloy compositions and radically different processing approaches over the last decades. In recent years, thermal spray technologies have evolved from fairly crude processes that were relatively difficult to control into increasingly precise tools, tailored to take into account the properties of both the deposited material and the required coatings. The limitation of some coating types (for instance High velocity oxygen fuel (HVOF) process, Plasma spray systems, thermal spray technology of coating, etc) seem to be overcome for some materials by the other thermal spray process, called cold gas spray coating. Fig. 2.1 shows a comparison of different coating methods by considering the temperature and velocity of the particles [1, p.53]. In this diagram, the much lower process temperature in cold spray coating with respect to other coating types, has been noted. The cold spray coating was originally developed in the mid-1980 at the Theoretical and Applied Mechanics of the Russian Academy of Science Institute in Novosibirisk by Dr. Anatolii Papyrin and his colleagues [2]. They successfully deposited a wide range of pure metals, metal alloys, and composites onto a variety of substrate materials, and demonstrated the feasibility of cold spray process for various applications. Cold gas-dynamic spray (or simply cold spray) is a process of applying coatings by exposing a metallic or dielectric substrate to a high velocity (300-1200 m/s) jet of small (1-50 μm) particles accelerated by a supersonic jet of compressed gas at a temperature that is always lower than the melting point of the material, resulting in coating formation from particles in the solid state. It is worth noting that the powders do not melt before impacting the substrate [1, p.49] which makes cold spray process commendable for many different coating applications dealing with various materials not only metals but also polymers, composites, etc. Bonding of the particles in this process occurs due to the high kinetic energy upon impact; therefore, the velocity of the particle plays the most important role in material deposition. During the process, powders are accelerated by injection into a high velocity stream of gas which is generated through a converging-diverging (deLaval) nozzle. As the process continues, the particles impact the substrate and form bonds with it, resulting in a uniform almost porosity-free coating with high bonding strength [1, p.49]. Low temperature also aids in retaining the original powder chemistry and phases in the coating, with alterations that are just due to deformation and cold working. Bonding of particles in cold gas spraying is presumed to be the result of extensive plastic deformation and related phenomena at the interface [3]. It is to be underlined that the particles remain in the solid state and are relatively cold, so the bulk reaction on impact and the cohesion of the deposited material, is accomplished in solid state. Schematic diagram of the cold spray equipment is shown in Fig. 2.2a; Fig. 2.2b represents multi-stage coating formation obtained by cold spray process. Because of avoided (or low) oxidation of the particles, deposited material by cold spray coatings are more durable with better bonding strength [1, p.2]. Interfacial instability due to differing viscosities and the resulting roll-ups and vortices, promote interfacial bonding by increasing the interfacial area, giving rise to material mixing at the interface and providing mechanical interlocking between the two materials. As mentioned, it is well recognized that particle velocity prior to impact [1, 4] is the main parameter that determines what phenomenon occurs upon the

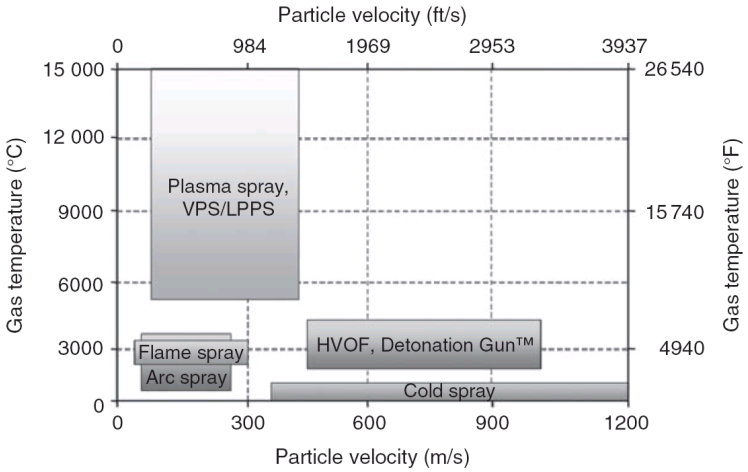

Figure 2.1: *Temperature/velocity regimes for common thermal spray processes [1, p. 53]*

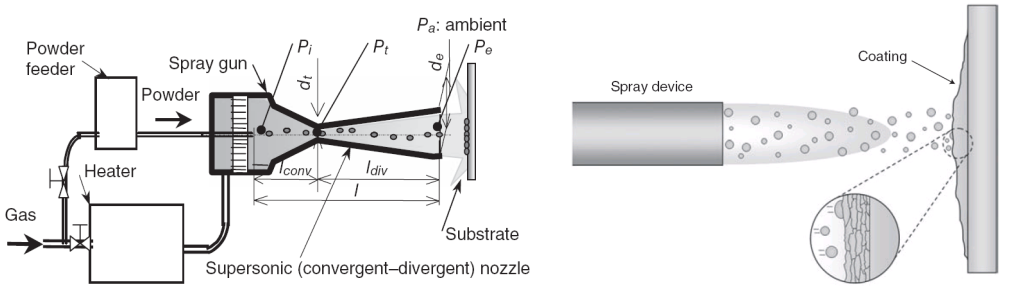

(a) *Schematic of coating machine [1, p. 118]*

(b) *Multi-stage bonding of the particles in cold spray process [1, p. 44]*

Figure 2.2: *Schematic view of the machine and the bonding of material in cold spray coating [1, p.44,118],*

impact of spray particles, whether it would be the deposition of the particle or the erosion of the substrate. Critical velocity (CV) for a given powder is defined as the velocity that an individual particle must attain in order to deposit after impacting the substrate [1, p.22]. In other words for a given material, the CV is the velocity at which the transition from erosion of the substrate to deposition of the particle takes place. Experimental investigations also reveal that successful bonding is achieved only above this certain amount of particle velocity, the value of which is associated with temperature and thermo-mechanical properties of the sprayed material [4, 5], as well as the characteristics of the substrate [6–8]. On the other hand, the lower the CV of the particles in the process is (i.e. by changing the parameters such as temperature of the gas), the more efficient and less expensive process will be obtained. Temperature of the particles is among the most effective parameters on both CV and deposition efficiency (DE) [1, p.32]. Indeed, the drastic increase of DE in cold spray process can be attributed to the increase of both the velocity of sprayed particles (which increases the pressure and temperature at the impact moment) and the temperature of the sprayed particles and the substrate [7]. Cold spray technology can be used to produce both protective coatings and prototyping/freeform fabrication in not only strategic industries such as defense and aerospace, but also in various other general industries such as steel, utilities, paper and pulp, etc. High performance materials such as superalloys and nanostructured materials are used to produce complex and intricate components of various high tech industries. Established cold spray process can cater to economical, fast prototyping and fabrication of these components [9].
NC coatings with grain sizes in the nanometer range are, on the other hand, known to exhibit superior hardness and strength. The search for nanostructured coatings is driven by the improvement in coating technologies and the availability of various kinds of synthesized nanopowders which can be used as feedstock materials for thermal spray processes. In this regard, although coating with nano size particle in cold spray coating is not feasible due to the back flow, it has been shown that this process has a great potential for deposition of different NC grain metallic powders in micro size [10–12]. On the other hand, as it has been discussed in Chapter. 1, the cold spray coating is one of the only techniques that can be considered in both deposition and severe plastic deformation (SPD) categories [13].
In this chapter, a very brief review of cold spray coating, the process and its important parameters, application, and finally the possibility of obtaining NC surface coated material via this process, has been studied. In Section 2.2, different effective parameters have been studied; it has been tried to show, how it is possible to evaluate the process quality and which parameters have considerable effect on the results. In Section 2.3, the advantages and disadvantages of the cold spray coating have been briefly reviewed; the advantages have been presented in more details. Different possible applications of cold spray coating have been reviewed in Section 2.4. In the very last Section, the production of NC material via cold spray coating has been briefly reviewed. The effect of coating on fatigue life has been studied in Section 2.5; although there are few available studies on the effect of coating on fatigue life, the results and approaches presented in the literature have been studied and reviewed.

2.2 Cold spray coating process

In cold spray coating process, the micro powders (mostly metallic), are deposited by their high kinetic energy due to supersonic flow of the gas. The high velocity of the particles is obtained by a divergent-convergent (deLaval) nozzle. Practically, by using supersonic gases such as Helium, and passing the powders and the gas through the nozzle, the required velocity for bonding (300-1200 $\mathrm{m/s}$) will be obtained. The gas temperature along with many other process parameters, play considerable role in coating quality from increasing DE to the porosity control of the final deposition. The coating process per se, based on the operating pressure of the flow gas, is divided into two high and low pressure categories which will be discussed in more detail in Chapter.6. As well as any other methods of powder spray, DE can be considered as an important criterion in order to evaluate the process. A simple way to measure the DE, is dividing the mass of the substrate after coating by the weight of all particles interacting with the substrate. There are many reasons that make it practically impossible to obtain a DE that is equal to unity. First, polydisperse powders are usually used. As the jet during its impingement is spreading along the substrate surface, the finest particles either do not reach the surface at all or impact at acute angles, which deteriorate particle attachment. Although the largest particles are incident at a close-to-normal

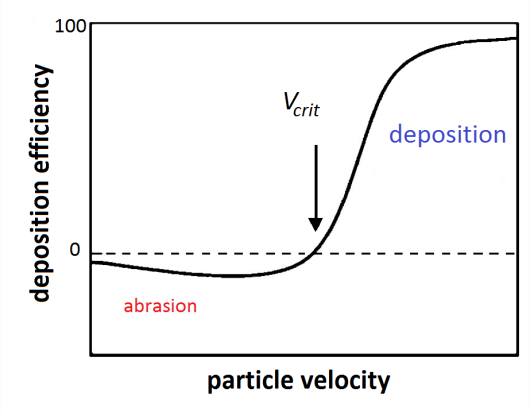

Figure 2.3: *Schematic of the correlation between particle velocity and deposition [14].*

angle (i.e., the angle between the particle impact velocity and the substrate surface is close to $90°$), their velocities may be insufficient for particle attachment. Second, the particle velocity at the jet periphery can be lower than its limit for particle attachment. In addition, if the velocity is not sufficiently high, the surface should be self-activated by the impacted particles [3]. Incidentally, the effect of different parameters in the coating is evaluated by their effect on the DE. Although, in some cases it might not be an appropriate criterion and there are some other parameters which might decrease the DE, due to the simplicity of its measurement, it can be considered as the best method for evaluation of the process. Of course, there are some other parameters such as porosity of deposition, strength of the bonding, etc which in many cases are more important than DE; anyway it can be generally assumed that higher DE leads to lower porosity and stronger coating.

2.2.1 Principal process parameters

There are few interacting parameters in cold spray coating which make the process relatively simple. Pressure and temperature of the gas, gas type and powder feeder rate, are the main controllable parameters. The studies show the other not direct parameters such as quality of the powders, nozzle design, properties of the substrate and in case of automatic coating, robot velocity control, might have also important effects on the coating quality and the resulting DE.

- **Velocity of the particles**
  Velocity of the particles plays the most important role in the coating quality due to the intrinsic of the coating process. Unfortunately, it is not possible to directly control this parameter; besides almost all process parameters have direct or indirect effects on the particles' velocity. Indeed the coating process begins, as the particle velocity exceeds the critical value. Besides the DE rapidly increases to $50 - 70\%$ as the particle velocity significantly exceeds the critical value. For certain types of material, as discussed before, successful deposition requires a certain minimum particle velocity namely the CV, the value of which depends most significantly on the thermo-mechanical properties of the powder and substrate materials [1, 3]; below this CV, impacting particles are generally observed to cause erosion of the substrate. The relationships between the DE and particle velocity, presented in Fig. 2.3, were investigated by [14]. It is to be mentioned that normally, a feedstock powder will contain a range of particle size and consequently a distribution of particle velocities. Assadi *et al.* [4] have used numerical simulation to work out the effect of various material properties on the CV in cold spraying. They summarized these effects into a simple expression which will be discussed in the next chapter. Raletz *et al.* [15] present an imaging technique that allows fast measurement of the in-flight particles' velocity . The measuring method is first evaluated by comparing the CV of copper (sprayed on copper substrate) available in the literature, with the measured one.
  Numerically, there are different techniques that can be used to calculate the gas flow of cold spray

Table 2.1: *The physical properties and qualitative costs of candidate processes [1, p. 80]*

Gas	Sonic velocity (m/s)	Density s.t.p. (kg/m^3)	Inert or reactive	Cost
Air(80%N_2+20%O_2)	343	1.225	Reactive	Cheap
Nitrogen(N_2)	349	1.185	Partially inert	Cheap
Hydrogen(H_2)	1303	0.085	Reactive	Expensive
Argon(Ar)	319	1.69	Inert	Expensive
Helium(He)	989	0.168	Inert	Very Expensive

systems. [1, p.118] along with other researchers [16–19] have presented a series of numerical models in order to estimate the velocity of the particles. Eq. 5.6 shows the most general differential equation presented in [1, p.121] for estimating the particle velocity with respect to the velocity of the gas. Particle acceleration and heating in a gas flow within the nozzle are obtained by solving the equations of motion and heat transfer. The spray particle velocity that can be reached via a cold spray device is limited only by the gas velocity. Using high pressure gas flow, long nozzles, and small particles result in particles traveling at the gas velocity. The gas velocity can be increased by using low molecular weight gases, high temperatures, and large expansion ratio nozzles. However, practical limits exist for all of the process variables. Thus, it is desirable to produce a sufficient spray particle velocity, with an optimal design, so that the guns can be compact and the gas use would be minimized [19].

$$\frac{dV_p}{dt} = \frac{3C_D\rho_g}{4D_p\rho_p}\left(V_g - V_p\right)\left|V_g - V_p\right| \tag{2.1}$$

The formulation obviously shows the direct relationship of the particle velocity and gas velocity which depends, of course, on initial condition of the process, nozzle shape, and the gas properties. The dynamic of the process has been studied in more detail in Chapter 5.

- **Gas type**:
  The fundamental resource in cold spray coating is the process gas which forms the supersonic jet stream that is used to accelerate the powder particles above the CV for deposition and consolidation. Ideally, the gas needs to have a high sonic velocity and mass in order to transfer momentum to the powder. It is also important that the gas is inert, so that it is safe for fine metal powders which are potentially explosive and does not change the properties of the deposit. It is also preferable that the gas is cheap because of the high consumption rates involved [1, p.79]. A list of candidate gases is presented in Tab. 2.1. The two main gases used in cold spray coating are helium and nitrogen, both of which are inert. Initially, cold spray was developed with helium, principally because of its high sonic velocity, which is approximately three times that of nitrogen. Although, hydrogen has the highest sonic velocity in the list, it can spontaneously combust upon contact with air at high velocities. Numerically, the ratio of specific heat (γ) of the gas has a direct effect on the gas velocity [19]; thus, helium, which has a bigger γ, is a better driving gas. Fig.2.4 shows the effect of two different driving gases on the velocity of the particles. It shows that by using helium the velocity of the gas would be more than two times of the gas velocity driven by air [20].

- **Nozzle geometry** The parameters such as super sonic gas with high temperature and pressure, small particles, etc are not able to produce a supersonic flow without the convergent-divergent nozzle. The nozzle design can increase the velocity of the particles and consequently the DE in the very same process. There are several numerical techniques which have been used to find the optimum design of the nozzle by considering the default process parameters. Recent analysis have used computational fluid dynamics (CFD) methods to simulate complex phenomenon in two dimensions. The one-dimensional approximation is simple and sufficiently correct to be used for expressing the effect of nozzle geometry on the internal nozzle flow [1, p.118]. Fig.2.5 [1, p.124] shows the effect of different nozzles with the same process parameters on the particle and gas

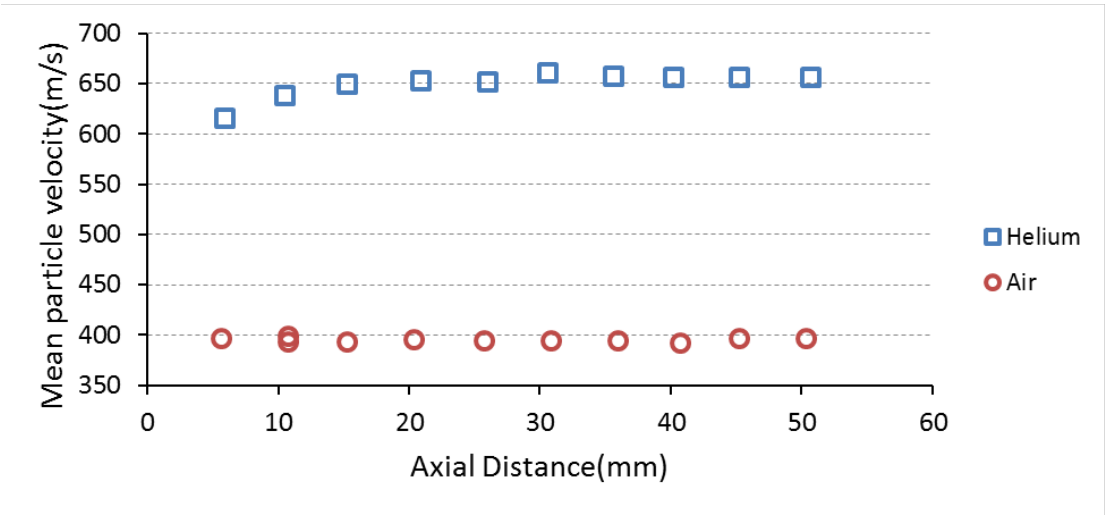

Figure 2.4: *Mean particle velocity versus z-axis position [20]*

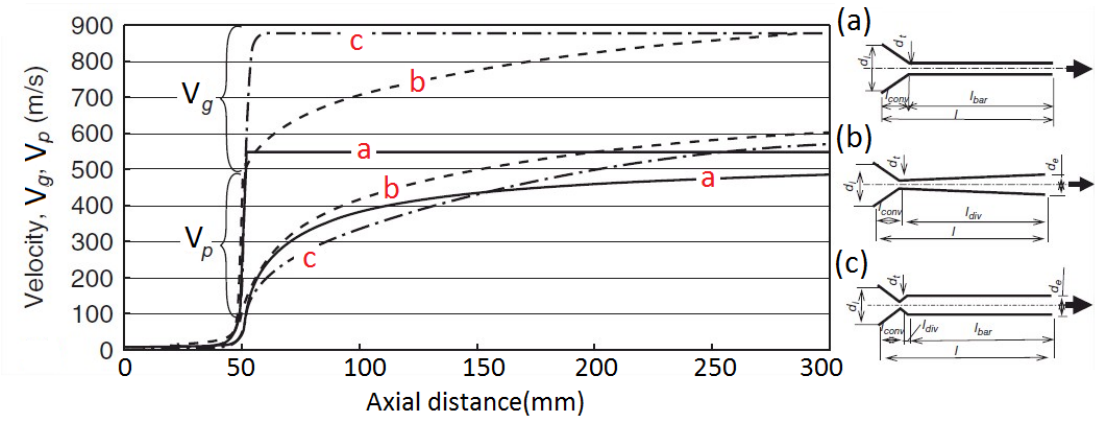

Figure 2.5: *Effect of nozzle geometry on calculated velocity of gas and particles [1, p.124]*

velocity. For more details, there are many trials with numerical and analytical solutions for nozzle design, presented in [1, 3, 16, 18, 19].

- **Temperature**
  By inserting a heat exchanger in the circuit of the process, the temperature of the gas and consequently the temperature of the particles can be increased. It has been observed that higher process temperature will result in lower consumption and better DE of the deposited materials. Fig. 2.6 shows the effect of the process temperature on the DE of three different materials. It can be concluded that the particle and the substrate temperatures have significant effects on the spraying process [2, p.26]. By the way, based on the formula presented by Assadi *et al.* [4] to assess the CV, the temperature of the particle has direct effect on the particles' CV (Eq.4.1).

- **Powders**
  The flow rate of a powder is an essential characteristic that determines the feasibility of cold spray processing. Powders with flow rates above $60s/50g$ tend to build up and block the gas flow in the deLaval subsonic and supersonic nozzles [1, p.107]. Assuming that cold spray parameters are optimized, the particle morphology and density affect the actual impact velocity, and subsequently the coating density and DE [21]. Li *et al.* [21] showed that the particle velocity decreases with an increase in particle diameter. It is possible to find the best powder size distribution based on the

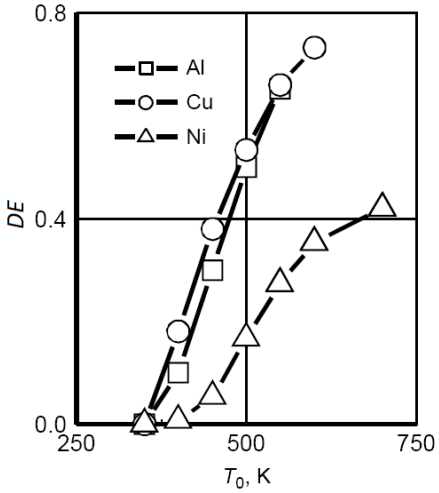

Figure 2.6: *DE of aluminum, copper, and nickel powders sprayed on copper [2, p.27]*

fluid dynamic behavior of the process [19]. Higher particle temperatures associated with higher preheat gas temperature, result in lower CV requirements. An increase in particle temperature ultimately leads to higher surface oxidation levels for non-noble metals. High oxygen contents of the cold spray powder require, in turn, higher CV for coating formation [21]. Fig. 2.7 shows the effect of particle size on CV. Not only the particle size but also the powders morphology

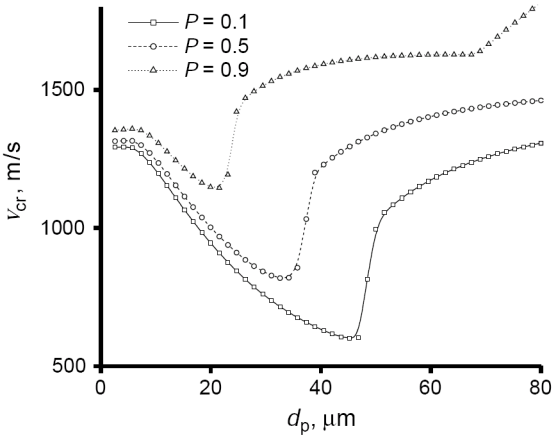

Figure 2.7: *Particle impact velocity versus the particle diameter for a prescribed particle−adhesion [2, p. 88]*

has considerable effect on the process quality. Fig. 2.8 shows particle morphology of some different materials. Jodoin *et al.* have studied the effect of particle morphology on the quality of coating [22]. They reported that the smaller particle size range exhibits a higher average particle velocity. Consequently, higher acceleration and, therefore, higher particle impact velocity are to be expected when using a powder with a smaller particle size distribution.

- **Substrate**
  Legoux *et al.* [7] surveyed the change in substrate temperature during the deposition process for three different materials, measured by means of a high speed IR camera. The coating formation was investigated as a function of (1) the surface temperature of the substrate, measured during deposition, (2) the gun transverse speed, and (3) the particle velocity. Both single particle impact

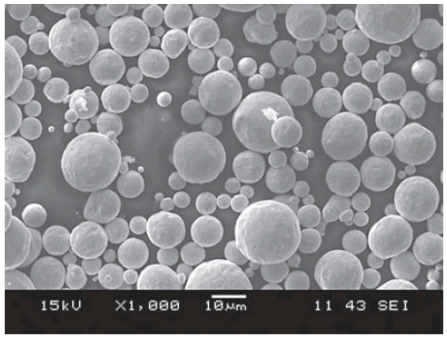

(a) *Scanning electron microscopy observation of nitrogen gas atomized silver metal powder, 5-20 micron particle size.*

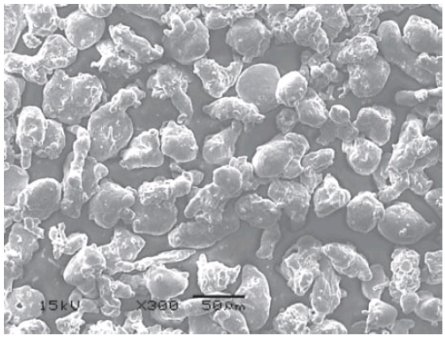

(b) *Scanning electron microscopy observation of annealed air atomized aluminum, 3600 ppm surface oxygen.*

Figure 2.8: *Morphology of some cold spray powders [1, p. 107]*

samples and thick coatings were produced and characterized. As it can be observed in Fig. 2.9, the zinc DE decreases with temperature. On the other hand, it increases for Al and remains almost unchanged for the samples coated by tin. This difference might be due to the melting points variations for each of these powders [7]. Zhang *et al.* [23] have worked on spraying aluminum powder on a range of substrates. The examined substrates included metals with a quite wide range of hardness, polymers, and ceramics. The substrate surfaces had low roughness before deposition of aluminum. It has been shown that initiation of deposition depends critically upon substrate type. A number of phenomena have been observed following spraying onto various substrates, such as substrate melting, substrate and particle deformation, as well as some evidences of a metal-jet formation. Such phenomena have been related to the processes that occur during impact of the particles on the substrate. Metallic substrates which are mostly harder than the aluminum particles, generally promoted the deposition. Initiation was seen to be rapid on hard metallic substrates, even when deformation of the substrate was not visible. Siegmann *et al.* [24] studies shows that the topography of a roughened substrate (or bond coat) plays the key role in coating adhesion, and in the phenomena which can influence adhesion. It is also reported that the complex nature of the substrate topographies cannot be adequately characterized over the entire range by conventional methods such as average roughness, and that with a greater roughening of the substrate surface (from polished to grit-blasted), DE of metallic powders increases slightly [17].

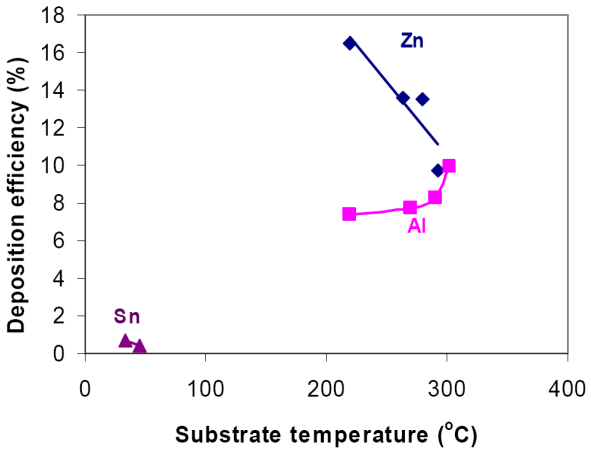

Figure 2.9: *DE as a function of substrate temperature [7]*

2.3 Advantages of cold spray coating

As any other material processing technique, the cold spray process has its own positive and negative points. The main advantage of the cold spray process is that it is a solid-state process, which results in unique coating characteristics. Some of the main advantages of cold spray process are listed bellow [1, p.62]:

- *High DE*
  Very high DE values have been achieved through cold spray process for most metals, alloys and composites. For instance, DE values in excess of 95% are obtained for aluminum, copper and their alloys.

- *High deposition rate*
  The spray footprint of the cold spray beam is narrow and well defined. A typical spray beam has about 10 mm diameter with sharp edges. A narrow spray beam with appreciable powder feed rate translates into very high deposition rate (DR) values. For most materials, it is possible to produce a 1-2 mm thick coating in a single pass.

- *No or little masking*
  As noted above, the particle beam in the cold spray process is narrow and well defined. Although a typical spray beam has a diameter of about 10 mm, it is possible to design special rectangular nozzles and obtain spray beams as small as 1-2 mm wide with sharp edges.

- *No grit blast*
  The cold spray process can be viewed as a triplex (grit blast-spray coat-shot peen) process. As expected, the velocity distribution across the spray beam shows Gaussian distribution. When the system is running with optimized parameters, particles in the core have velocities higher than the CV and the particles at the rim have lower (than CV) velocities. When the spray beam is scanned, the particles at the leading edge impact on the substrate surface with less than the critical deposition velocity (V_c) which leads to solid particle erosion of the surface, resulting in in-situ micro-grit blasting.

- *High density*
  Moreover, any loosely bound particles are sputtered away, and deposited splats are micro-peened by the trailing edge particles of the spray beam. Finally, every subsequent pass of the spray beam 'shot peens' the underlying layer and thereby increases its density.

- *Flexibility in substrate-coating selection*
  Since cold spray does not heat and melt the coating material, the formation of weak interfaces is avoided. Hence, the engineer has the flexibility to select the materials on the basis of design requirements.

- *Minimum thermal input to the substrate*
  In conventional thermal spray processing, the substrate is heated by the flame to varying degrees. In the cold spray process, conversely, there is no high temperature jet to heat the substrate, and the substrate receives only the stagnation enthalpy of the impacting particles.

- *High bond strength*
  Cold sprayed coating exhibits very high bond strength over many substrate materials including metals (aluminum, copper, titanium, nickel, etc.), alloys (Inconels, steels, etc.) and sometimes composites (metal matrix composites, carbon composites, etc.)

- *Compressive residual stresses*
  In the cold spray process, the coating is generated by plastic deformation in the solid state and hence the residual stress across the entire coating thickness is compressive in nature.

- *Ultra-thick coating*
  A cold sprayed coating is compressively stressed, ultra-thick layers can be produced over many

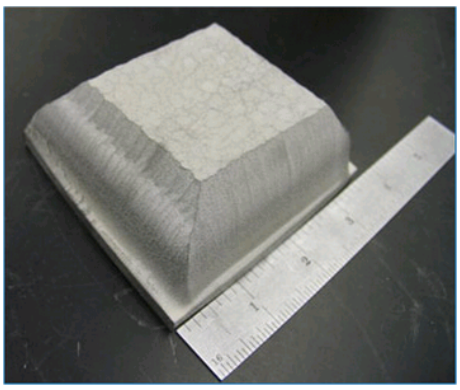

Figure 2.10: *An example of thick deposition by cold spray coating [25]*

substrates without bond failure. This aspect has been particularly used in some applications such as replacement of thick electroplated layers. Fig.2.10 shows an example of the thick deposition by cold spray coating.

- *No phase changes*
  As expected, oxidation, decomposition, formation of metastable phases, preferential loss of some constituent, etc., occur during any high temperature processing. During the cold spray process, the particles remain close to the ambient temperature and hence no phase changes occur. It has been proven by using XRD diffraction to check the diffraction angles of the material before and after coating [21].

- *No oxidation*
  Cold spray does not heat the material to high temperature. Moreover, an inert gas is used to propel the particles, which effectively shields the splats that are formed over the substrate. Hence, oxidation of the particle is almost completely avoided in the cold spray process.

- *No grain growth*
  Cold spray is a low temperature, solid-state consolidation technique and can be used to process temperature-sensitive materials such as nanomaterials and amorphous materials.

- *Strength and hardness*
  Mechanical property evaluation has shown that the ultimate tensile strength (UTS) of cold sprayed coatings is always higher than the bulk values. Moreover, coatings exhibit higher hardness than the bulk values, due to the high degree of plastic deformation of the particles [26].

To come to the disadvantages, cold spray main disadvantage arises due to the plastic deformation process, which leads to a loss of ductility of the coating. In cold spray coating , the sprayed material has near-zero ductility in the as-sprayed condition; another weak point is probably the fact that although composites can be sprayed, pure ceramics and some alloys can not be processed in this way; in cold spray coating the substrate requires at least limited ductility of the substrate to produce well bonded coating; as with many other coating techniques, cold spray is also a line-of-sight process. In summary, the above mentioned facts can be considered as the disadvantages of cold spray coating.

2.4 Applications

The advantages of cold spray coating mentioned in the previous section lead to everyday increasing industrial applications of this surface treatment. The following items are some of the important current applications of cold spray coating used all over the world. It is to be noted again that cold spray coating can be considered a young technique with respect to other types of thermal coating.

2.4.1 Wear resistance

The material with high wear resistance are generally carbide materials such Cr_3C_2 or TiC which are mostly difficult to coat by cold spray coating. Considering, the current state of the art, most cold spray depositions have been made with nitrogen and have focused mainly on metallic materials. Ceramics typically do not plastically deform to the extent that metallic materials do. Presently no commercial carbide wear-resistant cold spray are available, but this should change in the next few years with the rapid advancements being made in cold spray technology areas [1, p. 265]. Wolfe *et al.* used cold spray coating successfully in order to coat $Cr_3C_2 wt.\%$ NiCr and $Cr_3C_2 - 25wt.\%Ni$ coating on 4140 alloy for wear resistance applications. The obtained results are presented in detail in [1, p.264]. To summarize, the results show the average VHN values of the Cr_3C_2-based coatings ranged from 300 to 900 VHN which strongly suggests that the hardness (and thus wear resistance) can be tailored over a wide range of values to meet a variety of hardness specifications. In general, optimized stand-off distance, powder feed rate, traverse speed, and nozzle design, lead to over 57% and 37% increase in average VHN for the agglomerated and sintered powder and powder blends, respectively. This work and many other papers [27–29] show the potential of using cold spray coating in wear resistance applications.

2.4.2 Corrosion protection

The advantages of cold spray technology for deposition of corrosion-resisting layers are evident; a major consideration in the selection of cold spray processing for a given application is its cost relative to alternatives. This may be a significant factor for cost-sensitive situations such as automobile manufacturing. Considering the cost implications of cold spray passivation in comparison with alternatives for galvanizing of steel, cold spray processing leads to cost penalties of at least a factor of two when compared to wire flame spraying. Costs of specialty powders contribute to this, as well as instances where helium is the propellant gas of choice for the application. The use of air or nitrogen gas may contribute to cost reductions; however the stipulation that the feedstock be particulate in nature is not readily overcome at this point [1, p.306]. Cold spraying offers both unique opportunities for selective processing and restoration; at the same time, it presents challenges of scale-up, cost reduction, powder handling, and safety issues; all of which are well-known to the thermal spray community. Beyond extension of the process to familiar areas such as sacrificial galvanic protection, is the prospect of unique application of unconventional passivations such as deposition of aluminum directly on magnesium alloys [1, p. 311].

2.4.3 Repair of damaged components

The US Army Research Laboratory (ARL) Center for Cold Spray Technology [25] has developed a cold spray process to reclaim magnesium components that show significant improvement over existing methods and is in the process of qualification for use on rotor-craft. The cold spray repair has been shown to have superior performance in the tests conducted up to date; it is inexpensive, can be incorporated into production, and has been modified for field repair, making it a feasible alternative over competing technologies [1, p.327]. The feasibility of using the cold spray process to repair non-structural magnesium aircraft components, has demonstrated satisfactory results obtained from adhesion, corrosion testing, and microstructural analysis. Adhesion of the coating was considered to be the most important evaluating criteria. These values represent the strength of the adhesive used, as all failures occurred at the interface between the adhesive and the coating. The cold spray coating was not pulled off the substrate and the coating did not fail cohesively [1, p.350]. Fig.2.11 shows the microstructure of the cold spray repair.

2.4.4 Coating and NC

Novel fabrication technology of nanoparticles is versatile and includes a wide range of vapor, liquid and solid state processing techniques. Available techniques for the synthesis of nanoparticles via vapor routes, range from physical vapor deposition and chemical vapor deposition to aerosol spraying. The solid state route preparation takes place via mechanical milling and mechanochemical synthesis. Among these, mechanical milling and spray conversion processing are commonly used to produce large quantities of nanopowders [30]. NC coatings with grain sizes in the nanometer range are also known

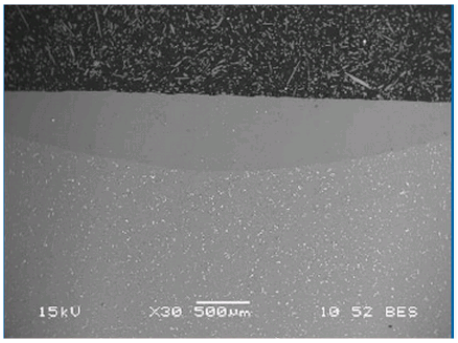

Figure 2.11: *Microstructure of cold spray repair [25]*

to exhibit superior hardness and strength. The search for NC coatings is driven by the improvement in coating technologies and the availability of various kinds of synthesized nanopowders. Such nanopowders can be used as feedstock materials for thermal spray processes. Thermal spraying offers the unique advantage of moderate to high rate of throughput and the ability to coat target materials with complex shapes using nanostructured feedstock powders prepared from vapor, liquid and solid routes [30]. Unfortunately, using the nano size powders in cold spray coating due to the presence of the back flow is not possible. However, NC powders in micro size are reported to be successfully used in cold spray coating by Ajdelsztajn *et al.* [12]. The hardness of coated NC-Ni have been comparable with other NC producing techniques such as electrodeposition. Cold spraying has been successfully used also to obtain highly dense NC copper alumina metal matrix composite coatings [31]. Phani *et al.* [31] showed that grain size is the most dominant factor affecting the electrical conductivity of the coatings. However, the existing models are not able to account for the low conductivity observed in the as-coated specimens. Fig.5.1 shows the as-sprayed copper alumina coating and agglomerated NC copper alumina powder presented by [31]. In another interesting study performed by Yandouzi *et al.* [11], the composite materials

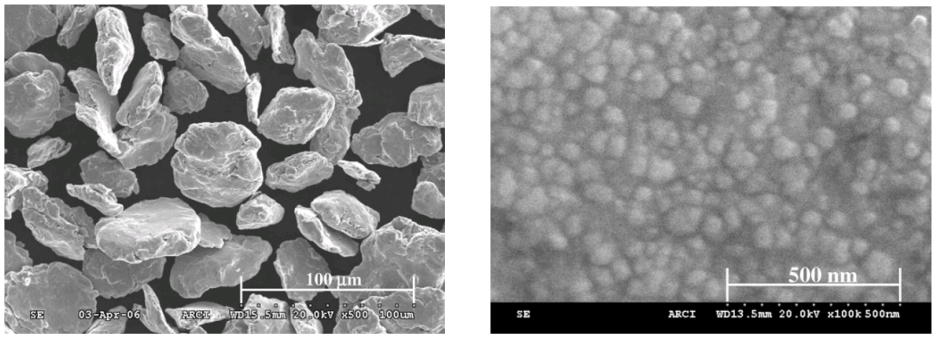

(a) *agglomerated NC copper alumina powder* **(b)** *As-sprayed copper alumina coating*

Figure 2.12: *The micrograph of the a) nano powders and b) samples coated by nano powders [31]*

of an Al-12Si matrix reinforced with 20wt.% B_4 particles were deposited by cold spray coating. The cryomilling has been used to produce NC composite powders.

2.5 Effect of cold spray coating on fatigue strength

The effect of cold spray coating process on the fatigue strength is of particular interest to the author; There are many researches studying the effect of other types of thermal spray coatings on fatigue endurance; however, in the case of cold spray coating, there are not many records available in the literature. The two most important studies in this regards are developed by Price *et al.* [32] and Sansoucy*et al.* [33]. It is to be highlighted that they have shown quite different results. Price *et al.* [32] studied the effect of

cold Spray deposition of a titanium coating on fatigue behavior. Coatings were deposited onto samples with two different surface preparation methods (as-received and grit-blasted). The fatigue life of the as-received and grit-blasted materials, both before and after coating were estimated. A 15% reduction in fatigue endurance was observed after application of the coating on the substrate, but no significant reduction was observed on its application to the grit-blasted substrate. It has been shown that titanium coatings have a detrimental effect on the fatigue endurance of Ti6Al4V. Compressive stresses found within the coating are usually associated with increased fatigue endurance; however, those found within cold spray titanium coatings are too low to prevent fatigue crack formation and advancement. it is concluded that probably these parameters lead to premature fracture. Sansoucy *et al.* [33] in particular, work on bending fatigue and the bonding strength of the Al-Co-Ce coatings. The results show that Al-Co-Ce coatings improved the fatigue behavior of Al-2024-T3 specimens compared to uncoated and Alclad specimens. It is suggested that the increase in the fatigue properties can be attributed to the compressive residual stresses induced in the coatings and to the high adhesion strength of the coatings to the substrates. The fatigue results can be rationalized on the basis of two important factors: the existence of compressive residual stresses, and the high adhesion of the coatings to the substrate. The high velocity impacts of particles cause plastic deformation of the underlying layers and generate compressive residual stresses. It should be considered that Price *et al.* [32] have reported negligible compressive residual stresses on the coated samples and the material which has been coated. The SEM observations also showed delamination in deposition material after fatigue test which represented no, or very few, contribution of the deposited materials to the fatigue test. There is an interesting study by Ibrahim *et al.* [34] on fatigue behavior of the samples coated by NC titania powders through thermal spray. It is to be noted that in their case, the coating method is not cold spray coating, nanostructured and conventional titania (TiO_2) coatings were thermally sprayed using air plasma spray (APS) and HVOF processes. Rotating bending test has been applied to specimens. The results indicate that the HVOF-sprayed nanostructured titania coating, exhibited higher fatigue lives compared to the air plasma spray conventional titania coating. As it was expected, and mentioned in Chapter. 1 the coating of nanocrystalline powders increased the fatigue endurance of the samples in the case study of Ibrahim *et al.* [34].

2.6 Conclusion

In conclusion, cold spray is still an emerging, but very promising, technology. In some applications, it offers a way to overcome important limitations of traditional thermal spray technologies, such as high levels of porosity and oxide in the sprayed material. However, it is also more limited in the range of materials and substrates that are process compatible; there are currently quite limited applications and property data for cold sprayed materials as compared to the traditional thermal spray processes. Nevertheless, cold spray coating represents an important new process capability that may replace more traditional spray processes in selected applications. Moreover, it is likely to lead to new applications that are not suited to traditional thermal spray technologies. Cold spray offers the potentially valuable possibility of new design, manufacturing, and component reclamation alternatives for those willing to explore the intriguing new opportunities that it provides.

Bibliography

[1] V. Champagne, *The cold spray materials deposition process, Fundamentals and application*. Woodhead Publishing, 2007.

[2] A. Papyrin, V. Kosarev, S. Klinkov, A. Alkhimov, and V. Fomin, *Cold Spray Technology*. Elsevier, 2006.

[3] R. McCune, W. Donlon, E. Cartwright, A. Papyrin, E. Rybicki, and J. Shadley, "Characterization of copper and steel coatings made by the cold-gas-dynamic spray method," *ASM International*, pp. 397–403, 1996.

[4] H. Assadi, F. Gaurtner, T. Stoltenhoff, and H. Kreye, "Bonding mechanism in cold gas spraying," *Acta Materialia*, vol. 51, pp. 4379–4394, 2003.

[5] A. Alkimov, V. Kosarev, and A. Papyrin, "A method of cold gas dynamic deposition," *Dokl. Akad. Nauk SSSR*, vol. 318, pp. 1062–1065, 1990.

[6] T. V. Steenkiste, J. Smith, R. Teets, J. Moleski, D. Gorkiewicz, R. Tison, D. Marantz, K. Kowalsky, W. Riggs, P. Zajchowski, B. Pilsner, R. McCune, and K. Barnett, "Kinetic spray coatings," *Surf. Coat. Technol.*, vol. 111, pp. 62–71, 1999.

[7] L. Legoux, E. Irissou, and C. Moreau, "Effect of substrate temperature on the formation mechanism of cold sprayed aluminum, zinc, and tin coating," *Journal of Thermal Spray Technology*, vol. 16, pp. 619–627, 2007.

[8] P. Gao, C. Li, G. Yang, and C. L. Y. Li, "Influence of substrate hardness on deposition behavior of single porous wc-12co particle in cold spraying," *Surface & Coatings Technology*, vol. 203, pp. 384–390, 2008.

[9] J. Karthikeyan, J. Lindeman, and C. C. Berndt, "Cold spray processing of titanium powder," *Thermal Spray:Surface Engineering via Applied Research*, pp. 255–262, 2000.

[10] J. Mondoux, B. Jodoin, L. Ajdelsztain, J. M. Schoenung, and G. E. Kim, "Nanostructured aluminum coatings produced using cold spraying technology," in *Thermal Spray Solutions. Advances in Technology and Application / Verband Für Schweiβen and verwandte Verfahren DVS-Verlag GmbH, Dusseldorf/Germany*, 2004.

[11] M. Yandouzi, A. J. Böttger, R. W. A. Hendrikx, M. Brochu, P. Richer, A. Charest, and B. Jodoin, "Microstructure and mechanical properties of b4c reinforced al-based matrix composite coatings deposited by cgds and pgds processes," *Surface & Coatings Technology*, vol. 205, pp. 2234–2246, 2010.

[12] L. Ajdelsztajn, B. Jodoin, and J. M. Schoenung, "Synthesis and mechanical properties of nanocrystalline ni coatings produced by cold gas dynamic spraying," *Surface & Coatings Technology*, vol. 201, pp. 1166–1172, 2006.

[13] H. A. Padilla and B. L. Boyce, "A review of fatigue behavior in nanocrystalline metals," *Experimental Mechanics*, vol. 50, pp. 5–23, 2010.

[14] F. Gärtner, T. Stoltenhoff, T. Schmidt, and H. Kreye, "The cold spray process and its potential for industrial applications," *Journal of Thermal Spray Technology*, vol. 15, pp. 223–232, 2006.

[15] F. Raletz, M. Vardelle, and G. Ezo'o, "Critical particle velocity under cold spray conditions," *surface & coating Technology*, vol. 201, pp. 1942–1947, 2006.

[16] B. Samareh, O. Stier, V. Lüthen, and A. Dolatabadi, "Assessment of cfd modeling via flow visualization in cold spray process," *Journal of Thermal Spray Technology*, vol. 18, pp. 934–943, 2009.

[17] T. Stoltenhoff, H. Kreye, and H. J. Richter, "An analysis of the cold spray process and its coatings," *Journal of Thermal Spray Technology*, vol. 11, pp. 542–550, 2002.

[18] M. Grujicic, W. S. DeRosset, and D. Helfritch, "Flow analysis and nozzle-shape optimization for the cold-gas dynamic-spray process," *Journal of Engineering Manufacture*, vol. 217, 2003.

[19] R. C. Dykhuizen and M. F. Smith, "Gas dynamic principles of cold spray," *Journal of Thermal Spray Technology*, vol. 7, pp. 205–212, 1998.

[20] D. L. Gilmore, R. C. Dykhuizen, R. A. Neiser, T. J. Roemer, and M. F. Smith, "Particle velocity and deposition efficiency in the cold spray process," *J. Therm. Spray, Technol.*, vol. 8, pp. 576–582, 1999.

[21] C. J. Li, W. Y. Li, and H. Liao, "Examination of the critical velocity for deposition of particles in cold spraying," *Journal of Thermal Spray Technology*, vol. 15, pp. 212–222, 2006.

[22] B. Jodoin, L. Ajdelsztajn, E. Sansoucy, A. Z. c, P. Richer, and E. J. Lavernia, "Effect of particle size, morphology, and hardness on cold gas dynamic sprayed aluminum alloy coatings," *Surface and Coatings Technology*, vol. 201, pp. 3422–3429, 2006.

[23] D. Zhang, P. H. Shipway, and D. G. McCartney, "Cold gas dynamic spraying of aluminum: The role of substrate characteristics in deposit formation," *Journal of Thermal Spray Technology*, vol. 14, pp. 109–116, 2006.

[24] S. Siegmann and C. A. Brown, "Scale-sensitive fractal analysis for understanding the influence of substrate roughness in thermal spraying," in *1st United Thermal Spray Conference - Thermal Spray: A United Forum for Scientific and Technological Advances*, 1997.

[25] http://www.arl.army.mil/www/default.cfm.

[26] J. Haynes, A. Pandey, J. Karthikeyan, and A. Kay, "Cold sprayed discontinuously reinforced aluminum (dra)," in *Proceedings of ITSC, Seattle, ASM International, Materials Park, Ohio*, 2006.

[27] K. Spencer, D. M. Fabijanic, and M. X. Zhang, "The use of $alal_2o_3$ cold spray coatingsnext term to improve the surface properties of magnesium alloys," *Surface and Coatings Technology*, vol. 204, pp. 336–344, 2009.

[28] C. H. Hager, J. Sanders, S. Sharma, A. Voevodin, and A. Segall, "The effectoftemperatureongrossslipfrettingwearofcold-sprayednickel coatings on ti6al4v interfaces," *Tribology Internationa*, vol. 142, pp. 491–502, 2009.

[29] S. R. Bakshi, D. Wang, T. Price, D. Zhang, A. K. Keshri, Y. Chen, D. G. McCartney, P. H. Shipway, and A. Agarwal, "Microstructure and wear properties of aluminum/aluminum-silicon composite coatings prepared by cold spraying," *Surface & Coatings Technology*, vol. 204, pp. 503–510, 2009.

[30] S. C. Tjong and H. Chen, "Nanocrystalline materials and coatings," *Materials Science and Engineering*, vol. 45, pp. 1–88, 2004.

[31] G. S. P. S. Phani, V. Vishnukanthan, "Effect of heat treatment on properties of cold sprayed nanocrystalline copper alumina coatings," *Acta Materialia*, vol. 55, pp. 4741–4751, 2007.

[32] T. S. Price, P. H. Shipway, and D. G. McCartney, "Effect of cold spray deposition of a titanium coating on fatigue behavior of a titanium alloy," *Journal of Thermal Spray Technology*, vol. 15, pp. 507–512, 2006.

[33] E. Sansoucy, G. E. Kim, A. L. Moran, and B. Jodoin, "Mechanical characteristics of al-co-ce coatings produced by the cold spray process," *Journal of Thermal Spray Technology*, vol. 16, pp. 651–660, 2007.

[34] A. Ibrahim, R. S. Lima, C. C. Berndt, and B. R. Marple, "Fatigue and mechanical properties of nanostructured and conventional titania (tio_2) thermal spray coatings," *Surface & Coatings Technology*, vol. 201, pp. 7589–7596, 2007.

Chapter 3

Shot Peening and Surface Nano-crystallization

3.1 Introduction

Shot peening (SP) is a well-established and popular surface treatment aimed at enhancing the resistance of metallic components which are exposed to cyclic loadings, wear, fretting and corrosion under applied stresses. The process consists of impacting the surface of component by multiple high velocity shots that induce a layer of plastic deformation near the surface. The SP process basically modifies the surface and the characterizing parameters of the near surface substrate including:

- surface texture or surface topography
- surface hardness or near-surface dislocation and microstructure modification
- elastic residual stress distribution

Air blast shot peening (ABSP) is the most widely used SP process through which small shots are projected by compressed air. The schematic of its equipment is illustrated in Fig.3.1. The plastically deformed layer would have altered physical properties, very often raised yield point that is known as work-hardening; however, the other considerable effect of peening process is induction of residual stresses. When a single shot impacts the part's surface with sufficient impact energy, it creates a small indentation or dimple in metal surface. The indented surface goes under tensile stress and an equal and opposite compressive force that tends to push the dimple back out again. To some extents it succeeds but when the compressive force encounters the equally strong effect of plastic deformation, it remains at and just below the surface as residual stress. Indeed, the elastically stressed region tends to recover to fully unloaded state, while the plastically deformed region sustains some permanent deformation. These inhomogeneous elasto-plastic deformations result in development of a compressive residual stress field in

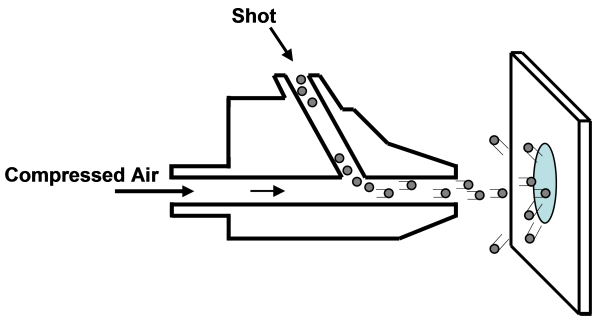

Figure 3.1: *Schematic illustration of ABSP equipment*

the exposed upper layer. The layer with compressive residual stress reduces the likelihood of premature failure under cyclic loading conditions and therefore improves the fatigue life of the peened component [1–5] Fig 3.2 shows a typical residual stress field induced by SP where the main parameters are:

- σ_{Smax}: surface residual stress
- σ_{Cmax}: maximum compressive residual stress
- σ_{Tmax}: maximum tensile residual stress
- d: the depth where the residual stress changes sign (from compressive to tensile).

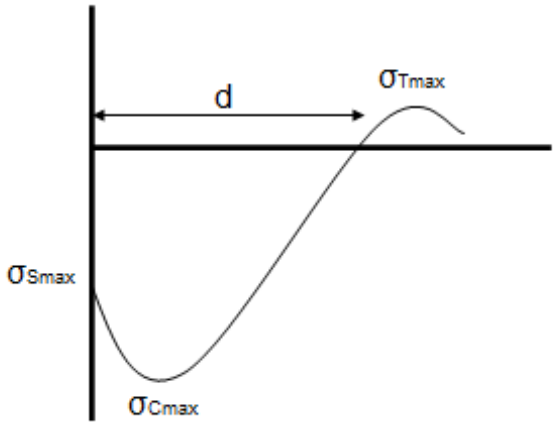

Figure 3.2: *Schematic illustration of residual stress profile caused by SP*

3.2 Shot peening control parameters

SP is considered as a very simple process for the majority of its applications, i.e. on steel parts made of less sophisticated grades in their varieties of microstructure and in the automotive industry of the late 50s/early 60s. However when it comes to more high performance metallic materials (high strength steels, titanium alloys, high strength aluminium and magnesium alloys) or even technical ceramics, the mechanical surface treatments like SP and choice of their parameters must be performed more carefully, since these classes of material, due to their more complex compositions, are more sensitive than the steels from earlier years. Many parameters are known to influence the effectiveness of the SP treatment. These can be classified into the following three main groups [6]:

- shot parameters: type, size, shape, density, hardness, yield strength, stiffness, etc.
- target parameters: hardness, yield strength, stiffness, work-hardening, chemical composition, pre-stress condition, etc.
- flow parameters: mass flow rate, pressure, velocity, angle of impingement, stand off distance.

In practice, however, SP process is not described by each of the single mentioned process parameters, but by Almen intensity, Coverage percentage and type of the used peening media. The choice of media material and size depends on the properties of the material to be peened, the component geometry, the costs and the required final results.

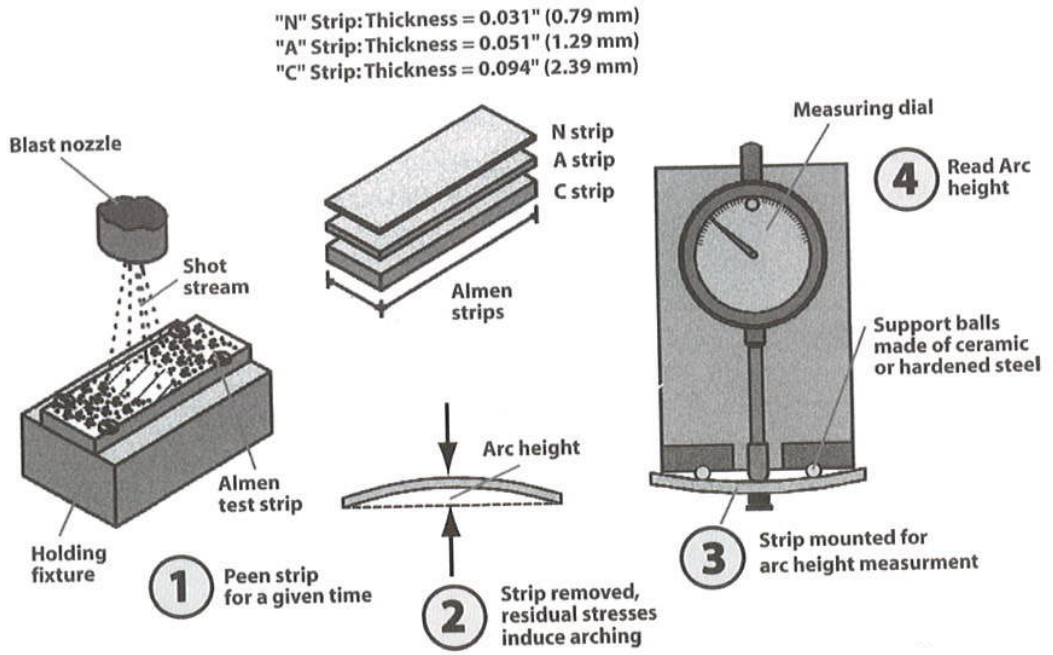

Figure 3.3: *The process to obtain a single arc height on a saturation curve [7]*

3.2.1 Almen intensity and saturation curve

Determining the impact energy level of shot stream is an important means of insuring its repeatability and facilitates the control of process effects. During the 1940's, J.O. Almen [1] developed a standard process to measure the kinematic energy transferred by the shot stream. SP specifications refer to this energy as intensity at saturation. Measurement of peening intensity is accomplished by determining its effect on standardized test strips, called Almen strips, with a standardized tool, called Almen gauge. The method of intensity measurement derived by J.O. Almen has been universally accepted and adopted by engineers in their design consideration. Fig.3.3 illustrates how to measure SP intensity with the proper tools. There are three types of Almen strip specified. The standard test strips of spring steel SAE1070 tempered to 44-50 HRC have different thicknesses for usage at different intensity levels [8, 9]. After the strip has been exposed to the shot stream and removed from the holding fixture, the gauge stem is placed against not peened surface. The measured strip deflection represents a single arc height at the given exposure time. Intensity is expressed as the arc height of a shot peened test strip at saturation point which is defined as the earliest point of the saturation curve that, if the exposure time is doubled, the arc height increases by 10% or less. For determining the intensity of peening process, it is necessary to establish a saturation curve; and its Establishment is accomplished by peening a series of Almen strips, using different exposure times, with all other SP parameters kept constant. Plotting the arc height deflection of different strips as a function of exposure time will define a curve with the general shape as shown in Fig. 3.4. The saturation time (T) is the earliest point on the curve where doubling the exposure time (2T) produces no more than a 10% increase in the arc height.

3.2.2 Surface coverage

Coverage is practically the most important 'measurable' variable of SP process. It has proved to be more important than intensity since while a little more or a little less Almen intensity will have, generally, no measurable effect on the part's resistance to failure, a little less than 100% coverage can result in a significant reduction in fatigue life. If the mode of failure is stress corrosion, less than full coverage may offer no protection at all [3]. Coverage is defined as the ratio of the area covered by peening indentations to the complete surface being treated, expressed as a percentage, where parts of the surface with double

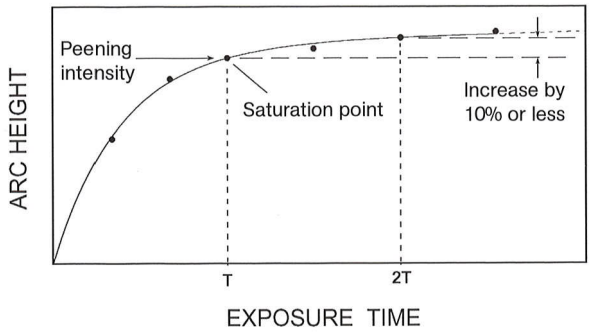

Figure 3.4: *Schematic saturation curve [10]*

hits are not taken into account. Coverage of 98% is a degree of coverage which can be assessed visually. Thus 98% surface coverage is usually considered as full coverage according to SAE 2277 [11]. Kirk *et al.* in [12, 13] analyzed the theoretical basis of coverage control using Avrami equation [14]; Assuming that shot particles generate constant diameter circular indentations and that the shot particles arrive at the surface in a statistically random manner but at a uniform rate. They explain that at the early stages, the indentations are most likely to occur without overlap so that coverage increases almost linearly with time. Later on, there will be more and more overlap of indentations. As the surface progressively becomes covered, the probability of overlap increases so that the rate of coverage decreases. Eventually when a large proportion of the area has been impacted; there remains smaller and smaller area to be covered. Hence the approach to 100% coverage can be expressed exponentially and obtaining 100% coverage would be theoretically impossible [12].

3.3 Shotpeening process to obtain nano-structured surface

As mentioned before, SP is a very well-known surface treatment. Fatigue, rolling contact fatigue, fretting and stress corrosion are operative situations where SP has proved to be able to strongly improve the performance of mechanical parts and structural elements. In industry, SP is widely used due to its flexibility, which makes it possible to be applied to components of almost any shape. Recent researches have successfully shown that different SP processes are able to introduce NC layers with altered characteristics, as concern their depth, the dimension of the crystals and microstructural properties. Such an attention to SP for obtaining NC surfaces is justified by strong applicative impact that SP can have, once its capability to obtain NC surfaces with appropriate characteristics is proved. Moreover its ability to be simply performed on commercial scale makes SP attractive to provide NC layers with high productivity [15]. However, a clear relationship between the processes, their parameters and also the mechanical properties of the obtained NC layers is still to be found. The concept of surface nanocrystallization by SP is that during the process with the hit of high energy shots, many pits and also extruded ridges around the edge of the pit are formed on the surface. When the ridge is hit by another particle, the contact area between sample and the particle can decrease significantly, therefore the strain and strain rate will be increased. Additionally, the collision mode also is changed from single direction to multiple directions due to the ridge, which is more favorable to the accumulation of dislocations. With the proceeding of collisions, some areas will approach the critical condition of nanocrystallization after several suitable hits [16].

3.4 Fatigue behavior of surface nanocrystallized material obtained by shot peening

Residual compressive stresses introduced during severe plastic deformation (SPD) process can also effectively stop the initiation and propagation of fatigue cracks. This trend is true especially when the applied stresses are relatively low, that is, in the fatigue life range with a longer life ($> 10^6$ cycles), since under this condition, the external stresses may be overweighed by the residual compressive stresses. Originally, it was assumed that fatigue improvements due to SP were attributable to the induced compressive residual stresses on the surface. Recently, however, microstructural characterization of shot peened material has revealed surface micro-structures that may include not only stable nanocrystals (NC) but also high dislocation densities, martensite and second phases [17], which might contribute to fatigue strength improvement. An important key to enhanced fatigue performance in NC metals lies in the potential for these materials to suppress the crack initiation process [18]. Rotating bending fatigue tests have been performed by Adachi [19] on case-hardened (carburized and oil quenched) gear steels (JIS SCM415 (CrMo steel)), notched with a stress concentration factor of Kt=3, shot peened by extremely high intensity conditions. Microstructural observation of the specimens revealed the presence of white etching layers near surface. Based on recent theories those white etching layers could have been the sign of surface nanocrystallization [20], even though in Adachi paper there is no comment about the presence of NC surface layer. The results indicated of 200% improvement in fatigue life with respect to not peened specimens [19]. Wen et al. [21] studied the fatigue strength of commercial pure titanium treated by high energy shot peening (HESP), through rotating bending fatigue tests performed on notched specimen with an stress concentration factor of Kt=1.27. In their case, surface damage, roughness, and edge of specimen, reduced the fatigue limit and in some cases even caused the function of NC layer to be counteracted. They applied repeening using low energy small shots in order to amend the surface state after HESP process. The surface roughness of the specimens was decreased by 40% after repeening process. Comparing with the fatigue limit of not treated commercial pure titanium, the results were increased just 9% by conventional shot peening (CSP). However the fatigue limit was increased up to 34% with HESP and after repeening was increased to 52% with respect to annealed not treated specimen. In their study the fatigue cracks were mostly initiated from subsurface; in some cases the fatigue cracks initiated from the surface damages caused by HESP, while for repeened cases all the cracks initiated from subsurface [21]. Recent research by Bagherifard and Guagliano [22] also demonstrated that surface nano-crystalized smooth steel specimens, do not show considerable fatigue strength improvement with respect to the as received not peened series, particularly due to the high surface roughness induced by severe shot peening process that masks somehow the favorable effects of NC layer and deep residual stresses on final fatigue strength [22]. Tian *et al.* [23] mentioned that during any SPD based process, a large amount of lattice defects, i.e., high density dislocations are generated in the material in a very short time, and the near surface microstructure of the material is drastically changed. The high density dislocation clusters or tangled dislocations generated during the SPD process can accumulate further in the subsequent fatigue loading, and form micro-damages, such as voids and micro-cracks. Since usually no follow up recovery processes, i.e., annealing, are applied after SPD, the lattice defects or sometimes micro-damages are present in the SPD processed material. Therefore, for those properties, which are sensitive to micro-damages, such as fatigue, the existence of these defects may severely affect the behavior of the material. Thus, to fully utilize the surface nanocrystallization process to improve fatigue behavior of the material with a nanostructured surface layer, processing conditions need to be optimized.

3.5 Numerical simulation of shot peening

Various finite element models have been established to simulate the SP process which differ a lot in the simulation approaches: 2D, 3D and axis-symmetric models, type of analysis: static or dynamic, number of shots, material model and so on; considering a wide variety of modeling assumptions to perform parametric study on SP process, the existing simulations are mainly focused on estimation of induced residual stresses [22,24–29]. Applying numerical models for parametric study of the process specially to simulate severe shot peening (SSP) aimed at surface nanocrystallization is of great significance, taking

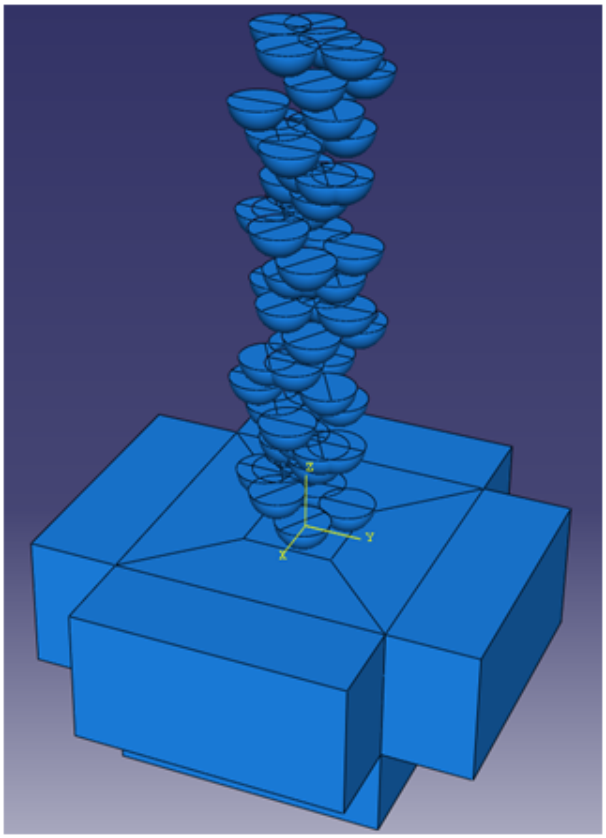

Figure 3.5: *3D FEM model proposed by Bagherifard et al. for shot peening [31]*

into account that still deep knowledge about correct choice of quantitative values of process parameters and their relationship to the grain size, refined layer thickness and uniformity of the nanocrystallized layer is lacking. It is evident that experimental investigation of the favorable treatment conditions for obtaining a well-defined nanostructured surface layer and the research of the relation between the treatment parameters and the characteristics of the generated surface layer is really expensive and that the definition of a numerical model to simulate SSP and to assess its effects on the surface would be of great importance and interest. However, it shall be taken into consideration that with respect of the previously developed shot peening models, the simulation of SSP has one more requirement that is the definition of an appropriate approach to assess the generation of nanostructured layer of material [22]. As previously mentioned, several methods have been suggested in the literature for numerical simulations of SP but there are very few studies dealing with simulation of SSP that leads to surface nanocrystallization. Dai et al. [30] performed impact simulation of surface nanocrystallization and hardening process (SNH) and compared the results in terms of roughness, residual stress and effective plastic strain with SP. They concluded that SNH process has a higher kinetic energy, produces a thicker work-hardened layer and a thicker surface region with larger residual compressive stresses, and generates higher effective plastic strains than the SP process; however they do not study the generation of nano-grained layer and estimation of its necessary conditions. The most recent simulation, developed by Bagherifard *et al.* [31], is a finite element simulation of air blast shot peening (ABSP) with unconventional and severe parameters, performed to provide quantitative description of effect of peening parameters in order to describe the distribution and magnitude of residual stresses and also the thickness of work-hardened layer. They have especially studied the critical assessment of the crucial conditions for formation of nanolayer. The model proposed by Bagherifard *et al.* showed in Fig.3.5 has been used as a reference model in this research, for studying the peening effect of the cold spray coating.

3.6 Conclusion

Formation of NC surface by means of shot peening based processes is a promising way to improve mechanical properties of metal alloys and in recent years has been the subject of increasing scientific and technological interest. Initial work has been performed to prove the possibility of obtaining NC surfaces by these methods and also to assess the microstructural characteristics of the obtained layers. More recently, researches have been focused to evaluate the mechanical properties of NC surfaces obtained by shot peening processes. The experimental results demonstrate that these methods are so efficient to produce NC surfaces and have potential application in various fields of industry. Thus surface nanocrystallization by shot peening has been used in this research to be applied to cold spray coated specimens as an alternative method for obtaining nanograins. The specimens subjected to cold spray and successive shot peening have been then characterized through numerical simulations and experimental tests.

Bibliography

[1] J. O. Almen and P. H. Black, *Residual stresses and fatigue in metals*. McGraw-Hill Publ. Company, 1963.

[2] S. A. Meguid, *Mechanics of shot peening.* PhD thesis, UMIST, UK, 1975.

[3] K. J. Marsh, *Shot peening: techniques and applications*. London, EMAS, 1993.

[4] A. Blarasin, M. Guagliano, and L. Vergani, "Fatigue crack growth prediction in specimens similar to spur gear teeth," *Fatigue & Fracture of Engineering Materials & Structures*, vol. 20, pp. 1171–1181, 1997.

[5] U. Martin, I. Altenberger, B. Scholtes, K. Kremmer, and H. Oettel, "Cyclic deformation and near surface microstructures of normalized shot peened steel sae 1045," *Materials Science and Engineering A*, vol. 246, pp. 69–80, 1998.

[6] S. Kyriacou, "Shot peening mechanics, a theoretical study," in *Proceedings of the* 6_{th} *International Conference on Shot Peening*, 1996.

[7] H. Gray, *Shot peening: a dynamic application and its future*. MFN-Metal Finishing News, 2009.

[8] S. A. 2432B, "Shot peening, computer monitored," *SAE International*.

[9] S. J442, "Test strip holder and gage for shot peening, sae surface enhancement division," *SAE international*.

[10] S. A. J443, "Procedures for using standard shot peening test strip," *SAE Surface Enhancement Division*.

[11] S. S. J2277, "Shot peening coverage," *Surface Enhancement 660 Committee*, 2003.

[12] D. Kirk and M. Y. Abyaneh, "Theoretical basis of shot peening coverage control," in *Proceedings of the 5th International Conference on Shot Peening*, 1993.

[13] D. Kirk, "Coverage: development, measurement, control and significance," *The Shot Peener*, vol. 16, pp. 33–36, 2002.

[14] M. Avrami, "Kinetics of phase change. i. general theory," *Journal of Chemical Physics*, vol. 12, pp. 1103–1112, 1939.

[15] Y. Todaka, M. Umemoto, Y. Watanabe, and K. Tsuchiya, "Formation of nanocrystalline structure by shot peening," *Materials Science Forum*, vol. 503, pp. 669–674, 2006.

[16] J. L. Liu, M. U. Y. Todaka, and K. Tsuchiya, "Formation of a nanocrystalline surface layer on steels by air blast shot peening," *Journal of Materials science*, vol. 42, pp. 7716–7720, 2007.

[17] U. Martin, I. Altenberger, B. Scholtes, and K. K. H. Oettel, "Cyclic deformation and near surface microstructures of normalized shot peened steel sae 1045," *Materials Science and Engineering*, vol. 246, pp. 69–80., 1998.

[18] H. A. Padilla and B. L. Boyce, "A review of fatigue behavior in nanocrystalline metals," *Experimental Mechanics*, vol. 50, pp. 5–23, 2010.

[19] A. Adachi, "., fatigue strength of gear steels shot peened in extremely high intensity conditions," in *Proceeding of ICSP-4, Tokyo (Japan)*, 1990.

[20] H. Saitoh, T. Ochi, and M. Kubota, "Formation of surface nanocrystalline structure in steels by air blast shot peening," in *Proceedings of the* 10^{th} *International Conference on Shot Peening Tokyo (Japan)*, 2008.

[21] A. L. Wen, R. M. Ren, S. Wang, and J. Y. Yang, "Effect of surface nanocrystallization method on fatigue strength of ta2," *Materials Science Forum*, vol. 620–622, pp. 545–549, 2009.

[22] S. Bagherifard and M. Guagliano, "Fatigue behaviour of a low-alloy steel with a nanostructured surface obtained by severe shot peening," *Engineering Fracture Mechanics*, 2011.

[23] Y. W. F. D. S. L. L. P. K. D. . .-. .-. Tian J.W., Villegas J.C., "A study of the effect of nanostructured surface layers on the fatigue behaviors of a c-2000 superalloy," *Materials Science and Engineering A*, vol. 468–470, pp. 164–170, 2007.

[24] C. Hardy, C. N. Baronet, and G. V. Tordion, "The elasto-plastic indentation of a half-space by a rigid sphere," *Int J Numer Meth Eng.*, vol. 3, pp. 451–462, 1971.

[25] K. Schiffner, G. Droste, and C. Helling, "Simulation of residual stresses by shot peening," *Computers and Structures*, vol. 72, pp. 329–340, 1999.

[26] S. A. Meguid, G. Shagal, and J. C. Stranart, "3d fe analysis of peening of strain-rate sensitive materials using multiple impingement model," *International Journal of Impact Engineering*, vol. 27, pp. 119–134, 2002.

[27] M. Guagliano, L. Vergani, M. B. M., and F. Gili, "An approach to relate the shot peening parameters to the induced residual stresses," in *Proceedings of the 7th International Conference on Shot Peening Warsaw (Poland)*, 1999.

[28] J. Schwarzer, V. Schulze, and O. Vöhringer, "Evaluation of the influence of shot parameters on residual stress profiles using element simulation," *Materials Science Forum*, vol. 462, pp. 3951–3956, 2003.

[29] H. Y. Miao, S. Larose, C. Perron, and M. Lévesque, "On the potential applications of a 3d random finite element model for the simulation of shot peening," *Advances in Engineering Software*, vol. 40–10, pp. 1023–1039, 2009.

[30] K. Dai, J. Villegas, Z. Stone, and L. Shaw, "Finite element modeling of the surface roughness of 5052 al alloy subjected to a surface severe plastic deformation process," *Acta Materialia*, vol. 52, pp. 5771–5782, 2004.

[31] S. Bagherifard, R. Ghelichi, and M. Guagliano, "A numerical model of severe shot peening (ssp) to predict the generation of a nanostructured surface layer of material," *Surface and Coating Technology*, vol. 204, pp. 4081–4090, 2010.

Part II

Numerical simulations

Chapter 4

Critical velocity calculation

4.1 Introduction

The important role of particle velocity in the bonding mechanism and the definition of critical velocity (CV), which is a minimum velocity at which the particles start bonding to the substrate, has been discussed in the Chapter2. Fig. 4.1 shows the very first particles bonded to the substrate along with the peening effect of the particles with velocities less than CV, that have created circular indentations on the substrate. Considering the direct effect of velocity on the deposition efficiency, the process optimization

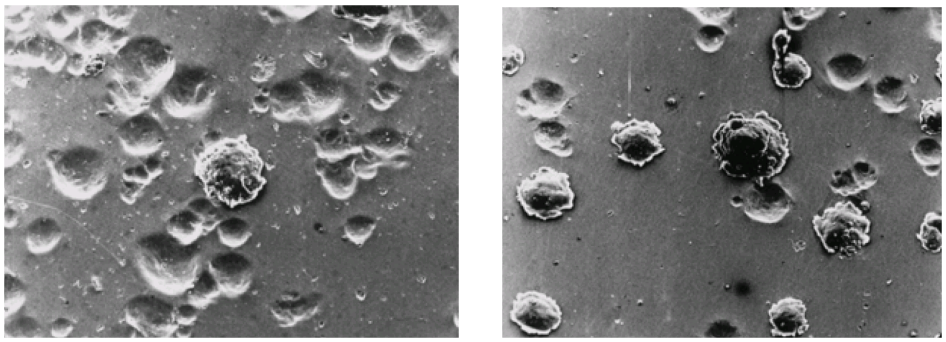

(a) $V_{pm} = 780m/s$ **(b)** $V_{pm} = 850m/s$

Figure 4.1: *Microscopy observation of copper substrate coated by aluminum particles [1]*

strongly depends on accurate calculation of CV of the process. Mechanical and thermal properties of the spray material such as temperature, shape, etc [2–4] and the substrate properties (roughness,hardness, temperature,etc) [3, 5] influence the CV value. There are different approaches in the literature to experimentally measure the CV; principally, all methods are based on the deposition efficiency test and particle velocity measurement. However, due to velocity distribution resulting from practical particle size distribution, it is not easy to yield the velocity where the transition from substrate erosion to particle deposition occurs [6]. In this regard, single particle impact is the key to study the CV of the process; in this regard numerical and experimental studies have been performed to reveal the impact process of single particles. The investigation of Alkhimov *et al.* [7, 8] and Zhang [5] are examples of studying the deformation, attachment, and contact temperature of individual particles. Theoretical estimation of CV is based on detection of adiabatic shear instability upon particle impact [9]. Adiabatic shear instability and the resultant plastic flow localization are the phenomena that are believed to play the major role in the particle/substrate bonding during cold spray process [9, 10]. Finding this instability which can be observed on trend of different physical parameters including strain, temperature, and stress, leads to numerical estimation of the CV. All particle deformations available in the literature as predicted by different authors, are almost equal [9–11], however it is curious that their results in case of the calculated CV are

different due to not only different methods but also dissimilar interpretations used for detection of the shear instability. For example, in case of Cu particles, which is the most common material employed in cold spraying, the reported CV is dispersed in a very large range from 250 m/s to over 640 m/s [2,11,12]. Shear instability, normally, appears as a singularity in the profile of parameters such as plastic equivalent (PEEQ) strain while defined as a function of time; even in the available numerical simulations, different criteria have been used for recognition of shear stability in the particle impact with different velocities. In the present study, the shear instability is acknowledged using a mathematical criteria based on a sensitive method for shear instability detection. Admittedly, the outputs of the finite element commercial software are discrete numbers. Finding the minimum velocity at which the shear instability occurs using these discrete data is tricky and challenging due to the discontinuity of the results. In order to overcome this problem, a sensitive mathematical method which is able to observe any small change in the smoothness of the result functions is developed for identification of shear instability. The output data for different physical and mechanical parameters have been elaborated using Wavelet transformation and the second derivative in Sobolev space in order to identify the minimum velocity at which shear stability occurs. The obtained results are eventually compared with the experimental results available in the literature and numerical results obtained by other researchers [13].

4.2 Experimental measurement of CV

The velocity of the particles in cold spray coating are measured by the Doppler laser vibrometer (LDV) [13, 14] which is normally used to make non-contact movement (vibration) measurements of a surface; its basic components are shown in Fig.4.2. The laser beam of the LDV is directed at the surface of interest, afterwards the vibration amplitude and the frequency caused by the motion of the surface are extracted from the Doppler shift of the laser beam frequency. The test beam then passes through the

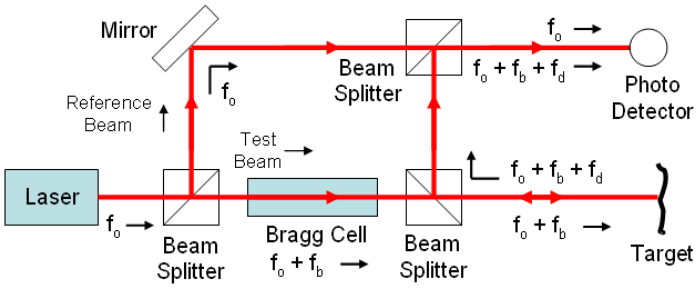

Figure 4.2: *Schematic of a typical laser vibrometer [15]*

Bragg cell, which increases a frequency shift f_b directed to the target. The motion of the target adds a Doppler shift to the beam given by $f_b = 2 \times v(t) \times \cos(\alpha)/\lambda$, where $v(t)$ is the velocity of the target as a function of time, α is the angle between the laser beam and the velocity vector, and λ is the wavelength of the light.

There are different commercial instruments such as DPV2000 by Technar [16] or SprayWatch by OSEIR [17] which have been mostly used in the literature for measuring the in-flight particles' velocity. The DPV 2000 particle diagnostics system (manufacturer: Technar) helps to determine the characteristics of spray particles during the flight phase in a specific area of the spray jet. The major problem for measuring cold particles velocities in cold spray coating is the lack of particle brightness that leads to use of extern lighting [13]. Fig. 4.3 shows the different pieces of the apparatus used by [13] for measuring the velocity of in-flight particles.

It should be considered that a wide transient region exists for particle deposition since the particles used to measure the CV have a size distribution which makes the accurate and exact estimation of CV, quite difficult. Thus, the accuracy of the measured data depends on the span of the particle size; i.e. a narrow span in particle size will result in a narrow transient region and consequently more accurate

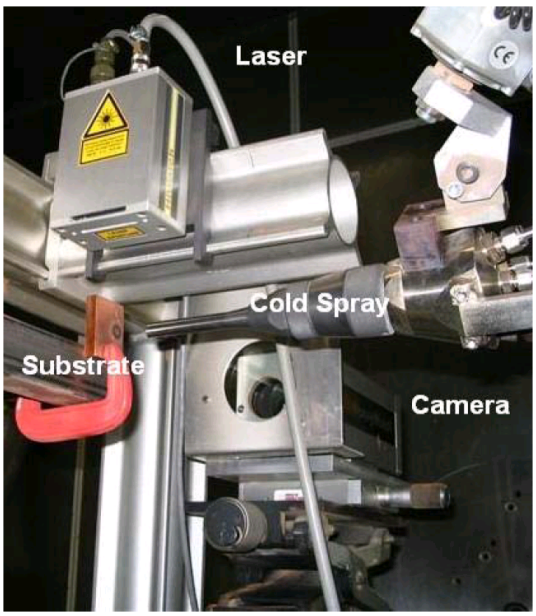

Figure 4.3: *In-flight particle diagnostic system [18]*

data [6]. In this regard, two different practical methods can be used for CV estimation. The first method is to estimate the CV based on the experimental observation of the particles rebounding from the surface using the Doppler system. Since the velocity of rebounding particles is about ten times lower than the velocity of the impacting particles, the system cannot calculate the two types of velocities [13]. The other method for CV estimation is to measure the deposition efficiency (DE); the DE gives an indication of the number of particles that have an impact velocity higher or equal to the CV. As it has been shown in Fig. 4.4a and Fig.4.4b, the DE has a trend based on the particle velocity; it is possible to use the trend by calculating the higher DE and estimating the minimum velocity for non-zero DE of the process. As

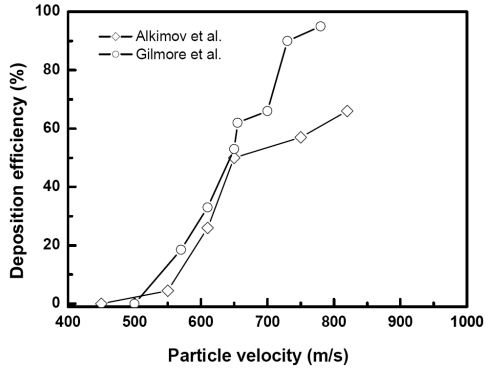

(a) *Deposition efficiency vs. particle velocity for Cu [6, 7, 19]*

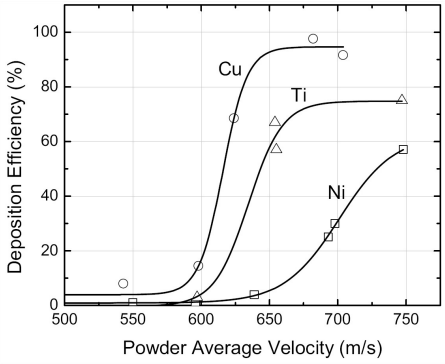

(b) *Deposition efficiency vs. particles average velocity for Cu, Ti and Ni powders [20]*

Figure 4.4: *Trend of deposition efficiency vs. particle velocity*

reported earlier by Alkimov *et al.* [7] for Cu particles of a mean size 10 μm, the deposition efficiency approaches to zero as particle velocity is reduced to about 500 m/s from a certain high level. Fig. 4.4a presented by Li *et al.* [6] has compared the results reported in Alkhimov *et al.* [7] and Glimore *et al.* [19].

4.3 Numerical simulation for CV assessment: a review

As mentioned in the previous section, experimental measurement of CV is a challenging task. Alternatively, numerical analysis of a single particle impact can be utilized in order to broaden the horizon of physical aspects of the coating phenomenon. It is strongly believed that adiabatic shear instability occurs when the velocity of the particles reaches, or passes, the so-called CV, that is, practically the velocity at which the particles bond to the substrate [9–11]. As a result, it is indicated that CV can be estimated theoretically by considering adiabatic shear instability through numerical simulation. In this regard, Assadi *et al.* [10], as the very first group tried to use finite element methods and numerical approaches for cold spray CV estimation, studying particles' deformation using Abaqus/Explicit 6.2-1 [21]. A very crucial issue in coating simulation is the correct choice of a material model which can consider both high strain rate due to the velocity of the particles and the temperature variations due to high energy impact of the powders. Johnson-Cook [22, 23] material model, not only has all the perquisite requirements of this simulation, but has also demonstrated [9–11] the capability of good prediction and rational corespondent with expected and experimental behavior of the material. Assadi *et al.* also suggested [10] that the process can be considered adiabatic and the heat transfer between the particle and substrate can be not considered. The main reason is based on duration of the whole impact which is less than some ns; and as they have mentioned the wave propagation would be a bigger problem than heat transfer in the model. In the case of mesh convergency study, due to the fact that by decreasing the element size in the model the results do not converge to a constant value, there is a general agreement on using "zero element" method [10, 11, 24]. Assadi *et al.* [10] have used the axi-symmetry assumption and fixed displacement boundary condition for the model. They also presented a simple formulation for CV estimation (Eq.4.1) that has been later modified by Schmidt *et al.* [25].

$$V_{cr} = 667 - 14\rho + 0.8T_{melt} + 0.1\sigma_u - 0.4T_{init} \tag{4.1}$$

The very first formula presented by Assadi et al. considers density (ρ), melting temperature (T_{melt}), ultimate strength (σ_u), and initial temperature (T_{init}) of the particle, whereas the modified formula considers more properties of the particles. The formulation assumes that the substrate has no effect on the obtained CV. Li *et al.* [11] have tried to use LS-DYNA [26] that is another FE commercial software for CV calculation. They have supposed the Rosin-Rammler [27] distribution for the particle size; by assuming an indirect relationship between velocity of the particle and its size, a maximum particle size d_c in a process by CV V_c can be adhered to the substrate, measured as: $d_c = \left(\frac{k}{V_c}\right)^{1/n}$ in which *k* and *n* are related to spray conditions. The criterion for CV calculation as mentioned before, is the occurrence of shear instability in the model. The results obtained by Li *et al.* are completely different from the results presented in other publications available in the literature [7, 9, 10, 13]. Li *et al.* have put forward that the oxygen content in the particle in experimental tests increases the measured CV and that by decreasing the oxygen content inside the particles, the CV value will become closer to their measurements. The other interesting developed numerical simulation belongs to Grujicic *et al.* [9] using the very same numerical model of Assadi *et al.* [10] presented in Fig.4.5. Analytically studying the shear instability, Grujicic *et al.* have introduced, based on the approach of Schoenfeld and Wright, [28] another parameter called as Shear Localization (SL) as a criterion for finding the shear instability and consequently the CV, presented as follow:

$$SL = \left(-\frac{\partial^2 \sigma_e / \left(\partial \epsilon_p \partial \epsilon_p\right)}{\left(\partial \sigma_e / \partial \dot{\epsilon}_p\right) \sigma^e} \right)_{\sigma_e = \sigma^e_{max}} \tag{4.2}$$

where σ^e_{max} denotes the maximum value of the flow stress at a given impact particle velocity. Finally, it is stated that based on the numerical method, the localization in a material occurs when the SL value is larger than $1.6 \times 10^{-4} \pm 0.2 \times 10^{-4} s$. Tab.4.1 shows the different estimations of CV available in the literature for Cu. In this case [6] stated that the oxygen content might be the reason to cause this variance in the results. The author believes that the different criteria used to find the shear instability might be the main reason for the different results. Oxygen content might experimentally affect the CV of the process, but the numerical results based on the very same approaches are also different in [9–11].

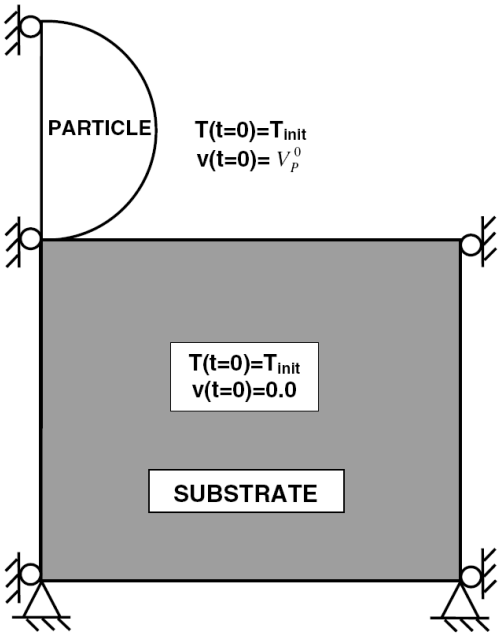

Figure 4.5: *An axisymmetric computational model and the particle and substrate boundary conditions in cold spray coating simulation [9]*

Table 4.1: *CV for Cu reported in the literature [6]*

Investigator	Critical velocity (m/s)	Oxygen content (wt%)	Particle size (μm)
Alkhimov *et al.* [7]	500		10
Stoltenhoff *et al.* [12]	550-570	0.1-0.2	5-25
Gilmore *et al.* [19]	640	0.336	19,22
Li *et al.* [11]	290-360	0.02	64.1
Li *et al.* [11]	550	0.14	20.5
Li *et al.* [11]	610	0.38	20.5
Schmidt *et al.* [25]	250-280		20
Schmidt*et al.* [25]	500		25
Raletz *et al.* [18]	422-437		10-33

4.4 A new approach to find the CV by FEM

The difference in the numerical methods as it has been shown in Tab. 4.1 leads to the important conclusion that although the physical background of the coating phenomenon is agreed on by scholars, yet a standard criterion able to find the shear instability in the numerical results is not clear. The problem in the case of FEM simulations, is that the output of the software is in discrete numbers and instability, as it will be discussed in the next section, appears as a discontinuity in the results. Therefore, in this study a mathematical approach is applied in order to control the smoothness of the discrete results and make it possible to recognize the discontinuity with a good accuracy. In this regard, a FEM model has been developed which will be presented in detail in the following sections.

4.4.1 FEM model

A 3D full model of particle impact on substrate has been simulated using ABAQUS/Explicit [29] with Lagrangian formulation. Different partitions shown in Fig. 4.6 are created to obtain an optimized mesh distribution in order to reduce the number of elements in non-impact zones. Fig. 4.6 shows the developed FE model with the annotations to describe its different parts. It is to be mentioned that similar to all other cold spray simulations, the physical bonding has not been modeled and the particles are detached after impacting the substrate. However the deformation of the particles and the consequent substrate surface profile is quite equal to what happens in real process, as it is specifically verified in the next sections. Different analysis have been performed varying the velocity of the particles in the range of 200-1000 m/s. In all cases, the duration of numerical analysis has been set to provide enough time for the particle to detach from the substrate and therefore, to fully complete the considered process. General contact without friction has been regarded as the interaction model between the particle and the substrate [29]. All the dimensions in the model for instance the substrate dimensions, size of the elements, etc. have been chosen as ratios of the particle diameter. The model can be developed also in 2D; however in this case the 3D geometry has been chosen that can be used in the future investigations on impact of more than one particles in different directions. C3D8R 8-node linear brick elements with reduced integration and hourglass control have been used [29].

4.4.2 Boundary condition

One of the demanding aspects of high velocity impact simulations is the wave speed spread through the elements and the fluctuations of this wave which remains in the model preventing the possibility of having stable results. As it has been mentioned also by Assadi *et al.* [10] the waves induced by the impact of the particles have a notable effect on the results. By using the common material models (even Johnson-Cook), the mentioned wave is not damped through the elements, due to the fact that there is no damping parameter considered in the material model. Adding boundary condition by fixing the displacement in a region of the model, the wave will return due to the fact that the boundary condition will act as a wall for the induced wave. Although, the effect of the results instability are not negligible, except for [10], no other researchers have considered the problem of dynamic wave in their numerical model. In this case, Bagherifard *et al.* [24] used the so called "Infinite elements" as boundary condition in the numerical simulation of shot peening. The shape and orientation of this element type (CIN3D8) are similar to C3D8R element excluding that the infinite element must be attached such that the infinite end faces away from the model. Infinite elements are allowed only with linear elastic behavior, so they must be positioned sufficiently distant from the non-linear interaction region to ensure accuracy [29]. The infinite elements do not reflect the wave induced by the impact simulating an infinite model. It is to be mentioned that unfortunately, the wave in the particles can not be damped.

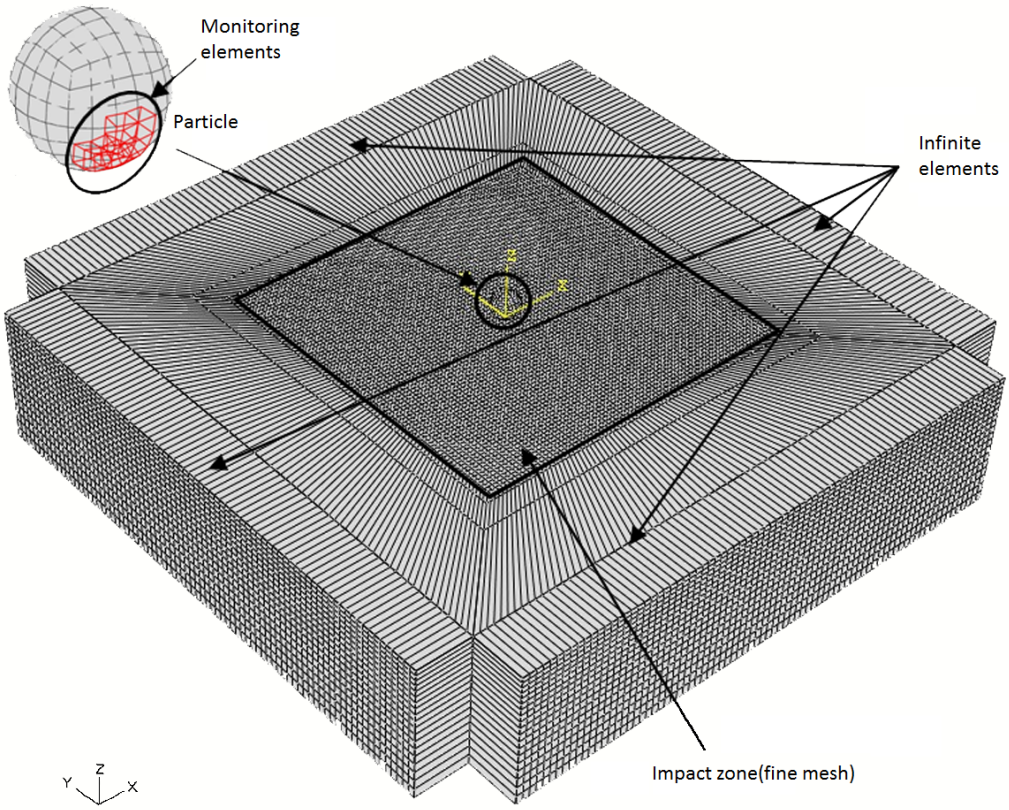

Figure 4.6: *Isometric view of the developed 3D model*

4.4.3 Material model

The plastic strain energy which is released as heat, rises the temperature and accounts for material softening. Indeed, fluctuations in stress, strain, temperature or microstructure, and the inherent instability of strain softening can give rise, obviously, to plastic flow (shear) localization which confirms the importance of the material model in FE simulation. Among different models which are able to consider the strain rate, there is a general agreement on Johnson-Cook [22] model presented in Eq.4.3 for cold spray coating simulation.

$$\sigma_{eq} = \left[A + B\left(\epsilon_P\right)^n\right]\left[1 + C ln\left(\dot{\epsilon_P}/\dot{\epsilon_{P0}}\right)\right] \times \left[1 - \left(\frac{T - T_{init}}{T_{melt} - T_{init}}\right)^m\right] \tag{4.3}$$

In which A (MPa) is yield stress, B (MPa) is the hardness modulus, ϵ_p and ϵ_{p0} are PEEQ deformations, $\dot{\epsilon_p}$ and $\dot{\epsilon_{p0}}(1/s)$ are equivalent plastic deformation rates, n is hardening exponent, C and m are constants, T(T_{init})(K) is temperature, and T_{melt} (K) is the melting temperature of the material. The model offers no physical basis for the eventual failure but seeks (through a large experimental database) to give a phenomenological description of the strain and loading conditions under which failure is known to occur. Failure due to adiabatic shear is accounted for by including experiments dominated by thermal instability within the database, typically experiments involving torsion of thin-walled specimens deformed at high rates (torsional split-Hopkinson bar experiments).Tab.4.2 presents the constant properties of Johnson-Cook model for some materials [22]. The problem of Johnson-Cook model is that there are numerous parameters which shall be measured for each material. Fortunately, the Johnson-Cook model has been embedded in the commercial software such as Abaqus [21], and there is no need to develop extra codes to implement it in the numerical model.

Table 4.2: *Johnson-Cook constant for different materials [22, 30, 31]*

Material	Hardness (Rockwell)	Density (kg/m^3)	Specific heat (J/kgK)	Melting temp (K)	A(MPa)	B(MPa)	n	C	m
OFHC Copper	F-30	8960	383	1356	90	292	0.31	0.025	1.09
Cartridge Brass	F-67	8520	385	1189	112	505	0.42	0.009	1.68
Nickel 200	F-79	8900	446	1726	163	648	0.33	0.006	1.44
Armco Iron	F-72	7890	452	1811	175	380	0.32	0.06	0.55
Carpenter Iron	F-83	7890	452	1181	290	339	0.40	0.055	0.55
1006 Steel	F-94	7890	452	1811	350	275	0.36	0.022	1.00
2024-T351 Aluminum	B-75	2770	875	775	265	426	0.34	0.015	1.00
7039 Aluminum	B-76	2770	875	877	337	343	0.41	0.010	1.00
4350 Steel	C-30	7830	477	1793	792	510	0.26	0.014	1.03
S-7 Tool Steel	C-50	7750	477	1763	1539	477	0.18	0.012	1.00
Tungsten Alloy	C-47	17000	134	1723	1506	177	0.12	0.016	1.00
DU-0.75Ti	C-45	18600	117	1473	1079	1120	0.25	0.007	1.00
7075-T651 Aluminum	87	2800	960	910	527	676	0.71	0.017	1.61
7075-T6 Aluminum	87	2800	960	910	546	674	0.72	0.059	1.56

4.4.4 Damage control

Due to large deformation of the particles upon impact with the high velocity, it is needed to add a damage control mechanism to the model. The arbitrary lagrangian eulerian (ALE) method [32] proposed by Li *et al.* in [33], are supposed to provide a suitable way to examine the particle deformation in cold spray. The other method proposed again by Li *et al.* [34, 35] is using the Johnson-Cook damage control material model instead of the ALE, due to observed problems with ALE in some cases. Their statement has been examined also in this work; the results indicated that by using ALE, the deformation of the particles are far from reality or the simulation is blocked due to deformation errors. The latter case has been confirmed also by Li *et al.* [34]. Fig. 4.7 shows deformation of a particle by changing different parameters of ALE mechanism embedded in the software. The Johnson-Cook (JC) damage model is

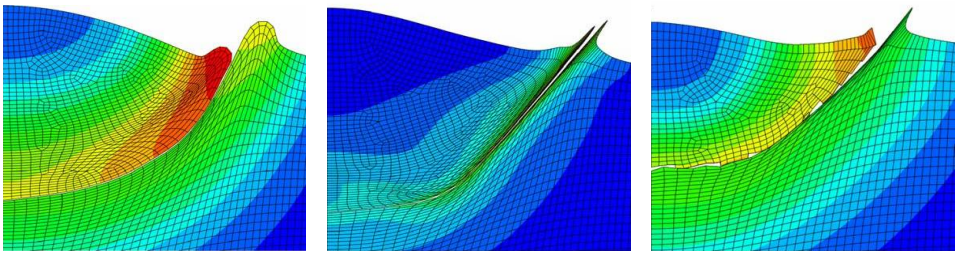

Figure 4.7: *The deformation obtained using ALE assumption and changing different parameters*

presented in Abaqus/Explicit as "Johnson-Cook dynamic failure model". The JC dynamic failure model is based on the value of the PEEQ at element integration points, where failure is assumed to occur when the damage parameter exceeds 1. The damage parameter, ω, is defined as $\omega = \sum \left(\frac{\Delta \bar{\epsilon}_p}{\bar{\epsilon}_{pf}} \right)$ [23] where $\Delta \bar{\epsilon}_p$ is an increment of the PEEQ, $\bar{\epsilon}_{pf}$ is the strain at failure, and the summation is performed over all increments in the analysis. The strain at failure is assumed to be dependent on a non-dimensional plastic strain rate, $\dot{\epsilon}^*$; a dimensionless pressure-deviatoric stress ratio, p/σ_{eq} (where p is the pressure stress and σ_{eq} is the Von-Mises stress); and the non-dimensional temperature, T*, defined earlier in the JC plasticity

Table 4.3: *Johnson-Cook damage parameters [23, 30]*

Material	d_1	d_2	d_3	d_4	d_5
OFHC-Copper	0.54	4.89	-3.03	0.014	1.12
Armco-Iron	-2.20	5.43	-0.47	0.016	0.63
Al-7075-T651	0.110	0.573	-3.4446	0.016	1.099
Al-7075-T6	0.451	-0.952	-0.068	0.036	0.679

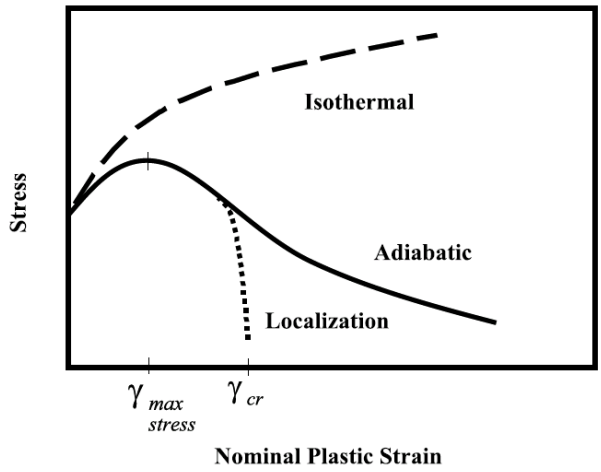

Figure 4.8: *Shear stress versus nominal shear strain for a typical work-hardened material during a torsion experiment [28]*

model. The dependencies are assumed to be separable and are of the form [23]:

$$\bar{\epsilon}^f = \left[d_1 + d_2 exp\left(d_3 \frac{\sigma_m}{\sigma_{eq}}\right)\right] \left[1 + d_4 ln\left(\dot{\epsilon}^*\right)\right] \left(1 + d_5 T*\right) \tag{4.4}$$

where d_1 to d_5 are failure parameters measured at or below the transition temperature, Tr. When this failure criterion is met, the deviatoric stress components are set to zero and remain zero for the rest of the analysis. the mesh size has less effect on the resultant output with material damage model than without material damage. Although the particle size has little effect on the deformation behavior of the whole particle, it has some effects on the damage of the contact interface elements [35]. By the latter discussion, JC failure control has been added to the model in order to control the damaged elements. Tab.4.3 presents the Johnson-Cook damage parameters for some materials.

4.4.5 Adiabatic shear instability

Observations of material failure during explosive and impact loading often include accounts of highly localized deformation that may either dominate or contribute to failure. This mechanism, which is called adiabatic shear instability, has been known and studied for many years; thus there is now a very large database from the perspectives of both material science and mechanics [28]. Fig. 4.8 [28] illustrates the typical response of a work-hardened material. In slow loading, or if adiabatic heating is somehow suppressed, the material may show continuous hardening out to large shear strains, as indicated by the upper curve in Fig. 4.8. However, plastic working will heat the material, and since metals tend to soften with increasing temperature, eventually the flow stress will reach a maximum at $\gamma_{maxstress}$, followed by strain softening, as indicated schematically by the middle curve. In a perfect material with perfectly uniform distributions of stress, strain, and temperature, softening may continue indefinitely. In a work-hardened material, the adiabatic stress, reaches a maximum at some temperature and plastic strain. More details are available in the references [28]; thus it seems possible to choose initial conditions in such

a way that the boundary layer is suppressed, which does not make significant difference in the time of localization. There are four variables in the Johnson-Cook material model (Eq.4.3), PEEQ, equivalent stress, strain rate, and temperature. Grujicic *et al.* [9] presented the behavior of the latter parameters by changing the particles' velocity in the model (4.9). As discussed earlier, if each of these physical

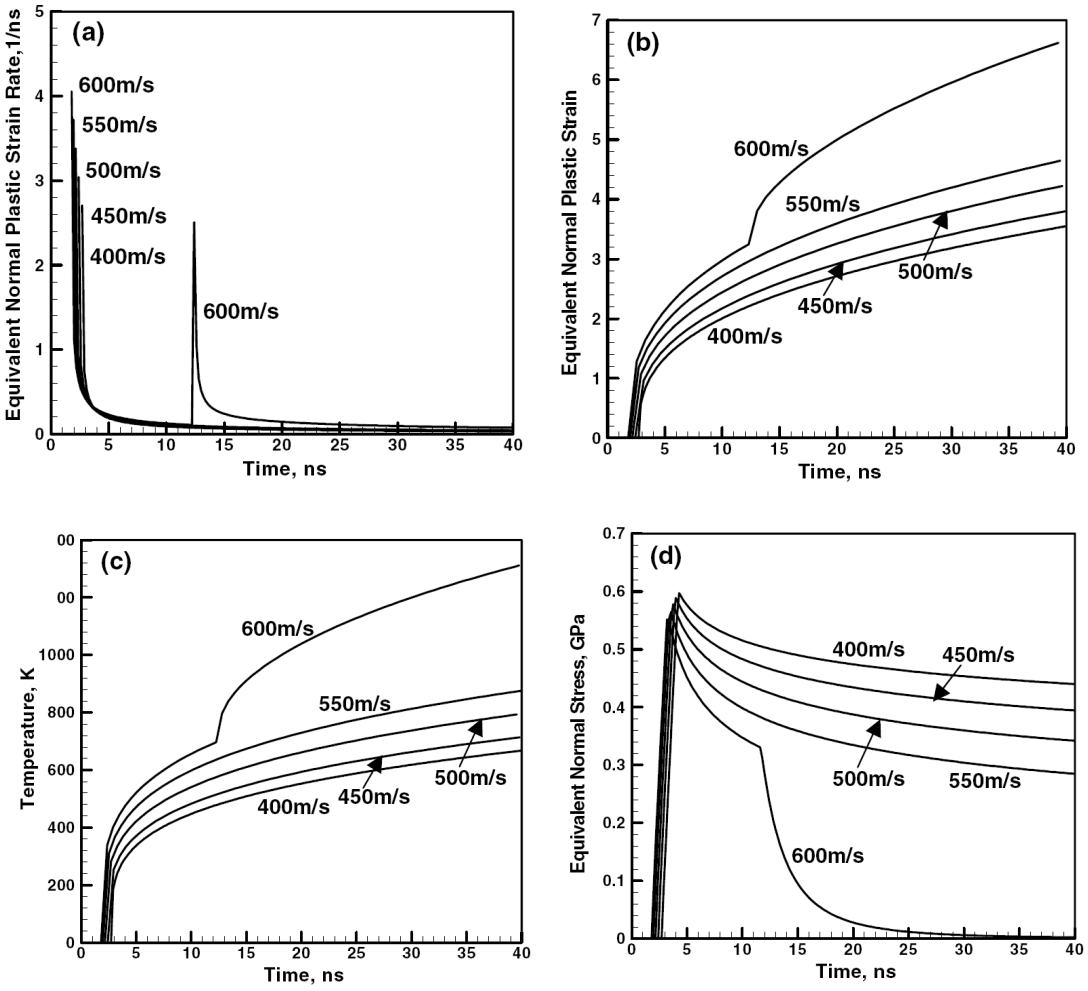

Figure 4.9: *Temporal evolutions of: (a) equivalent plastic strain rate; (b) PEEQ; (c) temperature; and (d) equivalent normal stress in an element at the copper-particle surface during the particle collision with a copper substrate for various initial impact particle velocities [9].*

parameters are studied as function of time, the shear instability can be considered as a singularity or discontinuity in their profile function. This idea will be used later in order to find the minimum velocity which causes shear localization in the results.

4.4.6 Mesh convergence study

It is well-known that element size strongly affects the results of numerical simulations. A very dense mesh has been generated on the impact area and the element sizes have been gradually increased getting far from the impact zone. "C3D8R" linear hexahedron 8 noded reduced integration point elements have been used to mesh the particle and the substrate. Half infinite "CIND8" elements have been used to cover the substrate side faces. The size of the elements in the impact zone has been chosen as ratios of the particle diameter which are 1/10th, 1/15th, and 1/20th. Similar size of elements has been chosen in

each analysis for the particle and the impact zone. As mentioned in the literature [11] in case of particle impact numerical simulation, the results of CV do not converge by decreasing the element size. Since as the mesh size is decreased, variations of instable parameters are almost linear, the extrapolation of instable results to a meshing size of zero has been used to stand for the real one. This so called "zero element" method provides final result independent from elements size [10, 11]. The method is applied to the final results as presented in Fig.4.23

4.4.7 Challenges in finding the shear instability

In most cases, specially in coating process, finding the shear localization is quite a challenge. Fig.4.10 shows the similar graph presented in Fig.4.9.

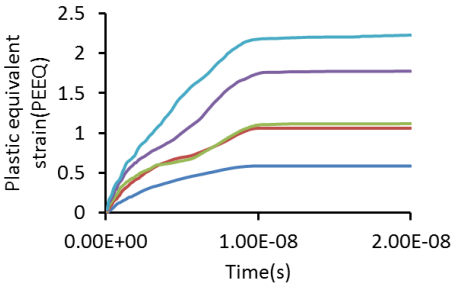

(a) *Behavior of PEEQ at different velocities*

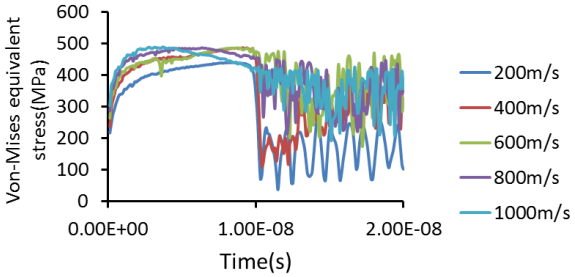

(b) *Behavior of Von-Mises stress at different velocities*

Figure 4.10: *An example of the software output for a) PEEQ and b) Von-Mises equivalent stress*

As it can be observed, for example in Fig.4.10a in 400m/s and 600m/s, the singularity can be seen with different behaviors which seems to be due to the noise induced by the wave in the results. In Fig.4.10b finding the instability is absolutely impossible, due to the noise in the results. Therefore, the following method has been presented in order to solve the latter problem. It shall be noted that, it is strongly believed that the nature of FEM results are the source of this problem; i.e. the output of the commercial explicit software depends on element size, time increment, and many other effective parameters. The criterion which can find the instability in the minimum velocity should be able to process discrete numbers.

4.4.8 Discrete numbers and Sobolev space

The Sobolev space is a vector space of function equipped with a norm that is combination of L^p-norm of the function itself as well as its derivatives up to given order. There are many criterion for smoothness of mathematical functions; a strong notion of smoothness is the differentiability and a yet stronger notion is the continuity of its derivative. Indeed, application of Sobolev functions and partial differential equations indicate that it is useful to know how the maximal operator preserves the smoothness of functions [36]. In this regard, Wavelet transformation and the second derivative in Sobolev space have been implemented

on the discrete output of different physical and mechanical parameters to accurately detect the minimum velocity at which shear stability occurs. In this section a concise description of these mathematical definitions is presented. For $\Omega \subseteq \mathbb{R}$, $L^2(\Omega)$ is defined to be the space of functions $f : \Omega \to \mathbb{R}$ such that:

$$\|v\|_{L^2(\Omega)} = \Big\{ \int_\Omega |v(x)|^2 \, dx \Big\}^{1/2} < \infty. \tag{4.5}$$

In order to measure the smoothness properties of a function in an average sense it is common to introduce Sobolev spaces $H^m(\Omega)$ consisting of all functions $f \in L^2(\Omega)$, with derivatives up to order m in $L^2(\Omega)$, i.e.

$$\|f\|_{H^m(\Omega)} = \|f\|_{L^2(\Omega)} + \sum_{\alpha=1}^{m} \|f^{(\alpha)}\|_{L^2(\Omega)} < \infty. \tag{4.6}$$

Characterizing the smoothness properties of a function is briefly recalled through Wavelet coefficients as following [37].
Let $\{\psi_{j,k}(x)\}_{j\geq 0, k\in\mathbb{Z}}$ be an orthonormal basis of $L^2(\Omega)$ (see e.g. [37] for a detailed discussion), then a function $f \in L^2(\Omega)$ belongs to the Sobolev space $H^m(\Omega)$ if and only if

$$E_m(f) = \Big(\sum_{j\geq 0} \sum_{k\in\mathbf{Z}} 2^{2jm} |d_{j,k}|^2 \Big)^{1/2} < \infty, \tag{4.7}$$

where $d_{j,k} = \int_\Omega f(x)\, \psi_{j,k}(x) dx$ are the Wavelet coefficients of the function f. It is important to remark that the quantity $E_m(f)$ is equivalent to the Sobolev norm $\|f\|_{H^m(\Omega)}$. In the sequel, the quantity E_2 will be used to monitor the behavior of average regularity of the second derivative of a given sequence $\underline{f} = \{f_n(x)\}_{n=0}^N$ of functions. In particular, computing the following quantity is of interest

$$J_2(\underline{f}) = \max_{0\leq n\leq N-1} |E_2(f_{n+1}) - E_2(f_n)|, \tag{4.8}$$

$J_2(\underline{f})$ measures the maximum variation of the H^2-Sobolev norm of a given sequence of functions. The reliability of the quantity J_2 as an indicator to identify the CV is well validated in Section 4.5.

The Wavelet basis are also suitable to be used in a straightforward way to perform compression (or denoising) of a given signal. Let $f = \sum_{j,k} d_{j,k}\psi_{j,k}$ be the Wavelet decomposition of a given signal $f(x)$ and $T > 0$ be a threshold parameter. The filtered version $\tilde{f}$ of the signal f can be computed in the following way [37]

$$\tilde{f} = \sum_{|d_{j,k}|\geq T} d_{j,k}\psi_{j,k}. \tag{4.9}$$

This procedure, which retains the main features (i.e. the largest Wavelet coefficients) of the given signal, has been employed to denoise the strain rate and Von-Mises stress results for the monitored elements. Thus, by checking the $\tilde{f}$ for each signal, which in this case would be an output of the FE software (i.e. stress, strain), the biggest jump in $\tilde{f}$ by changing the velocity shows the position of CV.

4.4.9 Algorithm of the process

The algorithm developed for finding CV requires performing a series of numerical tests in Abaqus and evaluating the second derivative of different physical parameters which are practically affected by shear instability in the Johnson-Cook material model. In this regard, Python [38] is used to develop a sub-routine to be implemented in Abaqus for performing the numerical tests automatically. The developed algorithm is described as following:

1. based on the experimental results, no material bonding occurs in cold spray coating with velocities less than 200 m/s and almost all the tested materials bond with a velocity lower than 1000 m/s.

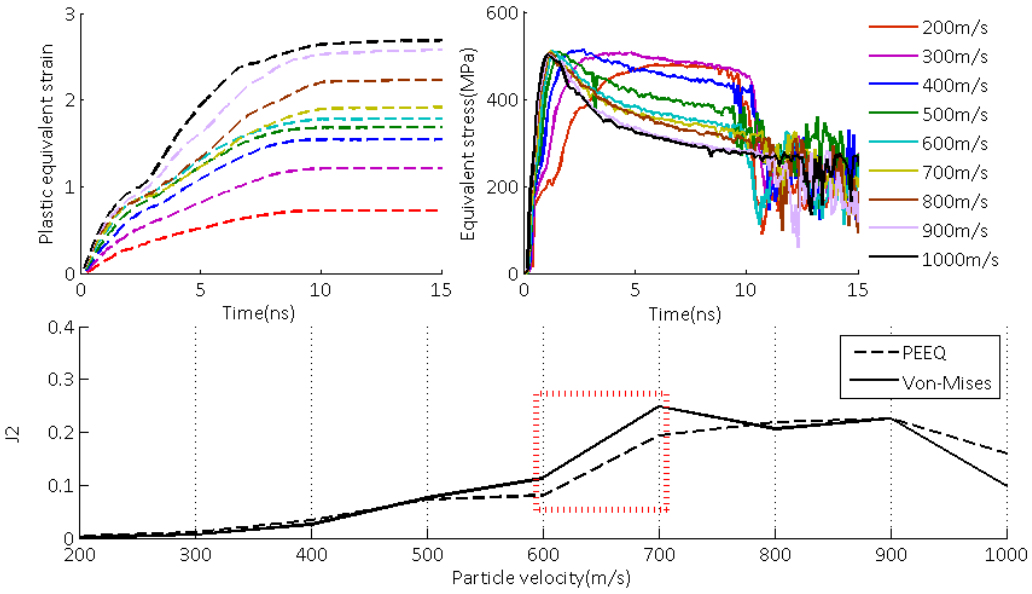

Figure 4.11: *The results for PEEQ and equivalent Von-Mises stress for Cu on Cu and related J_2 for each velocity*

Thus, the first step has been set to perform 8 sets of analysis with different velocities in the practical range of 200-1000 m/s, in order to obtain an approximation of CV for the considered material types.

2. then for each parameter, the maximum jump in second derivative in the Sobolev space based on Wavelet transform has been located. Having performed this step, the CV for the considered shot and substrate material type is achieved in the range of 100 (due to the step of velocity change set to 100 m/s). In order to reach a better judgment of the material behavior, the evaluation is performed for different parameters such as PEEQ, equivalent Von-Mises stress, temperature of the particle and equivalent plastic strain rate. These properties all appear in the Johnson-Cook [22] material model. Fig.4.11 shows the results of equivalent plastic strain along with Von-Mises equivalent stress for Cu-Cu and the related J_2 calculated based on Eq.4.8. The red dashed box in the below graphs shows the maximum jump in J_2 which has been interpreted as the CV first zone.

3. in the view of the results obtained in previous step, another series of analysis are performed using a smaller pace in order to obtain a narrower range of the CV approximation. For example, if in the second step, the CV is found to be between 600 m/s and 700 m/s, in this level, the analysis are performed changing the particle velocities from 600 m/s to 700 m/s with the pace of 10 m/s.

4. the 2^{nd} step is repeated over to obtain an accurate enough evaluation of the CV.

5. after having detected the CV, the whole process should be reproduced with three different sizes of mesh in order to assess the linear variation trend and then apply the zero element size extrapolating method and eventually obtain the mesh size independent CV.

Fig. 4.12 shows the flowchart of CV detection algorithm based on the second derivative of the physical parameters. It is worthy to note that due to many numerical limitations such as the minimum number of increments in Abaqus and analysis time and also the numerical sensitivity of the chosen procedure, it is hardly practical to obtain an absolute value for the CV. Thus the results will be stated in a delicate range of CV. The whole process is controlled by a Python code that is presented in Appendix A. The code creates the model, changes the element types in the infinite part, launches the analysis, and gets all the necessary results from Abaqus. Fig.4.13 shows the user interface of the code. As input, the python

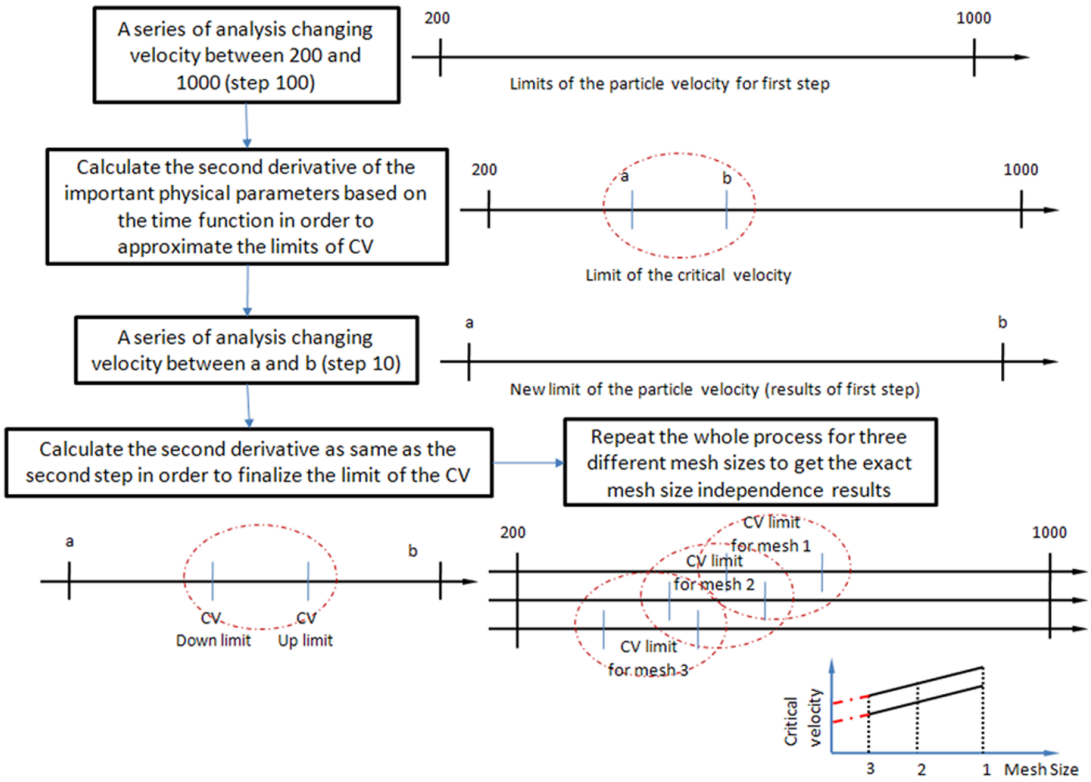

Figure 4.12: *Flowchart of CV calculation algorithm*

file asks for, initial velocity, step for velocity, maximum velocity, particles' diameter, temperature of the particle and substrate, mesh size, and finally the material of the substrate and the particle. The python code is able to perform the whole simulation for each pass. Then, the results should be processed through a mathematical software in order to perform the Wavelet transform and to calculate the second derivative of the results in frequency domain in the Sobolev space. The second step of the process has been handled in Matlab 2007 [39]. The Matlab code is presented in Appendix A. The advantage of this method is that it does not add any other new parameter and it does not depend on any other criterion outside of the results, checking them to find the instability. It checks mathematically the smoothness of different physical parameters as a function of time by assuming the shear localization to be a disturbance in the behavior. Obviously, the procedure for CV assessments takes more time compared to the other presented models.

4.4.10 Denoising Technique

As presented in Fig. 4.10, and admitted by [40], the noise in the numerical results makes it quite difficult to judge the final behavior of the CV. The noise is mostly observed in stress parameters and also in the strain rate. In this regard, a denoising technique based on the Wavelet [37] transform has been utilized in order to obtain noiseless behavior of the two latter parameters. Roughly speaking, denoising is based on deleting the low frequency parts of the Wavelet transform. Matlab software has been used in order to perform Wavelet transformation on the parameters in frequency domain. Fig. 4.14 shows the properties of a variable after Wavelet transformation. As it can be seen, different frequency levels will be stored in different sections of an array called "C" (Fig.4.14); thus, by deleting these sections and transforming the new variable into time domain, the noise which results from low frequency parameters should be omitted. The low frequency noises will be omitted from the original signal. Fig. 4.15 shows the canceling process and its effect on the frequency domain. In this figure different sections created in Matlab for wavelet transformation have been presented by dashed lines. To find the best results, the

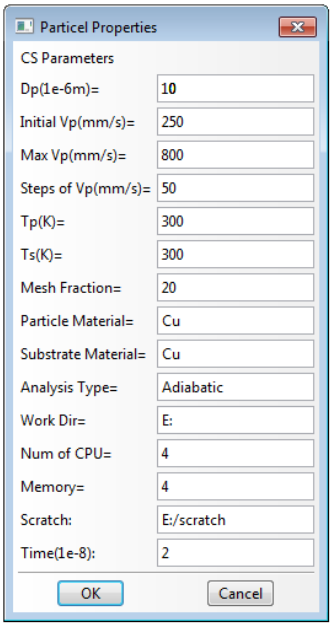

Figure 4.13: *Python code user interface*

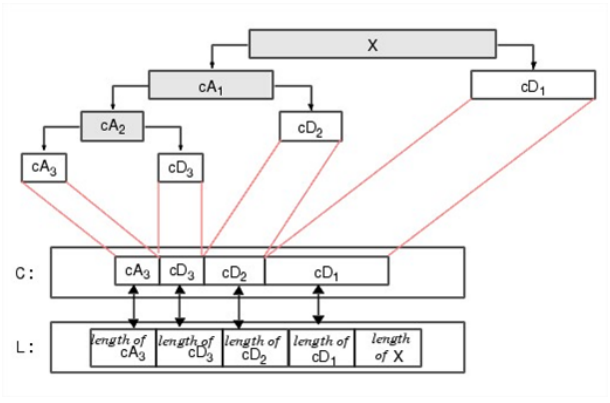

h

Figure 4.14: *Parameters map after Wavelet transform in Matlab [39]*

cross validation criterion has been used which, roughly speaking, tries to optimize the mean integrated square error (MISE $M(t)$) between the Wavelet shrinkage estimator $\widehat{f}_t(x)$ and the true function $f(x)$ in Eq.4.10 [41].

$$M(t) = E \int \left\{ \widehat{f}_t(x) - f(x) \right\}^2 dx \tag{4.10}$$

The signals after the red line have been canceled and the results have been shown in Fig. 4.15b. Fig. 4.16 shows the effect of canceling the signal different segments in time domain on the original signal.

4.5 Evaluation of the numerical model

In order to assess the numerical model, two different categories of the results, deformation and CV, are compared with experimental measurements and other numerical results presented in the literature. Performing experimental measurement was not possible due to the lack of instruments (DLV); thus, the results have been compared with the experimental measurement presented by Raletz *et al.* [13].

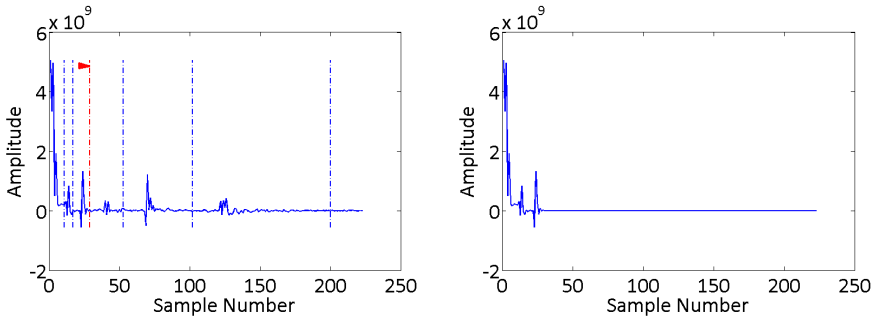

(a) *The original signal in frequency domain*

(b) *Denoised signal by canceling the data after red line*

Figure 4.15: *An example of canceling the noise of the signal in frequency domain*

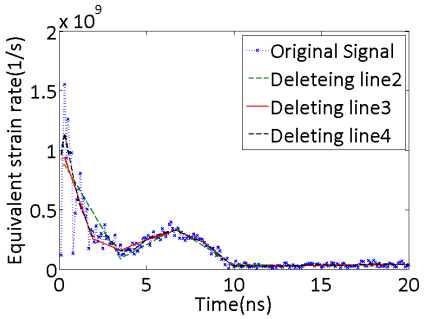

Figure 4.16: *Different denoised signals by canceling different sections*

In [13] three different combinations (Cu on Cu, Cu on SS316, and Ni on Cu) of powder-substrate have been tested to calculate the CV. The process parameters such as temperature in the numerical model developed in this thesis, are chosen based on the presented information in [13]; while the deformation of the particles, for each case, have been compared to other numerical simulations and single particle experimental SEM observation data available in the literature.

4.5.1 Particle deformation

Fig. 4.17 shows an example of 3D deformation of the Cu on Cu combination for 600 m/s. In this figure, the high deformation and jet produced by the softening of the material can be observed. The three

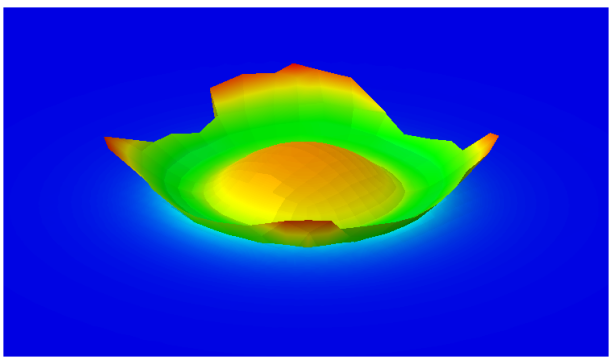

Figure 4.17: *3D deformation of the particle in the model for Cu on Cu @600m/s*

combinations tested in [13] are: Cu on Cu, Cu on SS316, Ni on Cu. The literature shows [42] a perfect porosity free deposition of these combinations. The deformation of the particles for different velocities in two time steps have been shown in Fig. 4.18 for Cu on Cu, Fig. 4.19 for Cu on SS316, and Fig.4.20 for Ni on Cu. Deformations of different particles show the trend of the softening in the material.

(a) *200 m/s@5ns* **(b)** *200 m/s@10ns*

(c) *400 m/s@5ns* **(d)** *400 m/s@10ns*

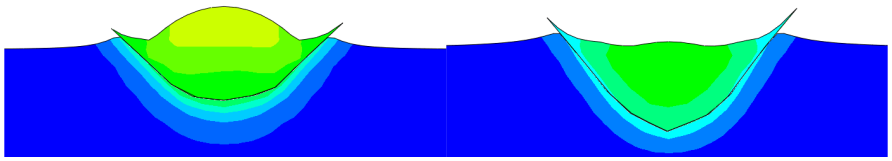

(e) *600 m/s@5ns* **(f)** *600 m/s@10ns*

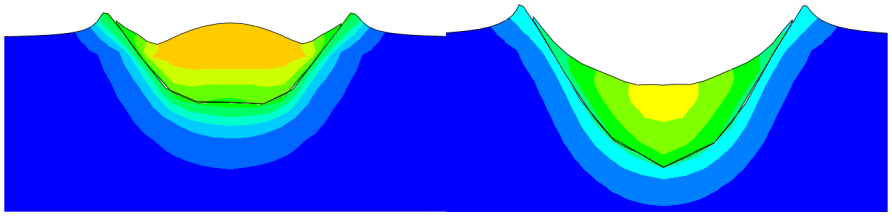

(g) *800 m/s@5ns* **(h)** *800 m/s@10ns*

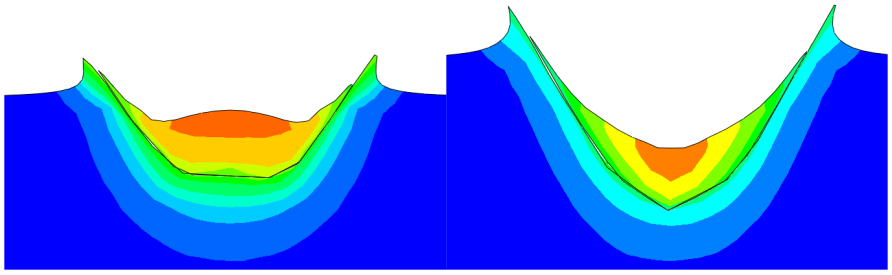

(i) *1000 m/s@5ns* **(j)** *1000 m/s@10ns*

Figure 4.18: *Deformation of Cu particle on Cu substrate a)200 m/s @5ns b) 400 m/s @5ns c) 600 m/s @5ns d) 800 m/s @5ns e)1000m/s @5ns*

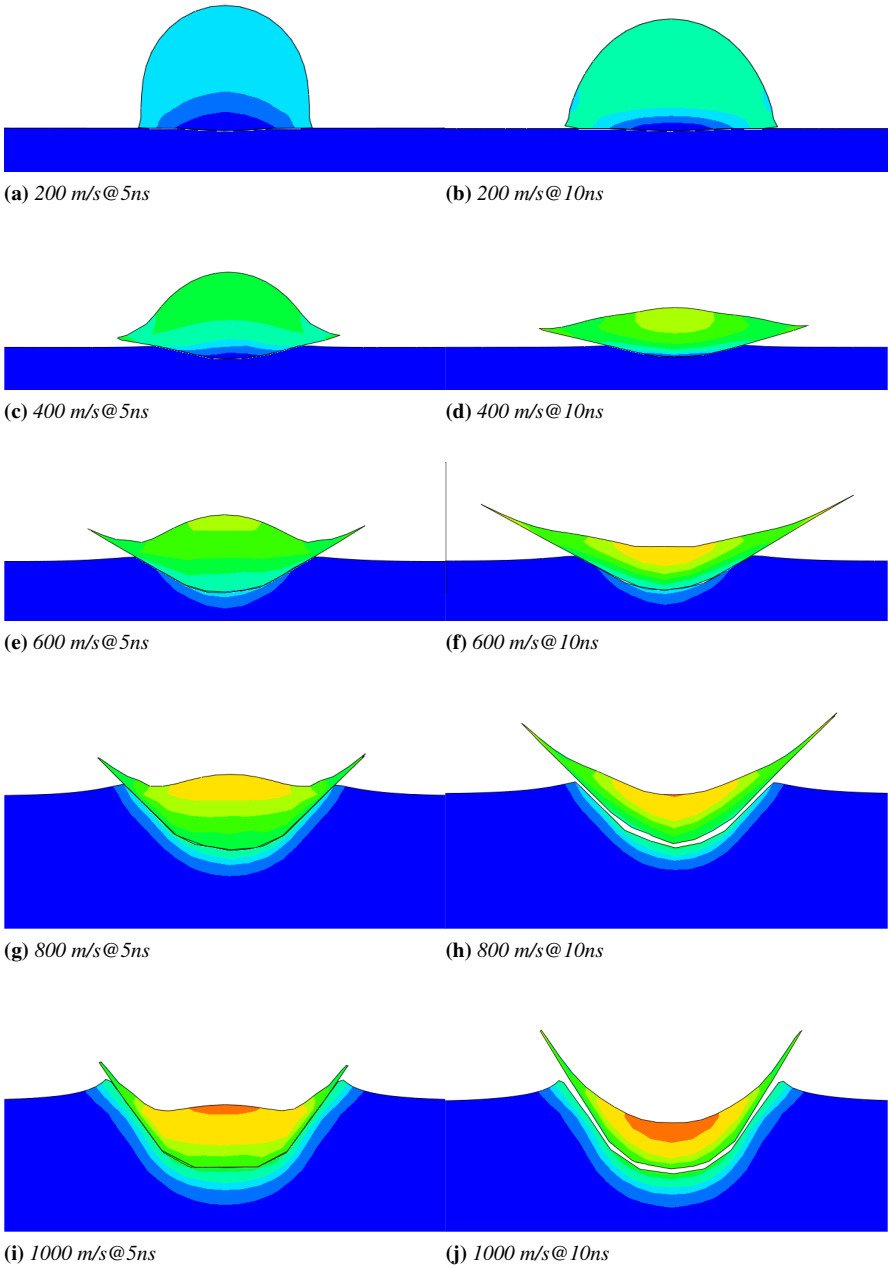

(a) *200 m/s@5ns* **(b)** *200 m/s@10ns*

(c) *400 m/s@5ns* **(d)** *400 m/s@10ns*

(e) *600 m/s@5ns* **(f)** *600 m/s@10ns*

(g) *800 m/s@5ns* **(h)** *800 m/s@10ns*

(i) *1000 m/s@5ns* **(j)** *1000 m/s@10ns*

Figure 4.19: *Deformation of Cu particle on SS316 substrate a) 200 m/s @5ns b) 400 m/s @5ns c) 600 m/s @5ns d) 800 m/s @5ns e) 1000m/s @5ns*

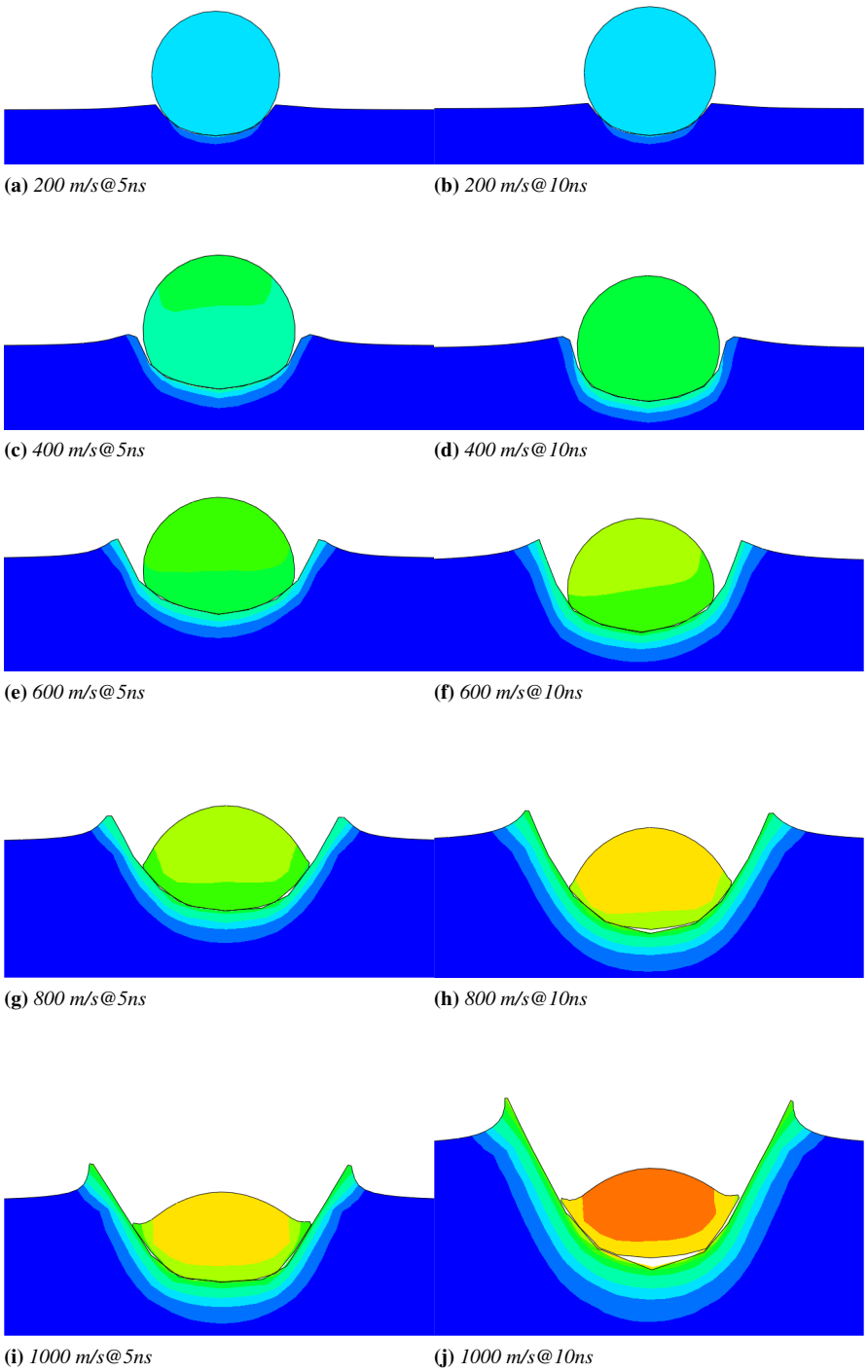

(a) *200 m/s@5ns* **(b)** *200 m/s@10ns*

(c) *400 m/s@5ns* **(d)** *400 m/s@10ns*

(e) *600 m/s@5ns* **(f)** *600 m/s@10ns*

(g) *800 m/s@5ns* **(h)** *800 m/s@10ns*

(i) *1000 m/s@5ns* **(j)** *1000 m/s@10ns*

Figure 4.20: *Deformation of Ni particle on Cu substrate a) 200 m/s @5ns b) 400 m/s @5ns c) 600 m/s @5ns d) 800 m/s @5ns e) 1000 m/s @5ns*

Fig. 4.18j shows a very highly deformed model, that is probably due to not considering the effect of bonding in the simulation; bonding of the particle to the substrate might decrease the energy of the movement and consequently the final deformation might be moderated.
In order to control the process duration and discover the entire procedure, it is necessary to check the velocity of the particles. Fig. 4.21a shows the evolution of particle velocity for the lowest point of the particle and represents the moment in which the velocity becomes zero under different impact conditions. According to Fig. 4.21a for Cu on Cu, Fig. 4.21b for Cu on SS316, and Fig. 4.21c for Ni on Cu, in which the results obtained for different materials and different velocities are presented, the analyzing time is clearly enough for simulation of the impact as well as the rebounding of the lowest particle point. Regardless the fact that whether the bonding between particle and the substrate happens or not, the particle tries to detach from the substrate after impact due to rebounding effect of the material; the detaching velocity of the particle is studied and presented in these figures which, as observed in the worst case, is about 100 m/s, that is, of course, not a negligible value. One of the parameters studied

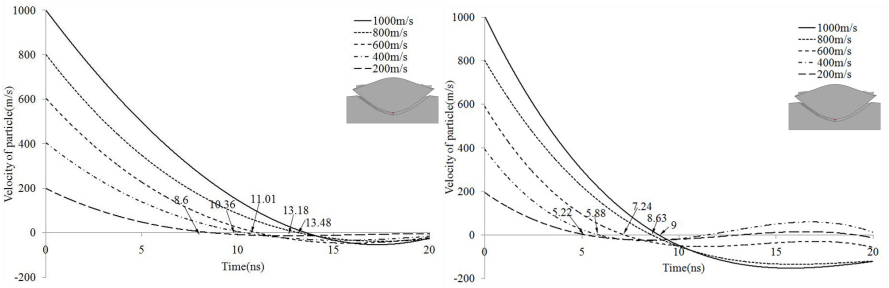

(a) *Cu on Cu* **(b)** *Cu on SS316*

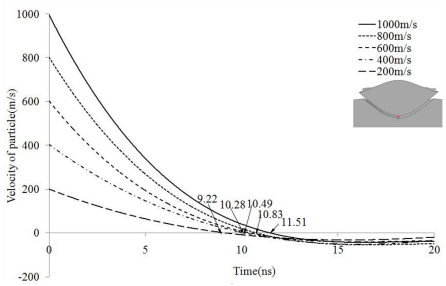

(c) *Ni on Cu*

Figure 4.21: *Zero velocity of lowest point of the particle after impact*

in particle deformation is compression ratio which roughly is the percentage of the particle deformation after impact. The R_c is measured by $R_c = (d_p - h_p)/d_p\%$ which d_p is the diameter of the particle and h_p as shown in Fig. 4.22. This figure shows the behavior of the R_c by changing the velocity in the process duration.

4.5.2 Comparison of CV

The final results of the presented process are shown in Tab.4.4. The calculated CV has been presented along with other numerical calculations and experimental measurement of Raletz *et al.* [13]. Fig. 4.23a-4.23c show the results for different mesh size and application of the "zero element" method in order to obtain the mesh size independent results. Tab.4.4 shows a good correspondence between the numerical simulation and experimental measurements; in the worst case, 15-12% difference is observed in the measured values by the presented process. It should be noted again that the time consumed by the proposed process is the biggest disadvantage of the process with respect to other numerical simulations available in the literature.

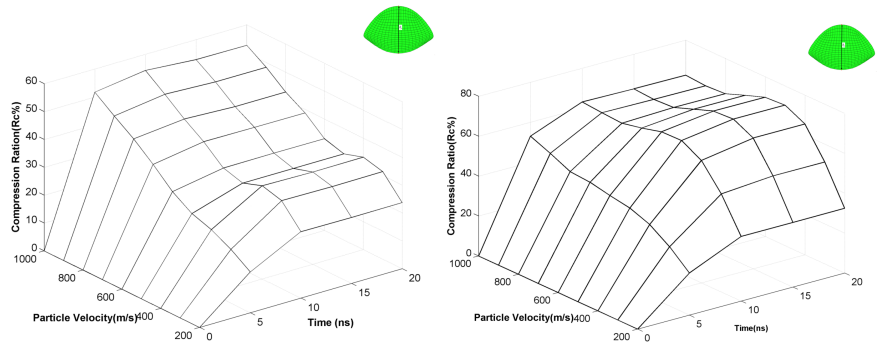

(a) *Cu on Cu* **(b)** *Cu on SS316*

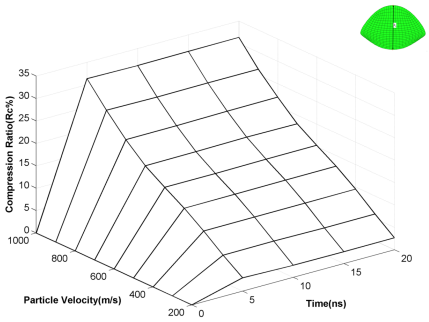

(c) *Ni on Cu*

Figure 4.22: *Compression ratio (R_c) as a function of time and particle velocity for different combinations*

Table 4.4: *Final measured results for CV*

			Experimental	Numerical results			
Powder	Substrate	Calculated	Raletz [13] CV (m/s)	Grujicic [9] CV (m/s)	Wen-Ya Li [11] CV (m/s)	SL [9] CV (m/s)	Assadi [10] CV (m/s)
Cu	Cu	407±5	422±45	575-585	298-356	571	570-580
Cu	SS316	415±45	437±47	570-580	NA	574	NA
Ni	Cu	459±45	512 ±59	570-570	NA	576	NA

4.6 Effect of the process parameters on CV

The presented process has been applied to other material sets in order to study the effect of two particular parameters on CV. Temperature of the particle is one the most important and effective parameters which has notable effect on both deposition efficiency and CV of the process. The other parameter, which has been studied, is the effect of shot peening which induces compressive residual stress on the substrate before cold spray coating. Shot peening also increases the roughness of the surface, it is believed [43] that the surface roughness induced by shot peening or any other surface treatment also decreases the CV value and as a result increases the deposition efficiency of the process; however due to difficulty in measuring and inducing the controlled roughness numerically, only the residual stresses induced by shot peening have been studied.

4.6.1 Temperature of the particles

The temperature of the particles is found to be an effective parameter in the coating process. Fig. 4.24 presented by [44] shows the effect of temperature on the deposition and CV of the impact. In the pre-

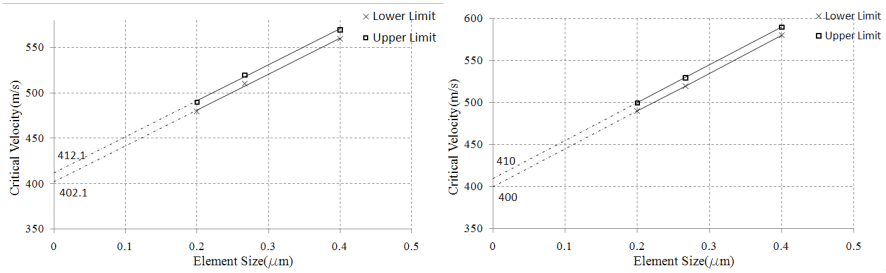

(a) *Cu on Cu* **(b)** *Cu on SS316*

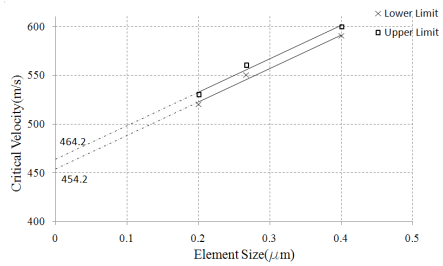

(c) *Ni on Cu*

Figure 4.23: *Application of zero element method for different materials showing the measured value in each element size*

sented figure, it can be observed that by increasing the temperature, the CV has been decreased and the window of deposition has become smaller. Thus it is concluded that a particle with very high velocity would not bond to the substrate. The effect of temperature has been studied on aluminum on aluminum

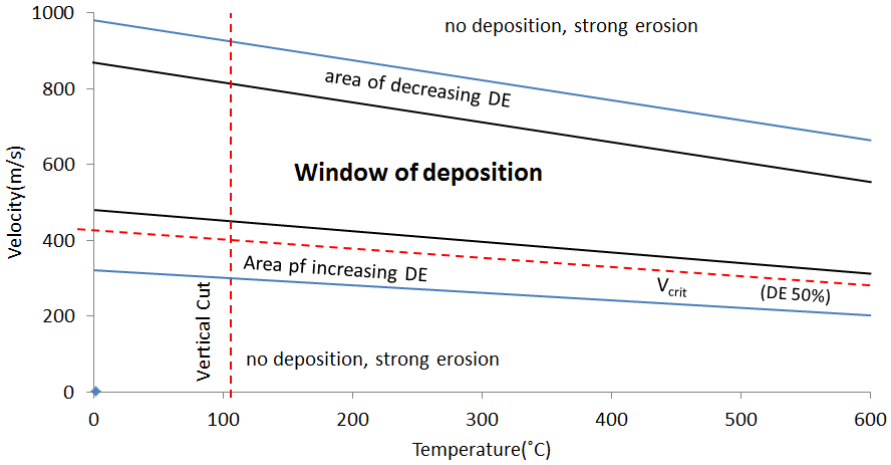

Figure 4.24: *Effect of temperature on the windows of deposition [25]*

combination. In a quarter of the presented model in the previous section, the temperature of the particle has been changed and the process of CV measurement has been applied in each simulation considering different temperatures. Fig.4.25 shows the effect of temperature on displacement. In this figure, the velocity of the particle is kept equal for all the simulations and its temperature has been changed from 500°K to 900°K. Fig. 4.25 shows the results of three of those simulations. In 900°K softening in the particle is being started and the deformation is completely different from that of the two other temperatures. It has to be mentioned again that the velocity is kept the same in all simulations. Fig. 4.26a shows

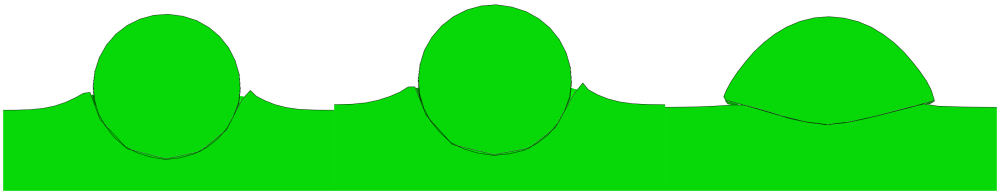

(a) $500°K$ **(b)** $700°K$ **(c)** $900°K$

Figure 4.25: *Deformation of the particle at different temperatures and the same velocity (500 m/s)*

the effect of temperature on compression ratio of the particle. In this graph the maximum R_C obtained at different velocities has been presented. It can be obviously observed that the higher the temperature is, the more the particle deforms. For instance, for the same velocity of 600 m/s, increasing the particle temperature from $300°$K to $650°$K the R_C increased from 30% to almost 70%. Fig. 4.26b shows three different CV measurements for Al on Al at three different temperatures. As it was expected, the CV of the process has been decreased, by increasing the temperature.

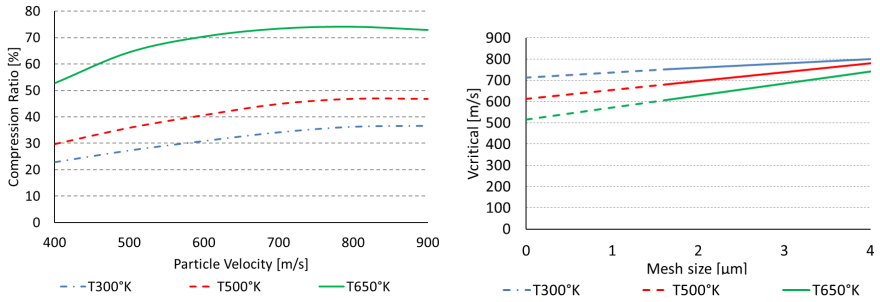

(a) *Effect of temperature on compression ratio (%)* **(b)** *Effect of temperature on CV*

Figure 4.26: *Effect of different temperatures with the same velocity (500 m/s) on R_C and CV*

4.6.2 Effect of Shot peening before coating

In order to study the effect of shot peening, a new model has been developed by adding three shots to model the peening process. Fig.4.27 shows the model developed for this purpose. In Fig. 4.27 the difference between the size of the shots and particles of cold spray coating can be observed. In the case of shot peened substrate, the temperature of the particle also has been changed, as it was considered also in the previous section. Therefore, the measured CV has been compared for 9 different case studies. The obtained residual stresses after shot impacts are shown in Fig. 4.28. The graph shows positive tensile residual stresses on the surface. Fig.4.29a shows compression ratio of the shot peened model at different temperatures. By comparing this figure with Fig.4.26a which does not consider the effect of peening, it is observed that the compression ratio is increased which might be due to the fact that harder substrate makes the particle to deform more than the softer one. Finally the "zero element" method has been applied for CV measurement on shot peened substrate simulations (Fig. 4.29b). The final results and the comparison of all the measured CV are presented in Tab. 4.5.

4.7 Conclusion

A 3D finite element analysis has been developed in order to calculate the CV in cold spray coating process. Abaqus 6.9-1 Explicit has been used to perform the numerical analysis, and Python 2.4-1 is used for elaborating Abaqus discrete outputs and performing a series of numerical tests to accurately detect

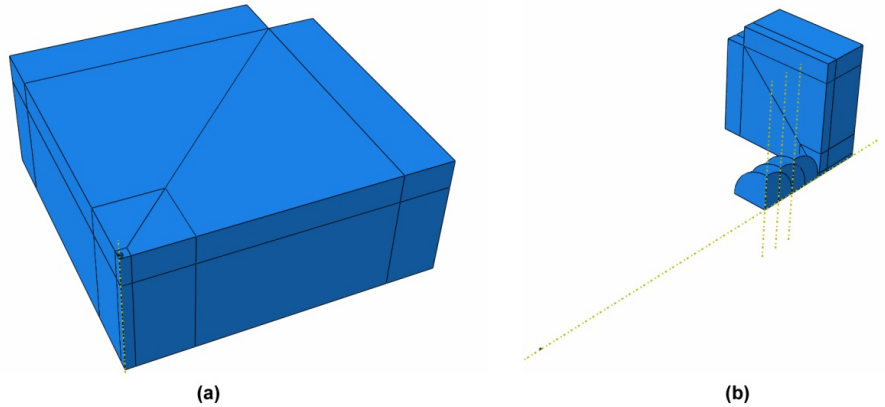

Figure 4.27: *The FE 3D model for studying shot peening effect a) cold spray coating b) shot peening and cold spray coating*

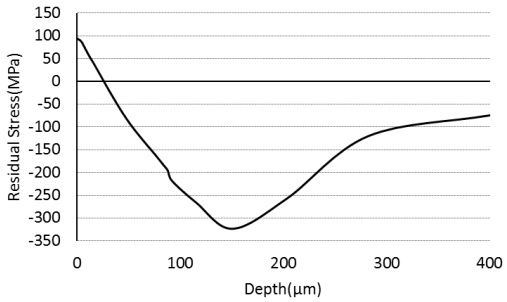

Figure 4.28: *Residual stress distribution in the model before the impact of the coating particles*

the shear instability and consequently the CV. Regarding the mesh convergence, "zero element" method has been applied to find element size independent results. The obtained results from the software are converted to Wavelet parameters in order to calculate the second derivative of each physical parameters in Sobolev space. The results are compared to previously developed numerical approaches available in the literature and the experimental tests of Raletz et al. [13]. A difference of up to 35% is observed between previous numerical simulations and Raletz experimental work [13], whereas the presented results in this article show a very good correspondence with the experimental measurements. This noteworthy difference with other numerical models can be attributed to the precise mathematical approach developed for recognition of shear instability. In view of the obtained results, the presented method is a useful tool to design a better experimental setup. Moreover, the sensitivity and accuracy of the described method

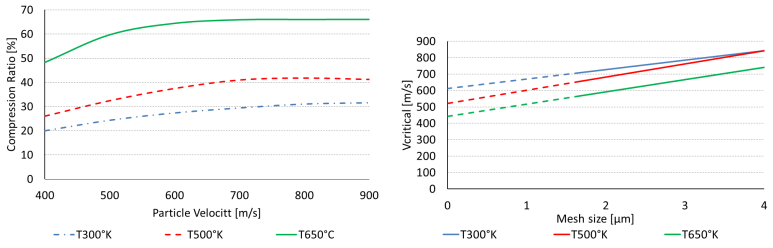

(a) *The effect of substrate shot peening on compression ratio (%)*

(b) *Calculating the final CV after shot peening by "zero element" method*

Figure 4.29: *Effect of shot peening on on R_C and CV*

Process	Temperature	CV (m/s)
Cold spray	300°K	719
With peening	300°K	612
Cold spray	500°K	613
With peening	500°K	521
Cold spray	650°K	515
With peening	650°K	442

Table 4.5: *The measured CV at different temperatures with and with shot-peening*

helps to survey the process and its qualification in order to increase the functionality of the deposited material with an optimum condition. Numerical approach has been used in order to study the effect of temperature and shot peening on the CV. The results show a reasonable trend in the final calculation of CV. Both temperature increase and shot peening application before cold spray, were found to be able to decrease the CV and consequently increase the deposition efficiency.

Bibliography

[1] A. N. Papyrin, S. V. Klinkov, and V. F. Kosarev, "Effect of the substrate surface activation on the process of cold spray coating formation," in *Proceeding of the International Thermal Spray Conference,May 2-4, Basel, Switzerland*, 2005.

[2] A. Alkimov, V. Kosarev, and A. Papyrin, "A method of cold gas dynamic deposition," *Dokl. Akad. Nauk SSSR*, vol. 318, pp. 1062–1065, 1990.

[3] T. V. Steenkiste, J. Smith, R. Teets, J. Moleski, D. Gorkiewicz, R. Tison, D. Marantz, K. Kowalsky, W. Riggs, P. Zajchowski, B. Pilsner, R. McCune, and K. Barnett, "Kinetic spray coatings," *Surf. Coat. Technol.*, vol. 111, pp. 62–71, 1999.

[4] Y. Ji, S. Yoon, G. Bae, S. Kumar, C. Lee, and H. Choi, "Influence of the interface temperature and strain gradients on the impact energy model of a soft particle on a hard substrate during kinetic spraying," *Metals and Materials International*, vol. 17, pp. 335–340, 2011.

[5] D. Zhang, P. H. Shipway, and D. G. McCartney, "Particle-substrate interactions in cold gas dynamic spraying," *Thermal Spray(ASM International)*, pp. 45–52, 2003.

[6] C. J. Li, H. Bang, G. J. Yang, W. Y. L, H. Bang, and C. X. Li, "Examination of the estimating approaches for the critical velocity in cold spraying," *Thermal Spray (ASM International)*, pp. 128–134, 2007.

[7] A. P. Alkhimov, S. V. Klinkov, and V. F. Kosarev, "Experimental study of deformation and attachment of microparticles to an obstacle upon high-rate impact," *Journal of Applied Mechanics and Technical Physics*, vol. 41, pp. 245–250, 2000.

[8] A. P. Alkhimov, A. I. Gudilov, V. F. Kosarev, and N. I. Nesterovich, "Specific features of microparticle deformation upon impact on a rigid barrier," *Journal of Applied Mechanics and Technical Physics*, vol. 41, pp. 188–192, 2000.

[9] M. Grujicic, C. Zhao, W. DeRosset, and D. Helfritch, "Adiabatic shear instability based mechanism for particles/substrate bonding in the cold-gas dynamic-spray process," *Materials and Design*, vol. 25, pp. 681–688, 2004.

[10] H. Assadi, F. Gaurtner, T. Stoltenhoff, and H. Kreye, "Bonding mechanism in cold gas spraying," *Acta Materialia*, vol. 51, pp. 4379–4394, 2003.

[11] C. J. Li, W. Y. Li, and H. Liao, "Examination of the critical velocity for deposition of particles in cold spraying," *Journal of Thermal Spray Technology*, vol. 15, pp. 212–222, 2006.

[12] T. Stoltenhoff, J. Voyer, and H. Kreye, "Cold spraying-state of the art and applicability," in *International Thermal Spray Conference, March 4-6, (Essen, Germany)*, 2002.

[13] F. Raletz, M. Vardelle, and G. Ezo'o, "Critical particle velocity under cold spray conditions," *surface & coating Technology*, vol. 201, pp. 1942–1947, 2006.

[14] Polytec, "Inc, http://www.polytec.com/eu/."

[15] L. D. vibrometer, "Wikipedia, http://en.wikipedia.org/wiki/laser_doppler_vibrometer."

[16] Technar, "http://www.tecnar.com/."

[17] OSEIR, "http://www.oseir.com/."

[18] F. Raletz, M. Vardelle, and G. Ezo'o, "Fast determination of particle critical velocity in cold spraying," in *Proceeding of the International Thermal Spray Conference,May 2-4, Basel, Switzerland*, 2005.

[19] D. L. Gilmore, R. C. Dykhuizen, R. A. Neiser, T. J. Roemer, and M. F. Smith, "Particle velocity and deposition efficiency in the cold spray process," *J. Therm. Spray, Technol.*, vol. 8, pp. 576–582, 1999.

[20] A. Rezaeian, R. R. Chromik, E. I. S. Yue, and J. G. Legoux, "Characterization of cold-sprayed ni, ti and cu coating properties for their optimizations," in *Proceeding of the International Thermal Spray Conference,June 2-4, Maastricht, Netherland*, 2008.

[21] D. Hibbitt, B. Karlsson, and P. Soerensen, "$abaqus^{TM}$ 6.2-1. user manual," 2001.

[22] G. R. Johnson and W. H. Cook, "A constitutive model and data for metals subjected to large strain, high strain rates and high temperature," *Proceedings of the 7th International Symposium on Ballistics*, vol. 4, pp. 541–547, 1983.

[23] G. Johnson and W. Cook, "Fracture characteristics of three metals subjected to various strains, strain rates, temperatures and pressures," *Eng. Frac. Mech.*, vol. 21, pp. 31–48, 1985.

[24] S. Bagherifard, R. Ghelichi, and M. Guagliano, "A numerical model of severe shot peening (ssp) to predict the generation of a nanostructured surface layer of material," *Surface and Coating Technology*, vol. 204, pp. 4081–4090, 2010.

[25] T. Schmidt, F. Gärtner, H. Assadi, and H. Kreye, "Development of a generalized parameter window for cold spray deposition," *Acta Materialia*, vol. 54, pp. 729–742, 2006.

[26] L. S. T. Corporation, "Ca, ls-dyna theorectical manual," 1998.

[27] P. Rosin and E. Rammler, "The laws governing the fineness of powdered coal," *Journal of the Institute of Fuel*, vol. 7, pp. 29–36, 1933.

[28] S. E. Schoenfeld and T. W. Wright, "A failure criterion based on material instability," *Int J Solids Struct*, vol. 40, pp. 3021–3037, 2003.

[29] D. Hibbitt, B. Karlsson, and P. Soerensen, "Abaqus/explicit 6.9-1 manual," 2002.

[30] N. Brar, V. Joshi, and B. Harris, "Constitutive model constants for al7075-t651 and al7075-t6," in *Constitutive Model Constants for Al7075-T651 and Al7075-T6*, 2009.

[31] http://asm.matweb.com/search/SpecificMaterial.asp?bassnum=MA7075T6.

[32] S. Ghosh and N. Kikuchi, "An arbitrary lagrangian-eulerian finite element method for large deformation analysis of elastic-viscoplastic solids," *Computer Methods in Applied Mechanics and Engineering*, vol. 86, pp. 127–188, 1991.

[33] W. Y. Li, H. Liao, C. J. Li, G. Li, C. Coddet, and X. Wang, "On high velocity impact of micro-sized metallic particles in cold spraying," *Applied Surface Science*, vol. 253, pp. 2852–2862, 2006.

[34] W. Y. Li, C. Zhang, C. J. Li, and H. Liao, "Modeling aspects of high velocity impact of particles in cold spraying by explicit finite element analysis," *Journal of Thermal Spray Technology*, vol. 18, pp. 921–933, 2009.

[35] W. Y. Li and W. Gao, "Some aspects on 3d numerical modeling of high velocity impact of particles in cold spraying by explicit finite element analysis," *Applied Surface Science*, vol. 255, pp. 7878–7892, 2009.

[36] V. Maz'ya, *Sobolev spaced in mathematics I*. International Mathematical Series, v.8, Novosibirsk, Russia, Springer Science, 2009.

[37] S. Mallat, *A Wavelet Tour of Signal Processing*. Academic Press, 1999.

[38] "Python documentation." http://docs.python.org/.

[39] "Matlab documentation version r2007b (7.5.0.342)."

[40] G. Bae, Y. Xiong, S. Kumar, K. Kang, and C. Lee, "General aspects of interface bonding in kinetic sprayed coatings," *Acta Materialia*, vol. 56, pp. 4858–4868, 2008.

[41] G. P. Nason, "Wavelet shrinkage using cross-validation," *Journal of Royal statistical society*, vol. 58, pp. 463–479, 1996.

[42] R. C. Dykhuizen, M. F. Smith, D. L. Gilmore, R. A. Neiser, X. Jiang, and S. Sampath, "Impact of high velocity cold spray particles," *J. Therm. Spray Technol.*, vol. 8, pp. 559–564, 1999.

[43] S. Siegmann and C. A. Brown, "Investigation of substrate roughness in thermal spraying by a scale-sensitive 3-d fractal analysis method," in *15th International Thermal Spray Conference - Thermal Spray: Meeting the Challenges of the 21st Century, Nice, France*, 1998.

[44] T. Schmidt, F. Gärtner, H. Kreye, and T. Klassen, "Correlation of particle impact conditions and coating properties in cold spraying," in *Proceeding of the International Thermal Spray Conference,May 2-4, Basel, Switzerland*, 2005.

Chapter 5

Numerical assessment of the coated surface

5.1 Introduction

The peening effect of cold spray coating, as an advantages of the process, induces compressive residual stresses, high plastic deformation, and high strain rate. A number of factors influence the coating residual stress including quenching due to cooling of the sprayed material, peening due to the plastic deformation of impacted particles, thermal mismatch resulting from different thermal expansion coefficients of coating-substrate materials and temperature gradient in multi-pass deposition processes. High plastic deformation and high strain rate as mentioned in Chapter 1 can produce NC grain and, in many cases, they are the main reasons for crystalline size reduction in the structure. Constant bombardment of particles on the same substrate and coating area results in increasing the residual stresses which cause the coating to peel near the substrate/coating interface [1]. In cold spray coating, with respect to other types of thermal spray coating, the lower temperature and higher velocity of the particles might affect the induced residual stresses. Fig. 5.1a [2] and 5.1b [3] show two examples of experimental residual stress measurements in coated samples. McCune *et al.* [2] have measured residual stresses for copper powders coating and in the paper by Bagherifard *et al.* [3] the stress induced by coating for aluminum powders is reported. The interesting common behavior observed in both graphs is the relaxation of the compressive

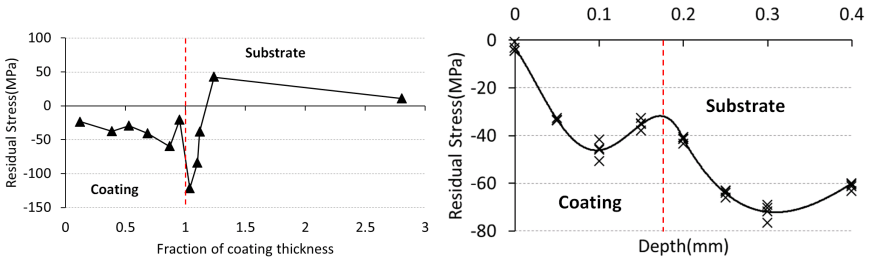

(a) *Copper powders by [2]* **(b)** *Aluminum powders by [3]*

Figure 5.1: *Residual stress measurement for different materials [2, 3]*

residual stresses in the interface of the coating and the substrate; conversely, the big difference in the presented results, is the reported stress in the substrate that is almost zero in [2] whereas in the other paper [3] it has a considerable value with respect to that of the deposited material.
On the other hand, the peening effect of the very high kinetic energy particles causes severe plastic deformation (SPD) on the substrate, which is known to be the main reason of grain refinement in metallic components. In this chapter, the peening effect of cold spray coating will be studied numerically in or-

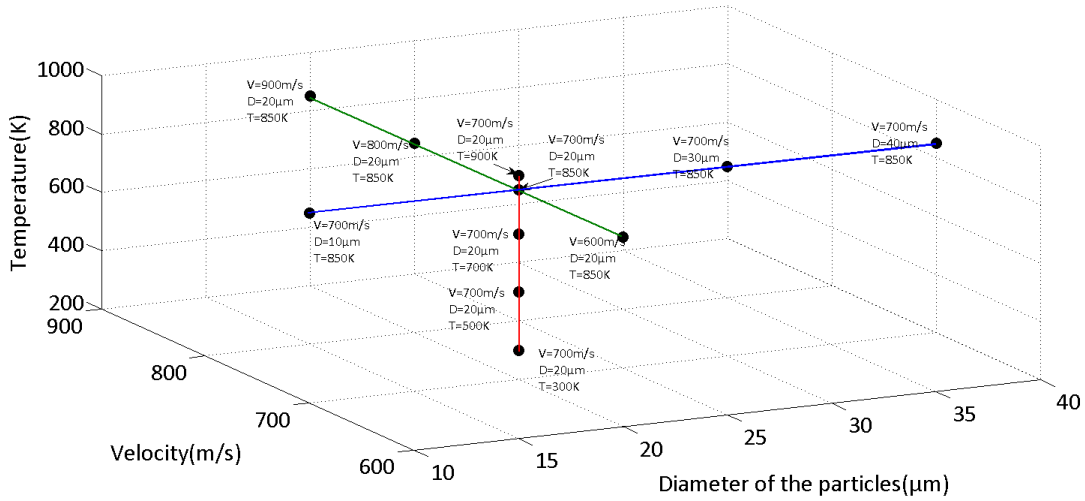

Figure 5.2: *Simulation plan for studying different physical parameters by numerical simulation*

der to survey two different important effects of the peening: first, the induced residual stresses by high velocity impact of the particles, and second, the possibility of recrystallization of the surface after the impact of the particles which will be caused by high rate intense deformation.

5.2 Introduction to the FEM model

In the numerical model it is not possible, of course, to consider all the parameters contributing to the phenomenon in reality; on the other hand, considering simplifying assumptions and regarding less parameters will, obviously, decrease the simulation time, i.e. there are some factors which has no or negligible effects on the final results; thus, before starting the simulation, it is necessary to know the importance of the parameters contributing to the phenomenon. In case of peening effect of coating, the role of three factors which are diameter, velocity, and temperature of the particles have been studied. In this regard different simulations have been performed in order to survey the effect of the mentioned parameters on the residual stress and equivalent plastic strain. The simulation plan has been shown in Fig. 5.2, where the green line presents variations for velocity, red line shows the variation in the temperature, and the blue line is for the diameter changes. The black dots show different simulation positions with respect to the three variables; on each point the chosen values for physical parameters have been written. The results indicate that the effect of these parameters are not negligible and they have to be considered in the model. Not only the importance of the parameters but also the feasibility of considering the latter parameters should be studied. For instance, the velocity of the particles in the FE model can not be calculated through numerical simulation; therefore analytical solutions or if possible experimental tests would be needed to measure the particle velocity based on the process initial condition and the coating machine set up. Finally, the results of the residual stress will be compared to the experimental measurements performed by Xray diffraction (XRD). In this regard, the numerical simulation has tried to simulate the peening effect of Al5052 substrate coated by Al7075 powders. The process parameters of the coating such as temperature and pressure are considered as the initial conditions of the numerical simulation which are explained in more detail in the following subsections.

5.2.1 Particle size

5.2.1.1 Single shot model

Based on Fig. 5.2, four different analysis have been performed to study the influence of particle size variation on peening effect of the coating process. The results, presented in Fig. 5.3, show that alteration of the particle size has great effect on both residual stress and equivalent plastic strain. It should be considered that although, bigger particles in the same process have lower velocities, the graphs confirm the expected result that using bigger particles in the process, the peening stress in the substrate will be increased.

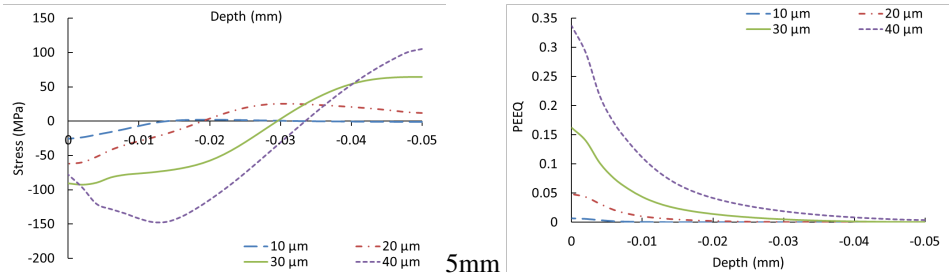

(a) *Residual stress* **(b)** *Equivalent plastic strain*

Figure 5.3: *Effect of particle size on different physical parameters with* $V = 700m/s$ *and* $T = 850°K$

5.2.1.2 Particle size considerations

The size of the particles in reality follow a random distribution. This randomness exists in both impact position and the particles' diameter. It is possible to obtain a narrow size distribution, however it does not mean that a process with a single particle size is plausible. Fig. 5.4 shows a scanning electron microscopy (SEM) image of Al7075 particles which shows that the particles used in the process are almost spherical with different sizes. The Rosin-Rammler model [4] is often used to approximate the particle size distribution [5]. This equation is useful for monitoring grinding operations for highly skewed distributions. Li *et al.* [6] have also used this distribution for particle size in cold spray coating numerical simulation. Eq. 5.1 shows the cumulative distribution function (CDF) for modified Rosin-Rammler model [7] which has been fitted to the particles' histogram obtained based on their SEM observation.

$$R(CFD) = \left\{1 - exp\left[-\left(\frac{Ln(D_p)}{Ln(D_{rr})}\right)^{Q}\right]\right\} \times 100\% \tag{5.1}$$

Fig.5.5a and Fig. 5.5b show the histogram obtained from powders sample measurement based on Fig. 5.4 and fitted Rosin-Rammler distribution. The CDF has been used for distracting the random numbers as the size distribution in the numerical model. In the case of the powder impact positions, although it is suggested [8, p. 62] that the position of the particles on the substrate follows a Gaussian distribution, due to small size of the impact zone, an uniform distribution has been considered for the position of the particles in this research. The number of shots has been chosen based on the coating thickness considering the compression ratio of a single shot considering the average velocity of the particles. In order to generate the arrangement of the particles, a Python code presented in Appendix B has been developed which uses the Rosin-Rammler fitted distribution for particle size and uniform distribution for particle position. Fig. 5.6 shows the position of the particles center (blue dots) with respect to the impact zone (red circle). The effect of randomness in the numerical simulation has to be studied through repeating the analysis with different parameters combinations; thus, different positions and different sizes might end to dissimilar results. In this regard, 5 different models with diverse random numbers for particles' size and position have been developed. Fig. 5.7 shows the distribution of the particle size and

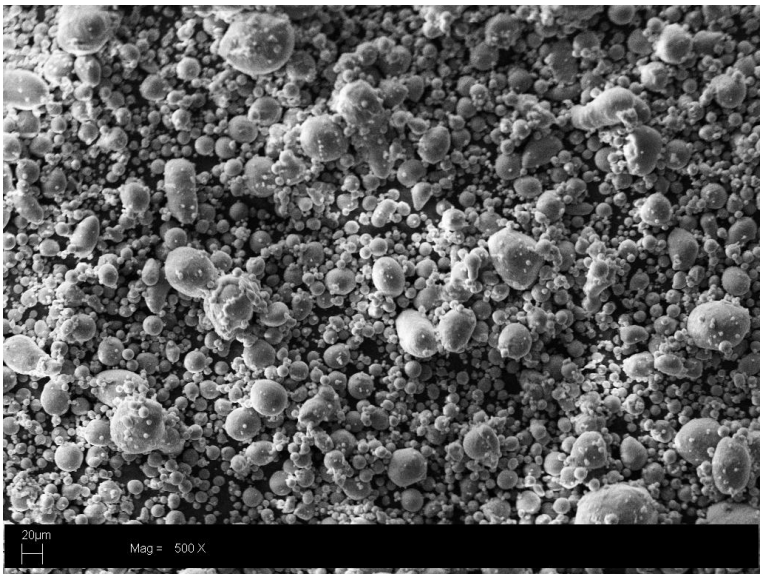

Figure 5.4: *Al7075 particle morphology and size distribution*

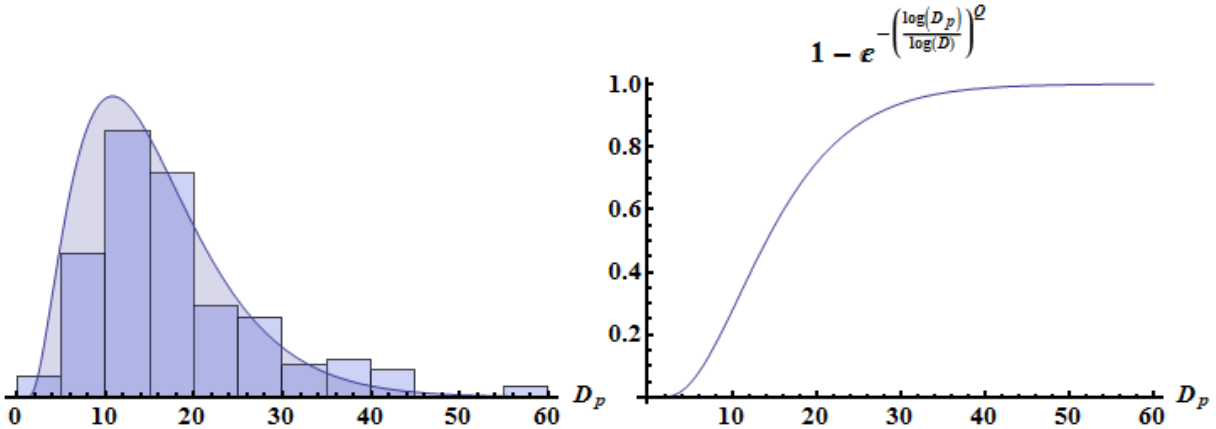

(a) *Histogram and Rosin-Rammler fitted function* **(b)** *CFD* ($D_{rr} = 16.87, Q = 5.52$)

Figure 5.5: *Histogram, fitted Rosin-Rammler, and the CDF of the particle size distribution*

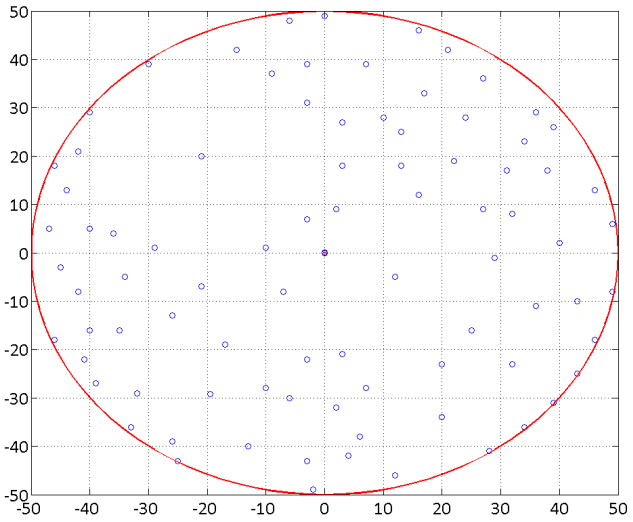

Figure 5.6: *The center of the particles (blue dots) in one of the models with respect to the impact zone (red circle)*

velocity in a model up to 100% coverage. As it will be described later, the velocity of the particles is a function of their diameter due to the fluid dynamic model of the process which will be explained in more detail later in this chapter. As it can be observed, smaller particles have higher velocities, as expected, with respect to the bigger ones. Rosin-Rammler distribution parameters,D_p and Q, (Eq. 5.1) as well as

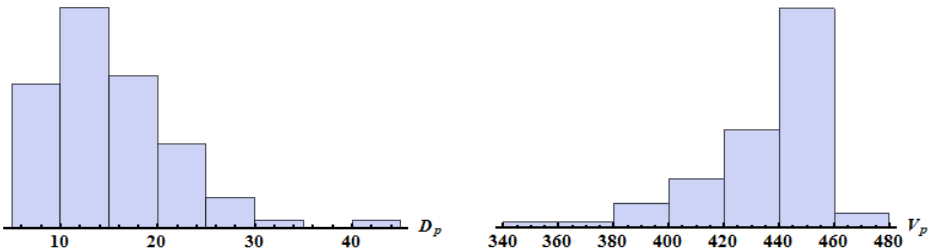

(a) *Histogram of the particles' diameter* **(b)** *Histogram of the particles' velocity*

Figure 5.7: *Histogram of the particles' size and velocity in one of the developed models*

its mean value used in the mentioned 5 models, along with the comparison of random distributions for the size of the developed models with respect to the particle size obtained from SEM observation, are presented in Fig. 5.8. The comparison shown in this figure confirms that the Python random generator has followed the forced distribution with good accuracy.

5.2.2 Particle velocity

5.2.2.1 Single shot model

Particle velocity effect has been studied through four single impact simulations with different velocities and same temperature ($T = 850°K$) and size for the particles ($D = 20\mu m$). The results presented in Fig. 5.9, do not show a significant effect of the velocity on the residual stress profile; on the other hand by increasing the velocity of the particles, the equivalent plastic strain of the substrate has been increased which will be considered as a criterion for the recrystallization of the substrate after particle impacts.

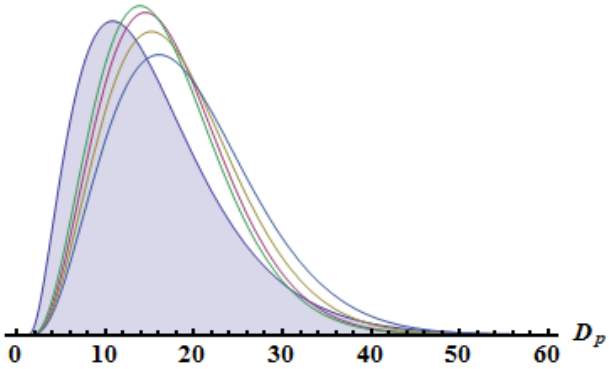

Model	D_p	Q	Mean
1	18.82	7.4	15.24
2	19.83	7.45	17.33
3	18.24	7.19	17.19
4	21.15	7.96	15.84
5	17.09	7.69	16.09

Figure 5.8: *Comparison of particles' random distribution in numerical model and experiment*

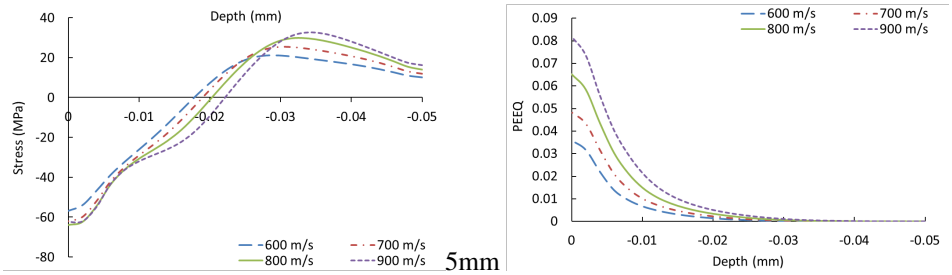

(a) *Residual stress* **(b)** *Equivalent plastic strain*

Figure 5.9: *Effect of the particle velocity on residual stress and equivalent plastic strain with* $D = 20\mu m$ *and* $T = 850°K$

5.2.2.2 Particle velocity considerations

In the previous chapter, it was shown that controlling the velocity or experimental measurement of the velocity, as the most important parameter of the process, is not an easy task; thus, numerical and analytical calculations are used to help estimating the impact velocity. Considering that, it is not in the aspect of this thesis to discuss the fluid analysis of the process in details, after a brief review of the literature, the following formulation presented by Grucijic *et al.* [9, 10] has been chosen in order to obtain an estimation of the impact velocity. Gas dynamic of the cold spray flow, presented by Dykhuizen and Smith [11], assumed that the gas flow conditions can be calculated without consideration of feedback from the powders flux. In the formulation, it is also assumed that the gas flow is isentropic (adiabatic and frictionless) and can be approximated as a perfect gas with constant specified heat [11]. By considering the latter assumptions, the gas flow equation can be obtained from classical texts on fluid flow [12]. The process gas flow is assumed to originate form a large chamber or duct where the pressure is equal to stagnation pressure (P_0) and the temperature is the total temperature (T_0) [11]. Eq. 5.2 measures the gas temperature, gas velocity, and mass balance at the throat; it should be considered that the ratio of specific heat, γ, for mono-atomic gases is 1.66 and for diatomic gases is 1.4. R is the specific gas constant (the universal constant divided by the gas molecular weight) [11].

$$\frac{T_0}{T^*} = 1 + \frac{\gamma - 1}{2}$$

$$V^* = \sqrt{\gamma R T^*}$$

$$\rho^* = \frac{\dot{m}}{V^* A^*}$$

$$P^* = \rho^* R T^* \tag{5.2}$$

Knowing the dimension of the nozzle, the exit Mach number Eq.5.3 of the gas can be obtained from the following isentropic relationships (Eq.5.5) [11]:

$$\frac{A}{A^*} = \left(\frac{1}{M}\right)\left[\left(\frac{2}{\gamma+1}\right)\left(1 + \frac{\gamma-1}{2}M^2\right)\right]^{(\gamma+1)/[2(\gamma-1)]} \tag{5.3}$$

The Mach number of the gas (Eq.5.3) can be estimated by Eq. 5.4 [9]; this equation provides a numerical estimation of Eq. 5.3:

$$M = \left[k_1 \frac{A}{A^*} + (1 - k_1)\right]^{k_2}$$

$$k_1 = 218.0629 - 243.5764\gamma + 71.7925\gamma^2$$

$$k_2 = -0.122450 + 0.28130\gamma \tag{5.4}$$

The properties of the gas at the exit of the nozzle after estimation of M can be calculated through Eq.5.5

$$\frac{T_0}{T_e} = 1 + \frac{\gamma - 1}{2}M^2$$

$$V_e = M\sqrt{\gamma R T_e},$$

$$\frac{\rho_0}{\rho_e} = \left(1 + \frac{\gamma - 1}{2}M^2\right)^{1/(\gamma-1)}$$

$$\rho_0 = \frac{P_0}{RT_0} \tag{5.5}$$

The acceleration of the particle velocity can be equated to the drag force on the particle (Eq.5.6) [11].

$$m\frac{dV_p}{dt} = mV_p\frac{dV_p}{dx} = \frac{C_D A_p \rho (V - V_p)^2}{2} \tag{5.6}$$

By assuming a constant velocity and density for the gas, Eq.5.6 can be integrated as Eq.5.7:

$$log\left(\frac{V - V_p}{V}\right) + \frac{V}{V - V_p} - 1 = \frac{C_D A_p \rho x}{2m} \tag{5.7}$$

The latter equation is also numerically estimated by Eq. 5.8 [9]. The following equations show a good correspondence with the analytical solutions presented in Eq. 5.7:

$$\left(\frac{V_p}{V}\right)_{18} = -e^{\sqrt{3\rho C_D x/\rho_p D_p}} + 1$$

$$\left(\frac{V_p}{V}\right)_{20} = -e^{-9\mu x/D_p^2 \rho_p V} + 1$$

$$\frac{V_p}{V} = 0.5\left(\frac{V_p}{V}\right)_{18} + 0.5\left(\frac{V_p}{V}\right)_{20} \tag{5.8}$$

The drag coefficient correlating equations for spherical particles used by Grujicic *et al.* [9] over a wide range of flow conditions as developed by Henderson [13], are presented in Eq. 5.9 for subsonic, supersonic with $M < 1.75$ and supersonic with $M > 1.75$:

Subsonic:

$$C_D = 24\left\{R_e + S\left[4.33 + \left(\frac{3.65 - 1.53T_p/T}{1 + 0.353T_p/T}\right) \times exp\left(-0.247\frac{R_e}{S}\right)\right]\right\}^{-1} + exp\left(\frac{-0.5M_r}{\sqrt{R_e}}\right)\left[\frac{4.5 + 0.38(0.03R_e + 0.48\sqrt{R_e})}{1 + 0.03R_e + 0.48\sqrt{R_e}} + 0.1M^2 + 0.2M^8\right] + \left[1 - exp\left(-\frac{M}{R_e}\right)\right]0.6S$$

Supersonic($1 < M < 1.75$):

$$C_D\left(M_\infty, R_{e_\infty}\right) = C_D(1.0, R_e) + \frac{4}{3}(M_\infty - 1.0) \times \left[C_D\left(1.75, R_{e_\infty}\right) - C_D\left(1.0, R_{e_\infty}\right)\right]$$

Supersonic($M > 1.75$):

$$C_D = \frac{0.9 + \frac{0.34}{M_\infty^2} + 1.86\left(\frac{M_\infty}{R_{e_\infty}}\right)^{1/2} \times \left[2 + \frac{2}{S_\infty^2} + \frac{1.058}{S_\infty}\left(\frac{T_P}{T}\right)^{1/2} - \frac{1}{S_\infty^4}\right]}{1 + 1.86\left(\frac{M_\infty}{R_{e_\infty}}\right)^{1/2}} \tag{5.9}$$

The latter equations, make the calculation really complex; on the other hand Grujicic *et al.* studied the value of the drag coefficient in the cold spray coating, the results of which are presented in Fig. 5.10. This figure shows that the variation of the drag coefficient from the **unity** is less than 3%. Finally, Grujicic *et al.* [9] presented the impact velocity (Eq. 5.10) in accordance with many previous experimental

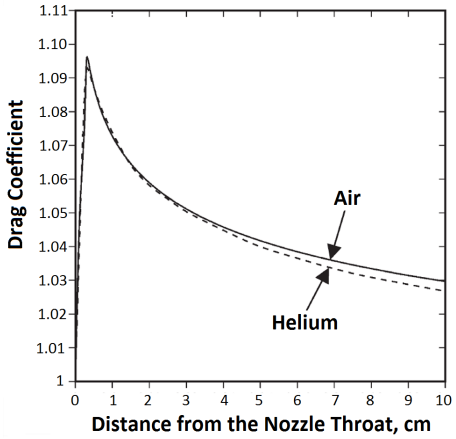

Figure 5.10: *Variations of drag coefficient along the nozzle's diverging section*

and computational analysis:

$$V_p^{impact} = V_p e^{-3L^{st}\rho^{st}/4\rho D_p}$$

$$\rho^{st} = R_e(-1.04 + 2.27M_e - 0.21M_e^2)$$

$$L^{st} = R_e(0.97 - 0.02M_e) \tag{5.10}$$

In which $R_e = \frac{\rho_g D_p |V - V_p|}{\mu_g}$ is the Reynold number based on the particle diameter and μ_g is the gas viscosity calculated by Sutherland's formula5.11 [14, 15].Tab. 5.1 shows the constant values in the Eq.5.11.

$$\mu = \mu_0 \left(\frac{a}{b}\right) \left(\frac{T}{T_0}\right)^{3/2}$$

$$a = 0.555T_0 + C, b = 0.555T + C \tag{5.11}$$

These equations have been used in order to estimate the velocity of the particles based on their diameter

Table 5.1: *Constant parameters in Sutherland equation [14]*

	Sutherland's Constant(C)	$T_0(^\circ R)$	μ_0(centipoise)
Standard air	120	524.07	0.01827
Nitrogen,N_2	111	540.99	0.01781

obtained from random distribution.

5.2.3 Particle temperature

5.2.3.1 Single particle model

Particle temperature is a function of particle velocity and diameter. The results for simulations by temperature variations for single particle impact are presented in Fig. 5.11. It is shown that by increasing the temperature, the peening stress remains the same till the particle temperature gets close to the melting point. A considerable decreasing is observed in both residual stress and plastic strain by increasing the

temperature from $700°K$ to $900°K$ which might be due to the material softening.

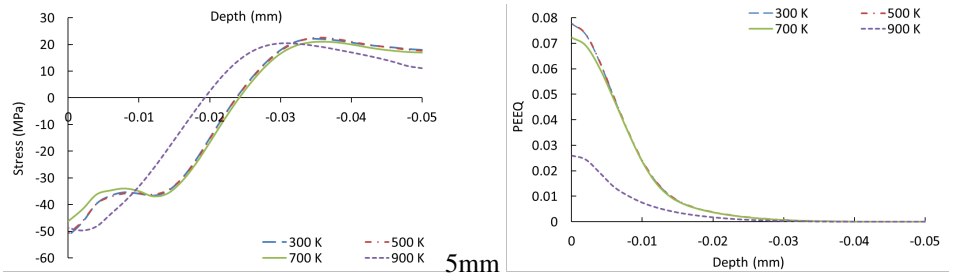

(a) *Residual stress* **(b)** *Equivalent plastic strain*

Figure 5.11: *Effect of the particle temperature on different physical parameters*

5.2.3.2 Particle temperature consideration

There are not many records of particle temperature at impact time; Grujicic *et al.* [10] showed that the particle temperature deviation in the process is negligible (less than $1°K$). On the other hand, Papyrin *et al.* [16] presented an analytical formulation for the particle temperature at the contact surface. Fig. 5.12 shows the dependency of the particle temperature at impact to velocity and diameter of the particles. The

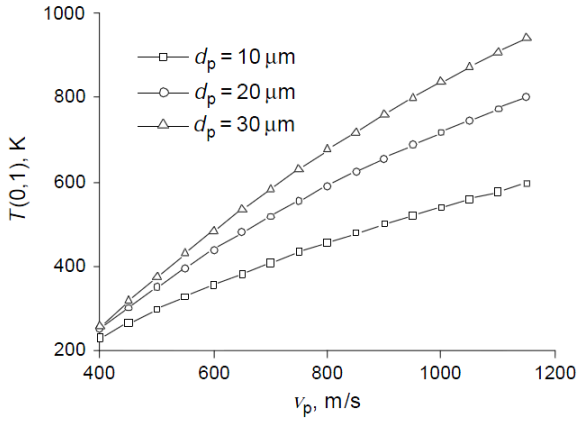

Figure 5.12: *Contact temperature at $t = t_c$ versus particle velocity [16]*

following formulation presented by Papyrin *et al.* has been used in order to estimate the temperature of the particles in the developed model [16, p.169]:

$$\rho_P v_P C_P \frac{dT_P}{dx} = Nu\frac{6k}{d_P^2}(T_0 - T_P) \Rightarrow T_P = T_0 + Cexp\left(Nu\frac{6k}{d_P^2}x/\rho_P v_P C_P\right)|_{@x=impactdist}$$

$$Nu = 2a + 0.459bRe^{0.55}Pr^{0.33}$$

$$a = exp(-M)(1 + 17M/Re)^{-1}, b = 0.666 + 0.333exp(-17M/Re) \tag{5.12}$$

where k stands for thermal conductivity, Re_P for the Reynolds number for particles, C_P for the heat capacity of the particles, $Pr = \frac{c_P \mu}{k}$ for the Prandtl number, c_P for the specific heat, and μ for the dynamic viscosity measured based on Eq. 5.11. It is assumed that the particle moves along the axis of the gas-dynamic path, ignoring the influence of particles on the gas, and considering two different

aspects: finding the gas parameters at the axis and finding the particle velocity and temperature from the known values of gas parameters. The constant C that appears in the equation of the Tp, is a result of solving the differential equation which depends on the initial temperature of the particles.

5.3 Numerical model

A numerical model has been develop in Abaqus/Explicit 6.9 [17], in order to simulate the multiple impact of the particles. The model is geometrically similar to the model presented in Chapter 4 by considering that this time the deformation and behavior of the substrate is the object of the simulation. The aim of the study is finding the residual stress and plastic deformation of the substrate after multiple impacts. As discussed in the previous section, the model should be able to consider different parameters of the process which are size, temperature, and velocity of the particles. On the other hand, the material model plays an important role in the results and the behavior of the substrate/particle; different material models have been used and the results have been compared with the experimental tests; based on the final comparison the combined isotropic kinematic hardening model [18] has been chosen for the substrate and the Johnson-Cook model [19] has been used for the powders. The results should be obtained in the same way which were obtained in the experimental measurements. Fig. 5.13a and Fig. 5.13b show different views of the model developed in Abaqus. In this Figures, the arrangement and the size of the particles have been presented with respect to the red circle which represents the impact zone. The results in the impact zone have been elaborated to obtain the final data. The elaborating process will be explained in detail later in this section.

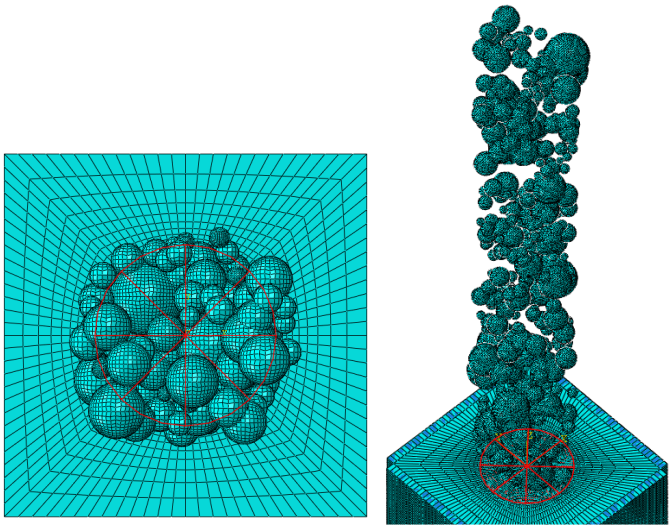

(a) *FEM model from top view* **(b)** *FEM model from isometric view*

Figure 5.13: *An example of developed model for residual stress calculations; the red area represents the "impact-zone"*

5.3.1 Obtaining the results

The profile of the residual stresses induced by the particles' impact in the substrate, obtained from the numerical simulation has to be compared with the experimental measurements in order to verify the whole numerical approach and assumptions. The experimental measurement of the stress is executed by XRD which will be explained in detail in Chapter. 6. Briefly, in the XRD measurement is performed on a set of grains under the collimator of the device and the average value of all measurements is presented as the

final result. In this regard, as considered by Bagherifard *et al.* [20], the final result of the numerical simulation has to be the average value in the area equal to the one affected by X-ray during the measurement. In the case of cold spray coating, due to the small size of the particles, to obtain at least a 100% coverage of the powders on the impact area, the number of particles for the simulation would be roughly more than 1000 which is numerically, not impossible, but extremely expensive; considering that in experiment the applied coverage is more than 600%. Therefore, in this regard by assuming that the average value over $1/10$ of the X-ray affected area would present the average of the whole area, the number of impacts has been reduced to around 30-40 particles in order to simulate 100% coverage. In the next section the average of the results in one layer has been presented in Fig. 5.16. Thus the averaging process for each layer of the elements, makes the final profile of the residual stress in the depth of the model; in the case of plastic strain the very same approach has been applied. The averaging process has been performed by developing a Python [21] code presented in Appendix B. The Python code extracts all the data from the model in a circular area with a diameter of 1/10 of the XRD collimator which in this case is 0.1 mm, and calculates the final average value of the measured parameters.

5.3.2 Process implementation

In order to implement the discussed method, a Python code based on the flowchart presented in Fig. 5.14 has been developed; the flowchart is explained in the following algorithm:

1. The first step starts from the point that the Rosin-Rammler model fitted to the particles' distribution and its parameters, Q, D_{rr}, are determined. The interface of the software will ask about these parameters and also the initial pressure and temperature of the process.
2. The other important parameter is the number of the particles which in this case has been approximately estimated by considering the thickness of the coating and compression ratio of a single shot. The following process will be repeated in a loop based on the number of the particles:
    - A random number should be chosen based on the Rosin-Rammler model; however, it is not possible to choose this number directly through Python; indeed by using the inverse function of CDF, it is possible to get a random number in uniform distribution and convert it to any distribution. A graph presented in Fig. 5.14 shows the process of getting a random number in other distributions, in this case Rosin-Rammler.
    - Velocity and temperature of the particles will be calculated based on the D_P obtained in the previous session.
    - In order to position the particles, two random numbers have to be obtained. These random numbers should be in a circle with the radius of R. So, they have to follow the relation mentioned in the flowchart.
    - Another random number has to be created for the vertical distance levels to which the particles would be divided. There is a limit for this number in order to reduce the calculation time. The time of the simulation is calculated based on the levels number and the velocity of each particle, considering the maximum time as the total simulation duration.
3. The time needed for solving the model, of course, depends on the number of particles and their vertical level. Considering a PC with four CPUs 2.53 GHz, takes almost 5 hours to finish each example simulation.
4. the results should be obtained by the method mentioned previously regarding the average value in each depth.

5.4 Results of multi-impact model

In-plane residual stress and equivalent plastic strain have been studied after solving the five different models. The substrate deformation after multiple impacts has been shown in Fig. 5.15. The results

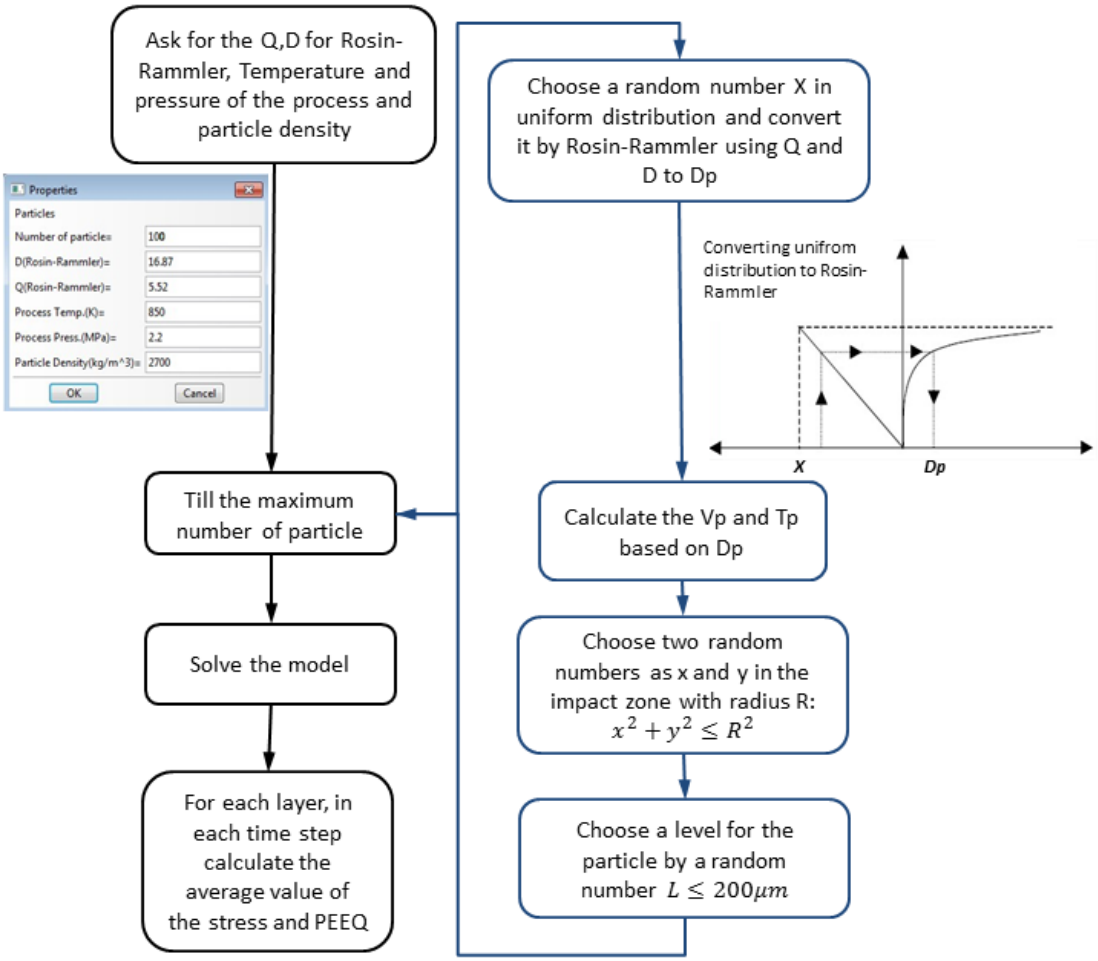

Figure 5.14: *Flowchart of the Python code, considering the modeling and simulation steps*

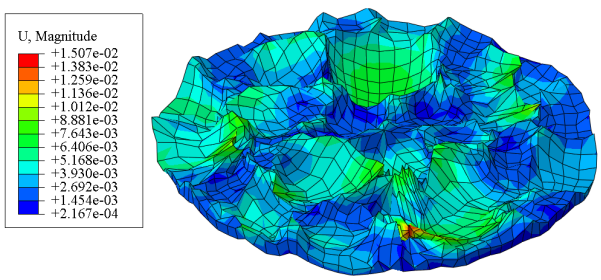

Figure 5.15: *Deformation of the impact zone obtained from the numerical simulation*

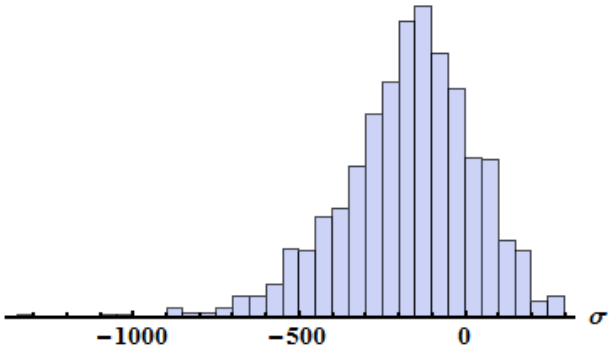

Figure 5.16: *Distribution of the stress on the surface of the model*

present the severe deformation of the substrate surface due to the particles' impact. As it has been mentioned, the results are obtained through calculation of the needed physical parameters' average in different depths of the model. Fig. 5.16 shows the histogram of the stress in one of the developed models. In this case, the average value of the presented data is -170 MPa which has been assumed as the final result on the surface. In the evolution of the residual stress shown in Fig. 5.17, it can be observed that residual stress maximum value and also its depth, vary by adding the number of particles in the model. To have a better perspective of the effect of multiple impacts on the results, in terms of both

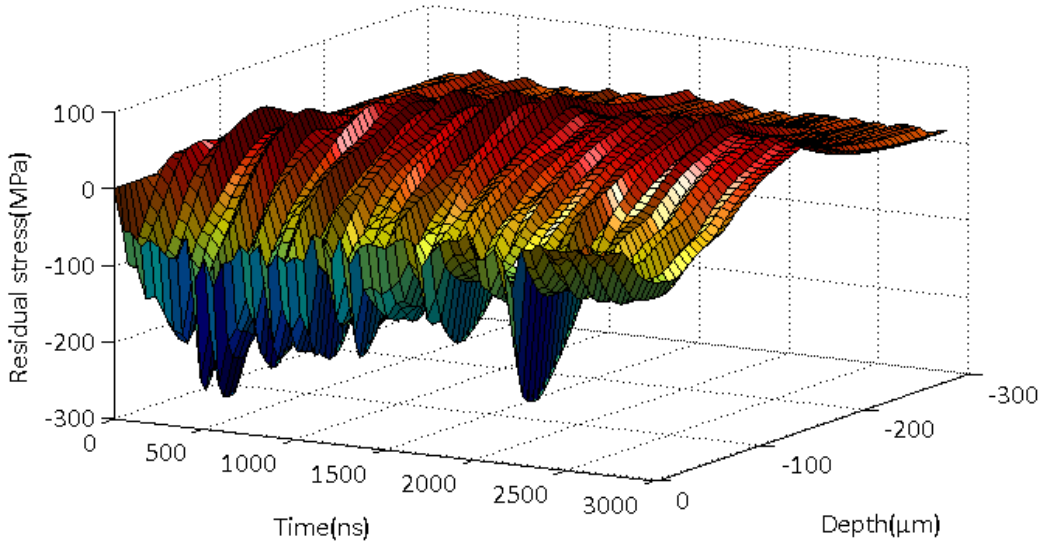

Figure 5.17: *Evolution of the residual stress with respect to time and depth*

residual stress and equivalent plastic strain, two parameters have been studied through time: first, the depth of the compressive residual stress and in the case of the plastic strain the depth of the deformation diffusion; second, the maximum value obtained in both stress and strain after impact in each time step. From the results presented in Fig. reffig:stressanddepthwithtime and Fig. 5.18b the following items can be concluded:

- after the first impacts, the maximum residual stress increases and then it starts decreasing till it reaches a saturated value. As it can be clearly noted, this parameter shows considerable variations. It is also to be mentioned that the black line fitted to the data can not show the saturated value after

the impact.

- equivalent plastic strain shows an exponential behavior, after a while its rate is decreased and is somehow saturated to a final value similar to the residual stresses.
- in the case of the depth for both residual stress and plastic strain, almost the same trend with different rates has been observed. It seems that by increasing the number of particles the final results for the depth will not show considerable changes.

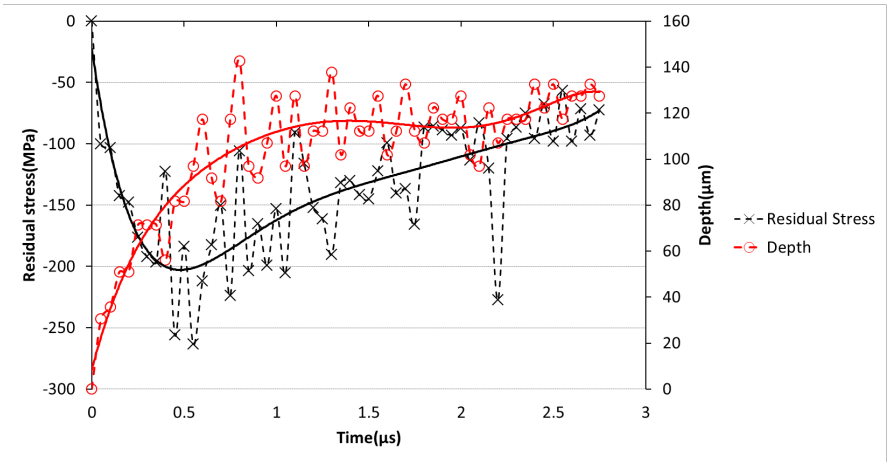

(a) *Residual stress*

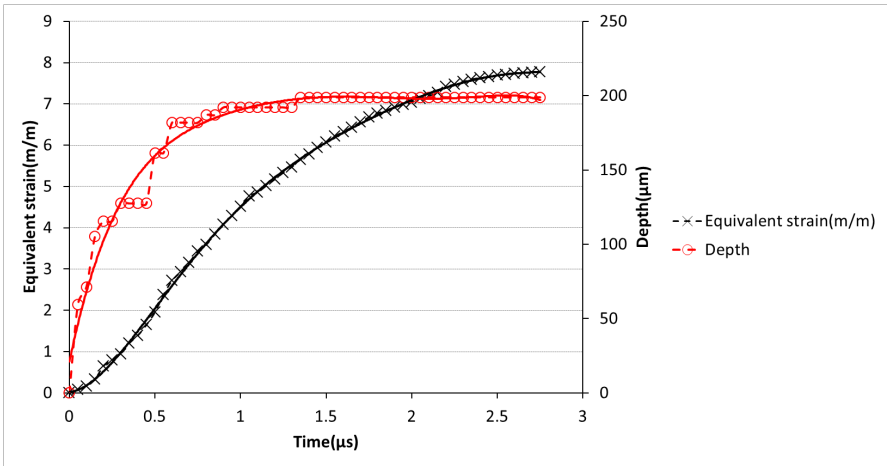

(b) *Equivalent plastic strain*

Figure 5.18: *Evolution of the depth and the maximum value of residual stress and plastic strain*

The final result, after simulation of different models, has to be obtained by considering the average value of all the models. Fig. 5.19a shows the average value of the final results, in which the red line represents the average value and the two dashed red lines refer to the variation of the results in different models. The black lines show different XRD measurements on the samples; in this case the dashed line shows the range and solid black line shows the average final value of the experimental measurements. As it can be observed, the numerical results cannot predict the profile of the residual stress but the maximum compressive stress is correctly estimated. Fig. 5.19b shows the average value for equivalent plastic strain, the two blue and red dashed lines refer to the criteria presented by Umemoto *et al.* [22] and Valiev *et al.* [23] respectively for estimation of grain refinement. This figure predicts the change of the grain size on the substrate after coating; this issue will be studied experimentally in the next chapters.

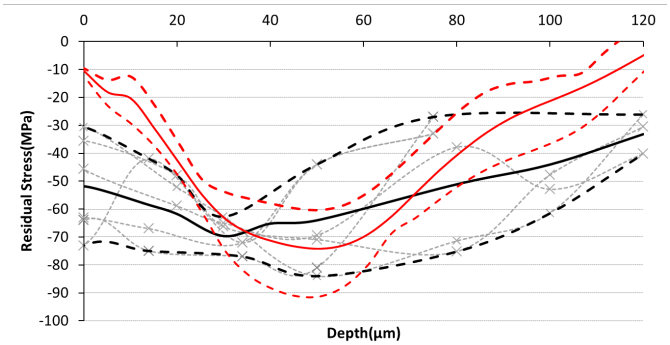

(a) *Residual stress (red line refers to numerical and black line represents the experimental results; dashed lines are the margin for both numerical and experimental variations)*

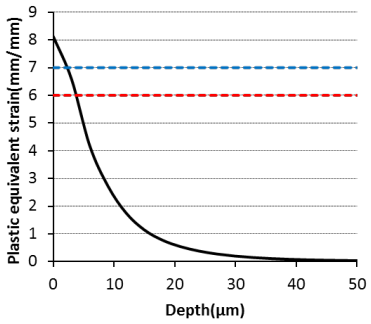

(b) *Equivalent plastic strain (Blue line shows the limit of SPD suggested by Umemoto et al. [22] and the red one represents the Valiev criteria [23]*

Figure 5.19: *The final results of the numerical models*

5.5 Conclusion

A numerical method based on FEM analysis has been presented in order to estimate the peening effect of coating on the substrate. The developed model considers the randomness of the particles both in terms of size and impact position. For particle size distribution, SEM is used to have a microscopic view of particles. Rosin-Rammler distribution is fitted to the results obtained from SEM observation. Particle velocity and temperature upon impact, which are both functions of the particles' size, have been estimated by the numerical models presented in the literature. The results are obtained based on an average value of the physical parameters on each element layer of the model. The statistical overview of each step has been presented in order to prove the points of using the average value for the final results. Due to using random numbers for particles' size and impact position distribution, it is necessary to solve different models in order to study the effect of randomness on final results. In this regard, the randomness shows a great effect on residual stress profile but almost no effect on equivalent residual strain. Comparison of the numerical results with experiment, does not show a good correspondence in the residual stress profile; however the maximum stress estimated by numerical simulation is in the range of the experimental measurements. It is to be underlined that high dispersion is observed also in the experimental measurements, as presented in Chapter 6. The accumulated plastic deformation fulfills the criteria for generation of nanocrystalline on the surface; this hypothesis will be studied experimentally in more details in the next chapter.

Bibliography

[1] K. Taylor, B. Jodoin, J. Karov, and P. Richer, "Particle loading effect in cold spray," in *Proceeding of the International Thermal Spray Conference,May 2-4, Basel, Switzerland*, 2005.

[2] R. C. McCune, W. T. Donlon, O. O. Popoola, and E. L. Cartwright, "Characterization of copper layers produced by cold gas-dynamic spraying," *Journal of Thermal Spray Technology*, vol. 9, pp. 73–82, 2000.

[3] S. Bagherifard, I. F. Pariente, R. Ghelichi, M. Guagliano, and S. Vezzù, "Effect of shot peening on residual stresses and surface work-hardening in cold sprayed coatings," *Key Engineering Materials*, vol. 417, pp. 397–400, 2010.

[4] P. Rosin and E. Rammler, "The laws governing the fineness of powdered coal," *Journal of the Institute of Fuel*, vol. 7, pp. 29–36, 1933.

[5] T. Allen, *Powder sampling and particle size determination*. Elsevier, USA, 2003.

[6] C. J. Li, W. Y. Li, and H. Liao, "Examination of the critical velocity for deposition of particles in cold spraying," *Journal of Thermal Spray Technology*, vol. 15, pp. 212–222, 2006.

[7] K. N. Ramakrishnan, "Modified rosin rammler equation for describing particle size distribution of milled powders," *Journal of Materials Science letters*, vol. 19, pp. 1903–1906, 2000.

[8] V. Champagne, *The cold spray materials deposition process, Fundamentals and application*. Woodhead Publishing, 2007.

[9] M. Grujicic, C. L. Zhaoa, C. Tonga, W. S. DeRosset, and D. Helfritch, "Analysis of the impact velocity of powder particles in the cold-gas dynamic-spray process," *Materials Science and Engineering*, vol. 368, pp. 222–230, 2004.

[10] M. Grujicic, W. S. DeRosset, and D. Helfritch, "Flow analysis and nozzle-shape optimization for the cold-gas dynamic-spray process," *Journal of Engineering Manufacture*, vol. 217, 2003.

[11] R. C. Dykhuizen and M. F. Smith, "Gas dynamic principles of cold spray," *Journal of Thermal Spray Technology*, vol. 7, pp. 205–212, 1998.

[12] A. H. Shapiro, *the dynamic and thermodynamics of compressible fluid flow*. Ronald Pres, 1953.

[13] C. B. Henderson, "Drag coefficient of spheres in continuum and rarefied flows," *AIAA J.*, vol. 14, pp. 707–708, 1976.

[14] C. Robert, ed., *CRC Handbook of Chemistry and Physics*. CRC Press, 1984.

[15] *Flow of fluids through valves, fittings, and pipe*. Crane Company, 1988.

[16] A. Papyrin, V. Kosarev, S. Klinkov, A. Alkhimov, and V. Fomin, *Cold Spray Technology*. Elsevier, 2006.

[17] D. Hibbitt, B. Karlsson, and P. Soerensen, "Abaqus/explicit 6.9-1 manual," 2002.

[18] J. Lemaitre and J. L. Chaboche, *Mechanics of Solid Materials*. Cambridge University Press, 1994.

[19] G. R. Johnson and W. H. Cook, "A constitutive model and data for metals subjected to large strain, high strain rates and high temperature," *Proceedings of the 7th International Symposium on Ballistics*, vol. 4, pp. 541–547, 1983.

[20] S. Bagherifard, R. Ghelichi, and M. Guagliano, "A numerical model of severe shot peening (ssp) to predict the generation of a nanostructured surface layer of material," *Surface and Coating Technology*, vol. 204, pp. 4081–4090, 2010.

[21] "Python documentation." http://docs.python.org/.

[22] M. Umemoto, Y. Todaka, and K. Tsuchiya, "Formation of nanocrystalline structure in steels by air blast shot peening," *Materials Transactions*, vol. 44, pp. 1488–1493, 2003.

[23] R. Valiev, "Nanostructuring of metals by severe plastic deformation for advanced properties," *Nature Materials*, vol. 3, pp. 511–516, 2004.

Part III

Experimental analysis

Chapter 6

Microstructural analysis and coating characterization

6.1 Introduction

The numerical simulations helped to have a better understanding of the coating phenomenon; however, the simulation alone is not enough to study the effect of coating on the structure. Microstructural analysis of the specimens open new windows to interpret the physical background of different phenomena. There are many different experimental tests and techniques which nowadays are being used for studying the microstructure of materials. Some of them have been briefly reviewed in Chapter 1; X-Ray diffraction (XRD), scanning electron microscopy (SEM) and micro-hardness measurements are the most used techniques in this work. SEM observations permit to characterize heterogeneous organic and inorganic materials on a nanometer (nm) to micrometer (μm) scale. The popularity of the SEM, stems from its capability of obtaining three-dimensional-like images of the surfaces of a very wide range of materials. These images are used in a wide variety of media from scientific journals to popular magazines and even the movies. Although the major use of the SEM is to obtain topographic images in the magnification range of 10-10000$\times$, it is much more versatile. The area to be examined or the micro-volume to be analyzed in the SEM, is irradiated with a finely focused electron beam which may be swept in a raster across the surface of the specimen to form images or may be static to obtain an analysis at one position. The types of signals produced from the interaction of the electron beam with the sample include secondary electrons, backscattered electrons, characteristic x-rays, and other photons of various energies. The imaging signals of greatest interest are the secondary and backscattered electrons because these vary primarily as a result of differences in surface topography. The secondary electron emission, confined to a very small volume near the beam impact area for certain choices of the beam energy, permits images to be obtained at a resolution approximating the size of the focused electron beam. The three-dimensional appearance of the images is due to the large depth of the scanning electron microscope field as well as to the shadow relief effect of the secondary and backscattered electron contrast [1]. On the other hand, XRD is a powerful tool for measuring, that is currently in wide spread use in different engineering fields. In many cases, XRD is the only technique when accurate, fast, high spatial resolution and non-destructive analysis is required. XRD techniques can be generally used to provide quantitative data required to [2]:

- identify and quantify residual stresses and their associated gradient in the component;
- determine fatigue strength and damage tolerance;
- optimize and validate processes that may be life enhancing;
- monitor processes and product quality on an on-going basis;
- help validate and enhance failure analysis;
- quantify and track the stress state of a component through its life cycle;

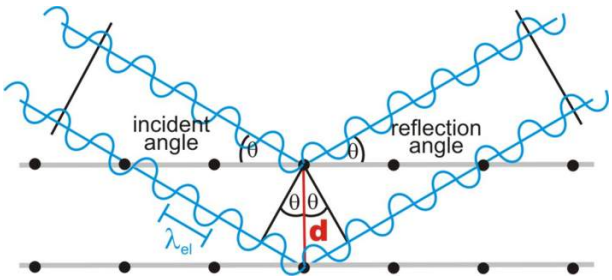

Figure 6.1: *Wave deflection after impact of the atomic layers and Brag-Law parameters [4]*

- crystallography and grain size measurement;

In peening based processes such as cold spray coating, XRD can be used to verify component integrity at each step and to provide a more complete characterization of the process and its effects on fatigue resistance. Besides, XRD measurement can help establish and control precise process parameters as well as track residual stress variations in fabrication processes and those due to in-service use. XRD has been used for both residual stress measurement and grain size estimation. In the case of grain size measurement, additional elaboration of the data is needed in order to estimate the grain size of the structure. In this chapter, the method used for crystallography of the structure has been explained with more details. The XRD grain size measurement approach has also been described. After calibrating the method with other measuring techniques such as transmission electron microscopy (TEM), it has been applied to the differently treated specimens in order to verify the existence of the nanostructure on the samples' surface. In the second part of this chapter, the coating parameters and SEM observations of the treated samples are presented.

6.2 XRD measurements

XRD technique is used to determine the distance between crystallographic planes (d-spacing); thus its application is limited to crystalline, poly-crystalline and semi-crystalline materials. When a material is in tension, the d-spacing increases and when a material is in compression the d-spacing decreases [2]. Measurements by X-rays is based on the so-called Bragg reflection in which an incident X-ray beam is reflected at several atomic layers; the presence of residual stresses produces a shift in the X-ray diffraction peak angular position that is directly measured by the detector [3]. Using a special anode material (normally chromium for steel) and a filtering system, it is possible to know exactly the wavelength of the X-rays. Once the wavelength of the X-rays and the angle are known in the Bragg's law: $\lambda = 2d\sin(\theta)$, the d-spacing between the atomic layers can be calculated (Fig.6.1). In a special case when the incident angle and reflected angle are the same with respect to the surface, since the atomic layers are parallel to the surface (orientation angle$\psi = 0°$), the orientation angle ψ of the atomic layers should be varied by beaming in another direction on the surface of the component, the beam will be reflected at other orientated layers. The distance d_0 of an atomic lattice without stress and the related angle θ_0 are well-known. Thus knowing d and $d\theta$, the strain can be calculated using $\Delta d/d\theta$. If d_0 is not known, the value of d obtained from the first measurement ($\psi = 0°$) can be used instead of d_0 without substantial error on the residual stress result. For the $sin2\theta$ method, where a number of d-spacings are measured, stresses are calculated from an equation derived from Hooke's law for isotropic, homogeneous, fine grained materials [2]. X-rays are reflected within a thin layer of around 10 μm in the component and the area of the measurements lies between 1 mm^2 and 50 mm^2 [5]. For performing XRD measurement on surface treated specimens, special cares shall be taken. The surface of treated component normally has a quite high roughness. The measured layers by diffractometer have a typical thickness of around 10 μm, which depends on different wavelengths of X-rays (or in other words the material of the anode). The intensity of the X-ray beam drops exponentially with depth. That means the residual stresses in layers at or near the surface determine the result, because the detector averages over all reflection not considering the intensity. The surface roughness structure of for example a shot peened component is sometimes

as big as or bigger than the thickness of the used atomic layers for determining the residual stress; as a consequence, the surface structure and the orientation angle of the incident beam have a considerable influence on the results [5]. In this study to characterize the state of residual stresses, XRD analysis of surface layer in the treated specimens was performed using an AST X-Stress 3000 XRD (radiation Cr Kα, irradiated area 1 mm^2, $\sin(2\Psi)$ method, diffraction angles (2θ) scanned between $-45°$ and $45°$). Measurements have been carried out step by step removing a very thin layer of material, using an electro-polishing device in order to obtain the in-depth trend of residual stresses. For material removal a solution of acetic acid (94%) and perchloric acid (6%) has been used in case of Al specimens. The results of the in-depth residual stress measurements were corrected by using the method described by Moore and Evans [6].
The residual stress trend along with another parameter measured by XRD that is full width half maximum (FWHM), are shown in Fig.6.2a. FWHM represents the full width of the diffraction peak at half of the maximum intensity, measured directly by the software of the test machine [7]. It is a factor related to the surface state of the material and characterizes grain size and internal strain of the crystals. It is also measured as an index of hardening. The other important parameter which can be extracted from the XRD measurement is the integral breadth of the diffraction pattern shown in Fig.6.2b.
The diffraction pattern has been used also for grain size estimation of the structure. In this chapter

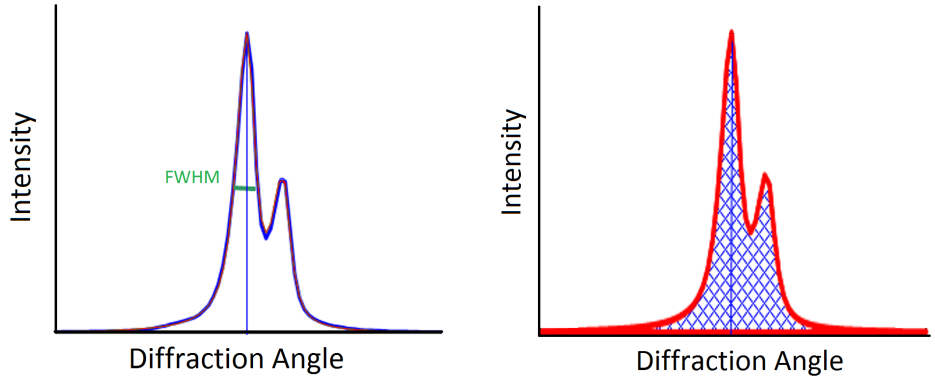

(a) *Full Width Half Maximum(FWHM)* **(b)** *Integral Breadth*

Figure 6.2: *The important parameters of the diffraction curve*

the mathematical method used for grain size measurement along with its experimental validation are presented; this grain size measurement method has been applied to different treated samples in order to verify the generation of the nanograins on their surface.

6.3 Grain size measurement

Grain size strongly affects many important properties of metals and their alloys. It is also known that grain size is one of the factors affecting fatigue strength of metals [8]. More in general, grain size affects the ability of a material to resist the damage phenomena that can lead to premature, cost-demanding and dangerous failures. Anyway, assessment of the results of these processes and effective grain size determination is not an easy task and requires complex and expensive experimental analysis. For instance, TEM or high resolution XRD are needed, thus requiring a non negligible effort in terms of time and resources. Indeed accurate determination of crystallite size and micro-strains by XRD, that is based on line broadening analysis, is a quite complicated process which requires precise and detailed modeling of Bragg reflections [9, 10]. It has to be mentioned that the value measured for the grain size by XRD diffraction is the mean value of the cubic root of the grain volume; thus considering the latter expression, grains with the average volume of less than 100 nm, should at least in one direction have a dimension of less that 100 nm. In situ XRD units normally provide high resolution multiple reflection patterns which can be elaborated by grain size measurement methods available in the literature. These methods allow

a detailed and accurate analysis of imperfections; yet their use is justified if the data are of high quality and the required expertise and computing facilities are available to analyze the data. However many applications are not worth the costs in terms of time and effort required by such analysis. On the other hand, portable XRD units, ever more used for the possibility to perform measurements on large size components, are basically adopted for residual stress measurements and offer just a medium resolution reflection available at a limited angle range and prevent the observation of more than one or two diffraction peaks for most of the material of technological interest. Among the most often used approaches in estimating the grain size and lattice micro-strains from the XRD data, there are methods based on the Scherrer formula [11] and the Stokes and Wilson formula [11, 12]. The Scherrer formula can be used to evaluate the crystallite size directly if there is no lattice micro-strain [11]. Similarly, the Stokes and Wilson formula can be utilized to determine the lattice micro-strain if the crystallite size is sufficiently large (> 1000 nm) [11,12]. In cases where broadening is due to both fine crystallites and lattice micro-strains, utilization of both mentioned methods can be misleading [13]. The common measures of dispersion already used in early studies of diffraction broadening, have been the width of the line profile at half the maximum intensity (FWHM) and the integral breadth, that is the integrated intensity divided by the maximum intensity (in other words it is the width of the rectangle having the same area and height as the observed peak profile [10]). In order to use the FWHM and integral breadth (Fig.6.2), an analytical function shall be assigned to the diffraction line profile. The earliest functions to be used and still employed are Cauchy and Gaussian functions. Early works assume that both lattice micro-strains and nanograins induce Cauchy broadenings, or imply the assumption of Gaussian broadenings produced by both lattice micro-strains and nanograins [11, 14]. However it is now accepted that if the wavelength spectrum consists of a single line and geometrical effects are small, the grain refinement induces Cauchy broadening; whereas the profile arising from lattice strain is more nearly Gaussian [11, 15]. There are some theoretical justifications for this assumption and experimental evidence has also been reported [16, 17]. It was demonstrated by van de Hulst and Reesinck [18] that a closer approximation is given by the convolution of these curves, namely the Voigt function [19]. Langford [15] subsequently derived an explicit equation for the Voigt function and showed that the breadths of the Cauchy and Gaussian components can easily be found from the ratio of the FWHM of the broadened profile to its integral breadth. In this study the single XRD profile obtained from a portable X-ray diffractometer has been elaborated using the Voigt function following the single line analysis method developed by De Keijser *et al.* [20,21]; it has been demonstrated that at the expense of some loss of accuracy, it is possible to perform the grain size measurement using the data obtained from portable diffractometer, based on this rapid technique which is simple to apply. The method has been also applied to measure the grain size on specimens which have been surface nanocrystallized via severe shot peening [22]. Performing a series of measurements considering different parameters, it was possible to determine the best measurement conditions to assess the grain size. The results obtained from this single peak analysis showed good agreement with those derived using an in situ high energy synchrotron XRD and also TEM observations performed on the same set of specimens [22].
The applied method is based on representing the experimental data by a Voigt function that is a convolution of Cauchy (Lorenzian) and Gaussian functions which are generally used in diffraction profile analysis. This method provides the possibility of using portable X-ray diffraction units for breadth interpretation of diffraction line profiles. This approach was applied to a surface nanocrystallized Al 7075 specimen and the results showed good agreement with the measurements performed by other techniques including in situ X-ray diffraction and TEM.

6.3.1 The method of Voigt function

The Voigt profile is a line profile resulting from the convolution of two broadening mechanisms, one of which would produce a Gaussian profile and the other would produce a Cauchy (Lorentzian) profile. The Voigt function is usually represented following [15], where $I_c(x)$ and $I_g(x)$ represent Cauchy and Gaussian function respectively:

$$I(x) = \int_{-\infty}^{+\infty} I_c(u) I_g(x-u) du \tag{6.1}$$

The measured line profile h is considered as the convolution of the standard profile g with the structurally broadened profile f which along with g are assumed to be Voigt functions; so, they are presented as the convolution of Cauchy and Gaussian functions. Accordingly:

$$h_C = g_C * f_C, g_G = g_G * f_G \tag{6.2}$$

where subscripts *C* and *G* stand for the Cauchy and Gaussian components of the corresponding profiles [20]. According to Eq. 6.2 the integral breadth of f_c and f_G are given by:

$$\beta_C^f = \beta_C^h + \beta_C^g, \left(\beta_G^f\right)^2 = (\beta_G^g)^2 + (\beta_G^g)^2 \tag{6.3}$$

The Cauchy and Gaussian components can be obtained from the ratio $2\omega/\beta$ for the *h* and *g* profiles [20]. The details of the calculation process can be found in [15]. To avoid complicated calculations and graphical methods, the procedure was presented by the following empirical formulae that can be straight forwardly handled without any computational costs and complexity [20].

$$\beta_C/\beta = a_0 + a_1\phi + a_2\phi$$

$$\beta G/\beta = b_0 + b\phi + b_{12}(\phi - 2/\pi)^{1/2} + b_1\phi + b_2\phi^2 \tag{6.4}$$

where $\phi = 2\omega/\beta, a_0 = 2.0207, a_1 = -0.4803, a_2 = -1.7756, b_0 = 0.4620, b_{12} = 1.4187, b_1 = -2.2043, b_2 = 1.8706$.
It is also mentioned that the maximum error introduced by using the latter equations is about 1%, and in the majority of the cases the error is very much less than this [20]. In order to separate size and strain effects, it is necessary to assume that the size and strain profiles have a particular form. As it was noted by Langford [15] they can be taken as Voigtian and, if two or more reflections are available, size and strain effects can be determined from the variation of β_C^f and β_G^f with *hkl*. However, in a single-line analysis it is assumed that the Cauchy component of the f profile is only due to crystallite size and that the Gaussian contribution arises from strain. In a single-line analysis the apparent crystallite or domain size D (the volume-weighed domain size in the direction parallel to the diffraction vector [21]) is given by:

$$D = \lambda/\beta_C^f \cos(\theta) \tag{6.5}$$

and strain *e* by

$$e = \beta_G^f/4\tan(\theta) \tag{6.6}$$

Where β is measured on a 2θ scale and if $K\alpha$ radiation is used, λ and θ are the wavelength and angular position of α_1 component [20]. It is stated that asymmetry of the functions can induce some errors; however serious errors only occur in the size and strain values when the asymmetry is large and the structural broadening is small [20]. In order to implement the latter method, a code has been developed in Matlab 2007 presented in Appendix. C.

6.4 Experimental verification

To obtain an accurate estimation of grain size, random errors shall be reduced by getting data of high quality thus regulating the exposure time to accumulate more counts and obtain good peak-to-background ratio. The exposure time is normally chosen based on the sharpness and shape of the diffraction peaks. For increasing the intensity of the peaks, it is recommended to increase the exposure time or to use larger diameter collimators [7]. The following practical criteria are suggested to verify the accuracy of the residual stress measurements, observing the peaks height on the relative scale [7]:

Table 6.1: *Typical mechanical characteristics of the considered Al specimens [23]*

σ_Y(MPa)	UTS(MPa)	E(GPa)	ν
503	572	71.7	0.33

- The maximum intensity of the peak shall be at least 20 points higher than the background noise.
- The ratio of the maximum intensity of the peak and the background noise shall be about 3, and not less than 2.
- The maximum intensity of the peak shall be between 60 and 100 points regarding the available type of XRD, stating that above this limit there will be no significant improvements, apparently in terms of stress measurements.

Accordingly a large diameter collimator and a quite long exposure time have been used in the XRD measurements aimed at grain size estimation. The diffractometer generally introduces instrumental broadening of the diffraction lines. Correction for instrumental effects shall be applied by using a specimen with null or negligible structural line broadening which helps in eliminating the instrumental broadening. A standard specimen for residual (macro) stress analysis is generally not suited for line broadening analysis, since it should not contain macro stresses, whereas it may contain micro stresses which anyway cause line broadening. Thus for line broadening analysis and grain size measurements a specimen not giving rise to any structural broadening that is a well annealed Al standard powder, has been used to obtain the standard profile. The specimen to be studied was an aluminium alloy (Al7075-T6) surface nanocrystallized by severe shot peening process [22]. Typical material characteristics of this alloy are presented in Tab. 6.6. A particular combination of peening parameters was applied in order to increase the kinetic energy of the shot impacts. A cross sectional view of the specimen which shows the presence of a distinct nanocrystallized region separated with sharp boundaries from the underlying layer is represented in Fig. 6.3. The underlying layer is the work hardened layer which is strongly deformed.

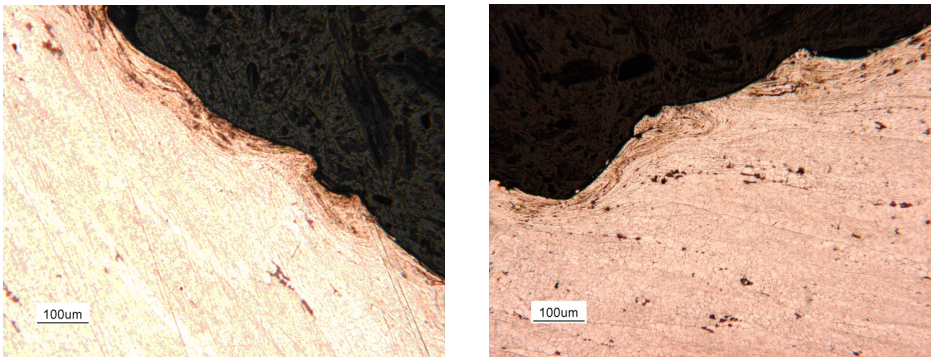

Figure 6.3: *Near surface layer optical microscopy observation of the Al specimenŠs section*

A flat specimen was selected for the measurements so that a 3 mm diameter collimator could be easily used. After trial and error procedure, the exposure time was also set on 400s, taking into account that for normal residual stress measurements performed on the same class of material, normally a 1 mm diameter collimator with an exposure time of 30s, results in a quite good quality peak and generally accurate results. The peaks profiles obtained from two different measurements performed by exposure time of 30s and 400s are compared in Fig. 6.4. It is clearly observed that peak resolution and peak height that is number of counts is considerably increased by increasing the exposure duration. XRD analysis on the surface layer of the as-treated specimen as well as the standard specimen was performed using an AST X-Stress 3000 XRD. $CrK\alpha$ radiation was used and 311 (Miller indices) line for normal diffraction ($\psi = 0$) was recorded. The wavelength is $\lambda = 0.2291$ nm and θ that is the angular position of $\alpha 1$ component, was set to $139°$. Using the peak fit possibility of the X-Stress software, a Pearson VII function

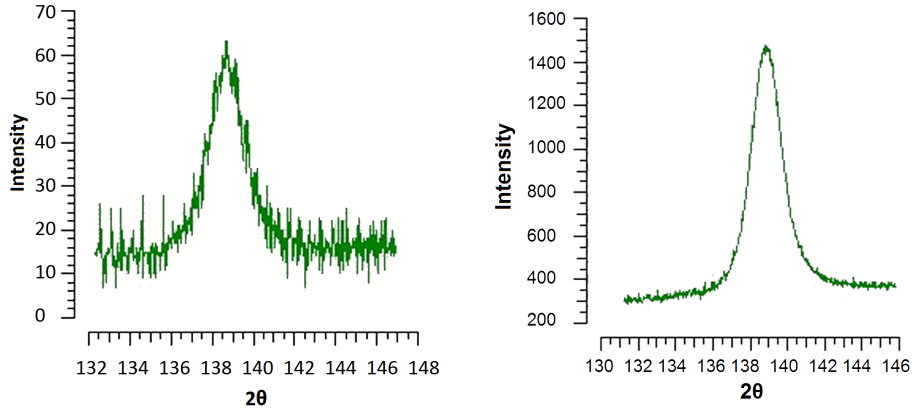

(a) *30s exposure* **(b)** *400s exposure*

Figure 6.4: *fig:Peak profiles obtained from measurement performed by (a) 30s exposure time (b) 400s exposure time*

Table 6.2: *Crystallite size and strain in Al specimen obtained from the single line Voigt analysis (311 line)*

	Standard specimen	Surface nanocrystallized specimen
ϕ	0.911	0.83597
β_C	0.0021809	0.884739
β_G	0.018555	1.73077
β_C^f	-	0.013261
β_G^f	-	0.023837
D (nm)	-	49.33
$e \times 10^3$	-	2.2281

was fitted to the obtained peak which made in possible to calculate the Integral breadth of the profile, both for standard and treated specimens. Pearson VII function shows better results with respect to other profile fittings [24]. Pearson VII presented in Eq. 6.7 needs four different constants $a_0 - a_4$ which have to be obtained by fitting the function to the results of XRD measurement.

$$Y = \frac{a_0}{\left[1 + 4\left(2^{1/a_3} - 1\right)\left(\frac{x - a_1}{a_2}\right)\right]^{a_3}} \tag{6.7}$$

Having obtained FWHM directly from the software, it is possible to calculate the strain and grain size value, using Eq. 6.4. Fig. 6.5 represents the software interface showing the peak profile and the fitted profile obtained from the measurement performed on Al specimen. The obtained results in terms of microstrain and grain size are presented in Tab. 6.2. It is possible to note that the resulting grain size is about 50 nm. In the same Table the broadening parameters of the Cauchy and Gaussian components of the line profile are shown. To assess the accuracy of the results obtained through elaborating the signal measured by the portable XRD, it was necessary to perform measurements with other well established grain size measurement techniques as in situ XRD and TEM. Also in these cases measurements were performed on the same surface nanocrystallized specimens for determining average grain size and the microstrain in the surface layer. Diffraction peaks of a Si internal standard sample were used as a reference, to represent the instrumental broadening. The experimental data were analyzed via MAUD program (Materials Analysis Using Diffraction) [25], through Rietveld procedure using isotropic size-

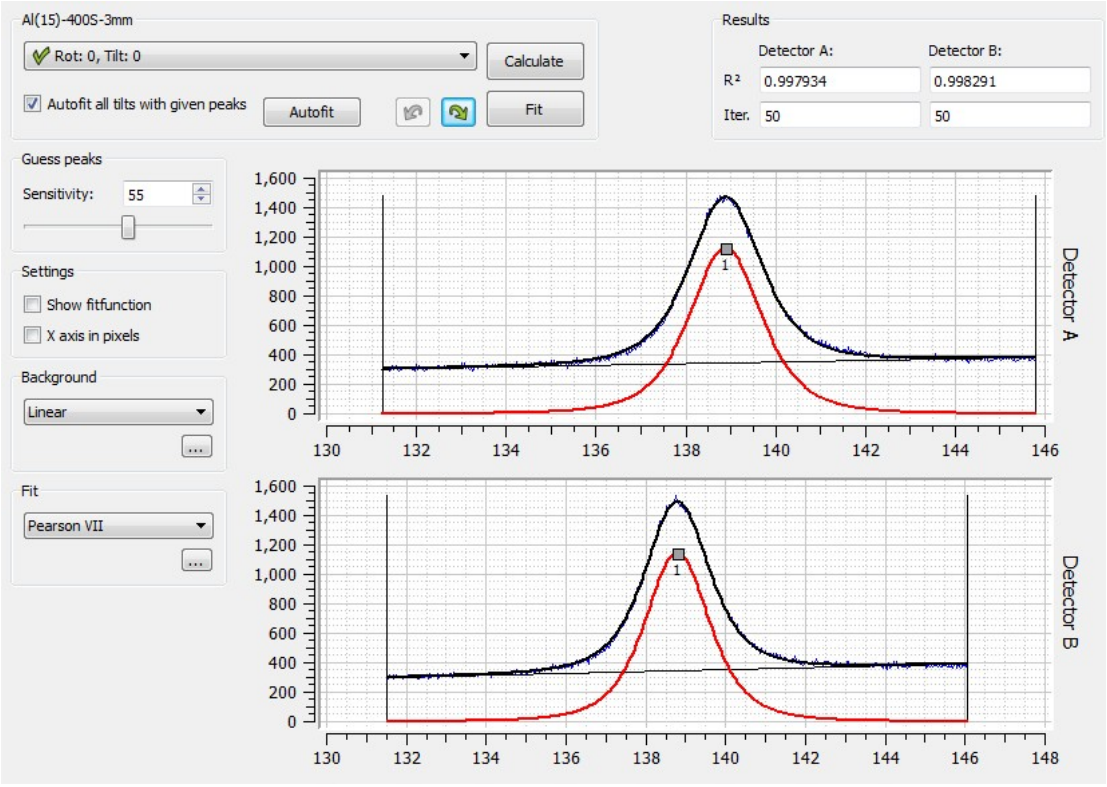

Figure 6.5: *Original and fitted peak profiles obtained for the surface nanocrystallized Al specimen*

Table 6.3: *Final comparison of the grain size and microstrain with different methods*

	Full angle diffraction	TEM	Portable machine
Grain size(nm)	53	50	**49.33**
Micro strain(m/m)	0.00233	-	**0.00222**

strain model [26]. The Rietveld method uses multiple reflections of experimental data and can determine structural and microstructural parameters (lattice parameters, atomic coordinates, thermal factors, crystallite size, microstrain and so on). For the top surface layer, evident broadening of Bragg diffraction peaks was seen owing to a grain refinement and increase in the atomic-level microstrain. Fig. 6.6 shows the obtained XRD patterns. The average grain size was found to be about 53 nm and the measured mean microstrain was 0.00233 (r.m.s.). The results show good agreement with the ones obtained by application of single line analysis. To perform TEM observations very thin pieces of specimens were first cut by electrical discharge machine (EDM), then were mechanically polished from the untreated side and finally the last step of thinning was performed by means of ion milling with proper incident angles. Fig. 6.7 shows TEM bright-field image and the corresponding selected area diffraction (SAD) pattern obtained at impacted surface of surface nanocrystallized Al specimen. The bright field image (Fig. 6.7a) represents irregularly shaped grains the average size of which is measured to be 50 nm. This mean size is close to the average grain size obtained from in situ XRD measurement as well as the single line profile analysis. The final comparison has been presented in Tab. 6.3

6.5 Cold spray coating parameters

In order to study the effect of coating on fatigue strength of coated components, test specimens have been prepared based on ASTM-B93 [27]. More details of the specimen characteristics will be presented

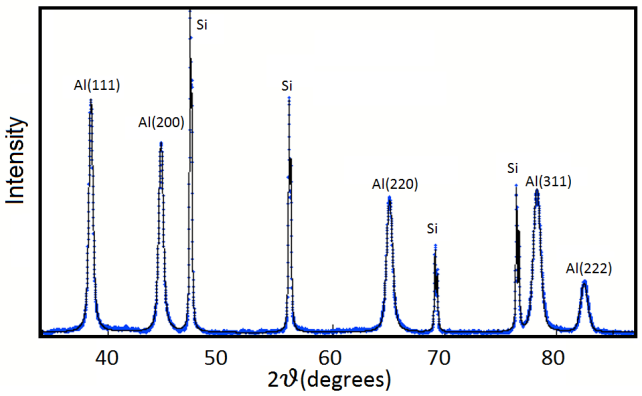

Figure 6.6: *X-ray diffraction patterns of the surface nanocrystallized Al specimen*

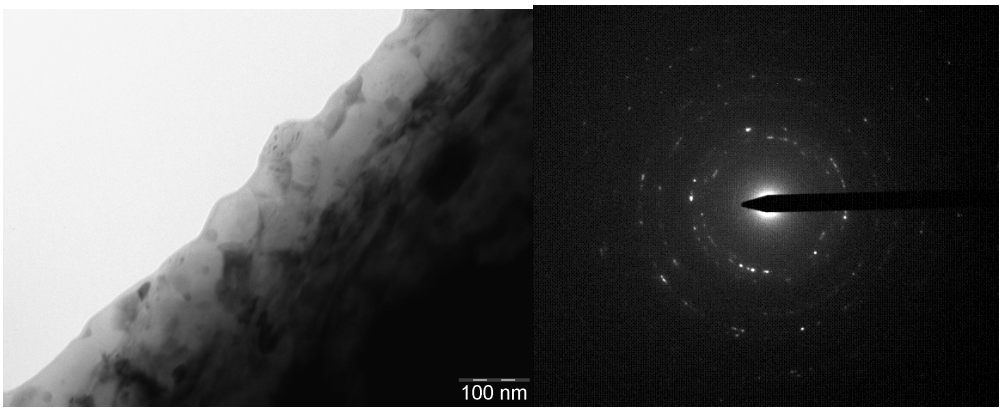

Figure 6.7: *Plane-view TEM observations and grain size distributions of specimen A a) bright-filed image of the impacted surface showing the formation of nanograins b) correspondent SAD pattern*

Table 6.4: *Operating parameter ranges of the stationary and portable systems [28, p.5]*

	High Pressure	Low pressure
Working gas	N_2, air, He	N_2, air, He
Has pressure (bar)	20-45	6-8
Gas preheat (°C)	20-800	30-550
Gas flow rate (m^3/h)	50-150	15-30
Nozzle exit Mach number	2-3	2-3
Powder flow rate (g/s)	0.1-1.0	0.06-0.1
Particle size (μm)	5-100	10-50

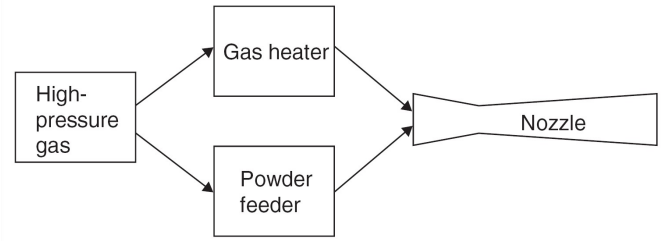

Figure 6.8: *Typical configuration of high pressure coating system [28, p.2]*

in the next Chapter. Al-5052 has been coated using low pressure apparatus by different sets of aluminum powders. The difference between the two categories of the coating is the process pressure and the system configurations that differ in the location of powder injection into the nozzle. Tab. 6.4 shows the working operation limits of two different categories; the principal differences separating the high and low pressure systems, are the gas pressure and the gas and powder flow rates, with the portable system utilizing readily available compressed air.

6.5.1 High pressure coating

High pressure cold spray system (so-called 'kinetic spray' system) is able to produce spray coatings using particle sizes greater than 50 μm and up to about 106 μm [28, p.2]. A modified version of this device is capable of producing coatings using particles of larger size (up to 120 μm) and is designed to heat a high pressure air flow up to about 650°C. After introduction of the particles, the heated air-particle jet is directed through a deLaval type nozzle to achieve particle exit velocities in the range of 300 m/s to 1000 m/s. The primary drawback of this system is that the spray material is injected into the heated gas stream prior to its passage through the deLaval nozzle. There is an inherent tendency for clogging, resulting in back pressure and spray gun malfunction. The second difficulty can be attributed to the low durability of the convergent throat portions of nozzle. Fig. 6.8 shows a system in which the main gas stream and the powder stream are both introduced into the mixing chamber of the converging-diverging nozzle. This configuration requires the powder feeder be capable of high gas pressure and is most often used in stationary cold spray systems, for which the cumbersome powder feeder is acceptable [28, p.2].

6.5.2 Low pressure coating

There are two fundamental aspects that serve to distinguish low pressure spray process from the established high pressure, or stationary, cold spray process:

- The utilization of low pressure gas (0.5-1 MPa instead of 2.5-3 MPa).
- Radial injection of powder instead of axial injection (in most cases).

Since the heated main gas stream is under high pressure, injection of the powder itself requires a high pressure powder delivery system which is quite expensive and not conducive to the design of portable

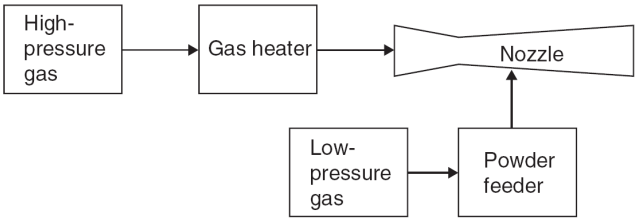

Figure 6.9: *Typical configuration of low pressure coating system [28, p.3]*

Table 6.5: *Chemical composition of the used aluminum alloys*

	Cr	Cu	Fe	Mg	Mn	Si	Ti	Zn
Al-5052-O	0.18-0.28	1.2-2	< 0.5	2.1-2.9	< 0.3	< 0.4	< 0.2	5.1-6.1
Al-7075-T73	0.15-0.35	< 0.1	< 0.4	2.2-2.8	< 0.1	< 0.25	-	< 0.1

cold spraying devices. This system involves injecting the particles by means of a positive pressure that exceeds that of the main gas pressure [28].
Through close examination of these differences, it can be noted that, due to a decrease in the gas mass flow rate, the particle content in the gas-particle jet is considerably higher in low-pressure systems [29]. Fig. 6.9 shows a system in which the powder stream is injected into the nozzle at a point downstream of the throat where the gas has expanded to low pressure.

6.6 Specimens and coated materials

6.6.1 Substrate

Al-5052, that is a very high strength non-heat-treatable alloys, has been chosen as the substrate for the coating. It has a fatigue strength about 110 MPa and is a good choice for structures subjected to dynamic vibration. This alloy has excellent corrosion resistance, particularly in marine atmospheres. The formability of this grade is excellent and in the annealed condition it offers strengths higher than 1100 or 3003 grades. Tab. 6.6 [23] shows the other properties of the Al-5052 and Tab. 6.5 [23] represents the chemical composition of the samples. Al-5052 is widely used for cooking utensils, food processing equipments, storage tanks, truck and trailer components, mail boxes, aircraft components, electronic chassis, boat hulls, deck houses, hatch covers, pressure vessels, ladders, railings, frames, drip pans, tool boxes, truck bumpers, inner and outer body panels and components in truck and auto industries, kitchen equipment, decorative trim, architectural uses, signable applications, and any parts and application requiring strength and good formability at reasonable cost.
Aluminium alloy 7075, chosen as the powders, is an aluminium alloy with zinc as the primary alloying element. It is strong, with a strength comparable to many steels, and has good fatigue strength and average machinability, but has less resistance to corrosion than many other Al alloys. The relatively high cost limits its use to applications where cheaper alloys are not suitable. Generally Al-7075 is very high strength material used for highly stressed structural parts. T73 temper offers improved stress-corrosion cracking resistance. Some applications of Al-7075 aircraft fittings are gears and shafts, fuse parts, meter shafts and gears, missile parts, regulating valve parts, worm gears, keys, bike frames, aircraft, aerospace and defense applications [23]. In order to study the effect of different particles on coated samples' fatigue endurance, pure aluminum powder has also been coated on Al-5052. In order to extract an appropriate statistical conclusion of the fatigue tests, it is necessary to have at least 15 samples for each test series [30]. There is a general agreement that grit blasting can increase the deposition efficiency of the coating and give stronger deposition of the material [31–33]; therefore, in order to examine the latter hypothesis the powders have been coated not only on as-received samples but also on grit blasted ones; i.e. each substrate material was considered in two different sets: as-received and grit blasted.

Table 6.6: *Properties of the two studied aluminum alloys*

	Hardness (Brinell)	Elastic modulus (GPa)	Elongation at break	Poisson's ratio	Yield strength (MPa)	Ultimate strength (MPa)	Fatigue strength (MPa)
Al-5052-O	47	70.3	25-30%	0.33	89.6	110	110
Al-7075-T73	135	72	13%	0.33	435	150	505

Table 6.7: *Coating parameters*

	Coating parameters	Al-7075	Pure Al
Al-5052	Pressure (bar)	16	16
	Temperature (°C)	500	350
	Standoff Distance (mm)	15	20
	Feeder Rotation (rpm)	3	4
	Gas	N_2	N_2
	Robot velocity (mm/s)	20	100
	Deposition Thickness (μm)	80-90	100-100
	Nozzle length (mm)	120	120
	Nozzle orifice diameter (mm)	2	2
	Nozzle exit diameter (mm)	6.3	6.3

6.7 Coating characterization

6.7.1 Coating parameters

The setup of the coating machine, for different sets has been presented in Tab.6.7. Coating process has been executed in University of Ottawa using a low pressure cold spray coating apparatus. The grit blasted samples have been coated by the same parameters as the not grit blasted ones. In the case of the coating thickness, for the grit blasted samples is almost 10% more than the as-received ones.

6.7.2 Coating microstructural analysis

The powder morphology for two different sets (Pure Al and Al-7075) are presented in Fig. 6.10. This figure shows AL-7075 powder have more spherical shapes compared to the pure Al powders. Powder size distribution is obtained by measuring the particle size in the SEM images. The Rosin-Rammler model has been fitted to each distribution; in the case of pure aluminum, although the powders do not have a clear spherical shape, they have been assumed spherical. The histogram shows the pure aluminum powders average size is bigger than Al-7075 powders (24 versus 17 μm). Fig. 6.11a and Fig. 6.11b show the cross section SEM observation of the coated samples. The figures show almost zero porosity for both coatings; the thickness, as it has been expected for pure aluminum deposition, is a little bit more than the samples coated by Al-7075. Fig. 6.12a and Fig. 6.12b show the SEM observation of the surface of different sets. In Fig. 6.12b the powders are distinguishable, while in the other one (Fig. 6.12a) the borders of the particles are not so clear, at the same enlargement. Thus, one can conclude that the bonding in the samples coated by Al-7075, is stronger than pure Al coatings, due to considerable mixing of the powders. The porosity in both coatings is almost zero.

6.7.3 Residual stress and micro-hardness measurement

Residual stress has been measured by AST X-Stress 3000 X-ray diffractometer. $CrK\alpha$ radiation was used and 311 (Miller indices) line for normal diffraction ($\psi = 0$) was recorded. The wavelength is $\lambda = 0.2291nm$ and θ that is the angular position of $\alpha 1$ component, was set to 139°. Electro-polishing technique has been used in order to remove layers of the material and to measure the residual stress in depth; the used solution has been a combination of 94% acetic acid and 6% perchloric acid. For each

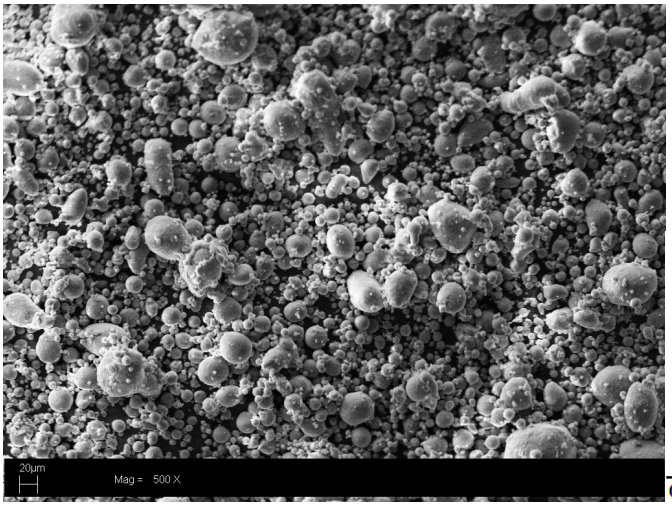

(a) *Powder SEM observation Al-7075*

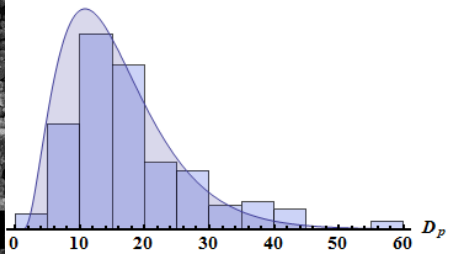

(b) *Size distribution Al-7075*

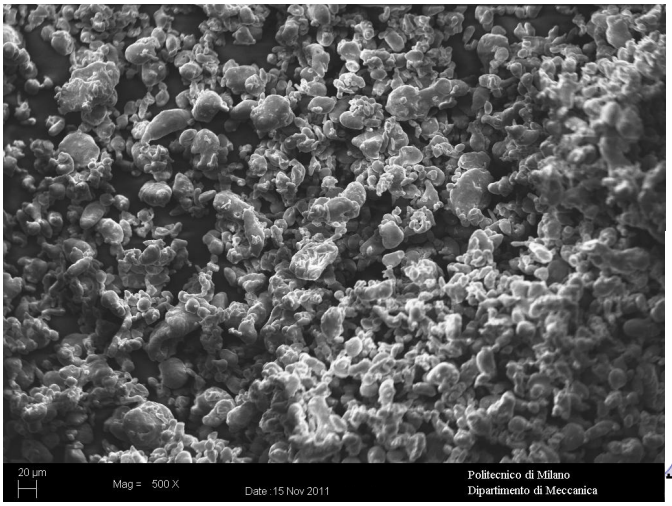

(c) *Powder SEM observation pure Al*

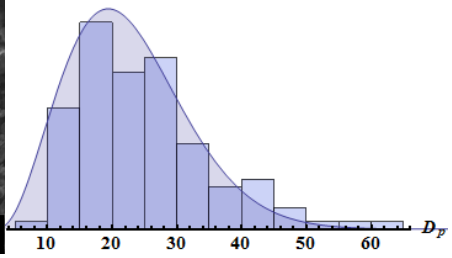

(d) *Size distribution pure Al*

Figure 6.10: *Powder SEM and size distribution*

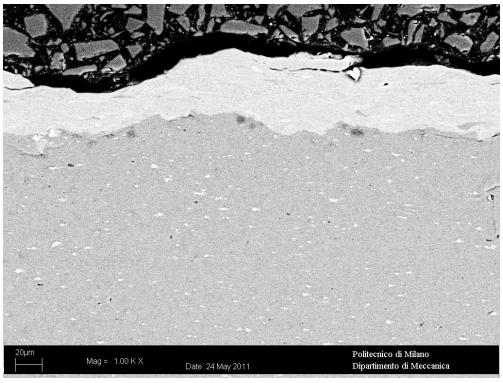

(a) *coated by Al-7075*

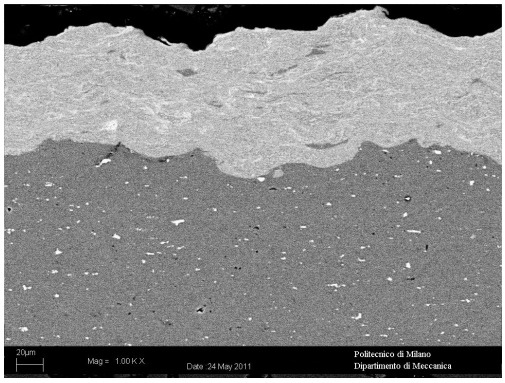

(b) *coated by pure Al*

Figure 6.11: *SEM observation of the coated samples' section*

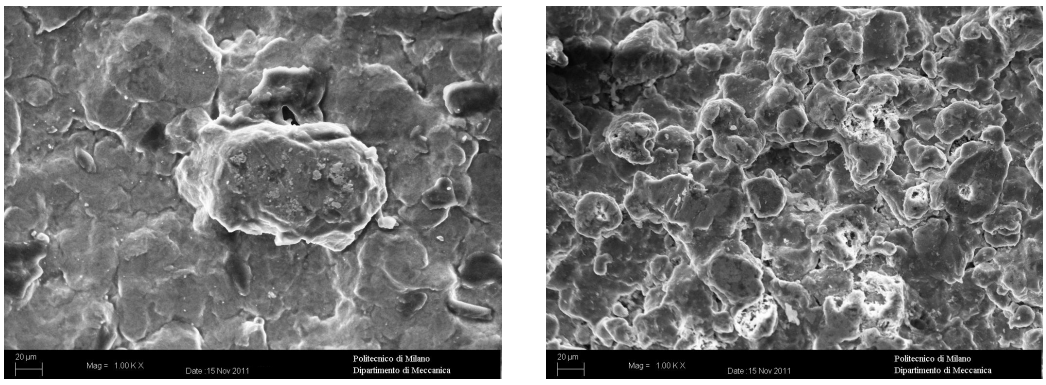

(a) *coated by Al-7075* **(b)** *coated by pure Al*

Figure 6.12: *SEM observation of the coated samples' surface*

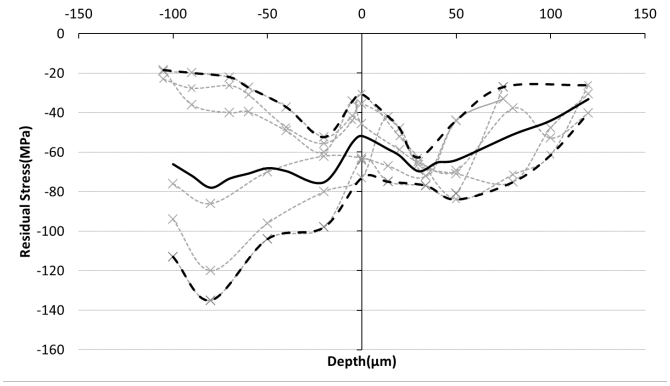

Figure 6.13: *Residual stress measurement on samples coated by Al-7075*

set, different measurements have been performed in three rotation angles (0, 45, and 90). The results for specimen coated by Al-7075 is presented in Fig. 6.13 and for specimen coated by pure Al in Fig. 6.14. In both figures, vertical axis refers to the position of the substrate surface; residual stress relaxation can be observed in both cases; similar results have been reported in the literature [34, 35]. Contrary to pure Al, the results for Al-7075 show high deviation in different measurements. The black line shows the average value and the dashed lines represent the margin of the results in different measurements. Although, Al-7075 is harder than pure aluminum, the maximum compressive stress in the substrate after coating by pure aluminum is almost 50% higher than the other sets coated by Al-7075. Micro-hardness measurements have been performed on the samples in different levels to study the effect of the coating on their hardness. The results presented in Fig. 6.15 show that Al-7075 powders increase the hardness of the samples in the surface; on the other hand, pure aluminum powders somehow decreased the micro-hardness of Al-5052. It can be concluded that the hardness of the coated sample is highly dominated by the hardness of the powders.

6.8 Severe shot peening

In order to generate nanograins on the structure surface, severe shot peening has been applied to the samples coated by Al-7075. The shot peening parameters are presented in Tab. 6.8. The grain size of the samples after shot peening, studied in the next chapter, are in the nanograin zone (<100nm). Fig. 6.16 shows the surface of the shot peened specimens. This image represents the highly deformed surface of the specimens due to high energy of the peening process.

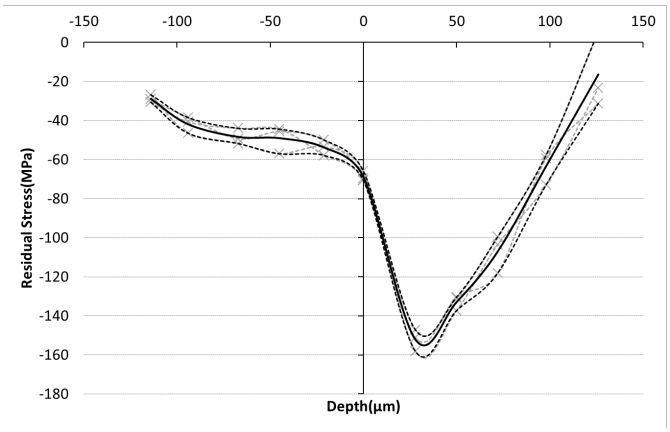

Figure 6.14: *Residual stress measurement of samples coated by pure aluminum*

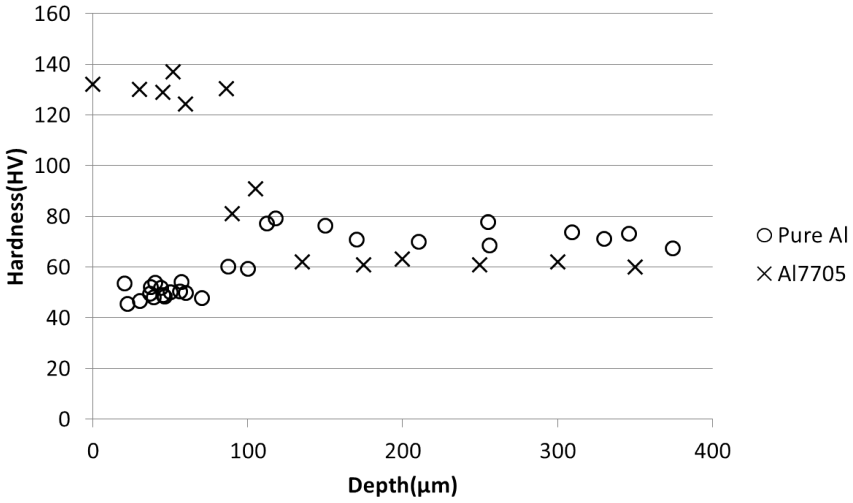

Figure 6.15: *Micro-hardness measurement*

Table 6.8: *Shot peening parameters*

Shot diameter	0.7 mm
Intensity	22 A
Coverage	3000%

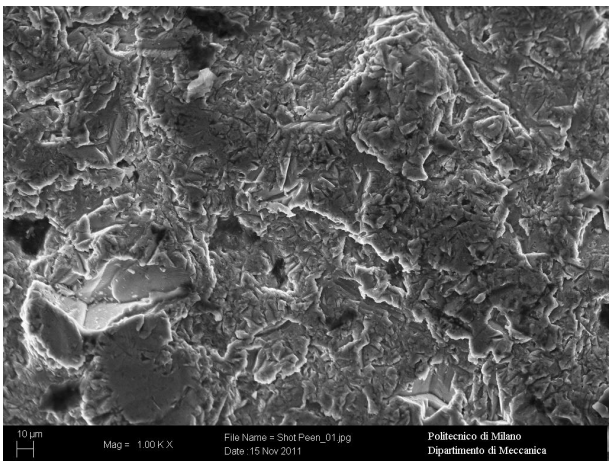

Figure 6.16: *Surface observation of the shot peened samples*

6.9 Application of grain size measurement to the treated samples

6.9.1 Coated samples

Grain size measurement is also performed on the coated samples. Electro-chemical polishing is used for removing the material in order to measure the residual stress in the depth of the specimen. Typically, the work piece is immersed in a temperature controlled bath of electrolyte and serves as anode, as it is connected to the positive terminal of a DC power supply, the negative terminal being attached to the cathode. The current passes from the anode, where metal on the surface is oxidized and dissolved in the electrolyte, to the cathode. At the cathode, reduction reaction occurs, which normally produces hydrogen. The residual stress measurement and also grain size estimation have been performed by XRD tests performed by AST X-Stress 3000 X-ray diffraction (radiation Cr Kα, irradiated area 3.14mm^2, $\sin 2\psi$ method, diffraction angles (2θ) scanned between -45 and 45), peak determination is performed with cross correlation method. The results have been presented for each angle ($2\theta = 138$) with Miller Index 104, time 400 s for each peak and the total time of 1 hour for 0°, 45°, and 90° for each measurement. Based on the Keijser *et al.* [20] method, or any other grain size technique, FWHM value of the XRD pattern can be considered as an index of the grain size i.e. higher FWHM refers to smaller grain size. Fig. 6.17 shows the results for FWHM obtained in the depth of the substrate and coated material; the red dashed lines show the position and the value of the maximum point which is in the interface of the substrate and the coating. This graph shows a big jump in the interface between the deposited material and the substrate. By using the Keijser *et al.* [20] method, the grain size in that zone is measured to be between 20-50 nm. The variation is due to different values related to different measurements. Existence of nanocrystalline in the substrate should help to improve the fatigue strength of the structure, as it has been discussed in Chapter 1. The recrystallization of the substrate after coating has been confirmed not only by the numerical results of the peening effect of the coating presented in Chapter.5 but also by Guetta *et al.* [36]. Fig. 6.18 shows the nanocrystallization of the substrate surface after coating. In this layer, two nanocrystallized phases were detected and identified as Al_2Cu and Al_4Cu_9 from Fourier transform analysis of high-resolution TEM images and from chemical composition analysis.

6.9.2 Samples treated by combined shot peening and cold spray coating

Severe shot peening shows the ability to change the grain size of the material [22]. XRD measurements have been performed on as-received samples, powders, coated samples, and finally shot peened-coated samples. The results for all measurements including the peak properties are presented in Tab. 6.9. The results obviously prove the presence of a nanocrystalline layer on the shot peened samples' surface; whereas, the grain size of the particles and coated samples are so close to nanostructure (<100nm) and the grain size on the substrate has been considerably changed. SEM observation of the surface of shot-

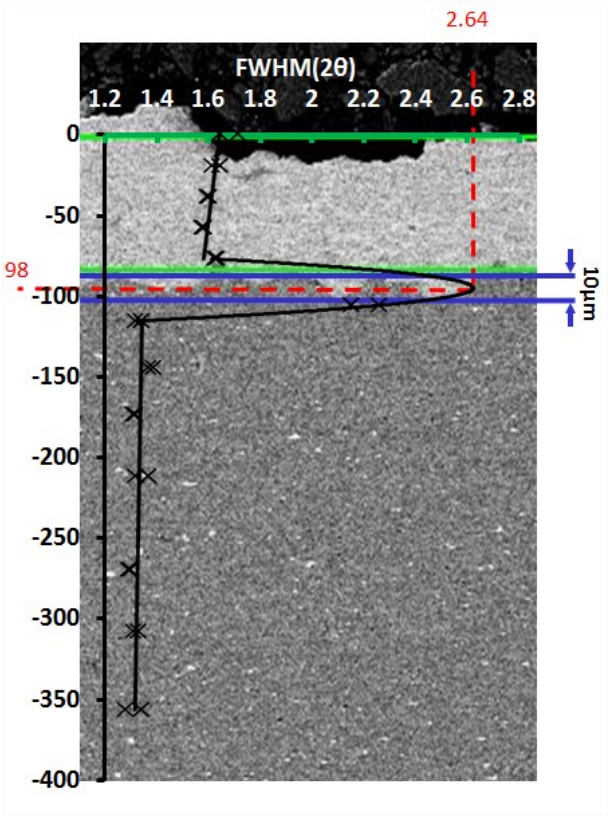

Figure 6.17: *Variation of FWHM through the specimen depth*

Table 6.9: *Grain size measurement for different treatments and samples*

	As-received	Powders	Coated	Coated and shot peened
FWHM	1.23	1.26	1.63	1.72
Integral Breadth	1.41	1.36	1.97	2.144
a_0	163.157	121.607	1340.72	942.096
a_1	250.853	236.098	257.38	276.425
a_2	39.6408	39.933	53.9	57.2155
a_3	3.2547	11.42	2.03681	1.7578
ϕ	0.8721	0.922	0.8234	0.8021
β_C^f	0.2513	0.0678	0.4212	0.0117
β_G^f	0.83095	0.958	0.70862	0.0158
D(nm)	**>1200**	**157**	**110**	**56**
$e \times 10^3$	0.77	1.2	1.49	1.5

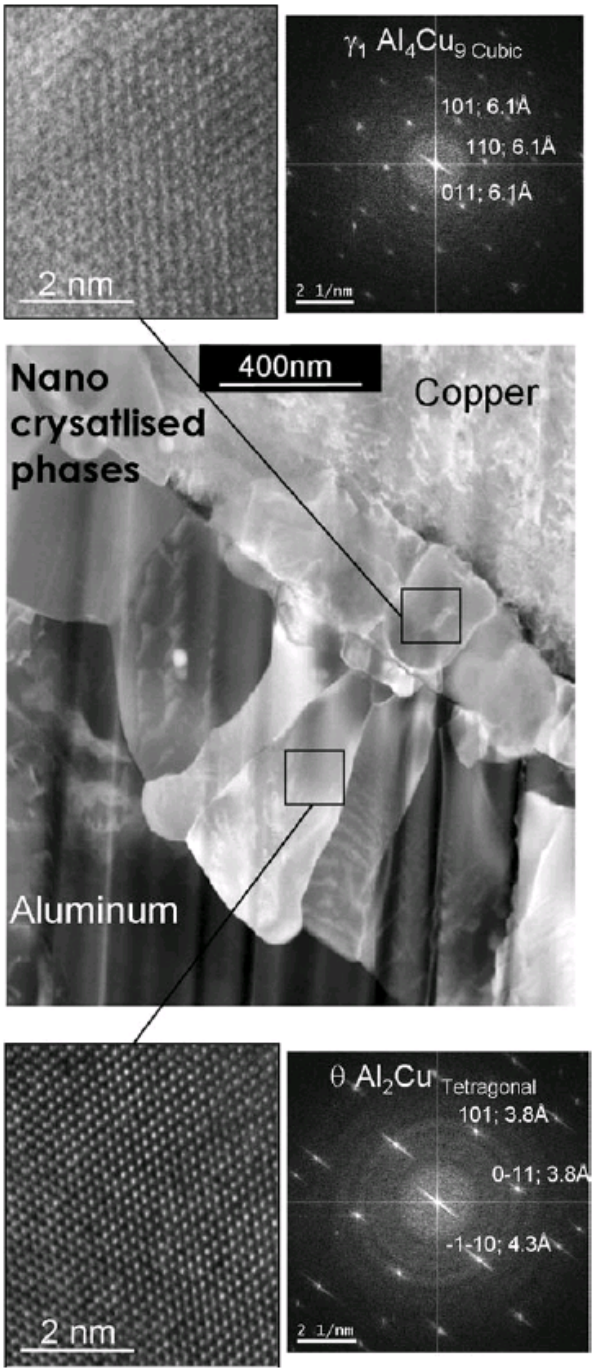

Figure 6.18: *Microstructure of the splat/substrate interface and Fourier transform analysis of corresponding high resolution images [36]*

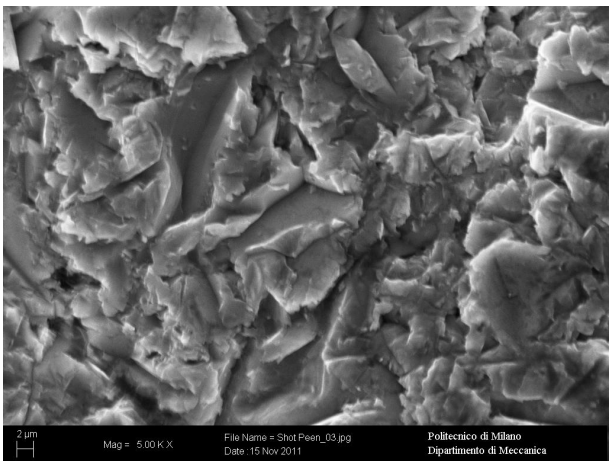

Figure 6.19: *SEM observation of shot peened specimen*

peened samples is presented in Fig. 6.19. Although, the SEM observation cannot approve the existence of Nanocrystalline, the image shows high plastic deformation of the surface.

6.10 Conclusion

Portable XRD device has been used to measure the grain size of differently treated samples. The output of the XRD measurements has been elaborated using a single line profile analysis. The results have been calibrated by TEM observation and also full angle diffraction tests dedicated to grain size measurement by in-situ high energy XRD. The results of these two established test methods, show a good correspondence with the output of single line analysis, that has been later, applied to the coated and shot peened samples to verify the existence of nanograins on their surface. XRD measurements have been performed on the surface and in depth by removing material using an electro-polishing device, in order to measure the grain size of the structure also in depth. Micro-structure analysis have been performed on the treated samples through SEM observation. SEM observation shows that the porosity of the coating for both sets is almost zero and in the case of Al-7075, the powders show stronger bonding with respect to the samples coated by pure Al. XRD residual stress measurements approve the presence of compressive residual stresses in the deposited material and the substrate. The hardness of the samples' surface after coating has been measured to be that of the deposited bulk material. Shot peening is applied to the coated samples in order to produce nanograins on their surface through severe plastic deformation. The results confirm, the generation of nanograins on the substrate which can be attributed to high plastic deformation or high strain rate as a result of the high energy impact of the shots. The possibility of grain size reduction on the surface of the substrate was numerically approved in Chapter 5. Effect of different treatments on grain size alteration and also fatigue strength will be studied and discussed in the next chapters.

Bibliography

[1] J. Goldstein, D. E. Newbury, D. C. Joy, C. E. Lyman, P. Echlin, E. Lifshin, L. Sawyer, and J. R. Michael, *Scanning Electron Microscopy and X-ray Microanalysis*. Kluwer Academic/Plenum publishers, 2003.

[2] M. Belassel, M. Brauss, and J. Pineault, *Shot peening: a dynamic application and its future*. MFN-Metal Finishing News, 2009.

[3] I. C. Noyan and J. B. Cohen, *Residual stress-measurement by diffraction and interpretation*. Springer-Verlag, 1987.

[4] "http://www.microscopy.ethz.ch/bragg.htm."

[5] E. Muller, "The difficulty of measuring the residual stress at shot peened surfaces," *Metal Finishing New*, vol. 11, pp. 60–61, 2010.

[6] M. G. Moore and W. P. Evans, "Corrections for stress layers in x-ray diffraction residual stress analysis," *SAE Trans*, vol. 66, pp. 340–345, 1958.

[7] "Xtronic manual, software user's guide," 2010.

[8] H. A. Padilla and B. L. Boyce, "A review of fatigue behavior in nanocrystalline metals," *Experimental Mechanics*, vol. 50, pp. 5–23, 2010.

[9] B. E. Warren, *X-Ray Diffraction*. Dover Publications, 1990.

[10] B. D. Cullity and S. R. Stock, *Elements of X-ray diffraction*. Prentice-Hall, 2001.

[11] H. P. Klug and L. E. Alexander, *X-ray diffraction procedures for polycrystalline and amorphous materials*. New York: Wiley, 1974.

[12] A. R. Stokes and A. J. C. Wilson, "The diffraction of x-rays by distorted crystal aggregates," *Proc. Phys. Soc.*, vol. 56, pp. 174–181, 1944.

[13] A. L. Ortiz and L. Shaw, "X-ray diffraction analysis of a severely plastically deformed aluminum alloy," *Acta Materialia*, vol. 52, pp. 2185–2197, 2004.

[14] G. K. Williamson, "X-ray line broadening from filed aluminium and wolfram," *Acta Metallurgica*, vol. 1, pp. 22–31, 1953.

[15] J. I. Langord, "A rapid method for analysing the breadths of diffraction and spectral lines using the voigt function," *J. Appl. Cryst.*, vol. 11, pp. 10–14, 1978.

[16] N. C. Halder and C. N. J.Wagner, "Analysis of the broadening of powder patternpeaks using variance, integral breadth, and fourier coefficients on the line profile," *Adv. X ray Anal.*, vol. 9, pp. 91–102, 1966.

[17] R. K. Nandi and S. P. Sengupta, "The analysis of x-ray diffraction profiles from imperfect solids by an application of convolution relations," *J. Appl. Cryst.*, vol. 11, pp. 6–9, 1978.

[18] H. C. V. de Hulst and J. J. M.Reesinck, "Line breadths and voigt profiles," *J. Astrophys.*, vol. 106, pp. 121–127, 1947.

[19] W. Voigt and K. Bayer *Akad.Wiss.*, vol. 42, pp. 603–620, 1912.

[20] T. H. D. Keijser, J. I. Langford, E. J. Mittemeijer, and A. B. P. Vogles, "Use of voigt function in a single-line method for the analysis of x-ray diffraction line broadening," *J. Appl. Cryst.*, vol. 15, pp. 308–314, 1982.

[21] E. J. Mittemeijer and U. Welzel, "The state of the art of the diffraction analysis of crystallite size and lattice strain," *Z. Kristallogr.*, vol. 223, pp. 552–560, 2008.

[22] S. Bagherifard, R.Ghelichi, and I. Pariente, "Experimental and numerical analysis of surface nanostructured materials obtained by high energy shot peening," in *Proceedings of the IGF XX. National Conference, Torino, Italy*, 2009.

[23] A. specification metals material data sheet, "http://asm.matweb.com," 2011.

[24] P. S. Prevéy, "The use of pearson vii distribution functions in x-ray diffraction residual stress measurement," *Lambda Technologies, Advances in X-Ray Analysis*, vol. 29, pp. 103–11, 1986.

[25] L. Lutterotti, S. Matthies, H. R. Wenk, A. J. Schultz, and J. Richardson, "Texture and structure analysis of deformed limestone from neutron diffraction spectra," *J. Appl. Phys.*, vol. 81, pp. 594–600, 1997.

[26] H. M. Rietveld, "A profile refinement method for nuclear and magnetic structures," *Journal of Applied Crystallography*, vol. 2, pp. 65–71, 1969.

[27] B593-96, "Standard test method for bending fatigue testing for copper-alloy spring materials," *ASTMi*, no. B593-96, 2009.

[28] V. Champagne, *The cold spray materials deposition process, Fundamentals and application*. Woodhead Publishing, 2007.

[29] R. Maev and V. Leshchynsky, *Introduction to Low Pressure Gas Dynamic Spray*. WILEY-VCH Verlag GmbH & Co. KGaA, 2008.

[30] W. Dixon and F. Massey, *Introduction to statistical analysis*. McGraw-Hill, 1969.

[31] T. S. Price, P. H. Shipway, and D. G. McCartney, "Effect of cold spray deposition of a titanium coating on fatigue behavior of a titanium alloy," *Journal of Thermal Spray Technology*, vol. 15, pp. 507–512, 2006.

[32] X. J. Ning, J. H. Jang, H. J. Kim, C. J. Li, and C. Lee, "Cold spraying of alâĂŞsn binary alloy: Coating characteristics and particle bonding features," *Surface & Coatings Technology*, vol. 202, pp. 1681–1687, 2008.

[33] D. E. Wolfe, T. J. Eden, J. K. Potter, and A. P. Jaroh, "Investigation and characterization of cr_3c_2 based wear-resistant coatings applied by the cold spray process," *Journal of thermal spray technology*, vol. 15, pp. 400–412, 2006.

[34] R. C. McCune, W. T. Donlon, O. O. Popoola, and E. L. Cartwright, "Characterization of copper layers produced by cold gas-dynamic spraying," *Journal of Thermal Spray Technology*, vol. 9, pp. 73–82, 2000.

[35] S. Bagherifard, I. F. Pariente, R. Ghelichi, M. Guagliano, and S. Vezzù, "Effect of shot peening on residual stresses and surface work-hardening in cold sprayed coatings," *Key Engineering Materials*, vol. 417, pp. 397–400, 2010.

[36] S. Guetta, M. H. B. F. Borit, V. Guinpont, M. Jeandin, M. Boustie, Y. Ichikawa, K. Sakaguchi, and K. Ogawa, "Influence of particle velocity on adhesion of cold sprayed splats," *Journal of Thermal Spray Technology*, vol. 18, pp. 331–342, 2009.

Chapter 7

Fatigue test

7.1 Introduction

Residual stresses induced in the substrate and the high plastic deformation that results in surface nanocrystallization, studied in the previous chapters, are the most effective factors with potential effects to increase the fatigue endurance of the treated structures. In Chapter 2 the effect of cold spray coating on fatigue behavior of the structure has been briefly reviewed. The work of Price *et al.* [1] and Sansoucy *et al.* [2] show two different effects of coating on the fatigue strength. Price *et al.* studied the effect of titanium coating on fatigue behavior of as-received and grit-blasted materials. A 15% reduction in fatigue endurance was observed after application of coating to the as-received substrate, but no significant reduction was observed on its application to the grit-blasted substrate. It has been shown that titanium coatings have a detrimental effect on the fatigue endurance of Ti6Al4V. On the other hand, Sansoucy*et al.*, show that Al-Co-Ce coatings improve the fatigue behavior of Al 2024-T3 specimens when compared to not coated and Alclad specimens. It is suggested that the increase in the fatigue properties of the specimens can be attributed to the compressive residual stresses induced in the coating and to the high adhesion strength of the coating to the substrates. The difference of the presented results in the two latter works might be due to the residual stress measured in the substrate as Price *et al.* [1] reported negligible compressive residual stress on the coated samples' surface and substrate. SEM observations in their work also show delamination in the deposited material after fatigue tests which indicates of no, or very little, contribution of the deposited materials to the fatigue strength. ASTM B593-96 [3] presents a standard method for bending fatigue test on Copper-Alloys; this standard has been used also by Sansoucy *et al.* [2] for examining the fatigue strength of coated samples. This standard suggests to mount a prepared test specimen of a specific wrought material flat-sheet or strip-spring into a fixed cantilever, constant-deflection type fatigue testing machine. The specimen is held at one end, acting as a cantilever beam, and cycled by flexure followed by reverse flexure until complete failure. The number of cycles to failure is recorded as a measure of fatigue-life. The very same procedure has been followed in the current work in order to examine the fatigue endurance of the coated samples. In each set, the coated samples fatigue strength has been compared to the as-received material which has been tested in the same way. The testing machine has been developed in the POLIMI Lab. of Mechanical Engineering Department and it has been calibrated in order to satisfy the requirements of the standard. The specimen presented by the standard has been studied numerically in order to have a better view of the behavior of the samples and their stress distribution. In this chapter the specimens, test machine, testing procedure, and the results of the fatigue tests are presented.

7.2 Testing machine setup

Test apparatus suggested by ASTM B-593 [3] is a fixed-cantilever, constant-deflection type machine. In this machine (Fig. 7.1) the test specimen shall be held as a cantilever beam in a clamp at one end and deflected by a concentrated load applied near the other end of the apex of the tapered section. Either the

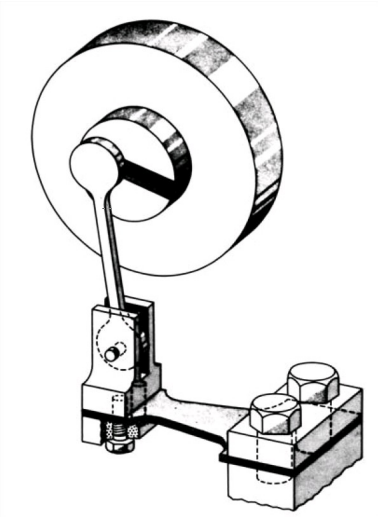

Figure 7.1: *Test apparatus suggested by ASTM-B593*

clamp or the loading member may be adjusted so that the deflection of the cantilever's free end is either completely reversed (mean displacement equal to zero (R=-1)) or greater in one direction of bending (mean displacement not equal to zero). The specimens, on the other hand, are designed for the bending test based on the approach suggested by standard. The detail design of the specimen, after conversion of the measures from US units, as they are presented in the standard, is presented in Fig. 7.2a along with a photo (Fig.7.2b) of the prepared specimen. The commercial test apparatus which works exactly based

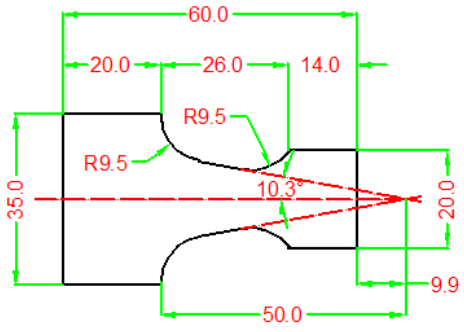

(a) *Detail design of the specimen*

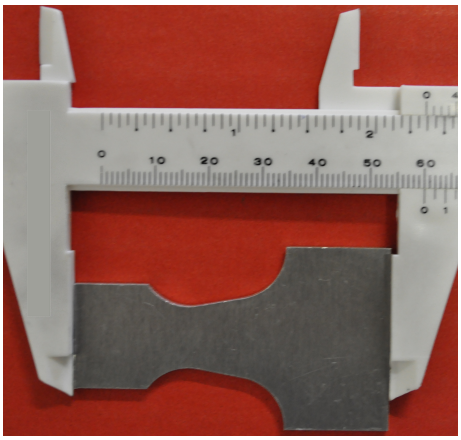

(b) *FEM model from isometric- view*

Figure 7.2: *Test specimen suggested by ASTM-B593 [3]*

on the same proposed method by the standard, apart from it's cost which is quite considerable, has some disadvantages. First of all, the low frequency testing of the samples for a run out of around 10 million cycles takes a long time considering the maximum frequency of this type of machine that is 20-25 Hz; i.e for 10 million cycles, almost a week is needed. Second, changing the specimen with different loads takes a considerable time; for each specimen the mechanism of the machine should be disassembled in order to change the course of the eccentric position of the rod connected to the specimen. Third, the test machine works based on fixed displacement and by changing the material type, the applied load should be calibrated again. And the last but not the least, the test machine is quite expensive. In this regard, a home made simple apparatus has been assembled at the Politecnico di Milano Lab. which is able to

Table 7.1: *The LSD V406A shaker main features*

Specification	Limit
Min frequency	2Hz
Natural frequency	9000Hz
Max displacement	17.6mm
Max velocity	1.78m/s
Max acceleration	490m/s^2
Max force	100N

satisfy the perquisite requirements mentioned in the standard. In this section a short description of the fatigue test machine is presented. The main features required by the test rig is a high frequency (up to 9 kHz), with respect to the common hydraulic test machines, and a harmonic force with a zero-peak amplitude up to 100 N. Fig. 7.3 shows the layout of different aspects of the machine along with a photo of the apparatus: As presented in Fig. 7.3a, it is possible to distinguish two main aspects: the hardware

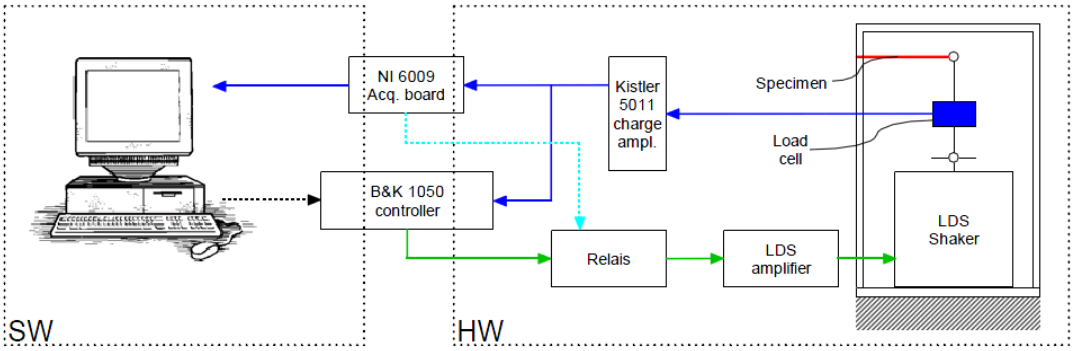

(a) *Layout of different aspects of the machine*

(b) *Photo of test apparatus*

Figure 7.3: *Different parts of the home made machine*

(HW) and the software (SW). The HW aspect includes the test machine composed of a LDS type V406A electrodynamics shaker and a reaction structure on which the specimen is rigidly connected (clamp, Fig. 7.3b). The main characteristics of the shaker are summarized in Tab. 7.1. The limits specified in the latter table are not the definite limits of the machine; each of the features of the machine is a function of the other parameters. Fig. 7.4 shows the diagram related to the applied limits of the machine. The white zone indicates the working zone of the machine based on which the test frequency shall be chosen.
The specimen is linked to the shaker by means of a rod with a mounted piezoelectric 2.5 kN load cell (type 9301). The transducer allows to measure the force applied to the specimen and to feedback it to the

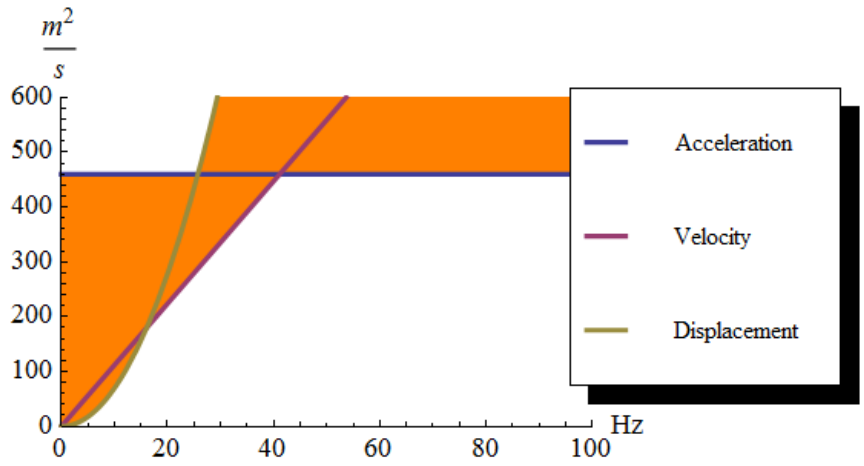

Figure 7.4: *White zone indicates the working zone of the machine*

controller unit. The double-hinge connection avoids undesired bending moment transfer. The controller unit is a $Brüel\ \&\ Kjr$ 1050 ($\pm$10 V input and output signals, 1 MHz clock base, PD compensator) driven by a software developed in NI LabVIEW. The controller allows setting the test frequency and amplitude that is continuously compared with the actual value measured by the load cell. Moreover a NI 6009 acquisition board is able to sample the force signal (1 kHz sampling frequency) and to send it to the SW (Fig. 7.5). It stores the data with a given law (e.g. 20 cycles every 60 s), analyzes the signal in real time (min/max value, FFT) and runs an algorithm to manage the alarm condition. In fact, to automatically stop the test when the sample is broken, it is possible to define a suitable threshold on the measured force harmonic component at the assigned frequency. The data acquisition from the software shows the ability of the shaker to apply almost noiseless sinusoidal loads; Fig. 7.6 shows an example of the data sampled by the software. It is possible to observe, as expected, the presence of the noise in the sampled data; it might be due to the acquisition frequency, i.e. the frequency of the information gathering is so close to the working frequency of the machine (1000 to 100) that may result to miss some data in the acquisition process. It is necessary to calibrate the developed test machine; this step will be explained in more detail in the following sections.

7.3 Test specimen

The geometry of the specimen (Fig. 7.2) is designed to obtain a uniform maximum stress throughout all sections perpendicular to the longitudinal axis; in order to have a better understating of the suggested model by ASTM, a FEM model ,shown in Fig. 7.7, has been developed. Fig. 7.8a shows the axial stress contour of the specimen. As it is observed, the stress distribution on this line is almost uniform; Fig. 7.8b shows comparison with the analytical solution developed by using solid mechanics formula based on the load distance. The blue color confirms that the stress has been distributed uniformly. The FEM analysis indicates of a slight stress concentration factor considering Von-Mises stress distribution at the end of the curves; Fig. 7.9a shows the obtained results for Von-Mises and Fig. 7.9b shows the stress on a path with the mean value expected by analytical solution. Admittedly, the position of the applied load, as it has been shown in Fig. 7.10, plays an important role in the applied stress to the specimen. Fig. 7.11 shows the attempts for finding the optimum value for this distance. The optimum value has been found in a way that the stress on the symmetry line is distributed uniformly on the path. In each tentative, the distributed stress has been compared to the ideal distribution which is shown by a horizontal line in Fig. 7.11a and the error function by using 7 different tentative data has been optimized. The final value for D, refers to Fig. 7.10, found to be 24.2 mm (Fig. 7.11b)

Figure 7.5: *The apparatus software for data acquisition of the load cell*

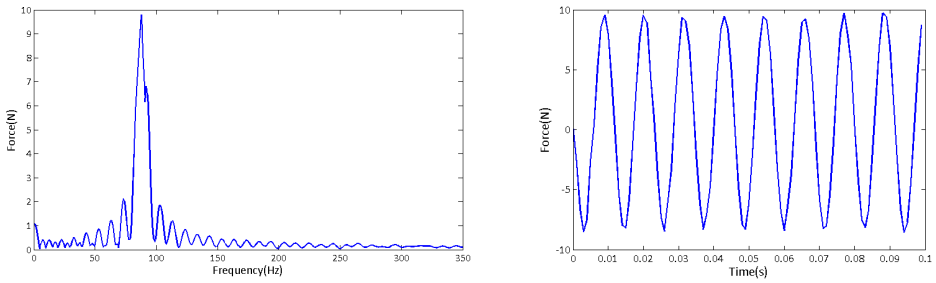

(a) *The sampled data in time domain* **(b)** *The sampled data in frequency domain*

Figure 7.6: *An example of the acquired data by SW*

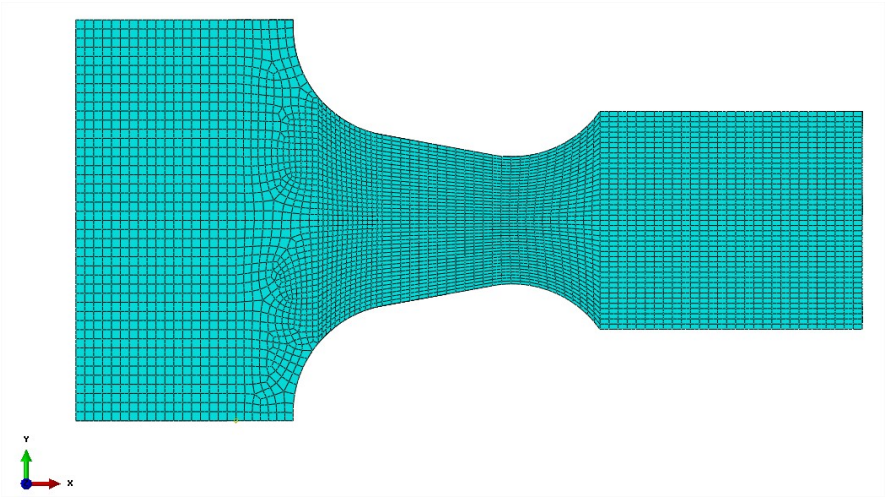

Figure 7.7: *FEM model for the standard fatigue test specimen*

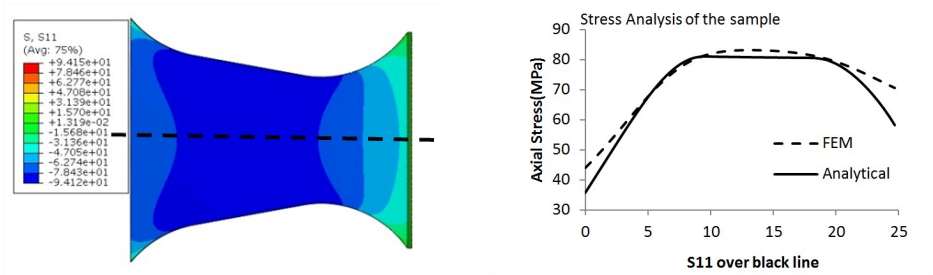

(a) *results of FEM model*

(b) *Stress on the black line compared to analytical solution*

Figure 7.8: *Result of the FEM model compared to analytical solution*

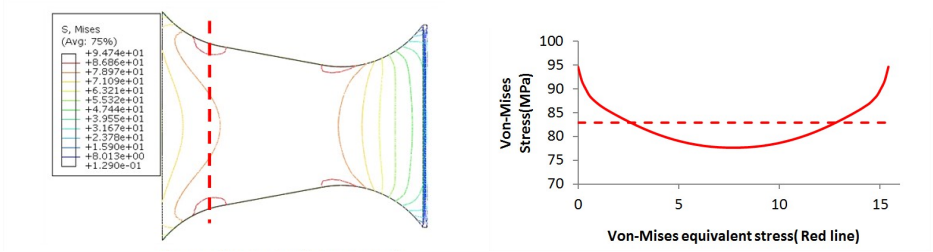

(a) *The zone with stress concentration*

(b) *The comparison of the stress with nominal one*

Figure 7.9: *Stress concentration in the test specimen*

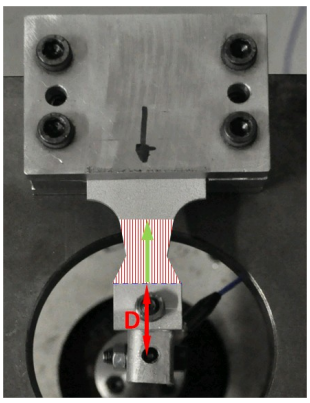

Figure 7.10: *Finding the applying load position D in order to have uniformly distributed stress on the hatched area*

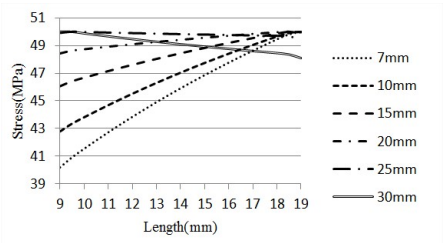

(a) *Stress on the hatched area in Fig. 7.10 for different D*

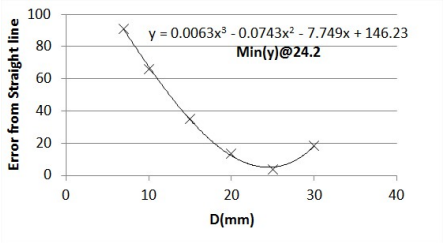

(b) *the error of the final results with an uniform distribution*

Figure 7.11: *Finding the D in Fig. 7.10*

7.4 test machine calibration

In order to evaluate the testing machine, Rosette strain gauges have been mounted on different specimens for measuring the stress on symmetry line and also on the curves. Fig. 7.12 shows the position of the strain gauges on the specimens. Two different arrangements have been chosen for the position of the strain gauges. First, to evaluate the analytical and numerical calculation in order to check if the stress has been distributed uniformly on the surface, two strain gauges, as shown in Fig. 7.12a, have been attached to the specimen. Second, in order to have an evaluation of the stress concentration factors, a strain gauge has been attached as close as possible to the curve of the specimen. As it has been shown in Fig. 7.12b it was not practically possible to put the strain gauge on the curve. To use the strain gauges, the exact value of material elastic modulus is needed. So, as it is shown in Fig. 7.13, tensile tests has been performed on the material in order to obtain *E*. The value of 70 GPa for elastic modulus of Al-5052 has been measured. The rest of the properties obtained from the test are presented in Tab. 6.6. Strain has been measured by changing the load and the frequency of the test in order to obtain the optimum parameters. Fig. 7.14 shows the results for strain gauge number 1 and 2, numbered as shown in Fig. 7.12a, as well as the comparison with analytical solution by changing the load. The graph shows that the analytical solutions are reliable to be used for stress calculation .

Fig. 7.15 shows the effect of frequency on the stress with a constant load (5 N). The stress does not remain the same, as it is expected, by changing the frequencies. The figure indicates that the stress remains constant up to almost 90 Hz and after that it starts to increase; it might be due to the dynamic response of the specimen which results in increasing the applied stress by increasing the frequency, under constant loading. Fig. 7.16 shows the results for the strain gauge on the edge and the comparison with the measurements on the symmetry line. Based on the latter results, there is a slight difference between the results on the curve and on the symmetry line. The final stress concentration factors estimated through

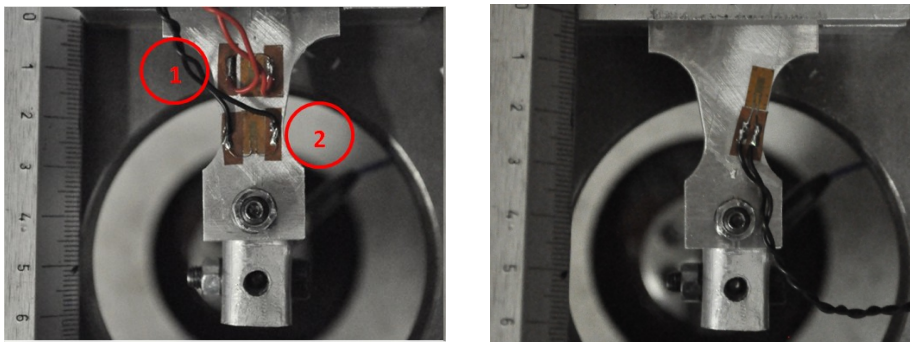

(a) *Rosette strain gauge on symmetry line* **(b)** *Rosette strain gauge on the curve*

Figure 7.12: *Position of the strain gauges*

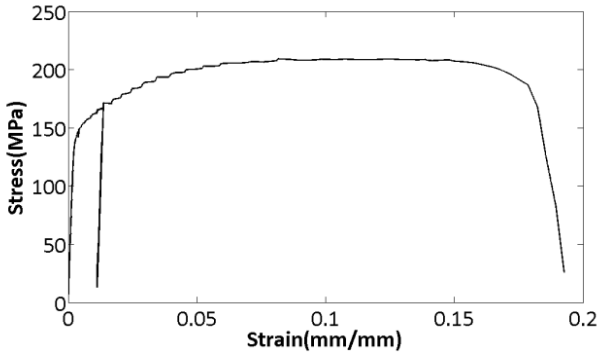

Figure 7.13: *Tensile test for elastic modulus measurement*

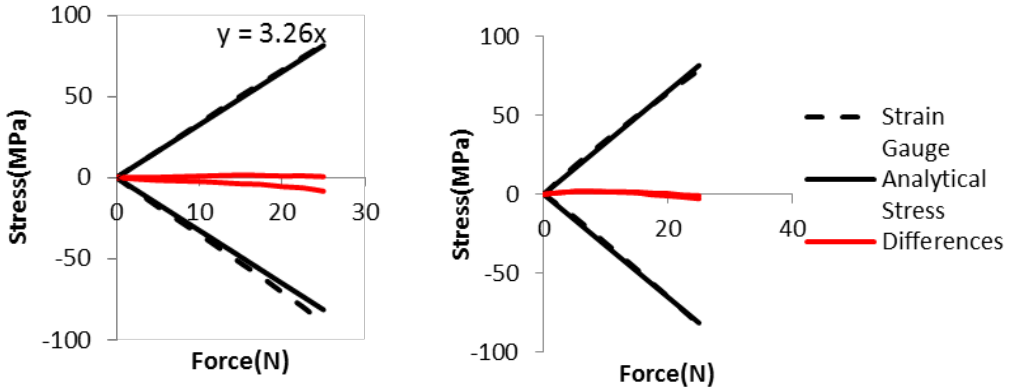

(a) *Strain gauge number 1* **(b)** *Strain gauge number 2*

Figure 7.14: *Strain gauge results for different positions based on Fig. 7.12*

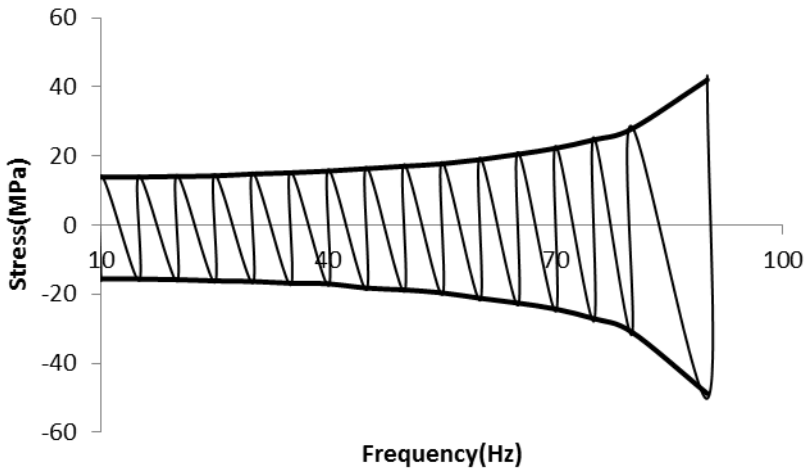

Figure 7.15: *Strain gauge results for different frequencies under constant load (5 N)*

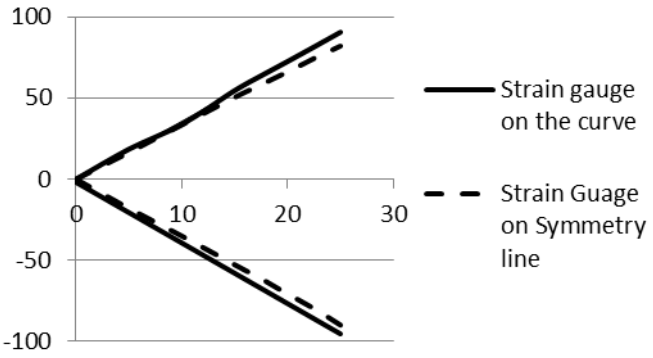

Figure 7.16: *Results of the strain gauge on the curve*

numerical and experimental solution are 1.13 and 1.10 respectively. The difference in the results can be contributed to geometrical problems for putting the strain gauge on the specimen curve.

7.5 Fatigue tests

The geometry of the specimen and also the specification of the machine have been presented in the previous section. Different sets of specimens with the same geometry and diverse treatments, have been tested in order to find their fatigue endurance. As it has been discussed in detail in Chapter. 6, various treatments have been applied to different aluminum alloy specimens, presented in Tab. 7.2. The specimens were tested using a load control pure bending fatigue machine. The specimens that passed 10 million cycles were considered as run-out. Brief *Staircase* method presented by Dixon and Massey [4] has been used for performing the tests with a stress step of 10 MPa and Hodge-Rosenblatt [5] approach has been considered for calculating the fatigue strength of the tested series. Fig. 7.17 shows one of the specimens with a crack propagated from its border. The crack propagation path confirms that the load has been applied properly.

Table 7.2: *General aspects of different test series*

Material	Treatment	Thickness(mm)
Al-5052	As-received (No treatment)	2.2
Al-5052	Grit-blasted (GB)	2.2
Al-5052	Coated by pure aluminum	2.49
Al-5052	GB-coated by pure aluminum	2.55
Al-5052	Coated by Al-7075	2.36
Al-5052	GB-coated by Al-7075	2.41
Al-5052	Coated by Al-7075-severe shot peening	1.68
Al-5052	GB-coated by Al-7075-severe shot peening	1.72

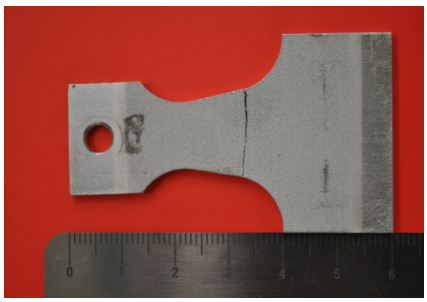

Figure 7.17: *A crack initiated and propagated in coated specimen due to fatigue loading*

7.6 Results

7.6.1 S-N diagram

The tests were performed also for the finite life part of the S-N diagram by testing some specimens with higher loads. Fig. 7.18 shows the S-N diagram obtained for different sets of the specimens that were presented in Tab. 7.2, including as-received and grit blasted series. The results presented in Fig. 7.18 show fatigue strength improvement for all treated series with respect to the as-received ones. Al-5052 specimens coated by pure aluminum have more or less the same fatigue endurance of grit blasted ones. On the other hand, the Al-5052 series coated with Al-7075 show a distinguished fatigue endurance improvement. Fig. 7.18 also indicates that different treatments change the line slope of the low cycle fatigue part. The grit blasted and as-received specimens show almost the same slope whereas grit-blasted series shows improved fatigue strength. The shot peened specimen with nanocrystalline has not improved the fatigue strength; the results are not presented in the figure; however it is to be mentioned that due to high deformation of the samples and the presence of micro-cracks, the fatigue endurance was not increased.

7.6.2 Fractography

SEM observations of broken specimens help understanding the fracture process. Fig. 7.19 shows the SEM observations of a specimen coated by pure aluminium. Fig. 7.19 (a) and (b) show the overall specimen section. Fig. 7.19 (c) shows the crack initiation on the specimen; based on the latter image, the crack has initiated on the substrate and has propagated through the structure. Fig. 7.19 (d) and (f) show that the deposited material has been delaminated from the substrate; it might be due to fatigue loading or the coating parameters. In Fig. 7.19 (f) the highly deformed coating particles can be observed. Fig. 7.19 (e) and (h) show the detail of a stripe which can be observed throughout the section of all broken specimens. This line might be induced by the pure bending test and the crack propagation path. Fig. 7.19 (g) shows that in some places the coating has gone under abrasion during the test. Fig. 7.20 shows the SEM observation for an Al-5052 specimen coated by Al-7075. Fig. 7.20 (b) and (c) show the overall section of the specimen; the stripe, as it was mentioned in Fig. 7.19, is observed also for this specimen.

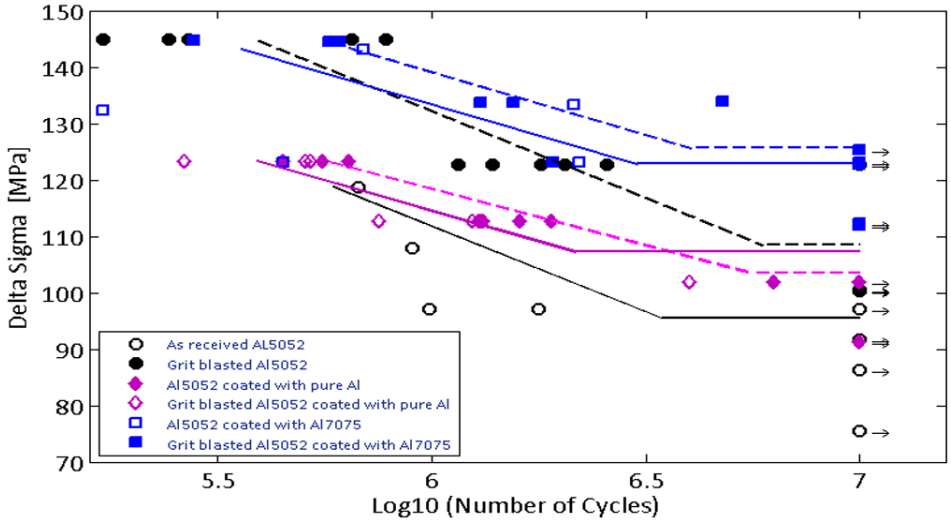

Figure 7.18: *The S-N diagram obtained from fatigue tests*

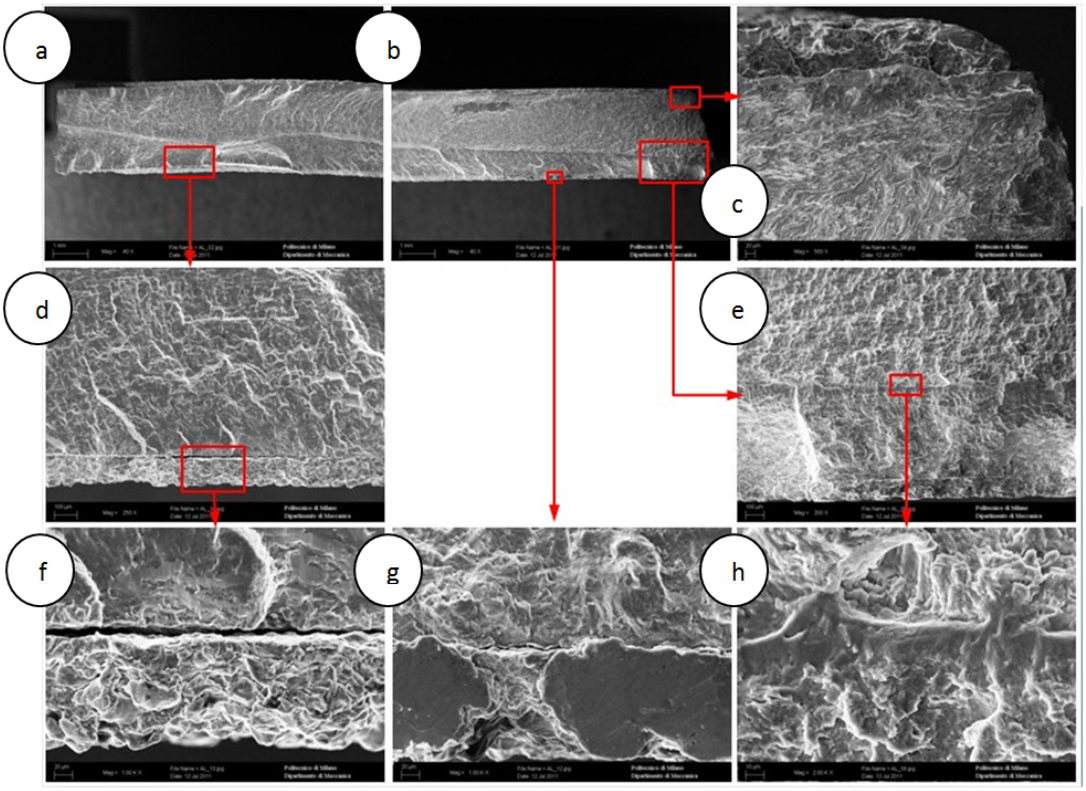

Figure 7.19: *Fracture surface SEM observation of specimen coated by pure aluminium*

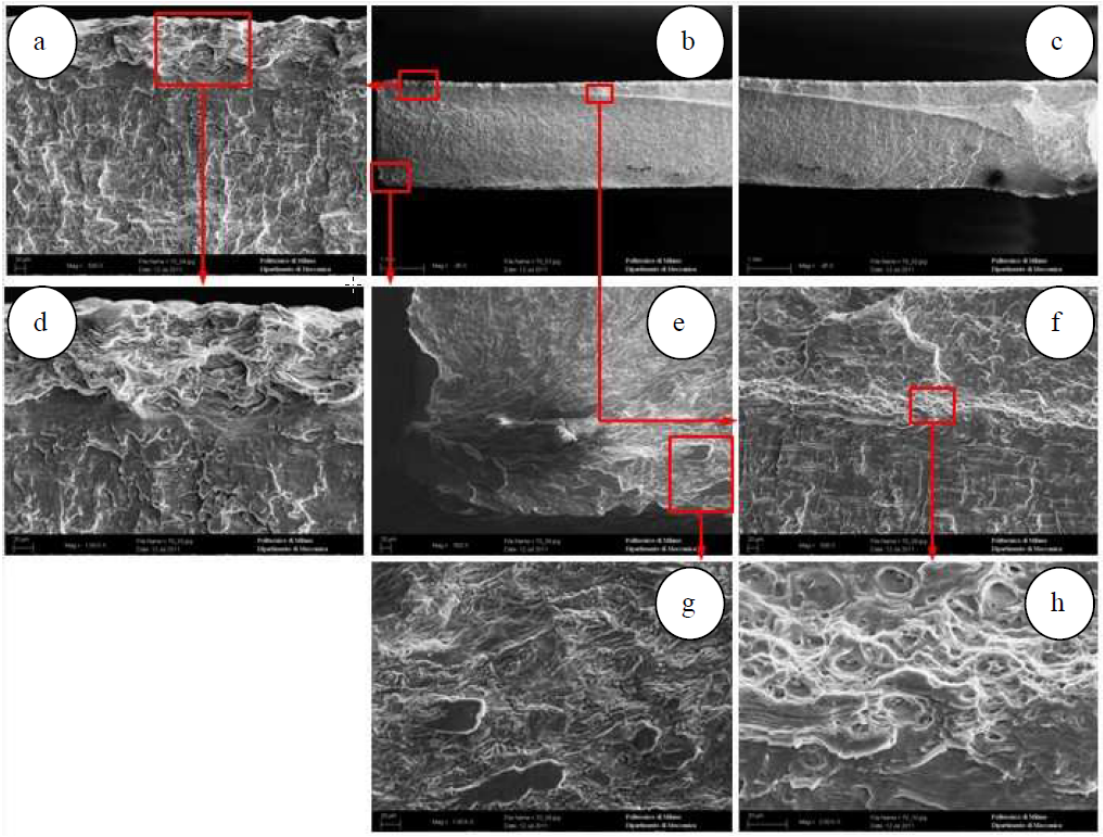

Figure 7.20: *Fracture surface SEM observation of specimen coated by Al7075*

On the other hand, in contrary to what was observed in Fig. 7.19, in Fig. 7.20 (a) and (d), the deposited material is strongly bonded to the substrate and the interface is not distinguishable. Fig. 7.20 (e) shows the crack initiation zone. The fact that the crack has initiated on the surface, confirms the participation of the deposited material in the fracture process. Fig. 7.20 (f) and (h) show more detailed views of the mentioned stripe in the specimen section. By comparing the last two figures (Fig. 7.19 and Fig. 7.20), it is clear that deposited material influences the fatigue fracture process; however the extent of this contribution depends strongly on the type of the deposited material. The results of the S-N diagram presented in Fig. 7.18 also confirm this hypothesis. Since the velocity of the particle and their kinetic energy were almost the same for both series (pure Al and Al7075) but the obtained fatigue strengths for these two sets of the specimens are different, it can be concluded that, apart from the residual stress, induced by the impact of the particles, the cold spray coating contributes to the fracture mechanism as well. As already mentioned, shot peening as an after treatment on coated samples, was not able to improve the fatigue strength of the specimens. Fig. 7.21 shows the micro-cracks introduced on the surface of the samples; in this case the crack is not very deep and has remained on the surface layer; however, it is big enough to decrease the fatigue life.

7.7 Conclusion

Effect of cold spray coating on the microstructural characteristics and the fatigue behavior of aluminum alloys have been studied. Different types of specimens with different treatments and coatings have been tested. The specimens were examined through microstructural analysis such as X-ray diffraction for residual stress as well as grain size measurement, SEM observation, and micro-hardness tests. According to the obtained results, the following conclusions can be drawn:

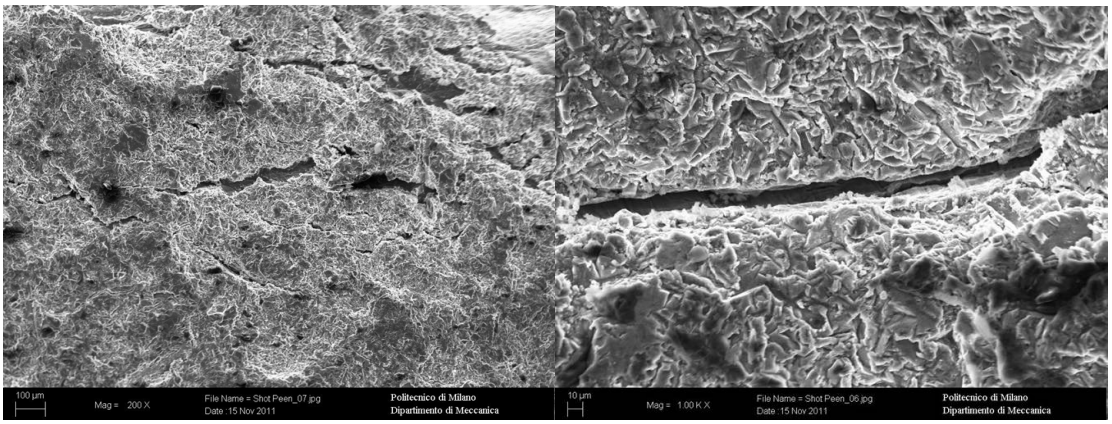

(a) **(b)**

Figure 7.21: *SEM observation on the surface of the shot peened samples*

- X-ray diffraction measurements exhibit compressive residual stresses in both deposited material and the substrate.
- Micro-hardness measurements of specimens coated by Al7075 indicate of considerable difference between the deposited material and the substrate hardness.
- Fatigue test results indicate that for the specimens coated by pure aluminum, grit blasting process, has no remarkable effect on the fatigue behavior.
- Fracture surface SEM observation of specimens coated by pure Al, acknowledge the fact that the coating in many cases has been delaminated from the specimens' surface. This observation shows that the deposited materials in some cases do not bear the applied load as the substrate does.
- The specimens coated by Al7075, which is twice harder than the substrate material, show higher fatigue endurance compared to the other treated series. From the SEM observation of these set of specimens, a different mechanism of cracking is observed which indicates that the deposited material helps the structure to resist more under the fatigue loading.
- Shot peening was not able to increase the fatigue endurance of the coated samples, although nanograins were generated on the samples' surface after combined coating and shot peening treatment. It must be due to the fact that, first the samples were not appropriate for such a severe treatments; second the high energy of the severe shot peening process creates micro cracks on the samples' surface which have deteriorating effects on the eventual fatigue strength.

On the basis of the previous points, it can be affirmed that by using more resistant coating with respect to the substrate material, a remarkable fatigue strength improvement can be obtained (up to 30%): this can be a key achievement in view of practical applications where fatigue damage can deteriorate cold sprayed Al alloy components functionality. By considering the fatigue limit of Al7075 ($\sim$150MPa) and the final results obtained from samples coated by this powder, it can be concluded that the fatigue behavior after coating, tries to follow the fatigue strength of the deposited material, in the case that the coated material has a higher fatigue endurance.

Bibliography

[1] T. S. Price, P. H. Shipway, and D. G. McCartney, "Effect of cold spray deposition of a titanium coating on fatigue behavior of a titanium alloy," *Journal of Thermal Spray Technology*, vol. 15, pp. 507–512, 2006.

[2] E. Sansoucy, G. E. Kim, A. L. Moran, and B. Jodoin, "Mechanical characteristics of al-co-ce coatings produced by the cold spray process," *Journal of Thermal Spray Technology*, vol. 16, pp. 651–660, 2007.

[3] B593-96, "Standard test method for bending fatigue testing for copper-alloy spring materials," *ASTMi*, no. B593-96, 2009.

[4] W. Dixon and F. Massey, *Introduction to statistical analysis*. McGraw-Hill, 1969.

[5] K. A. Brownlee, J. L. Hodges, and J. R. M. Rossenblatt, "The up-and-down method with small samples," *Journal of the American Statistical Association*, vol. 48, pp. 262–277, 1953.

Part IV

Conclusion

Chapter 8

Conclusion

8.1 Results and discussion

The researches prove the hypothesis started 20 years ago that nanocrystals (NC) can improve some properties of material which particularly depend on the material grain size. In order to benefit the advantages of NC in our daily life, the production of these materials plays the most important role. In this regard, cold spray as an innovative thermal spray coating technique can be used for deposition of NC powders, which can be produced by a wide variety of method, on the structure. In cold spray coating, the micro size powders bond to the substrate due to their high kinetic energy which is the result of the supersonic velocity of the gas passing through a deLavel nozzle. An inert gas such as helium or nitrogen with a high pressure and temperature, accelerate the powders till their velocity passes a certain value, so called as *critical velocity*. This critical velocity (CV) can be considered as a criterion for the particles whether they pass from erosion of the substrate to start deposing on it. Measuring the velocity of the particles due to many different factors such as their micro size, short standoff distance, etc., is not an easy task; as an apparent result of this difficulty, few experimental measurements of CV are available in the literature. Therefore, numerical methods have been utilized as a tool for estimating this important value and finally evaluating the whole process due to the fact that CV depends on many different properties of the powders and the substrate. It is to be mentioned that the bonding phenomena cannot be fully modeled in finite element (FE) simulation; Thus other approaches shall be considered for CV assessment through FE analysis. In this regard, scholars are in full agreement that the adiabatic shear instability and plastic flow localization play a major role in the particle/substrate bonding during the process, and that these parameters can be used to measure the CV of the process. The challenge of implementing this hypothesis on the discrete results of numerical simulations is to find the minimum particle velocity which causes such phenomenon in the results. The mentioned difficulty can be noticed by considering extremely different results presented by scholars using the very same criterion in order to find the CV in the processes which were almost identical.

In this work, a numerical simulation, which more or less follows the same approach suggested in the literature, is developed; the results of this numerical simulation are not interpreted by another physical criterion, but by using a mathematical approach which measures and compares the smoothness of different output data of the software for a wide range of particles' velocity. This method calculates the second derivative of different physical parameters as a function of time, obtained as discrete numbers, in Sobolev space. Due to the vibration induced by the particles' impact, a considerable noise which blurs the final judgement has been observed in the results; thus, a denoising process based on the Wavelet transform that cancels the low frequency part of the signal using a cross validation process, has been applied, providing clear data for a more accurate CV assessment. The estimated CV has been compared to the experimental measurements available in the literature; the comparison confirms a good correspondence of the performed numerical estimation and experimental measurement, the results of which are presented in Tab. 4.4. By implementing the explained method, different analysis have been performed to numerically study the effect of the particles' temperature as well as the effect of preceding shot peening. The final results presented in Tab. 4.5, show a rational trend, confirming the fact that both treatments

before coating are able to decrease the CV.
Cold spray coating intrinsically induces residual stresses and causes high plastic deformation in the substrate. Compressive residual stresses, in many cases, increase the fatigue endurance of the structure. Besides, high plastic deformation, as it has been discussed in previous chapters, can be considered as a criterion for grain refinement evaluation. A numerical model has been developed in order to estimate these two parameters. the model considers random distribution for particle size. Based on each particle size, it calculates the velocity and temperature which are functions of the particle size; analytical solutions presented in the literature have been used to estimate these parameters in the process. A Python code has been developed to control the whole modeling process before the solution and to elaborate the data once the analysis is finished. The result in terms of residual stress compared with experimental measurement by X-ray diffraction, does not show a good agreement in the beginning of its profile (Fig. 5.19) but the maximum in-depth value could be estimated with good approximation. The results of plastic deformation fulfill the criterion suggested in the literature for generation of the nanocrystalline on the substrate and evaluates the possibility of presence of nanograins in the interface.
Two different approaches can be considered to produce nanograins through cold spray coating: first, it is possible to produce nanocrystalline powders by severe plastic deformation (SPD) method such as milling, and depose the nano powders on the substrate; the second approach can be to apply a SPD method after the coating treatment. To the best of the knowledge of the author, this combined treatment has been applied for the first time in this research. In this regard, shot peening has been chosen as a post treatment to introduce SPD to the deposited materials. In order to approve the generation of nanograins through the combined coating-shot peening method, the grain size of the treated samples has been measured by implementing a numerical method on diffraction profile obtained from x-ray diffraction (XRD) measurements. This method is based on the assumption of Voigt function, separating grain size effect from micro-strain influence induced by the treatments. This single profile analysis is evaluated and approved by other well-known grain size measurement methods that are transmission electron microscopy (TEM) and full angle diffraction grain size measurement. This method has been used to measure the grain size on the coated specimens, to check the results of the numerical simulation for existence of nanograins on the substrate. The results approve the the fact that the impact of the cold spray particles on the substrate produce nanograins on its surface; other scholars have also reported the same observation for the coated samples. The grain size measurement shows that by applying a severe shot peening after coating, it is possible to obtain NC on the deposited material. The samples treated by combined shot peening and cold spray coating, were almost distorted due to the high energy of the impacts induced by both treatments.
In order to study the effect of cold spray coating on fatigue strength of the coated material, specimens designed based on ASTM standard, have been coated using different powders. A test machine which satisfies the requirements mentioned in the standard, has been assembled in the Labs. of Mechanical Engineering Department, Politecnico di Milano; This test machine has extra advantages with respect to the commercial version. The working frequency has been improved and the machine works based on the load control condition. The coating process has been performed at University of Ottawa using low pressure apparatus. The powders morphology and size dispersion has been studied by fitting a Rosin-Rammler distribution. The porosity of the coating was found to be almost zero and the interface of particle/substrate showed a good interlock. Fatigue tests have been performed on different series of specimens treated by grit blasting, cold spray coating, and shot peening with different combinations. The results of the W*ö*hler diagram, presented in Fig. 7.18, confirm the hypothesis that cold spray coating in general is able to improve the fatigue strength; in case of the tested specimens, at least 10% improvement was observed for all series; the test results indicated that the treated specimens' surface has the hardness of the deposited bulk material. In the best case, using a harder material as coating powder, the fatigue strength has been improved almost 30% and the author believes that in this case the final fatigue endurance is dominated by that of powders material.

8.2 Future work

This work has, hopefully, opened new doors to further investigation of cold spray process. The following items are suggested as future steps to broaden the horizon of cold spray knowledge, some of which are already under progress:

- although the numerical simulation for critical velocity assessment, presented in Chapter 4, shows reliable results compared to experimental measurements, the FEM simulation has its own limits for further understanding of this physical phenomenon. FEM simulation, in the case of NC powders, if not impossible to use, is absolutely difficult to implement. In this case, molecular dynamic simulation which is already under investigation, in a very new research has been found useful for deposition of particles without considering any other extra criterion, although it needs considerable computer facilities.

- even though the numerical model for residual stress profile estimation considers different parameters of the particles, it cannot model the bonding which might be the most important parameter in the process. It reduces the energy of the impact and causes softening in the whole material. However, accurate modeling of such phenomenon with FEM is technically impossible.

- fatigue strength investigation is focused on aluminum material. it would be interesting to continue the research on other material types to establish the hypothesis of the positive coating effect on fatigue strength. Moreover, the tests can be extended to other types of loading such as rotating bending or axial loading test.

- the NC in this work is produced by severe shot peening on coated specimens; this treatment imposes high plastic deformation on the specimens' surface layer and at the same time creates plenty of micro-cracks on the surface; consequently, it does not improve the fatigue life of the treated samples. As an alternative method, new series of specimens, can be coated by NC powders; this would be a more suitable way to produce NC on the surface of the studied specimens and it might increase the fatigue strength more than conventional coating particles. This approach has already been applied to a series of Al specimens and the tests are under progress.

- the last step to expand the research, would be to examine the process on a real product performing full-scale tests for different applications in order to evaluate the results.

Part V

Appendix

Appendix A

Code for Critical velocity

A.1 Python

```
import os
import shutil
from abaqus import *
from abaqusConstants import *
from part import *
from material import *
from section import *
from assembly import *
from step import *
from interaction import *
from load import *
from mesh import *
from job import *
from sketch import *
from visualization import *
from connectorBehavior import *
from abaqus import getInputs
import fileinput
from shutil import move
from odbAccess import *
from array import *
from Numeric import *
from math import *
import random
########################### Calculating The Area#################################
def Area(A1,A2,A3):
    a=sqrt((A1[0]-A2[0])**2+(A1[1]-A2[1])**2+(A1[2]-A2[2])**2)
    b=sqrt((A1[0]-A3[0])**2+(A1[1]-A3[1])**2+(A1[2]-A3[2])**2)
    c=sqrt((A2[0]-A3[0])**2+(A2[1]-A3[1])**2+(A2[2]-A3[2])**2)
    s=(a+b+c)/2
    area=s*(s-a)*(s-b)*(s-c)
    return area
########################### Calculating The Area#################################
############################ CREATING THE MODEL ##################################
def model(Dp,Vp,Tp,Ts,mf,shotmat,submat,step,cpunum,ram,scratch,time):
    Dp=float(Dp)
    Tp=int(Tp)
    mf=int(mf)
    cpunum=int(cpunum)
    ram=int(ram)
    Vp=int(Vp)
    size= float(7*Dp)*10**-3
    if step == 'Adiabatic':
      stepname='Adia'
    if step == 'Coupled':
      stepname='coup'
    substrate='Substrate'+submat
```

```
shot='Shot'+shotmat
particle='Particle'+shotmat
modelname=stepname+"D%d" %Dp+ "V%d" %Vp+"T%d"%Tp+submat+shotmat+"Mesh%d"%mf
#Create The working Dir
workdir=wd+"\\Temp\\Cold Spray\\6.9\\"+'Shot-'+shotmat+'Sub-'+submat+"\\"
        +stepname+"\\%d"%Dp+"\\%d"%mf
solvedir=wd+"\\Temp\\ForSolve"
if not os.path.exists(workdir):
    os.makedirs(workdir)
if not os.path.exists(solvedir):
    os.makedirs(solvedir)
if not os.path.exists(scratch):
    os.makedirs(scratch)
os.chdir(workdir)
path=workdir+"\\"+modelname+".cae"
# create the substrate model
# mdb.model(name=modelname)
mdb.Model(name=modelname)
mdb.models[modelname].ConstrainedSketch(name='__profile__', sheetSize=200.0)
mdb.models[modelname].sketches['__profile__'].rectangle(point1=(0.0, 0.0),
    point2=(size, size))
mdb.models[modelname].Part(dimensionality=THREE_D, name=substrate, type=
    DEFORMABLE_BODY)
mdb.models[modelname].parts[substrate].BaseSolidExtrude(depth=size/4,
    sketch=mdb.models[modelname].sketches['__profile__'])
del mdb.models[modelname].sketches['__profile__']
##
#The 4 Infinite boxes
#Number 1
mdb.models[modelname].ConstrainedSketch(gridSpacing=0.01,
    name='__profile__', sheetSize=0.57, transform=
    mdb.models[modelname].parts[substrate].MakeSketchTransform(
    sketchPlane=mdb.models[modelname].parts[substrate].faces[1],
    sketchPlaneSide=SIDE1,
    sketchUpEdge=mdb.models[modelname].parts[substrate].edges[4],
    sketchOrientation=RIGHT, origin=(size/2, size, size/8)))
mdb.models[modelname].parts[substrate].projectReferencesOntoSketch(
    filter=COPLANAR_EDGES, sketch=
    mdb.models[modelname].sketches['__profile__'])
mdb.models[modelname].sketches['__profile__'].rectangle(
    point1=(-size/8, size/2), point2=(size/8, -size/2))
mdb.models[modelname].parts[substrate].SolidExtrude(
    depth=size/10, flipExtrudeDirection=OFF, sketch=
    mdb.models[modelname].sketches['__profile__'],
    sketchOrientation=RIGHT, sketchPlane=
    mdb.models[modelname].parts[substrate].faces[1],
    sketchPlaneSide=SIDE1, sketchUpEdge=
    mdb.models[modelname].parts[substrate].edges[4])
del mdb.models[modelname].sketches['__profile__']
# Number2
mdb.models[modelname].ConstrainedSketch(gridSpacing=0.01,
    name='__profile__', sheetSize=0.57, transform=
    mdb.models[modelname].parts[substrate].MakeSketchTransform(
    sketchPlane=mdb.models[modelname].parts[substrate].faces[2],
    sketchPlaneSide=SIDE1,
    sketchUpEdge=mdb.models[modelname].parts[substrate].edges[9],
    sketchOrientation=RIGHT, origin=(size, size/2+size/20, size/8)))
mdb.models[modelname].parts[substrate].projectReferencesOntoSketch(
    filter=COPLANAR_EDGES, sketch=
    mdb.models[modelname].sketches['__profile__'])
mdb.models[modelname].sketches['__profile__'].rectangle(
    point1=(-size/8, size/2+size/20), point2=(size/8, -size/2+size/20))
mdb.models[modelname].parts[substrate].SolidExtrude(
    depth=size/10, flipExtrudeDirection=OFF, sketch=
    mdb.models[modelname].sketches['__profile__'],
    sketchOrientation=RIGHT, sketchPlane=
    mdb.models[modelname].parts[substrate].faces[2],
    sketchPlaneSide=SIDE1, sketchUpEdge=
```

```
    mdb.models[modelname].parts[substrate].edges[9])
del mdb.models[modelname].sketches['__profile__']
#Number 3
mdb.models[modelname].ConstrainedSketch(gridSpacing=0.01,
    name='__profile__', sheetSize=0.65, transform=
    mdb.models[modelname].parts[substrate].MakeSketchTransform(
    sketchPlane=mdb.models[modelname].parts[substrate].faces[5],
    sketchPlaneSide=SIDE1,
    sketchUpEdge=mdb.models[modelname].parts[substrate].edges[18],
    sketchOrientation=RIGHT, origin=(size/2+size/20, 0.0, size/8)))
mdb.models[modelname].parts[substrate].projectReferencesOntoSketch(
    filter=COPLANAR_EDGES, sketch=
    mdb.models[modelname].sketches['__profile__'])
mdb.models[modelname].sketches['__profile__'].rectangle(
    point1=(-size/8, size/2+size/20), point2=(size/8, -size/2+size/20))
mdb.models[modelname].parts[substrate].SolidExtrude(
    depth=size/10, flipExtrudeDirection=OFF, sketch=
    mdb.models[modelname].sketches['__profile__'],
    sketchOrientation=RIGHT, sketchPlane=
    mdb.models[modelname].parts[substrate].faces[5],
    sketchPlaneSide=SIDE1, sketchUpEdge=
    mdb.models[modelname].parts[substrate].edges[18])
del mdb.models[modelname].sketches['__profile__']
#Number 4
mdb.models[modelname].ConstrainedSketch(gridSpacing=0.01,
    name='__profile__', sheetSize=0.7, transform=
    mdb.models[modelname].parts[substrate].MakeSketchTransform(
    sketchPlane=mdb.models[modelname].parts[substrate].faces[5],
    sketchPlaneSide=SIDE1,
    sketchUpEdge=mdb.models[modelname].parts[substrate].edges[18],
    sketchOrientation=RIGHT, origin=(0, size/2, size/8)))
mdb.models[modelname].parts[substrate].projectReferencesOntoSketch(
    filter=COPLANAR_EDGES, sketch=
    mdb.models[modelname].sketches['__profile__'])
mdb.models[modelname].sketches['__profile__'].rectangle(
    point1=(-size/8, size/2), point2=(size/8, -size/2))
mdb.models[modelname].parts[substrate].SolidExtrude(
    depth=size/10, flipExtrudeDirection=OFF, sketch=
    mdb.models[modelname].sketches['__profile__'],
    sketchOrientation=RIGHT, sketchPlane=
    mdb.models[modelname].parts[substrate].faces[5],
    sketchPlaneSide=SIDE1, sketchUpEdge=
    mdb.models[modelname].parts[substrate].edges[18])
del mdb.models[modelname].sketches['__profile__']
##
#Partition the Infinite sections
mdb.models[modelname].parts[substrate].PartitionCellByPlanePointNormal(
    cells=
    mdb.models[modelname].parts[substrate].cells.getSequenceFromMask(
    ('[#1 ]', ), ), normal=
    mdb.models[modelname].parts[substrate].edges[3],
    point=
    mdb.models[modelname].parts[substrate].vertices[3])
mdb.models[modelname].parts[substrate].PartitionCellByPlanePointNormal(
    cells=
    mdb.models[modelname].parts[substrate].cells.getSequenceFromMask(
    ('[#1 ]', ), ), normal=
    mdb.models[modelname].parts[substrate].edges[23],
    point=
    mdb.models[modelname].parts[substrate].vertices[0])
mdb.models[modelname].parts[substrate].PartitionCellByPlanePointNormal(
    cells=
    mdb.models[modelname].parts[substrate].cells.getSequenceFromMask(
    ('[#2 ]', ), ), normal=
    mdb.models[modelname].parts[substrate].edges[35],
    point=
    mdb.models[modelname].parts[substrate].vertices[0])
mdb.models[modelname].parts[substrate].PartitionCellByPlanePointNormal(
```

```
    cells=
    mdb.models[modelname].parts[substrate].cells.getSequenceFromMask(
    ('[#4 ]', ), ), normal=
    mdb.models[modelname].parts[substrate].edges[11],
    point=
    mdb.models[modelname].parts[substrate].vertices[3])
##
#Partition the Contact Place
sizeCont=float(5*Dp)*10**-3
mdb.models[modelname].ConstrainedSketch(gridSpacing=0.01,
    name='__profile__', sheetSize=0.56, transform=
    mdb.models[modelname].parts[substrate].MakeSketchTransform(
    sketchPlane=mdb.models[modelname].parts[substrate].faces[2],
    sketchPlaneSide=SIDE1,
    sketchUpEdge=mdb.models[modelname].parts[substrate].edges[0],
    sketchOrientation=RIGHT, origin=(size/2, size/2, size/4)))
mdb.models[modelname].parts[substrate].projectReferencesOntoSketch(
    filter=COPLANAR_EDGES, sketch=
    mdb.models[modelname].sketches['__profile__'])
mdb.models[modelname].sketches['__profile__'].rectangle(
    point1=(-sizeCont/2, sizeCont/2), point2=(sizeCont/2, -sizeCont/2))
mdb.models[modelname].parts[substrate].PartitionCellBySketch(
    cells=
    mdb.models[modelname].parts[substrate].cells.getSequenceFromMask(
    ('[#8 ]', ), ), sketch=
    mdb.models[modelname].sketches['__profile__'],
    sketchPlane=
    mdb.models[modelname].parts[substrate].faces[2],
    sketchUpEdge=
    mdb.models[modelname].parts[substrate].edges[0])
del mdb.models[modelname].sketches['__profile__']
mdb.models[modelname].parts[substrate].PartitionCellByExtrudeEdge(
    cells=
    mdb.models[modelname].parts[substrate].cells.getSequenceFromMask(
    ('[#8 ]', ), ), edges=(
    mdb.models[modelname].parts[substrate].edges[0],
    mdb.models[modelname].parts[substrate].edges[1],
    mdb.models[modelname].parts[substrate].edges[2],
    mdb.models[modelname].parts[substrate].edges[3]),
    line=mdb.models[modelname].parts[substrate].edges[7],
    sense=FORWARD)
mdb.models[modelname].parts[substrate].PartitionCellByPlaneThreePoints(
    cells=
    mdb.models[modelname].parts[substrate].cells.getSequenceFromMask(
    ('[#1 ]', ), ), point1=
    mdb.models[modelname].parts[substrate].vertices[16],
    point2=
    mdb.models[modelname].parts[substrate].vertices[3],
    point3=
    mdb.models[modelname].parts[substrate].vertices[0])
mdb.models[modelname].parts[substrate].PartitionCellByPlaneThreePoints(
    cells=
    mdb.models[modelname].parts[substrate].cells.getSequenceFromMask(
    ('[#3 ]', ), ), point1=
    mdb.models[modelname].parts[substrate].vertices[11],
    point2=
    mdb.models[modelname].parts[substrate].vertices[10],
    point3=
    mdb.models[modelname].parts[substrate].vertices[13])
##Creating the Particle
Rp=float(Dp/2)*10**-3
mdb.models[modelname].ConstrainedSketch(name='__profile__', sheetSize=200.0)
mdb.models[modelname].ConstrainedSketch(name='__profile__', sheetSize=200.0)
mdb.models[modelname].sketches['__profile__'].ConstructionLine(point1=(0.0,
    -100.0), point2=(0.0, 100.0))
mdb.models[modelname].sketches['__profile__'].FixedConstraint(entity=
    mdb.models[modelname].sketches['__profile__'].geometry[2])
mdb.models[modelname].sketches['__profile__'].Arc3Points(point1=(0.0, Rp),
```

```
    point2=(0.0, -Rp), point3=(Rp, 0.0))
mdb.models[modelname].sketches['__profile__'].CoincidentConstraint(entity1=
    mdb.models[modelname].sketches['__profile__'].vertices[0], entity2=
    mdb.models[modelname].sketches['__profile__'].geometry[2])
mdb.models[modelname].sketches['__profile__'].CoincidentConstraint(entity1=
    mdb.models[modelname].sketches['__profile__'].vertices[1], entity2=
    mdb.models[modelname].sketches['__profile__'].geometry[2])
mdb.models[modelname].sketches['__profile__'].Line(point1=(0.0, Rp),
    point2=(0.0, -Rp))
mdb.models[modelname].Part(dimensionality=THREE_D, name=shot, type=
    DEFORMABLE_BODY)
mdb.models[modelname].parts[shot].BaseSolidRevolve(angle=360.0,
    flipRevolveDirection=OFF, sketch=
    mdb.models[modelname].sketches['__profile__'])
del mdb.models[modelname].sketches['__profile__']
##Partition the Particle
mdb.models[modelname].parts[shot].PartitionCellByPlanePointNormal(
    cells=
    mdb.models[modelname].parts[shot].cells.getSequenceFromMask(
    ('[#1 ]', ), ), normal=
    mdb.models[modelname].parts[shot].datums[1], point=
    mdb.models[modelname].parts[shot].InterestingPoint(
    mdb.models[modelname].parts[shot].edges[0], MIDDLE))
mdb.models[modelname].parts[shot].PartitionCellByPlaneThreePoints(
    cells=
    mdb.models[modelname].parts[shot].cells.getSequenceFromMask(
    ('[#3 ]', ), ), point1=
    mdb.models[modelname].parts[shot].vertices[1],
    point2=mdb.models[modelname].parts[shot].vertices[0],
    point3=mdb.models[modelname].parts[shot].vertices[2])
mdb.models[modelname].parts[shot].PartitionCellByPlanePointNormal(
    cells=
    mdb.models[modelname].parts[shot].cells.getSequenceFromMask(
    ('[#f ]', ), ), normal=
    mdb.models[modelname].parts[shot].edges[0], point=
    mdb.models[modelname].parts[shot].InterestingPoint(
    mdb.models[modelname].parts[shot].edges[6], MIDDLE))
##Defining The Materials
distortion=2*Rp
mdb.models[modelname].Material(name=shotmat)
mdb.models[modelname].materials[shotmat].Density(table=((M1[0], ), ))
mdb.models[modelname].materials[shotmat].Plastic(hardening=JOHNSON_COOK,
    table=((M1[3], M1[4], M1[5], M1[6], M1[7], M1[8]), ))
mdb.models[modelname].materials[shotmat].plastic.RateDependent(table=((M1[9],
    M1[10]), ), type=JOHNSON_COOK)
mdb.models[modelname].materials[shotmat].SpecificHeat(table=((M1[11], ), ))
mdb.models[modelname].materials[shotmat].InelasticHeatFraction(M1[12], )
mdb.models[modelname].materials[shotmat].Eos(table=((M1[13], M1[14], M1[15]),
    ), type=USUP)
mdb.models[modelname].materials[shotmat].eos.EosShear(table=((
    M1[16], ), ))
mdb.models[modelname].materials[shotmat].Conductivity(table=((
    M1[17], ), ))
mdb.models[modelname].materials[shotmat].JohnsonCookDamageInitiation(
    table=((M1[19], M1[20], M1[21], M1[22], M1[23], M1[7], M1[8], M1[9]), ))
mdb.models[modelname].materials[shotmat].johnsonCookDamageInitiation.
        DamageEvolution(table=((distortion, ), ), type=DISPLACEMENT)
mdb.models[modelname].Material(name=submat)
mdb.models[modelname].materials[submat].Density(table=((M2[0], ), ))
mdb.models[modelname].materials[submat].Elastic(table=((M2[1], M2[2]), ))
mdb.models[modelname].materials[submat].Plastic(hardening=JOHNSON_COOK,
    table=((M2[3], M2[4], M2[5], M2[6], M2[7], M2[8]), ))
mdb.models[modelname].materials[submat].plastic.RateDependent(table=((M2[9],
    M2[10]), ) , type=JOHNSON_COOK)
mdb.models[modelname].materials[submat].SpecificHeat(table=((M1[11], ), ))
mdb.models[modelname].materials[submat].InelasticHeatFraction(M2[12], )
mdb.models[modelname].materials[submat].Conductivity(table=((
    M2[17], ), ))
```

```
mdb.models[modelname].materials[shotmat].JohnsonCookDamageInitiation(
    table=((M2[19], M2[20], M2[21], M2[22], M2[23], M2[7], M2[8], M2[9]), ))
mdb.models[modelname].materials[shotmat].johnsonCookDamageInitiation.DamageEvolution(
    table=((distortion, ), ), type=DISPLACEMENT)
mdb.models[modelname].Material(name='Infinite')
mdb.models[modelname].materials['Infinite'].Density(table=((M1[0], ), ))
mdb.models[modelname].materials['Infinite'].Elastic(table=((M2[1], M2[2]), ))
## Defining The Sections
mdb.models[modelname].HomogeneousSolidSection(material=shotmat, name=
    'Particle', thickness=1.0)
mdb.models[modelname].parts[shot].SectionAssignment(
    offset=0.0, offsetField='', offsetType=MIDDLE_SURFACE, region=Region(
    cells=mdb.models[modelname].parts[shot].cells.getSequenceFromMask(
    mask=('[#ff ]', ), )), sectionName='Particle')
mdb.models[modelname].HomogeneousSolidSection(material=submat, name=
    'Substrate', thickness=1.0)
mdb.models[modelname].parts[substrate].SectionAssignment(
    offset=0.0, offsetField='', offsetType=MIDDLE_SURFACE, region=Region(
    cells=mdb.models[modelname].parts[substrate].cells.getSequenceFromMask(
    mask=('[#8f ]', ), )), sectionName='Substrate')
mdb.models[modelname].HomogeneousSolidSection(material='Infinite',
    name='Infinite', thickness=1.0)
mdb.models[modelname].parts[substrate].SectionAssignment(
    offset=0.0, offsetField='', offsetType=MIDDLE_SURFACE, region=Region(
    cells=mdb.models[modelname].parts[substrate].cells.getSequenceFromMask(
    mask=('[#170 ]', ), )), sectionName='Infinite')
## Assembly
shotassembly=shot+'-1'
subassembly=substrate+'-1'
mdb.models[modelname].rootAssembly.DatumCsysByDefault(CARTESIAN)
mdb.models[modelname].rootAssembly.Instance(dependent=ON, name=
    subassembly, part=
    mdb.models[modelname].parts[substrate])
mdb.models[modelname].rootAssembly.translate(instanceList=(
    subassembly, ), vector=(-size/2, -size/2, -size/4))
mdb.models[modelname].rootAssembly.Instance(dependent=ON, name=
    shotassembly, part=mdb.models[modelname].parts[shot])
mdb.models[modelname].rootAssembly.translate(instanceList=(
    shotassembly, ), vector=(0.0, 0.0, Rp))
mdb.models[modelname].rootAssembly.Set(edges=
    mdb.models[modelname].rootAssembly.instances[shotassembly].
    edges.getSequenceFromMask( ('[#400 ]', ), ), name='History')
mdb.models[modelname].rootAssembly.Set(faces=
    mdb.models[modelname].rootAssembly.instances[subassembly].faces.
    getSequenceFromMask(  ('[#8000 ]', ), ), name='Surface')
##Create Steps
time=time*1e-8
if step == 'Adiabatic':
        mdb.models[modelname].ExplicitDynamicsStep(adiabatic=ON,
        name='Step-1', previous='Initial', timePeriod=time)
        mdb.models[modelname].steps['Step-1'].setValues(maxIncrement=1e-10)
if step == 'Coupled':
        mdb.models[modelname].TempDisplacementDynamicsStep(name=
       'Step-1', previous='Initial', timePeriod=time)
#mdb.models[modelname].steps['Step-1'].setValues(
#        timeIncrementationMethod=FIXED_USER_DEFINED_INC, userDefinedInc=7.5e-11)
mdb.models[modelname].fieldOutputRequests['F-Output-1'].setValues(
    timeInterval=5e-09)
mdb.models[modelname].fieldOutputRequests['F-Output-1'].setValues(
    variables=('S', 'PE', 'PEEQ', 'LE', 'U', 'V', 'TEMP'))
mdb.models[modelname].historyOutputRequests['H-Output-1'].setValues(
    timeInterval=1e-10, rebar=EXCLUDE, region=
    mdb.models[modelname].rootAssembly.sets['History'],
    sectionPoints=DEFAULT, variables=('TEMP', 'PEEQ', 'ER11', 'ER22', 'ER33',
    'ER12', 'ER13', 'ER23', 'MISES'))
##Meshing
##The Particle
meshsize=float(Dp)/float(mf)*10**-3
```

```
    if step == 'Adiabatic':
        mdb.models[modelname].parts[shot].setElementType(
            elemTypes=(ElemType(elemCode=C3D8R, elemLibrary=EXPLICIT,
            secondOrderAccuracy=OFF, kinematicSplit=AVERAGE_STRAIN,
            hourglassControl=STIFFNESS, distortionControl=ON, lengthRatio=0.1),
            ElemType(elemCode=C3D6, elemLibrary=EXPLICIT), ElemType(elemCode=C3D4,
            elemLibrary=EXPLICIT)), regions=(
            mdb.models[modelname].parts[shot].cells.getSequenceFromMask(
            ('[#f ]', ), ), ))
    if step == 'Coupled':
        mdb.models[modelname].parts[shot].setElementType(
            elemTypes=(ElemType(elemCode=C3D8RT, elemLibrary=EXPLICIT,
            secondOrderAccuracy=OFF, kinematicSplit=AVERAGE_STRAIN,
            hourglassControl=STIFFNESS, distortionControl=ON, lengthRatio=0.1),
            ElemType(elemCode=C3D6T, elemLibrary=EXPLICIT), ElemType(elemCode=C3D4T,
            elemLibrary=EXPLICIT)), regions=(
            mdb.models[modelname].parts[shot].cells.getSequenceFromMask(
            ('[#f ]', ), ), ))
    mdb.models[modelname].parts[shot].seedPart(
        deviationFactor=0.1, size=meshsize)
    mdb.models[modelname].parts[shot].generateMesh()
    ##Substrate
    if step == 'Adiabatic':
        mdb.models[modelname].parts[substrate].setElementType(
            elemTypes=(ElemType(elemCode=C3D8R, elemLibrary=EXPLICIT,
            secondOrderAccuracy=OFF, kinematicSplit=AVERAGE_STRAIN,
            hourglassControl=STIFFNESS, distortionControl=ON, lengthRatio=0.1),
            ElemType(elemCode=C3D6, elemLibrary=EXPLICIT), ElemType(elemCode=C3D4,
            elemLibrary=EXPLICIT)), regions=(
            mdb.models[modelname].parts[substrate].cells.getSequenceFromMask(
            ('[#8f ]', ), ), ))
    if step == 'Coupled':
        mdb.models[modelname].parts[substrate].setElementType(
            elemTypes=(ElemType(elemCode=C3D8RT, elemLibrary=EXPLICIT,
            secondOrderAccuracy=OFF, kinematicSplit=AVERAGE_STRAIN,
            hourglassControl=STIFFNESS, distortionControl=ON, lengthRatio=0.1),
            ElemType(elemCode=C3D6T, elemLibrary=EXPLICIT), ElemType(elemCode=C3D4T,
            elemLibrary=EXPLICIT)), regions=(
            mdb.models[modelname].parts[substrate].cells.getSequenceFromMask(
            ('[#8f ]', ), ), ))
#     mdb.models[modelname].parts[substrate].setMeshControls(
    regions=
    mdb.models[modelname].parts[substrate].cells.getSequenceFromMask(
    ('[#8e ]', ), ), technique=STRUCTURED)
    meshno1=int(size/meshsize/2)
    meshno3=int(0.2*size/meshsize)
    mdb.models[modelname].parts[substrate].seedEdgeByNumber(
        edges=
        mdb.models[modelname].parts[substrate].edges.getSequenceFromMask(
        ('[#ff0b6d00 ]', ), ), number=meshno1)
    nbias1=int(ceil((size/4/meshsize/2-1)*2/14))
    nbias2=int(ceil((size/4/meshsize/2-1)*2)/2)
    if nbias2<5:
        nbias2=5
    mdb.models[modelname].parts[substrate].seedEdgeByBias(
        end1Edges=
        mdb.models[modelname].parts[substrate].edges.getSequenceFromMask(
        ('[#f000a2 ]', ), ), end2Edges=
        mdb.models[modelname].parts[substrate].edges.getSequenceFromMask(
        ('[#8 ]', ), ), number=nbias2, ratio=2)
    mdb.models[modelname].parts[substrate].seedEdgeByBias(
        end1Edges=
        mdb.models[modelname].parts[substrate].edges.getSequenceFromMask(
        ('[#1214 ]', ), ), end2Edges=
        mdb.models[modelname].parts[substrate].edges.getSequenceFromMask(
        ('[#48041 ]', ), ), number=nbias1, ratio=14)
    mdb.models[modelname].parts[substrate].generateMesh(
        regions=
```

```
    mdb.models[modelname].parts[substrate].cells.getSequenceFromMask(
    ('[#80 ]', ), ))
mdb.models[modelname].parts[substrate].generateMesh(
    regions=
    mdb.models[modelname].parts[substrate].cells.getSequenceFromMask(
    ('[#1 ]', ), ))
mdb.models[modelname].parts[substrate].generateMesh(
    regions=
    mdb.models[modelname].parts[substrate].cells.getSequenceFromMask(
    ('[#4 ]', ), ))
mdb.models[modelname].parts[substrate].generateMesh(
    regions=
    mdb.models[modelname].parts[substrate].cells.getSequenceFromMask(
    ('[#2 ]', ), ))
mdb.models[modelname].parts[substrate].generateMesh(
    regions=
    mdb.models[modelname].parts[substrate].cells.getSequenceFromMask(
    ('[#8 ]', ), ))
##Infinite Part
mdb.models[modelname].parts[substrate].setMeshControls(
regions=
mdb.models[modelname].parts[substrate].cells.getSequenceFromMask(
('[#170 ]', ), ), technique=BOTTOM_UP)
mdb.meshEditOptions.setValues(enableUndo=True, maxUndoCacheElements=0.5)
mdb.models[modelname].parts[substrate].generateBottomUpExtrudedMesh(
    cell=mdb.models[modelname].parts[substrate].cells[6],
    extrudeVector=(
    mdb.models[modelname].parts[substrate].vertices[12],
    mdb.models[modelname].parts[substrate].vertices[22]),
    geometrySourceSide=Region(
    faces=mdb.models[modelname].parts[substrate].faces.getSequenceFromMask(
    mask=('[#400000 ]', ), )), numberOfLayers=1)
mdb.models[modelname].parts[substrate].generateBottomUpExtrudedMesh(
    cell=mdb.models[modelname].parts[substrate].cells[8],
    extrudeVector=(
    mdb.models[modelname].parts[substrate].vertices[0],
    mdb.models[modelname].parts[substrate].vertices[26]),
    geometrySourceSide=Region(
    faces=mdb.models[modelname].parts[substrate].faces.getSequenceFromMask(
    mask=('[#2000000 ]', ), )), numberOfLayers=1)
mdb.models[modelname].parts[substrate].generateBottomUpExtrudedMesh(
    cell=mdb.models[modelname].parts[substrate].cells[4],
    extrudeVector=(
    mdb.models[modelname].parts[substrate].vertices[10],
    mdb.models[modelname].parts[substrate].vertices[20]),
    geometrySourceSide=Region(
    faces=mdb.models[modelname].parts[substrate].faces.getSequenceFromMask(
    mask=('[#10000 ]', ), )), numberOfLayers=1)
mdb.models[modelname].parts[substrate].generateBottomUpExtrudedMesh(
    cell=mdb.models[modelname].parts[substrate].cells[5],
    extrudeVector=(
    mdb.models[modelname].parts[substrate].vertices[6],
    mdb.models[modelname].parts[substrate].vertices[19]),
    geometrySourceSide=Region(
    faces=mdb.models[modelname].parts[substrate].faces.getSequenceFromMask(
    mask=('[#80000 ]', ), )), numberOfLayers=1)
mdb.models[modelname].parts[substrate].setElementType(
    elemTypes=(ElemType(elemCode=AC3D8R, elemLibrary=EXPLICIT), ElemType(
    elemCode=AC3D6, elemLibrary=EXPLICIT), ElemType(elemCode=AC3D4,
    elemLibrary=EXPLICIT)), regions=(
    mdb.models[modelname].parts[substrate].cells.getSequenceFromMask(
    ('[#170 ]', ), ), ))
mdb.models[modelname].parts[substrate].setElementType(
    elemTypes=(ElemType(elemCode=C3D8R, elemLibrary=EXPLICIT,
    secondOrderAccuracy=OFF, kinematicSplit=AVERAGE_STRAIN,
    hourglassControl=DEFAULT, distortionControl=ON, lengthRatio=0.1), ElemType(
    elemCode=C3D6, elemLibrary=EXPLICIT), ElemType(elemCode=C3D4,
    elemLibrary=EXPLICIT)), regions=(
```

```
    mdb.models[modelname].parts[substrate].cells.getSequenceFromMask(
    ('[#8f ]', ), ), ))
mdb.models[modelname].rootAssembly.regenerate()
mdb.models[modelname].rootAssembly.Surface(name='Surf-1',
    side1Faces=
    mdb.models[modelname].rootAssembly.instances[shotassembly].faces.
        getSequenceFromMask(
    ('[#cc4b0 ]', ), ))
mdb.models[modelname].rootAssembly.Surface(name='Surf-2',
    side1Faces=
    mdb.models[modelname].rootAssembly.instances[subassembly].faces.
        getSequenceFromMask(
    ('[#8000 ]', ), ))
mdb.models[modelname].ContactProperty('IntProp-1')
mdb.models[modelname].interactionProperties['IntProp-1'].TangentialBehavior(
    formulation=FRICTIONLESS)
mdb.models[modelname].ContactExp(createStepName='Initial',
    name='Int-1')
mdb.models[modelname].interactions['Int-1'].includedPairs.setValuesInStep(
    addPairs=((
    mdb.models[modelname].rootAssembly.surfaces['Surf-1'],
    mdb.models[modelname].rootAssembly.surfaces['Surf-2']), )
    , stepName='Initial', useAllstar=OFF)
mdb.models[modelname].interactions['Int-1'].contactPropertyAssignments.appendInStep(
    assignments=((GLOBAL, SELF, 'IntProp-1'), ), stepName='Initial')
##VELOCITY AND TEMPERATURE
mdb.models[modelname].Velocity(name='Predefined Field-1',
    omega=0.0, region=Region(
    cells=mdb.models[modelname].rootAssembly.instances[shotassembly].cells.
        getSequenceFromMask(
    mask=('[#ff ]', ), )), velocity1=0.0, velocity2=0.0, velocity3=-Vp*1000)
mdb.models[modelname].Temperature(createStepName='Initial',
    crossSectionDistribution=CONSTANT_THROUGH_THICKNESS, distributionType=
    UNIFORM, magnitudes=(Tp, ), name='Predefined Field-2', region=Region(
    cells=mdb.models[modelname].rootAssembly.instances[shotassembly].cells.
        getSequenceFromMask(
    mask=('[#ff ]', ), ),
    faces=mdb.models[modelname].rootAssembly.instances[shotassembly].faces.
        getSequenceFromMask(
    mask=('[#fffff ]', ), ),
    edges=mdb.models[modelname].rootAssembly.instances[shotassembly].
    edges.getSequenceFromMask( mask=('[#3ffff ]', ), ),
    vertices=mdb.models[modelname].rootAssembly.instances[shotassembly].
    vertices.getSequenceFromMask(      mask=('[#7f ]', ), )))
mdb.models[modelname].Temperature(createStepName='Initial',
    crossSectionDistribution=CONSTANT_THROUGH_THICKNESS, distributionType=
    UNIFORM, magnitudes=(Ts, ), name='Predefined Field-3', region=Region(
    cells=mdb.models[modelname].rootAssembly.instances[subassembly].cells.
        getSequenceFromMask(
    mask=('[#8f ]', ), ),
    faces=mdb.models[modelname].rootAssembly.instances[subassembly].faces.
        getSequenceFromMask(
    mask=('[#34dffff ]', ), ),
    edges=mdb.models[modelname].rootAssembly.instances[subassembly].edges.
        getSequenceFromMask(
    mask=('[#ffffffff ]', ), ),
    vertices=mdb.models[modelname].rootAssembly.instances[subassembly].
    vertices.getSequenceFromMask( mask=('[#ffff ]', ), )))
surfaceSet= mdb.models[modelname].rootAssembly.sets['Surface']
nodelabel=[]
for node in surfaceSet.nodes:
    nodelabel.append(node.label)
TotalArea=0
for element in surfaceSet.elements:
    coord=[]
    for num in element.connectivity:
        if num in nodelabel:
            index=nodelabel.index(num)
```

```
                coord.append(surfaceSet.nodes[index].coordinates)
        if len(coord)==4:
            elemArea=0
            elemArea=Area(coord[0],coord[1],coord[2])+elemArea
            elemArea=Area(coord[0],coord[1],coord[3])+elemArea
            elemArea=Area(coord[1],coord[2],coord[3])+elemArea
            elemArea=Area(coord[0],coord[2],coord[3])+elemArea
            TotalArea=TotalArea+(elemArea/2)
    ##Define the Job
    inputpath=workdir+'\\'+modelname+'.inp'
    inputnew=solvedir+'\\'+modelname+'.inp'
    myjob=mdb.Job(atTime=None, contactPrint=OFF, description='', echoPrint=OFF,
            explicitPrecision=SINGLE, getMemoryFromAnalysis=True, historyPrint=OFF,
            memory=ram, memoryUnits=GIGA_BYTES, model=modelname,
            modelPrint=OFF, multiprocessingMode=DEFAULT, name=modelname,
            nodalOutputPrecision=SINGLE, numCpus=cpunum, numDomains=cpunum,
            parallelizationMethodExplicit=DOMAIN, queue=None, scratch=scratch,
            type=ANALYSIS, userSubroutine='')
    mdb.saveAs(pathName=path)
    mdb.models[modelname].rootAssembly.regenerate()
    mdb.jobs[modelname].writeInput(consistencyChecking=OFF)
    ##Creat The New INP file
    for name in os.listdir(solvedir):
      fullpath=os.path.join(solvedir,name)
      os.remove(fullpath)
    change=open(inputpath,'r')
    new=open(inputnew,'w')
    lines=change.readlines()
    nodeplace=False
    for line in lines:
      if nodeplace and line[0:9]=='*Element':
          nodeplace=False
      if nodeplace:
          splited=line.split(',')
          nodenum=int(splited[0])
          if nodenum in nodelabel:
              nodez=float(splited[3])
              newline=splited[0]+splited[1]+splited[2]
      if line=='*Node':
         nodeplace=False
      if line=='*Element, type=AC3D8R\n':
         new.write("*Element, type=CIN3D8\n")
      elif not nodeplace:
         new.write(line)
    del change
    del new
 #   envfile=open(solvedir+"\\abaqus_v6.env",'w')
 #   envfile.write("""pre_memory = "4000 mb"
 #                            standard_memory = "4000 mb"
 #                            cpus=4
 #                            scratch="E:/scratch"
 #                            """)
 #   del envfile
    os.chdir(solvedir)
    mdb.JobFromInputFile(name=modelname,
            inputFileName=inputnew, type=ANALYSIS,
            explicitPrecision=SINGLE, nodalOutputPrecision=SINGLE, memory=ram,
            memoryUnits=GIGA_BYTES,parallelizationMethodExplicit=DOMAIN,
            multiprocessingMode=DEFAULT,numDomains=cpunum, userSubroutine='',
             numCpus=cpunum, scratch=scratch)
    odbfin=solvedir+'\\'+modelname+'.odb'
    a=[modelname,odbfin,inputnew,workdir,TotalArea]
    #mdb.close()
    return a
##############################################################################
fields = (('Dp(1e-6m)=','10'), ('Initial Vp(mm/s)=','250'),
         ('Max Vp(mm/s)=','800'),('Steps of Vp(mm/s)=','50'),
          ('Tp(K)=','300'), ('Ts(K)=','300'), ('Mesh Fraction=','20'),
```

```
         ('Particle Material=' , 'Cu'), ('Substrate Material=' , 'Cu'),
         ('Analysis Type=','Adiabatic'),('Work Dir=','E:'),('Num of CPU=','4'),
          ('Memory=','4'),('Scratch:','E:/scratch'),('Time(1e-8):','2'))
diam, velo, velomax, stepvp, tempp,temps, mefr, partmat, submat, steptype, wd, cpunum,
        ram, scratch,time=getInputs(fields=fields, label='CS Parameters',
         dialogTitle='Particel Properties', )
Dp=int(diam)
Tp=int(tempp)
Ts=int(temps)
mf=int(mefr)
cpunum=int(cpunum)
ram=int(ram)
Vpmin=float(velo)
Vpmax=float(velomax)
StepVp=int(stepvp)
time=float(time)
if steptype <> 'Adiabatic' or steptype <> 'Coupled':
  reply=getWarningReply(message="Analyse type should be 'Adaibatic' or 'Coupled'
        with "+"'", bottons(ok))
#Materil=[Density[0]g/mm3, Young's Module[1]MPa, Poisson's Ratio[2], A(J-C)[3]MPa
#         , B(J-c)[4]MPa, n(J-C)[5], m(J-C)[6], Melting Point(J-C)[7]K
#          , Transition Temperature(J-C)[8], C(RateDepen)[9],
#       , Epsilon Zero(RateDepen)[10], Specific Heat[11]J/kg*e+6, Inelastic Heat Fraction[12],
#       , C0(Hogioit)[13]mm/s, s(Hogiot)[14], Gamma(Hogiot)[15],
#   , Shear Modulos[16]MPa,Conductivity[17]mW/mmK, Name[18], Johnson cook damage Parameters[19-23]]
Cu=[8.96e-9,124000,0.34,90,292,0.31,1.09,1356,298,0.025,1,3.83e+08,0.9,
    3.91*10**6,1.5,1.93,48000,386, 'Cu',0.54,4.89,-3.03,0.014,1.12]
SS316=[8.031e-9,193000,0.3,388,901,0.8722,0.6567,1643,298,0.02494,1e-5,
    4.57e+08,0.9,4.63*10**6,1.334,2.18,82000,16, 'SS316',-0.77,1.45,-0.47,0,1.6]
Al2=[2.77e-9,73100,0.35,265,426,0.34,1.31,775,298,0.015,10500,8.75e+08,
    0.9,5.328e+06,1.338,2,26000,237, 'Al2',0.112,0.123,1.5,0.007,0]
Ti=[4.5e-9,116000,0.32,782.7,498.4,0.28,1,1935,298,0.028,2000,5.2e+8,
    0.9,5.22e+06,0.767,2,44000,219, 'Ti',-0.09,0.27,0.48,0.014,3.87]
Ni=[8.908e-9,200000,0.31,450,1728,0.65,1.3,1728,298,0.017,1.001,
    4.35e+08,0.9,4.53e+06,1.545,2.77,76000,90.9, 'Ni',-0.77,1.45,-0.47,0,1.6]
#Step could be 'Adiabatic' or 'Coupled'
if partmat=='Cu':
  M1=Cu
if partmat=='SS316':
  M1=SS316
if partmat=='Al2':
  M1=Al2
if partmat=='Ti':
  M1=Ti
if partmat=='Ni':
  M1=Ni
if submat=='Cu':
  M2=Cu
if submat=='SS316':
  M2=SS316
if submat=='Al2':
  M2=Al2
if submat=='Ti':
  M2=Ti
if submat=='Ni':
  M2=Ni
shotmat=M1[18]
submat=M2[18]
end=False
numit=0
Vp=Vpmin
while Vp<(Vpmax+1):
    #Vplist=[0,velo]
    #Find=False
    #while not Find:
    #Vp=Vplist[-1]
    solve=model(Dp,Vp,Tp,Ts,mf,shotmat,submat,steptype,cpunum,ram,scratch,time)
    result=solve[3]+'\\Results'+str(Vpmin)+'-'+str(StepVp)+'-'+str(Vpmax)
```

```
    result2=solve[3]+'\\Results'
    if not os.path.exists(result):
        os.makedirs(result)
    if not os.path.exists(result2):
        os.makedirs(result2)
    try:
        List=open(result+'\\List.dat','r+')
        List.readlines()
    except IOError:
        List=open(result+'\\List.dat','w')
    try:
        List2=open(result2+'\\List.dat','r+')
        List2.readlines()
    except IOError:
        List2=open(result2+'\\List.dat','w')
    mdb.jobs[solve[0]].submit(consistencyChecking=OFF)
    mdb.jobs[solve[0]].waitForCompletion()
    move(solve[1],solve[3])
    move(solve[2],solve[3])
    odb = openOdb(path=solve[3]+"\\"+solve[0]+".odb")
    historyRegionNameList=odb.steps['Step-1'].historyRegions.keys()
    nhistory=len(historyRegionNameList)
    historyOutputValues=[]
    EPnum=0
    file11=open(result2+'//PEEQ-'+str(Vp)+'.dat','w')
    file1=open(result2+'//TEMP-'+str(Vp)+'.dat','w')
    file2=open(result2+'//MISES-'+str(Vp)+'.dat','w')
    file3=open(result2+'//StRate-'+str(Vp)+'.dat','w')
    List2.write('PEEQ-'+str(Vp)+'.dat\n')
    List2.write('TEMP-'+str(Vp)+'.dat\n')
    List2.write('MISES-'+str(Vp)+'.dat\n')
    List2.write('StRate-'+str(Vp)+'.dat\n')
#    for k in range(nhistory):
#      name=odb.steps['Step-1'].historyRegions[historyRegionNameList[k]].point.element.label
#      L=len(odb.steps['Step-1'].historyRegions[historyRegionNameList[k]]-
          -.historyOutputs['PEEQ'].data)
      try:
          Peeq=open(result+'\\'+str(name)+'PEEQ.dat','r+')
          Peeq.readlines()
      except IOError:
          Peeq=open(result+'\\'+str(name)+'PEEQ.dat','w')
          List.write(str(name)+'PEEQ.dat\n')
      try:
          Mises=open(result+'\\'+str(name)+'MISES.dat','r+')
          Mises.readlines()
      except IOError:
          Mises=open(result+'\\'+str(name)+'MISES.dat','w')
          List.write(str(name)+'MISES.dat\n')
      try:
          Temp=open(result+'\\'+str(name)+'TEMP.dat','r+')
          Temp.readlines()
      except IOError:
          Temp=open(result+'\\'+str(name)+'TEMP.dat','w')
          List.write(str(name)+'TEMP.dat\n')
      try:
          StRate=open(result+'\\'+str(name)+'StRate.dat','r+')
          StRate.readlines()
      except IOError:
          StRate=open(result+'\\'+str(name)+'StRate.dat','w')
          List.write(str(name)+'StRate.dat\n')
      for j in range(1,L):
           Str=odb.steps['Step-1'].historyRegions[historyRegionNameList[k]].
                historyOutputs['PEEQ'].data[j]
           Tem=odb.steps['Step-1'].historyRegions[historyRegionNameList[k]].
                historyOutputs['TEMP'].data[j]
           Mis=odb.steps['Step-1'].historyRegions[historyRegionNameList[k]].
                historyOutputs['MISES'].data[j]
           E11=odb.steps['Step-1'].historyRegions[historyRegionNameList[k]].
```

```
            historyOutputs['ER11'].data[j]
        E22=odb.steps['Step-1'].historyRegions[historyRegionNameList[k]].
            historyOutputs['ER22'].data[j]
        E33=odb.steps['Step-1'].historyRegions[historyRegionNameList[k]].
            historyOutputs['ER33'].data[j]
        E12=odb.steps['Step-1'].historyRegions[historyRegionNameList[k]].
            historyOutputs['ER12'].data[j]
        E13=odb.steps['Step-1'].historyRegions[historyRegionNameList[k]].
            historyOutputs['ER13'].data[j]
        E23=odb.steps['Step-1'].historyRegions[historyRegionNameList[k]].
            historyOutputs['ER23'].data[j]
        PEEQRate=sqrt(E11[1]*E11[1]+E22[1]*E22[1]+E33[1]*E33[1]-E11[1]*E33[1]-E11[1]*E22[1]-
                    E33[1]*E22[1]+3*(E12[1]*E12[1]+E13[1]*E13[1]+E23[1]*E23[1]))
        Peeq.write(str(Str[0])+"         "+str(Str[1])+'\n')
        Temp.write(str(Tem[0])+"         "+str(Tem[1])+'\n')
        Mises.write(str(Mis[0])+"         "+str(Mis[1])+'\n')
        StRate.write(str(E11[0])+"         "+str(PEEQRate)+'\n')
        file11.write(str(Str[0])+"         "+str(Str[1])+'\n')
        file1.write(str(Tem[0])+"         "+str(Tem[1])+'\n')
        file2.write(str(Mis[0])+"         "+str(Mis[1])+'\n')
        file3.write(str(E11[0])+"         "+str(PEEQRate)+'\n')
    Peeq.close()
    Mises.close()
    Temp.close()
    StRate.close()
file11.close()
file1.close()
file2.close()
file3.close()
Vp=Vp+StepVp
List.close()
odb.close()
```

A.2 Matlab

```
clear all
close all
name='bior2.2';
list=fopen('List.dat','r');
s=2; % computes an estimate of H^s norm
nofig=1;
while 1
    file=fgetl(list);
    if isempty(file)==1,
       break;
    end
    path=load('-ascii',file);
    %n=2^11-1;
    %x=0:1/n:1;
    Sob=0;
    SobY=0;
    Vp=0;
    No=1;
    pl=[];
    pl(1)=1;
    for ll=2:length(path)
        if path(ll)<path(ll-1),
            No=No+1;
            pl(No)=ll;
        end
    end
    pl(No+1)=length(path);
    Sobarray=0;
    SobarrayY=0;
    SobDiv=0;
    for j=2:No+1
```

```
        Sob=0;
        norma_Hs=[];
        figure(nofig)
        mode=mod(nofig,4);
        switch lower(mode)
           case {1}
              nameplot='PEEQ';
           case 2
              nameplot='Mises';
           case 3
              nameplot='Tempereture';
           otherwise
              nameplot='Strain Rate';
        end
        subplot(2,3,1)
        norma_Ltwo=[];
        y=path(pl(j-1):pl(j)-1,2); % family of given signals
        x=path(pl(j-1):pl(j)-1,1);
        plot(x,y,'black')
        title(file)
%         text(-pi/4,sin(-pi/4),'\leftarrow sin(-\pi\div4)',...
%              'HorizontalAlignment','left')
        xlabel('Time(s)')
        ylabel(nameplot)
        hold on
        maxlev=wmaxlev(size(y),name);
        l=maxlev;
        C=[];
        L=[];
        [C,L] = wavedec(y,l,name);     % computes wavelet coefficients
        energy=C(1:L(1))*C(1:L(1))';
        for ii=2:length(L)-1
             %computes H^s norm of y(x) as weighted sum of wav. coeffs.
            Sob=Sob+ norm(2^(s*(ii-1)).*C(L(ii-1)+1:L(ii)))^2;
        end
        C(L(3)+1:end)=0;
        Y = WAVEREC(C,L,name);
        subplot(2,3,4)
        plot(x,Y,'black')
        xlabel('Time(s)(Filtered Data)')
        ylabel(nameplot)
        hold on
        [C1,L1]=wavedec(Y,l,name);
        energyY=C1(1:L1(1))*C1(1:L1(1))';          %computes L^2 norm of y(x)
        norma_Ltwo=[norma_Ltwo energy];       %stores values of L^2 norm
       %norma_Ltwo=[norma_LtwoY energyY];
        for ii=2:length(L1)-1
            SobY=SobY+ norm(2^(s*(ii-1)).*C1(L1(ii-1)+1:L1(ii)))^2;
        end
        norma_Hs=[norma_Hs Sob];           %stores values of H^1 norm
        Sobarray(j-1)=Sob;
        SobarrayY(j-1)=SobY;
        Vp(j-1)=(j-2)*100+200;
        subplot(2,3,[2,5])
        plot(Vp,Sobarray,'black')
        xlabel('Velocity(m/s)')
        ylabel('Sobolev')
        if j>2
            SobDiv(j-1)=Sobarray(j-1)-Sobarray(j-2);
            subplot(2,3,[3,6])
            plot(Vp,SobDiv,'black')
            xlabel('Velocity(m/s)')
            ylabel('Jump in Sobolev value')
        else
            SobDiv(j-1)=0;
        end
        pause
    end
```

```
    nofig=nofig+1;
end
```

Appendix B

Code for peening effect model

B.1 Python code for making the model

```
import os
import shutil
from abaqus import *
from abaqusConstants import *
from part import *
from material import *
from section import *
from assembly import *
from step import *
from interaction import *
from load import *
from mesh import *
from job import *
from sketch import *
from visualization import *
from connectorBehavior import *
from abaqus import getInputs
import fileinput
from shutil import move
from odbAccess import *
from array import *
from Numeric import *
from math import *
from random import *
################### DISTANCE ############################
def dist(A,x,y):
    distance=sqrt((A[0]-x)**2+(A[1]-y)**2)
    return distance
################### OTHER POINTS ########################
def other(points,diameters):
    posfind=False
    otherp=[]
    c=[]
    for xx in range(-50,50):
        x=xx*0.001
        rangey=int(sqrt(abs(0.050**2-x**2))*1000)
        for yy in range(-rangey,rangey):
            y=yy*0.001
            c.append([x,y])
            for rr in range(len(points)):
                el=points[rr]
                dia=diameters[rr]*10**-3
                dis=dist(el,x,y)
                if dis<dia/2:
                    posfind=False
                    break
                else:
```

```
                    posfind=True
            if posfind:
                otherp.append([x,y])
    return otherp
##########################################################
################ GRAVITY ################################
#def Gravity(otherp,MDia):
    otherpcopy=otherp+[1]
    otherpcopy.remove(otherpcopy[-1])
    gravp=[]
    for el in otherp:
        atemp=[]
        if el in otherpcopy:
            atemp.append(el)
            for el1 in otherpcopy:
                dis=dist(el,el1[0],el1[1])
                if dis<=MDia:
                    atemp.append(el1)
            gravx=0
            gravy=0
            for a in atemp:
                gravx+=a[0]
                gravy+=a[1]
            gravp.append([gravx/len(atemp),gravy/len(atemp)])
            for ele in atemp:
                try:
                    otherpcopy.remove(ele)
                except ValueError:
                    continue
        else:
            continue
    return gravp
##########################################################
###############V Impact###################################
def Vimpact(Dp,P0,T0,rhop):
        Dp=Dp/1000 #mm
        Ae=6.13**2*3.1415/4 #mm2
        At=2**2*3.1415/4 #mm2
        Ln=120 #nozzle length mm
        gamma=1.4 #unitless
        Mol=14.0067
        Rspec=0.297 #KJ/kgK
        rho0=10**3*P0/Rspec/T0 #kg/m^3

        k1=218.0629-243.5764*gamma+71.7925*gamma**2
        k2=-0.122450+0.281300*gamma
        M=(k1*Ae/At+1-k1)**k2

        Tgas=T0/(1+((gamma-1)/2)*M**2)
        Vgas=M*sqrt(gamma*Rspec*Tgas*1000)
        rho=rho0/(1+M**2*(gamma-1)/2)**(1/(gamma-1))

        mu0=0.01781
        a=0.555*527.07+111
        b=0.555*Tgas*1.8+111
        mu=mu0*(a/b)*(Tgas*1.8/540.99)**(3/2)*10**(-3) #N s/m2
        Ln=Ln*0.001
        Dp=Dp*0.001
        vp18=-exp(-sqrt(3*rho*Ln/rhop/Dp))+1
        vp20=-exp(-9*mu*Ln/(rhop)/Dp**2/Vgas)+1
        Vp=0.5*Vgas*(vp18-vp20)
        Re=rho*Dp*abs(Vgas-Vp)/mu
        rhost=Re*(-1.04+2.27*M-0.21*M**2)
        Lst=Re*(0.97-0.02*M)
        Vimpact=Vp*exp(-3*rhost*Lst/(4*rhop*Dp))
        results=[Vp,M,Re,mu]

        return results
```

```
############################################################
def Tparticle(Vp,Temp0,Dp,rhop):
    Ln=120
    Dp=Dp/1000 #mm
    a=exp(-Vp[1])/(1+17*Vp[1]/Vp[2])
    b=0.666+0.333*exp(-17*Vp[1]/Vp[2])
    Cp=960 #J/kgK
    k=130 #W/mK
    Pr=Cp*Vp[3]/k
    Nu=2*a+0.459*b*(Vp[2]**0.55)*(Pr**0.33)
    Tp=Temp0+exp(6*Nu*Ln/(rhop*Vp[0]*Cp*DShot**2))
    return Tp
############################################################
def modeling(DShot,nameP,l):
    DShot=float(DShot)
    if DShot<10:
        meshsize=0.001
    else:
        meshsize=0.002
    mdb.models['Model-1'].ConstrainedSketch(name='__profile__', sheetSize=200.0)
    mdb.models['Model-1'].sketches['__profile__'].ArcByCenterEnds(center=(0.0, 0.0)
        , direction=COUNTERCLOCKWISE, point1=(0.0, (DShot/2)*10**-3),
        point2=(0.0, -(DShot/2)*10**-3))
    mdb.models['Model-1'].sketches['__profile__'].Line(point1=(0.0,
        (DShot/2)*10**-3), point2=(0.0, -(DShot/2)*10**-3))
    mdb.models['Model-1'].sketches['__profile__'].ConstructionLine(point1=(0.0,
        -100.0), point2=(0.0, 100.0))
    mdb.models['Model-1'].Part(dimensionality=THREE_D,
        name=nameP, type=DEFORMABLE_BODY)
    mdb.models['Model-1'].parts[nameP].BaseSolidRevolve(angle=360.0,
            flipRevolveDirection=OFF, sketch=
            mdb.models['Model-1'].sketches['__profile__'])
    del mdb.models['Model-1'].sketches['__profile__']
    mdb.models['Model-1'].parts[nameP].PartitionCellByPlanePointNormal(cells=
        mdb.models['Model-1'].parts[nameP].cells.getSequenceFromMask(('[#1 ]',
        ), ), normal=mdb.models['Model-1'].parts[nameP].datums[1], point=
        mdb.models['Model-1'].parts[nameP].InterestingPoint(
        mdb.models['Model-1'].parts[nameP].edges[0], CENTER))
    mdb.models['Model-1'].parts[nameP].PartitionCellByPlaneThreePoints(cells=
        mdb.models['Model-1'].parts[nameP].cells.getSequenceFromMask(('[#3 ]',
        ), ), point1=mdb.models['Model-1'].parts[nameP].vertices[1], point2=
        mdb.models['Model-1'].parts[nameP].vertices[0], point3=
        mdb.models['Model-1'].parts[nameP].vertices[2])
    mdb.models['Model-1'].parts[nameP].PartitionCellByPlanePointNormal(cells=
        mdb.models['Model-1'].parts[nameP].cells.getSequenceFromMask(('[#f ]',
        ), ), normal=mdb.models['Model-1'].parts[nameP].edges[0], point=
        mdb.models['Model-1'].parts[nameP].InterestingPoint(
        mdb.models['Model-1'].parts[nameP].edges[5], CENTER))
    mdb.models['Model-1'].parts[nameP].SectionAssignment(
        offset=0.0, offsetField='', offsetType=MIDDLE_SURFACE, region=Region(
        cells=mdb.models['Model-1'].parts[nameP].cells.getSequenceFromMask(
        mask=('[#ff ]', ), )), sectionName='Particles')
    mdb.models['Model-1'].parts[nameP].seedPart(deviationFactor=0.1, size=
        meshsize)
    mdb.models['Model-1'].parts[nameP].generateMesh()
############################################################
def position(DShot,nameP,Pnum,p,levelshot):
      Assname=nameP+'-'+str(Pnum)
      mdb.models['Model-1'].rootAssembly.Instance(dependent=ON, name=Assname,
        part=mdb.models['Model-1'].parts[nameP])
      mdb.models['Model-1'].rootAssembly.translate(instanceList=(Assname, ),
        vector=(0.0,0, DShot/2*10**-3))
      mdb.models['Model-1'].rootAssembly.translate(instanceList=(Assname, ),
        vector=(p[0],  p[1],0) )
   #   levelshot=sum(diameters)-DShot
      mdb.models['Model-1'].rootAssembly.translate(instanceList=(Assname, ),
          vector=(0, 0, levelshot*10**-3))
############################################################
```

```
def predefined(nameP,Pnum,Vp,Temp0):
    Assname=nameP+'-'+str(Pnum)
    mdb.models['Model-1'].Velocity(distributionType=MAGNITUDE, field='', name=
        Assname+'Vel', omega=0.0, region=Region(
        cells=mdb.models['Model-1'].rootAssembly.instances[Assname].cells.getSequenceFromMask(
        mask=('[#ff ]', ), ),
        faces=mdb.models['Model-1'].rootAssembly.instances[Assname].faces.getSequenceFromMask(
        mask=('[#fffff ]', ), ),
        edges=mdb.models['Model-1'].rootAssembly.instances[Assname].edges.getSequenceFromMask(
        mask=('[#3ffff ]', ), ),
        vertices=mdb.models['Model-1'].rootAssembly.instances[Assname].
        vertices.getSequenceFromMask(
        mask=('[#7f ]', ), )), velocity1=0.0, velocity2=0.0, velocity3=-Vp*1000.0)
    mdb.models['Model-1'].Temperature(createStepName='Initial',
        crossSectionDistribution=CONSTANT_THROUGH_THICKNESS, distributionType=
        UNIFORM, magnitudes=(Temp0, ), name=Assname+'Temp', region=Region(
        cells=mdb.models['Model-1'].rootAssembly.instances[Assname].cells.getSequenceFromMask(
        mask=('[#ff ]', ), ),
        faces=mdb.models['Model-1'].rootAssembly.instances[Assname].faces.getSequenceFromMask(
        mask=('[#fffff ]', ), ),
        edges=mdb.models['Model-1'].rootAssembly.instances[Assname].edges.getSequenceFromMask(
        mask=('[#3ffff ]', ), ),
        vertices=mdb.models['Model-1'].rootAssembly.instances[Assname].-
        -vertices.getSequenceFromMask(
        mask=('[#7f ]', ), )))
##########################################################
def touchcount(points,diameters):
    touchno=[]
    c=[]
    for xx in range(-50,50):
        x=xx*0.001
        rangey=int(sqrt(abs(0.050**2-x**2))*1000)
        for yy in range(-rangey,rangey):
            y=yy*0.001
            c.append([x,y])
            count=0
            for rr in range(len(points)):
                el=points[rr]
                dia=diameters[rr]*10**-3
                dis=dist(el,x,y)
                if dis<dia/2:
                    count=count+1
            touchno.append([x,y,count])
    return touchno
##########################################################
fields = (('Coverage=','10'),('D(Rosin-Rammler)=','16.87'),('Q(Rosin-Rammler)=','5.52')
        ,('Process Temp.(K)=','850'),('Process Press.(MPa)=','2.2'),('Particle Density(kg/m^3)=','2700'))
cov,Drr,Qrr,Temp0,Pres0,rhop=getInputs(fields=fields, label='Particles',dialogTitle='Properties', )
cov=int(cov)
Drr=float(Drr)
Qrr=float(Qrr)
Temp0=float(Temp0)
Pres0=float(Pres0)
rhop=float(rhop)
finaltouchp=[]
PartVel=[]
PartTemp=[]
levelshots=[]
diameters=[]
Pnum=0
for i in range(cov):
    ts=[]
    Area=pi*0.5**2
    otherp=[]
    points=[]
    DShot=0
    while DShot<7:
        DShot=uniform(0,1)
```

```
        DShot=exp(log(Drr)*(-log(1-DShot))**(1/Qrr))
    diameters.append(DShot)
    nameP='Shot'+str(len(diameters))+'-'+str(int(DShot))
    modeling(DShot,nameP,len(diameters))
    r=uniform(0,0.05)
    ang=uniform(0,2*pi)
    a=r*cos(ang)
    b=r*sin(ang)
    points.append([a,b])
    finaltouchp.append(points[-1])
    level=uniform(0,cov*60)
    position(DShot,nameP,Pnum,points[-1],level)
    levelshots.append(level)
    Vp=Vimpact(DShot,Pres0,Temp0,rhop)
    Tp=int(Tparticle(Vp,Temp0,DShot,rhop))
    PartVel.append(Vp[0])
    PartTemp.append(Tp)
    predefined(nameP,Pnum,Vp[0],Tp)
    otherp=other(points,diameters)
    times=[]
    while len(otherp)>0:
          Pnum=Pnum+1
          DShot=0
          while DShot<7:
            DShot=uniform(0,1)
            DShot=exp(log(Drr)*(-log(1-DShot))**(1/Qrr))
          diameters.append(DShot)
          nameP='Shot'+str(len(diameters))+'-'+str(int(DShot))
          modeling(DShot,nameP,len(diameters))
          ptemp=[]
          meanT=[]
          for j in range(20):
              try:
                   p=randint(1,len(otherp))
              except ValueError:
                   break
              p=otherp[p-1]
              ptemp.append(p)
              points.append(p)
              otherp=other(points,diameters)
              meanT.append(len(otherp))
              points.remove(p)
          p=ptemp[meanT.index(min(meanT))]
          points.append(p)
          finaltouchp.append(points[-1])
          level=uniform(0,cov*60)
          levelshots.append(level)
          position(DShot,nameP,Pnum,p,level)
          Vp=Vimpact(DShot,Pres0,Temp0,rhop)
          Tp=int(Tparticle(Vp,Temp0,DShot,rhop))
          times.append(level/Vp[0]/1000000)
          PartVel.append(Vp[0])
          PartTemp.append(Tp)
          predefined(nameP,Pnum,Vp[0],Tp)
          otherp=[]
          otherp=other(points,diameters)
maxL=max(levelshots)
time=max(times)
mdb.models['Model-1'].steps['Step-1'].setValues(timePeriod=time*1.2)
x=[]
y=[]
touchno=touchcount(finaltouchp,diameters)
result=open('D:\\Model1-Cov'+str(cov)+'.dat','w')
result.write('Number of partcle         x            y           diameter       Level
           Velocity     Temperature')
result.write('\n')
nshot=0
#for j in range(len(finaltouchp)):
```

```
    nshot=1+nshot
    result.write(str(nshot)+'    '+str(finaltouchp[j][0])+'    '+str(finaltouchp[j][1])+
    '     '+str(diameters[j])+'    '+str(levelshots[j])+'     '+str(PartVel[j])+
    '     '+str(PartTemp[j])+'\n')
result.write('\n')
result.write('\n')
result.write('Touch Counter:')
result.write('\n')
su=0
ma=0
for el in touchno:
    result.write(str(el[0])+'    '+str(el[1])+'    '+str(el[2])+'\n')
    su=su+el[2]
    if ma<el[2]:
        ma=el[2]
percent=zeros(ma+1)
for el in touchno:
    percent[el[2]]=percent[el[2]]+1
su=float(su)/len(touchno)
for k in range(len(percent)):
    result.write(str(k)+'x times impacted:'+str(percent[k])+
                '('+str(100*percent[k]/len(touchno))+'%)'+'\n')
result.write('Average touch='+str(su)+'\n')
result.write('max touch='+str(ma)+'\n')
result.write('Simulation Time='+str(time))
result.close()
```

B.2 Code for obtaining the result

```
from odbAccess import *
from array import *
from Numeric import *
from math import *
from part import *
from material import *
from section import *
from assembly import *
from step import *
from interaction import *
from load import *
from mesh import *
from job import *
from sketch import *
from visualization import *
from connectorBehavior import *
##import psyco ; psyco.jit()
##from psyco.classes import *
#### Reading the Displacement###################################
#models=['Model1','Model2','Model3','Model4']
nameee='Model1-700Ext-Combined'
odb = openOdb(path='F:\\Temp\\Thesis\\'+nameee+'.odb')
nodeindex=[]
nodelabel=[]
Z=[]
assembly = odb.rootAssembly
add=True
#for node in assembly.nodeSets['TARGET'].nodes[0]:
       a=node.coordinates[2]
       nodeindex.append(node.label)
#       if not(a in Z):
              for el1 in Z:
                     if abs(a-el1)>0.0001:
                            add=True
                     else:
                            add=False
                            break
```

```
            if add:
               Z.append(a)
               Z=list(sort(Z))
#instance=assembly.instances['PART-1-1']
elset=assembly.elementSets.keys()
numNodes = numElements = 0
elements=assembly.elementSets[elset[0]].elements[0]
nodes=assembly.nodeSets['TARGET'].nodes[0]
Frames=odb.steps['Step-1'].frames
k=len(Z)
check=0
MeanS11=zeros([k,2],'f')
MeanPEEQ=zeros([k,2],'f')
s11=0
s22=0
Time=[]
fram=0
S11=open('D:\\S11-'+nameee+'.dat','w')
pe1=open('D:\\PEEQ-'+nameee+'.dat','w')
S11.write('Depth'+'       ')
pe1.write('Depth'+'       ')
#for lastFrame in Frames:
#S11.write(str(lastFrame.frameValue)+'        ')
#pe1.write(str(lastFrame.frameValue)+'        ')
lastFrame=Frames[-1]
stress = lastFrame.fieldOutputs['S']
peeq=lastFrame.fieldOutputs['PEEQ']
field1=stress.getSubset(region=assembly.elementSets[elset[0]])
field2=peeq.getSubset(region=assembly.elementSets[elset[0]])
Time.append(lastFrame.frameValue)
#for v in field1.values:
   try:
          node1=nodes[nodeindex.index(v.nodeLabel)]
   except ValueError:
          continue
   for ell in Z:
          if abs(node1.coordinates[2]-ell)<0.0001:
                 i=Z.index(ell)
                 break
   MeanS11[i][0]=MeanS11[i][0]+v.data[0]
   MeanS11[i][1]=MeanS11[i][1]+1
#for v in field2.values:
   try:
          node1=nodes[nodeindex.index(v.nodeLabel)]
   except ValueError:
          continue
   for ell in Z:
          if abs(node1.coordinates[2]-ell)<0.0001:
                 i=Z.index(ell)
                 break
   MeanPEEQ[i][0]=MeanPEEQ[i][0]+v.data
   MeanPEEQ[i][1]=MeanPEEQ[i][1]+1
S11.write('\n')
pe1.write('\n')
#for j in range(len(Z)):
       S11.write(str(Z[j])+'   ')
       pe1.write(str(Z[j])+'   ')
       #for i in range(len(Frames)):
       stress11=float(MeanS11[j][0])/MeanS11[j][1]
       peeq11=float(MeanPEEQ[j][0])/MeanPEEQ[j][1]
       S11.write(str(stress11)+'        ')
       pe1.write(str(peeq11)+'        ')
       S11.write('\n')
       pe1.write('\n')
pe1.close()
S11.close()
odb.close()
```

Appendix C

Grain size measurement

C.1 Matlab code for grain size

```
%This subroutin works based on PEARSON VII curve fitting
close all
clear all
 % for long time standard powder Al 0 angle
betag_std=0.018555;
betac_std=0.0021809;
 %for long time std powder Al 45 angle
%betag_std=0.033003468495957;
%betac_std=8.224582713023463e-005;

clc
t=1;
kk=0;
def = {'Standard','139','0.2291','1.955','1125.9','242.8','66.4','2.2'};
#while t>0
    kk=kk+1;
    dlgTitle = 'Curve Parameters';
    prompt = {'Name','Diffraction Angle=','\lambda:','FWHM','a0:','a1:','a2:','a3:'};

    lineNo=1;
    answer = inputdlg(prompt,dlgTitle,lineNo,def);
    name=char(answer(1));
    DiffPo=str2double(answer(2));
    lambda=str2double(answer(3));
    FWHM=str2double(answer(4));
    a0=str2double(answer(5));
    a1=str2double(answer(6));
    a2=str2double(answer(7));
    a3=str2double(answer(8));
    def = {name,num2str(DiffPo),num2str(lambda),num2str(FWHM),num2str(a0),
           num2str(a1),num2str(a2),num2str(a3)};
    pixel=0:0.1:512;
    Y=a0./(1+4*(2^(1/a3)-1).*((pixel-a1)/a2).^2).^a3;
    pixmax=pixel(find(Y==max(Y)));
    DiffPo2=14*pixmax/152+DiffPo-7;

    check=max(Y)/2;
    FWVec=[0 0];
    k=1;
    L1=0;
    L2=pixmax;
    PixTemp=(L1+L2)/2;
    err=100;
    while abs(err)>0.001
        YTemp=a0./(1+4*(2^(1/a3)-1).*((PixTemp-a1)/a2).^2).^a3;
        err=YTemp-check;
        if err<0
```

```
            L1=PixTemp;
            PixTemp=(L2+PixTemp)/2;

        else
            L2=PixTemp;
            PixTemp=(L1+PixTemp)/2;
        end
    end
    FWVec(1)=PixTemp;
    L1=PixTemp;
    L2=512;
    PixTemp=(L1+L2)/2;
    err=100;
    while abs(err)>0.001
        YTemp=a0./(1+4*(2^(1/a3)-1).*((PixTemp-a1)/a2).^2).^a3;
        err=YTemp-check;
        if err>0
            L1=PixTemp;
            PixTemp=(L2+PixTemp)/2;

        else
            L2=PixTemp;
            PixTemp=(L1+PixTemp)/2;
        end
    end
    FWVec(2)=PixTemp;
    FWHM2=FWVec(2)-FWVec(1);
    calib=FWHM2/FWHM;
    Integral=0;
    for i=1:length(pixel)-1
        Y1=a0./(1+4*(2^(1/a3)-1).*((pixel(i)-a1)/a2).^2).^a3;
        Y2=a0./(1+4*(2^(1/a3)-1).*((pixel(i+1)-a1)/a2).^2).^a3;
        Integral=Integral+(pixel(i+1)-pixel(i))*(Y1+Y2)/2/calib;
    end
#    teta=calib.*pixel+DiffPo-512/2/calib;
    IntB=Integral/max(Y);
    Phi=FWHM/IntB;
    PHI=DiffPo/2;
    LSch=180*lambda/(FWHM*cos(pi*DiffPo/360)*pi);
    LInt=180*lambda/(IntB*cos(pi*DiffPo/360)*pi);
    IntBRad=IntB*pi/180;
    BetaC_Beta=2.0207-(0.4803*Phi)-1.7756*Phi*Phi;
    Betag_Beta=0.642+1.4187*((Phi-(2/3.142))^0.5)-2.2043*Phi+1.8706*Phi*Phi;
    BetaCh=BetaC_Beta*IntBRad;
    BetaGh=Betag_Beta*IntBRad;
    BetaCf=abs(BetaCh-betac_std);
    BetaGf=(BetaGh*BetaGh-betag_std*betag_std)^0.5;
    LPaper=lambda/(BetaCf*cos(pi*DiffPo/360));
#    MStrain=BetaGf/(4*tan(pi*DiffPo/360));
    format short g
    disp(name)
    DiffAng=sprintf('Diffraction Angle=%f',DiffPo2);
    disp(DiffAng)
    FWdisp=sprintf('FWHM=%f',FWHM);
    disp(FWdisp);
    Intdisp=sprintf('Integral Breadth=%f\n',IntB);
    disp(Intdisp);
    disp('Grain Size based on:');
    Scher=sprintf('Scherrer formula=%f',LSch);
    disp(Scher);
    Integ=sprintf('Integral Breadth=%f',LInt);
    disp(Integ);
    Keijs=sprintf('Keijser Paper=%f',LPaper);
    disp(Keijs);
    MicroSt=sprintf('Micro Strain=%f',MStrain);
    disp(MicroSt)
    figure(kk)
    plot(teta,Y,'black','LineWidth',2)
```

```
    hold on
    Yhalf=[max(Y)/2 max(Y)/2];
    plot(14.*FWVec./512+DiffPo-7,Yhalf,'red')
    xlabel('Angle 2\theta')
    ylabel('Intensity')
    title(name)
    text(teta(40),0.9*max(Y),Keijs);
    text(teta(40),0.9*max(Y)-0.1*max(Y),FWdisp);
    text(teta(40),0.9*max(Y)-0.2*max(Y),Intdisp);
    %text(teta(40),max(Y)-0.3*max(Y),DiffAng);
    path1=strcat('F:\E\Projects\Cold Spray\XRD\',name,'.jpg');
    path2=strcat('F:\E\Projects\Cold Spray\XRD\',name,'.fig');
    saveas(figure(kk),path1)
    saveas(figure(kk),path2)

end
```